

Diagnostic of the solar photosphere with high spatial resolution using CH, CN and continuum spectral bands

Dissertation

zur Erlangung des Doktorgrades
der Mathematisch-Naturwissenschaftlichen Fakultäten
der Georg-August-Universität zu Göttingen

vorgelegt von

Vasily Zakharov
aus Moskau / Russland

Göttingen 2006

Bibliografische Information Der Deutschen Bibliothek

Die Deutsche Bibliothek verzeichnet diese Publikation in der Deutschen Nationalbibliografie; detaillierte bibliografische Daten sind im Internet über <http://dnb.ddb.de> abrufbar.

D7

Referent: Prof. Dr. F. Kneer

Korreferent: Prof. Dr. S. K. Solanki

Tag der mündlichen Prüfung: 24.03.2006

Copyright © Copernicus GmbH 2006

ISBN 3-936586-54-3

Copernicus GmbH, Katlenburg-Lindau

Druck: Schaltungsdienst Lange, Berlin

Printed in Germany

Contents

Contents	3
Summary	5
1 Introduction	7
2 High resolution imaging	17
2.1 Phase diversity image reconstruction	17
2.2 Observations	23
2.3 Data reduction	25
2.3.1 Dark frame and flat field	25
2.3.2 JPDS reconstruction	26
2.4 Results	27
3 High resolution spectroscopy of the solar photosphere	33
3.1 Observations	33
3.2 Data reduction of the spectra	36
3.2.1 Dark frame	37
3.2.2 Flat field	37
3.2.3 Doppler shift and line width	43
3.2.4 Slit position	45
3.2.5 Intensity	46
3.2.6 Bright Point Index	48
3.2.7 Line depression	49
3.3 Spectroscopy of small-scale magnetic features at the disc center	49
3.3.1 Main properties	49
3.3.2 Individual cases	54
3.3.3 Intensity contrast	60
3.3.4 Bright point index	62
3.3.5 Line depression	65
3.4 Spectroscopy of small-scale magnetic features near the limb	67
3.4.1 Main properties	67
3.4.2 Intensity contrast	72
3.4.3 Bright point index	74
3.4.4 Line depression	77
3.4.5 Strong velocity shifts seen in upper photosphere	78

3.5	Continuum intensity	80
3.6	Spectroscopy of large-scale magnetic phenomena	80
3.6.1	Pore	80
3.6.2	Sunspot	85
3.6.3	Velocity reference	85
4	Radiative MHD Simulations	89
4.1	MHD model	89
4.2	Radiative transfer and line synthesis	91
4.3	Center-to-limb variation	94
4.4	Results of radiative simulations at low resolution	97
4.4.1	Limb darkening	97
4.4.2	CLV of intensity contrast	101
4.5	MDI observations	103
4.5.1	Radiative simulations	106
4.5.2	Results of simulations and comparison with MDI observations . .	107
4.6	High resolution structure of the solar surface near the limb	112
4.6.1	High resolution observations	112
4.6.2	Simulated faculae	114
4.6.3	Origin of faculae and narrow, dark lanes	115
	Conclusions and outlook	123
	A Filter profiles	127
	B Contribution functions	131
	Bibliography	133
	Acknowledgements	143
	Lebenslauf	145

Summary

This thesis describes high-resolution imaging and high-resolution spectroscopic observations in the blue continuum and in molecular bands, their analysis and the interpretation of results. These refer to small-scale photospheric features, e.g. G-band bright points, ribbons, faculae etc. In addition, descriptions are given of the radiative diagnostics in the continuum of three-dimensional MHD simulations that have been carried out in order to study the physical structure of faculae and the center-to-limb variation of their brightness. The projects which have been carried out as part of this thesis and the most important results are:

- High-resolution simultaneous observations of the Sun in three spectral bands, the blue continuum (436.4 nm), the G band (430.5 nm) and the violet CN band-head (387.9 nm), have been carried out with the 1-m Swedish Solar Telescope (SST). Near diffraction limited spatial resolution was achieved in the filtergrams by means of the Joint Phase Diverse Speckle and the Multiframe Blind Deconvolution reconstruction techniques.
- The contrast of the photospheric bright points was studied in all three observed spectral ranges and compared with the computational predictions by other researches. It was found that on average over observed bright points their contrast in the blue CN band-head images is 1.4 times higher than that in the G-band images. This disagrees with the predictions of 3-D MHD simulations. The reasons for this discrepancy are discussed.
- High-resolution spectroscopic observations of small-scale magnetic activity manifestations in the solar photosphere were carried out simultaneously in the blue CN band-head (387.588–388.473 nm) and in a blue spectral band (436.1–436.9 nm) containing absorption lines of CH with the spectrograph installed on the SST. The analysis of the line-core depression of the CN and CH lines and the line-core intensity contrast of the bright points yielded that the bright points appear brighter in the CN than in the CH lines in the same spectral band.
- High-resolution narrowband images in the continuum near $\lambda = 705.7$ nm were obtained with the SST by applying the MFBD reconstruction technique. It is shown that magnetic features observed near the solar limb are accompanied by facular brightenings with a high contrast. The granulation pattern in plages near the limb has a three-dimensional appearance.
- Radiative Transfer computations in the continuum at $\lambda = 705.7$ nm in 3-D MHD models computed by the Max-Planck-Institut für Sonnensystemforschung and Uni-

versity of Chicago MHD groups have carried out. The studied models have different amount of average magnetic flux, i.e. 10 G, 200 G and 4000 G as well as MHD simulations of a pore (Cameron et al. 2004). The radiative transfer was computed by means of the STOPRO code. It was shown that concentrations of strong magnetic fields are responsible for the appearance of the 3-D granulation pattern, faculae, narrow dark lanes (at the limbward side of some granules) etc, whose radiative properties are very close to those obtained from the observations. The physical parameters of the atmosphere, which lead to the formation of photospheric phenomena as observed near the limb are discussed.

- Radiative Transfer computations in the continuum at $\lambda = 676.8$ nm and of the full Stokes vector in the Ni I line at $\lambda = 676.8$ nm in many snapshots of MHD models with different amounts of magnetic flux were carried out with the STOPRO code. The investigation with low spatial resolution of the center-to-limb variation (CLV) of the continuum contrast were analysed. The magnitude of the limb darkening in the simulations was directly compared with the observations by Neckel (1996). The results of Stokes-vector computations of the Ni I line were properly adapted to conditions of the MDI instrument on the SOHO spacecraft and directly compared with the observations obtained with it by Ortiz et al. (2002).

1 Introduction

The Sun is a special object in stellar astrophysics. It is the most prominent body in our solar system and contains approximately 98% of the total mass in the solar system. The Sun can be observed from Earth with high spatial resolution. Its outer visible layer is called the photosphere, which has a temperature of about 5780 K and emits 99.99 % of the energy generated in the solar interior by nuclear fusion, most of it in the visible spectral range. The solar spectrum consists of a continuum with thousands of dark absorption lines superposed. The lines are called Fraunhofer lines, and the solar spectrum is sometimes called the Fraunhofer spectrum. These lines are produced primarily in the photosphere.

Spectra of the CH and the CN molecules in the Sun

CH is an important molecule in cool stars. Its absorption bands extend from the near-ultraviolet to the mid-infrared with very strong contributions in the visible. The roughly 1 nm wide band near $\lambda = 430$ nm which contains CH lines is called the G band. At low spectral resolution this band-head resembles a single spectral line to which Fraunhofer (1817) assigned the letter "G". Between $429.5 \text{ nm} < \lambda < 431.5 \text{ nm}$ it is dominated by about 746 transitions 90% of them belonging to the $A^2\Delta - X^2\Pi$ electronic system (Jorgensen et al. 1996) of the CH molecule. The G band contains also many blends of other species like Fe, Ti, Ni, Cr, Ca, etc. In Fig 1.1 the mean solar spectrum near the G band at the disc center is presented, as observed by a Fourier Transform Spectrometer (FTS, Brault & Neckel 1987) operating at the Mc-Math telescope on Kitt Peak.

Another diatomic molecule, cyanogen CN, produces an absorption band in the blue of the solar spectra. The blue CN band-head is located near $\lambda = 388$ nm and contains absorption lines of the CN molecule owing to transitions of the $B^2\Sigma^+ - X^2\Sigma^+$ electronic system. In Fig 1.2 a section of the mean solar spectrum near the blue CN band-head at the disc center taken from the FTS atlas is presented. Additionally, many weak CH lines ($\log(gf) \leq -5$) of the $A^2\Delta - X^2\Pi$ electronic system and several strong lines of the CH $B^2\Sigma^- - X^2\Pi$ system, as well as a number of atomic lines are present in this spectral domain.

Magnetic activity of the Sun

The magnetic activity of the Sun is responsible for most fascinating structures and processes visible in solar observations obtained from Earth and from space: sunspots, plages, prominences, coronal loops, mass ejections etc. The photosphere of the Sun offers the oppor-

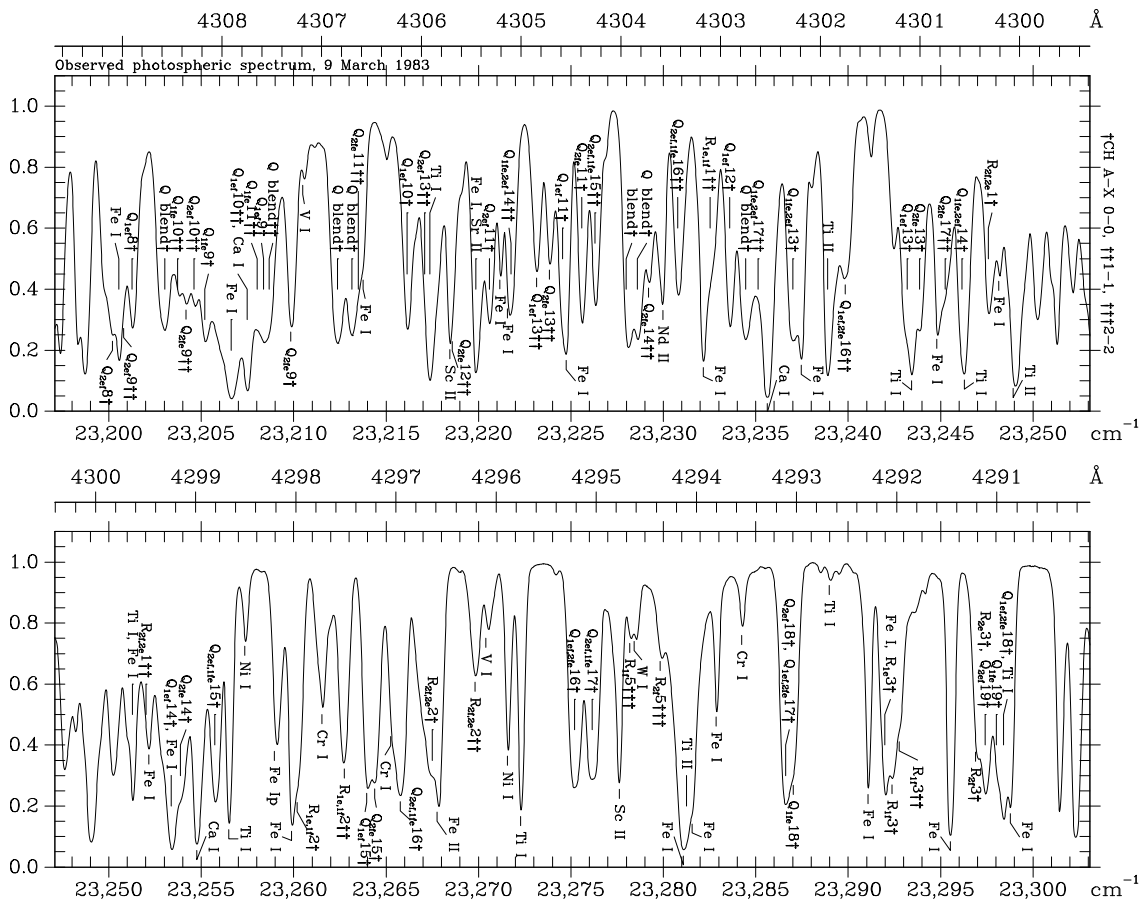


Figure 1.1: Fragment of the G-band spectrum taken from FTS atlas.

tunity to observe the structure and dynamics of magnetic fields at all scales directly with high spatial resolution. Well known magnetic features are the sunspots whose magnetic nature was firstly proved by George Elley Hale (1908), who measured the Zeeman splitting of spectral lines. The existence of small-scale magnetic fields was established by polarimetric observations of Sheeley (1967) afforded by the 80 cm solar image at the Kitt Peak National Observatory. Stenflo (1973) and Wiehr (1978) measured a magnetic field strength of about 2000 G in the network in quiet regions by analysing the weakening of Fe I lines (at 525.0 nm, 524.7 nm, 630.25 nm, 633.68 nm and 640.8 nm). Filter and spectrographic magnetogram studies (e.g. Keller et al. 1990, Zayer et al. 1990, Tarbell & Title 1977, Simon & Zirker 1974, Beckers & Schröter 1968) further supported the idea that the flux outside of sunspots was confined in isolated flux tubes with a unique field strength of 1500 - 2000 G, although many of magnetic flux was found in so-called "magnetic knots" - small dark structures equivalent to what we now call "micropores" (Topka et al. 1997, Spruit & Zwaan 1981). A review of early spectropolarimetric studies of the magnetic flux outside of sunspots can be found in Solanki (1993) or in Stenflo (1993). Many of observational studies carried out at up to 0.3 arcsec resolution generally supported the idea that virtually all of the small-scale structure in active and quiet network regions is composed of filamentary flux tubes of kilogauss strength (Nisenson et al. 2003, Berger & Title 2001, Muller et al. 2000, Berger et al. 1998, van Ballegooijen et al. 1998, Berger & Title 1996, Berger et al. 1995, Muller et al. 1994, Keller 1992, Muller & Keil

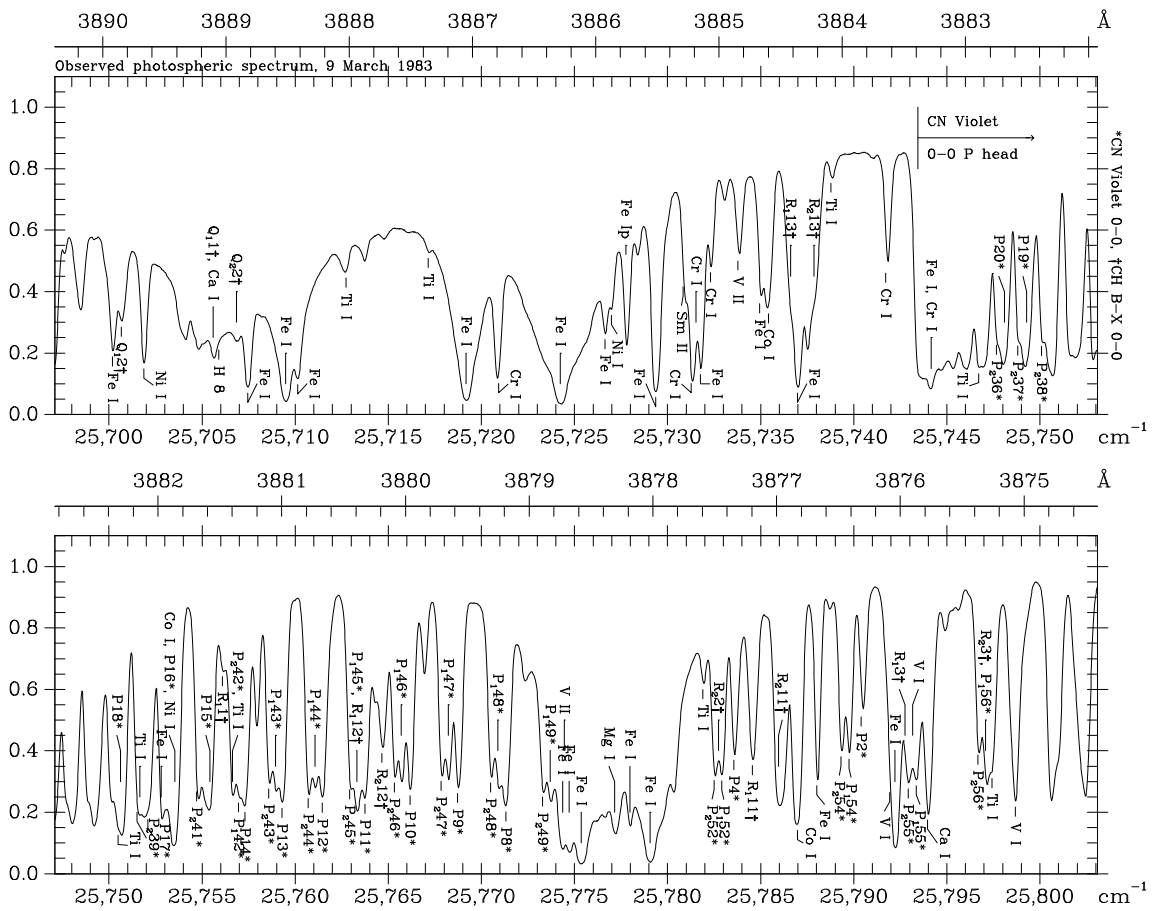


Figure 1.2: Fragment of the blue CN band-head spectrum taken from FTS atlas.

1983, Muller 1983).

G-band bright points as proxies of small-scale magnetic features

The G band has become the principal diagnostic to study photospheric magnetism at the highest achievable spatial resolution without polarimetry. Richard Muller made the first observations of the photosphere in the G band with the 50 cm refractor at the Pic du Midi Observatory, France. The obtained filtergrams displayed magnetic elements as tiny "network bright points" (Muller & Roudier 1984, Muller et al. 1989) with a size smaller than 0.5 arcsec. They showed that on 4308 Å filtergrams, bright points, the network elements, also called facular points, are more clearly identified, embedded in the granular pattern, which exhibit a high contrast. The bright points often have an elongated shape, sometimes being assembled in a string (see Fig. 1.3 for example). They appear around sunspots, in plage regions and in the network.

At the former 0.5 m Swedish Vacuum Solar Telescope (SVST) on La Palma, Spain, time series of up to 4 hours have been obtained under excellent seeing conditions (e.g. Berger et al. 1995, Berger et al. 1998, Berger & Title 1996). About 60% of the bright points are circular, while the remaining ones show an average eccentricity of 1.5. Berger

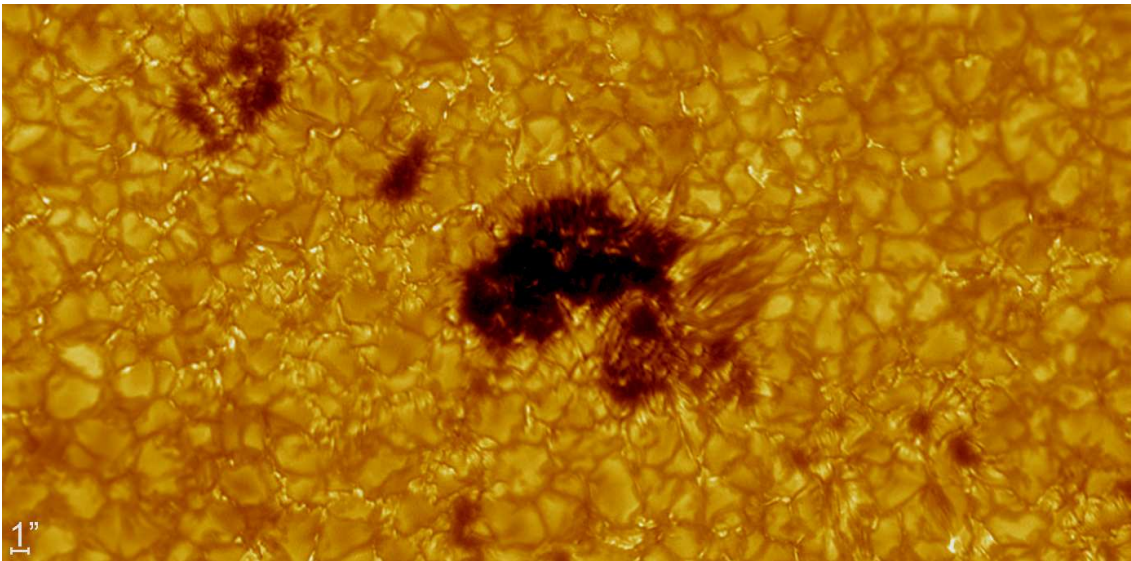


Figure 1.3: Joint phase diverse speckle reconstructed high-resolution G-band image of part of an active region NOAA0669 at 4.91° S, 8.14° E, $\mu = 0.97$, observed by the author with the SST on 7 September, 2004 at 14:30 (UT).

et al. (1995) measured the bright point diameter as 220 km (0.35 arcsec) on average, while the smallest bright point diameter so far seen is 120 km (0.17 arcsec) and the largest is 600 km (0.69 arcsec). Their measurements indicated a large spread in intrinsic bright point contrast. The measured area covered by bright points was found to be 1.8% of the total image area of the active region. Wiehr et al. (2004) measured, on basis of high-resolution observations including a speckle image reconstruction techniques (De Boer 1993), with the new 1-m Swedish Solar Telescope (SST), that the size of G-band bright points varies from 100 km to 300 km, with a most frequent value near 160 km (see also Puschmann & Wiehr (2006)). The lower limit of bright point size is still unknown. Berger et al. (1998) observed splitting and merging of bright points on an average time scale of 220 s and an average life time of 9 min. On timescales of the order of 100 s or less, significant morphological changes to all small-scale magnetic elements were observed by Berger & Title (1996). G-band observations with the Dutch Open Telescope (DOT, 45 cm reflector) by Nisenson et al. (2003) revealed a correlation time of BP motions of about 60 s. Keller (1992) and Keller & von der Lühe (1992) applied the method of speckle image reconstruction to their polarimetric data obtained with the SVST and showed that bright points exist co-spatially with strong magnetic fields. Co-temporal observations by Berger & Title (1996) of G-band images and magnetograms indicated that not all magnetic elements have an associated G-band bright point. Title & Berger (1996) made a modeling of bright point as a Gaussian bright core centered in a Gaussian dark surround and investigated changes of its intensity due to limited spatial resolution of the telescope. Their modeling showed that very small bright points, e.g. with a size of 0.1 arcsec, would disappear at a resolution of 0.4 arcsec whereas the magnetogram signal at the same resolution will remain non-zero. Bright points indicate both magnetic and non-magnetic features (Berger & Title 2001). Langhans et al. (2002) identified the former as intergranular downflows, and the latter as granular edges with upward motions which are a

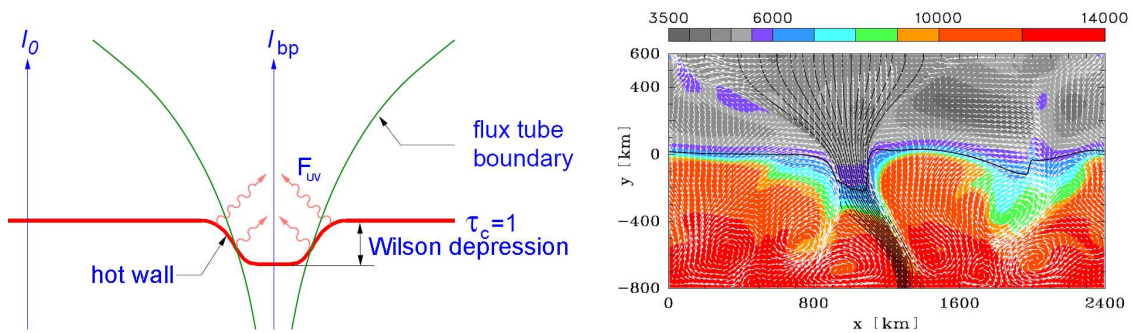


Figure 1.4: Flux tube modeling at different levels of sophistication. Left: magnetostatic diagram. Right: snapshot of a 2-D MHD simulation (O. Steiner, Kiepenheuer Institut in Freiburg) of a magnetic flux sheet, black and white arrows indicate magnetic field and velocity field, respectively. The temperature field is rendered with a color scale given in Kelvin.

source of confusion in magnetic element studies. Further investigations showed that *"All G-band bright points, properly distinguished from granulation brightenings, are magnetic in nature"* - Berger & Title (2001). They also showed that bright points are co-spatial and co-morphous with associated magnetic flux concentrations.

Recently, Berger et al. (2004) obtained G-band images co-temporal with the magnetograms and Dopplergrams of a remnant active region near the disc center with the SST and achieved an unprecedented spatial resolution on the order of 0.1 arcsec using high-resolution image reconstruction techniques. They found that magnetic flux as seen in both the magnetogram and the G-band image is typically structured into larger, amorphous, "ribbons" which are not resolved into individual flux tubes (see below). The higher values of the magnetic flux are found in localized concentrations embedded within the "ribbons". The Dopplergrams indicate relative downflows associated with all magnetic elements with some indication that higher downflows occur adjacent to the peak magnetic flux location.

Flux-tube models

G-band bright points are a manifestation of magnetic elements, which are concentrations of magnetic flux in photospheric layers. The basic theoretical picture of each magnetic feature is an isolated tube of magnetic flux. 90% or more of the network magnetic field is in form of magnetic flux tubes with a field strength of the order of 1.5 kG and typically a diameter of 100 km. They rise from below the solar surface in a roughly vertical direction with a rapid expansion. The concept of a flux tube was theoretically investigated by Spruit (1976), Spruit (1979) and many other authors, a summary can be found in Schrijver & Zwaan (2000). The left panel in Fig. 1.4 describes the magnetostatic flux tube where the magnetic pressure causes a reduction of the gas pressure inside to balance the outside gas pressure at all heights. The expansion of the tube with height is due to the exponential pressure drop-off. The lower gas pressure leads to a partial evacuation of the flux-tube atmosphere, which leads to a depressed iso-surface of the continuum optical depth in its

inside. The relatively transparent flux-tube interior allows to see deeper layers, by the Wilson depression of 200 km for pores of 1000 km diameter and 100 km for facular points. The horizontal wavy arrows designate sideways radiation by the walls which are hotter than the inside gas at certain heights due to a deficit in convective energy flux inside the flux tube (vertical arrows). The first observational verification of the "hot-wall" effect is presented in Spruit (1976), Spruit & Zwaan (1981).

The standard models of a flux-tube atmosphere come from, e.g., Solanki & Stenflo (1985), Solanki (1986), Solanki et al. (1991), Solanki & Brigljevic (1992), Bunte et al. (1993), Bruls & Solanki (1993), Briand & Solanki (1995). They describe the stratification of the physical parameters of the flux-tube atmosphere along its axis derived on the basis of a large amount of spectral line profiles, especially Stokes V of Fe I lines, measured with the Fourier Transform Spectrometer at the McMath-Pierce telescope at Kitt Peak. These data, however, have low spatial resolution, but good spectral resolution and provide the empirical best-fit flux-tube models under the assumption that the spatially averaged Stokes V profile can be characterized by a single mean atmosphere and a mean flux-tube density, i.e. "filling factor". Another approach in empirical modeling is to fit observations with the automated inversion technique, e.g. developed at the IAC by Ruiz Cobo & Del Toro Iniesta (1992), based on the calculation of response functions. The results recover the Solanki-type models with assumptions of 1-D stratification, magneto-static flux-tube shape and the Local Thermodynamical Equilibrium (LTE) line formation (Bellot Rubio et al. 1998).

Another approach is the numerical modeling of magneto-convection, i.e. the physical processes resulting from the interaction between convectively driven flows and a magnetic field in an electrically conducting fluid, for parameters appropriate for the solar photosphere. "Realistic" MHD simulations include elaborate physics of radiative transfer, partial ionization, "open" and transmitting boundary conditions in order to realistically approximate the Sun and to cover the whole branch of physical processes. The comprehensive simulation of "non-magnetic" solar granulation has been successfully done by, e.g. Nordlund (1984), Stein & Nordlund (1989), Stein & Nordlund (1998), Steffen et al. (1989), Atroshchenko & Gadun (1994), Gadun et al. (1999). Two-dimensional time-dependent MHD simulations of magnetic structures in the solar atmosphere and their dynamical and radiative interaction with the surrounding plasma have been presented in a series of papers by, e.g., Deinzer et al. (1984a), Deinzer et al. (1984b), Knölker & Schüssler (1988), Grossmann-Doerth et al. (1989), Knölker et al. (1991), Grossmann-Doerth et al. (1989), and Steiner (1998). The right panel in Fig. 1.4 illustrates this approach. The simulations illustrated the strong tendency for the magnetic field to be swept to and concentrated in the intergranular, downflow lanes. Steiner (1998) pointed out that the determination of the complicated internal structure and dynamic of magnetic elements requires observations with a spatial resolution better than 100 km in the photosphere. The simulation results can be compared with observations through radiative diagnostics and line synthesis. Thus the results of the simulations were directly compared with the polarimetric observations by Leka & Steiner (2001) of small magnetic structures in the solar photosphere obtained with the National Solar Observatory/High Altitude Observatory Advanced Stokes Polarimeter using magnetically sensitive Fe I spectral lines. 2-D models predicted the existence of shock waves in the upper photosphere caused either by the collision of the horizontal flows of neighbouring granules, or by the swaying

motion of the flux sheet when a fast motion of the sheet pushes the plasma in front of it, creating a vertically oriented bow shock moving horizontally, or by the deformation of the flux sheet due to the dynamics of convection. (e.g. Cattaneo et al. 1989, Solanki et al. 1996, Steiner et al. 1998, Gadun & Hanslmeier 2000 etc.). The observational evidences of this were obtained by, e.g. Nesis et al. (1992), Nesis et al. (1993), Solanki et al. (1996), Rybák et al. (2004). The latter observed shock signatures in the Fe II ($\lambda = 645.638$ nm) spectral line observed simultaneously with the G-band images. They found a particular relationship between the shock event and a G-band bright point located 2 arcsec from it, which suggests that the observed shock is a causal consequence of the magnetic flux concentration. The bending and horizontal displacement of flux sheets by convective flows and the excitation and propagation of shock waves within a flux tube are also seen in the simulations.

However, the 2-D simulations lack 3-D instabilities that may render flux tubes akin to the rapid changes seen in G-band bright points, and the radiative transfer is very simplified. MHD simulations of convective motions including magnetic field have been carried out in 3-D by, e.g., Nordlund (1986), Weiss et al. (1996), Cattaneo (1999), Emonet & Cattaneo (2001), Stein & Nordlund (2002), Vögler and Schüssler (2003) and Vögler et al. (2005). These simulations revealed a complex structure of magnetic flux concentrations which are very relevant to high-resolution observations. They clearly demonstrate a continuous displacement and rearrangement of magnetic flux in the network of intergranular downflows. They are able to reproduce and explain such photospheric features as G-band bright points (Schüssler et al. 2003, Shelyag et al. 2004) of facular brightenings (Keller et al. 2004, Carlsson et al. 2004).

Why are G-band bright points bright?

The "hot walls" excessively radiate into the flux tube (Cannon 1970, Spruit 1976, Trujillo Bueno 1990, Hasan et al. 1999) which causes the flux-tube atmosphere become heated through radiative influx by around 200 K with respect to the surroundings at equal geometrical height (Steiner 1990). According to "conventional wisdom" by Rutten (1999): "*magnetic elements brighten in the G-band because the CH lines cause radiation escape somewhat higher up in the atmosphere, where the flux tubes are hotter, while in deep layers from where the continuum radiation escapes, the temperature elevation is less pronounced*". Rutten (1999) also argues that the CH molecule, which has a quite low dissociation energy of only 3.5 eV, is very liable to photodissociation by the UV radiation of the "hot walls". However, Sánchez Almeida et al. (2001) found that the CH photo dissociation plays a minor role owing to high densities in the photosphere. Their synthetic LTE G-band spectra fulfill many observed properties of the G-band bright points. The synthetic contrast, however, far exceeds the observed contrast which was explained by the limited spatial resolution of present observations. Berger et al. (1995) concluded that *the enhanced contrast in the G-band is largely a consequence of enhanced CH depletion through molecular dissociation in the deep photospheric layers of the hotter flux-tube atmospheres compared to the quiet Sun surroundings*. They also challenged the effectiveness of CH dissociation by UV-radiation from the "hot walls".

A decreased CH-line depression in G-band spectra (in the range from 430.24 nm to

430.78 nm) of bright points compared to G-band spectra of the surrounding photosphere was proved by spectroscopic observations of Langhans et al. (2001), Langhans et al. (2002) and Langhans et al. (2004) with very high spatial and spectral resolutions.

Recently, the results based on realistic 3-D radiative MHD simulations and on a detailed treatment of the G-band spectrum synthesis and direct comparison with observations showed that the G-band brightening of small magnetic flux concentrations in the solar photosphere is most probably due to the lateral heating and spatial evacuation of the magnetic structures (Shelyag et al. 2004). The observed G-band contrast was quantitatively reproduced after smoothing the simulated image to mimic the image deterioration by telescope and Earth's atmosphere. The higher temperature in the flux tube leads to a strong reduction in the number density of the CH molecule in the magnetic flux concentrations and thus to weakening of the CH lines in the G-band.

The blue CN band-head, as alternate to the G-band, bright point diagnostic.

Effects, similar to the G band, can be observed in bands of another diatomic molecule, e.g. CN. The first low resolution images made using narrow-band filters centered on the CN violet band-head at 388.3 nm by Chapman (1970) and Sheeley (1971) already showed a high contrast between small-scale magnetic features and their surroundings. Rutten et al. (2001) presented simultaneous imaging observations in the G band and in the blue CN band-head (387.4 nm) obtained with SVST where the G-band bright points looks brighter in CN than in the G band. However, they did not provide a quantitative comparison of the contrasts.

Several authors have suggested that because of the shorter wavelength and a correspondingly higher sensitivity of the Planck function to temperature fluctuations the contrast of magnetic elements in CN-band filtergrams could be more pronounced, making the latter an even more attractive magnetic flux proxy. Numerical simulations in semiempirical models by Kiselman et al. (2001), Steiner et al. (2001), Steiner et al. (2003) showed that CN, in the region $10^{-4} \leq \tau_{cont} \leq 10$ behaves very similarly to CH, and the contrast of magnetic elements in CN is expected to be higher. They predicted that the computed contrast of a bright point is about 40% larger in the UV CN band-head (at 388 nm) images than in the G-band images. Computations by Berdyugina et al. (2003) using plane parallel model atmospheres showed the same trend. They argued that the superior contrast in the blue CN band-head is probably due to a higher dissociation energy (7.7 eV) of CN, and hence its higher temperature sensitivity, and higher density of lines in the band as compared to those of CH (3.5 eV) in the G band.

Faculae and solar irradiance

Magnetic elements into which much of the magnetic fields outside of sunspots is concentrated, have a rather complicated 3-D structure. Their position on the solar disc causes these features to be seen from Earth at different angles. At an increased heliocentric angle, the limbward side of the "hot walls" become visible, while the cool depressed "floors" are

hidden Spruit (1976). The bright photospheric features seen in the continuum in active regions near the limb are faculae (e.g., Muller 1975, Wang & Zirin 1987). The spatial correlation between continuum facular regions and the $H\alpha$ and Ca II K plages gives a strong indication that the bright facular grains represent the near-limb manifestations of small-scale magnetic flux concentrations, which near disc center are visible as G-band bright points (Beckers 1976).

From observations of the center-to-limb variation (CLV) of the continuum contrast (575 nm) of the network bright points, Auffret & Muller (1991) found that on average the contrast increases from 8% at the disc center to 27% at $\mu = 0.3$ and then decreases closer to the limb. Observations of Wang et al. (1998) yielded a maximum at $\mu \approx 0.15$. Akimov et al. (1985) found a local maximum near $\mu = 0.3$, an increase to $\mu = 0.16$, and a slight indication of a decrease to $\mu = 0.14$. Balloon-borne observations by Rogerson (1991), Hirayama (1978) and Akimov et al. (1985, cf. references therein) showed high contrast with a maximum at $\mu \leq 0.15$. Sütterlin et al. (1999) observed at SVST and found an increase of continuum contrast to 50% at $\mu = 0.17$ and did not find a strong decrease in a range of $0.1 < \mu < 0.17$. Okunev & Kneer (2004) found a monotonic decrease of the intensity contrast of polar faculae for $\mu < 0.4$. Ortiz et al. (2002) found from MDI observations a continuum (676 nm) contrast maximum near $\mu = 0.3$. Spatially highly resolved images of plage regions showed a decrease of the number density of large facular grains with decreasing μ (Auffret & Muller 1991, Sánchez Cuberes et al. 2002). They also pointed out an increase of faculae size from disc center to the limb. High-resolution, speckle reconstructed images in the continuum and the G band by Hirzberger & Wiehr (2005) showed that limb facular grains are clearly visible up to $\mu = 0.05$, i.e. only 1 arcsec from the solar limb.

Flux tube models of Spruit (1976), Deinzer et al. (1984b) predict low contrast at disc center and does not sufficiently reproduce observed high facular contrasts near the limb. Deinzer et al. (1984b) and Knölker et al. (1988a) invoke an additional heating process for the upper layers ("hot cloud") leading to significantly higher contrasts near the limb and also high contrast at disc center. Detailed analysis of the "hot cloud" model by Eker (2003) came to optimum parameters of the model which reproduce the former observations. Schatten et al. (1986) assume "hillocks" in the iso- τ surface produced by buoyancy from heating and a temperature increase below the surface, yielding a contrast increase up to the very limb. In this model, a facula consists of an uplifted photospheric feature (hillock) with a height of 150 km and a width of around 800 km. Modeling of flux tubes by Topka et al. (1997) showed that the limb darkening and disappearance of the cool "floor" from the observer's field of view are responsible for the appearance of faculae. They proposed that faculae are simply micropores, with a typical diameter of 350 km– 650 km and a Wilson depression of 100 km, seen from the side and, hence, the typical facula does not turn into a bright point at the disc center (the smaller flux tubes tend to be bright even at disc center due to relative hot "floor"). However, the facular contrast becomes zero at the very extreme limb since the "hot wall" disappears from view. Steiner (2005) considered magnetostatic flux sheet embedded in a plane parallel model atmosphere and few snapshots of 2-D numerical simulation and showed that extension of the facular contrast enhancement increases from center to limb from a few tenths to up to 1 arcsec as a consequence of enhanced radiation from the limbward surface outside the magnetic flux concentration. Keller et al. (2004) and Carlsson et al.

(2004) presented first simulations of faculae using realistic 3-D MHD simulations and explain their appearance mainly through the "hot wall".

An important question in solar physics is to what extent solar surface magnetism affects the solar irradiance. Radiometers on board satellites (e.g., SOHO) have revealed that the total solar irradiance changes in time. Solar irradiance variations on scales of days up to the solar activity cycle length are closely related to the evolution of the solar surface magnetic field, because the emergence and evolution of active regions is reflected in the irradiance records (Lean et al. 1998, Fligge & Solanki 2000). Sunspots and active region faculae are considered to be the dominant contributors to solar irradiance changes. The large number of faculae around sunspot maximum more than compensate the deficit due to sunspots, which explains the slightly higher solar irradiance at solar maximum (Fröhlich 2002, Krivova et al. 2003, Walton et al. 2003). The seemingly magnetically inactive internetwork provides a large fraction of the magnetic flux, of kilogauss and sub-kilogauss magnetic field strengths (Stenflo 1982; Domínguez Cerdeña et al. 2003, 2006; Sánchez Almeida 2003, 2004a, 2004b; Sánchez Almeida et al. 2003; Trujillo Bueno et al. 2004; Khomenko et al. 2005). The contribution of photospheric magnetic features to the solar irradiance depending on the amount of magnetic flux and disc position was observed by, e.g, Frazier (1971), Ortiz et al. (2002), Wenzler et al. (2002).

The main goals of this PhD project were to obtain high-resolution images of the network in the G band and in the violet band of CN simultaneously in order to analyse the contrast relations of small-scale magnetic features in these two spectral bands; to carry out high-resolution spectral analysis of G-band bright points using spectral lines of CN and CH molecules. The second part of this PhD project was aimed to carry out high-resolution observations of plage regions near the solar limb in continuum and to analyse the tiny structure of facular brightenings and provide a comparison with results of Radiative Transfer computations in 3-D MHD models. Realistic 3-D MHD simulations of solar surface magneto-convection allow us to investigate the physical mechanism behind changes in brightness and radiation flux, thus providing theoretical underpinning for a connection between surface magnetism and irradiance. A systematic study of solar surface simulations will improve our knowledge of the photometric properties of network and plage magnetic fields. Hence one may compare the results of radiative computations of the continuum intensity in these models with existing solar observations.

2 High resolution imaging

In this chapter basics of phase diversity algorithms for reconstruction of narrowband solar images will be presented. Results of observations of the small-scale solar features, observed simultaneously in CH and CN molecular bands and in the blue continuum carried out at the 1-m Swedish Solar Telescope (SST, see Scharmer et al. (2003a)) will be presented and analysed.

2.1 Phase diversity image reconstruction

The investigation of small-scale structures on the solar surface is one of the primary issues in solar physics. It requires the means to achieve the highest possible spatial resolution in our imaging observations. A minimum requirement for that is a spatial resolution of 0.3 arcsec (Title & Berger 1996) or better (Berger et al. 2004). According to diffraction theory the 0.97 m entrance pupil of the SST has a spatial resolution of 0.11 arcsec at $\lambda = 430$ nm. A principal disadvantage of ground-based solar telescopes is a reduced resolving power due to distortions of the wavefront due to the variable atmosphere of the Earth, i.e. bad seeing, which leads to smearing of solar images. Although the static aberrations of the optic elements also distort a wavefront the seeing is the primary obstacle to obtaining high-resolution images. The ultimate solution to the problem is to correct the wavefront in real-time using one or several adaptive mirrors, i.e. adaptive optics (AO) correction. However such a system so far never achieves diffraction limit of the telescope over a large field-of-view (FOV). Another possibility to solve the problem is to decrease distortions in the image through reconstruction methods. Among many postprocessing tools of image reconstruction there are two primary techniques of image reconstruction: Speckle Imaging (De Boer 1993) and the Phase Diversity (PD). In the first method the observer collects an array of solar images with short exposures, usually 100 of them, close in time so that the solar surface can be assumed to be constant and the differences in the images are only due to seeing effects. In the second case one should collect at least two simultaneous solar images corresponding to different focus positions.

Comparing these two methods we can point out several advantages of PD:

- PD reconstruction is sensitive to both sources of image degradations: seeing and static aberrations of the telescope's optic. This makes such methods efficient in restoring solar images obtained outside of the Earth's atmosphere, i.e. by space telescopes.
- PD is based only on knowledge of the optical parameters of the telescope and does not need statistical characteristics of the atmosphere as an input.

- PD reconstruction can be accomplished by use of only two images. This is especially important when observing at short wavelengths where the diffraction limit of the telescope is small and the characteristic time scale of the photospheric features evolution is smaller than 15 sec.

In this section we will briefly describe the main aspects of this method which we have used in postprocessing of our observations.

The PD concept was first proposed by Gonsalves (1982) and then, based on the formulation of Roddier & Roddier (1991), was applied to solar images by Restaino (1992). Details of the PD methods in their application to solar observations are exhaustively described in classical works, e.g. in Löfdahl & Scharmer (1994), Paxman et al. (1992), Paxman et al. (1996) or Tritschler (1995). It consists of the simultaneous recording of at least one focused d_0 and one defocused d_k image, i.e. a PD pair, of exactly the same object:

$$\begin{aligned} d_0 &= f \otimes t_0 + n_0 \\ d_k &= f \otimes t_k + n_k, \end{aligned} \quad (2.1)$$

where f is the "true" intensity distribution, t_0 and t_k are the corresponding actual point spread functions (PSFs) at the moment of exposure, n_0 and n_k - the amount of noise in the observed images and the symbol ' \otimes ' denotes a convolution operation. The amount of defocus for d_k is expressed in a unit that makes the equivalent phase shift at the edge of the entrance aperture of the telescope equal to $k\pi$ radians or $k/2$ waves. The amount of defocus Δz along the optical axis is:

$$\Delta z = 8\lambda\Delta n \left(\frac{f}{D} \right)^2, \quad (2.2)$$

where Δn is the phase shift in waves, f and D are the focal length and the entrance pupil diameter of the telescope respectively. Both the phase errors and the "true" object can be estimated by minimizing the error metric L in the Fourier domain, where the convolution can be replaced by a multiplication of the Fourier transforms, i.e. D_0 , D_k , T_0 , T_k and F :

$$L = \sum_{u,v} |D_0 - \hat{F}\hat{T}_0|^2 + \gamma \cdot |D_k - \hat{F}\hat{T}_k|^2, \quad (2.3)$$

where a hat symbol '^' denotes an estimated value, u and v are the spatial frequencies, which correspond to x and y in the image, and γ is a given ratio of the rms values of the noise levels in the two exposures:

$$\gamma = \frac{\sigma_0^2}{\sigma_k^2}. \quad (2.4)$$

This means that in principle a solution can be found even if the signal-to-noise ratio in focused and defocused diversity channels is different. Solving the equation $\partial L/\partial F = 0$ an optimum for the estimated object is:

$$F_M = Q^2 \cdot \left(D_0\hat{T}_0^* + \gamma D_k\hat{T}_k^* \right), \quad (2.5)$$

where '*' denotes the complex conjugate and

$$Q = \left(|\hat{T}_0|^2 + \gamma \cdot |\hat{T}_k|^2 \right)^{-1/2}. \quad (2.6)$$

Thus the minimization problem can be written as:

$$L_M = \sum_{u,v} |E|^2, \quad (2.7)$$

where the error function E is defined as:

$$E = Q \cdot \left(D_k \hat{T}_0 - D_0 \hat{T}_k \right). \quad (2.8)$$

The wavefront ϕ at the telescope's exit pupil is expanded in a set of basis functions $\{\phi_m\}$, e.g. Zernike polynomials (Noll 1976) or Karhunen-Loève (KL) functions (Orlov et al. 1997, Roddier 1990). For the focused channel:

$$\hat{\phi} = \sum_m^M c_m \phi_m, \quad (2.9)$$

and for the defocused channel:

$$\hat{\phi}_k = \theta_k + \sum_m^M c_m \phi_m, \quad (2.10)$$

where θ_k is the introduced phase distortion, i.e. defocus. However, instead of representing the wavefront through a set of basis functions, a point-by-point approach, which enables preciser estimation of high-order aberrations, is also possible (Lee et al. 2003). The solution procedure aims at finding a set of coefficients $\{c_m\}$ which leads to a minimum of the error metric in Eq. 2.7. This problem is solved iteratively from an initial estimate $\hat{\phi}=0$, i.e. $c_m=0$. Since $T_k = T_k(c_m)$ and $E = E(c_m)$ in the next iteration $\mathbf{c}_{r+1} = \mathbf{c}_r + \delta\mathbf{c}$:

$$\delta E = \sum_m^M \frac{\partial E}{\partial c_m} \delta c_m, \quad (2.11)$$

where

$$\frac{\partial E}{\partial c_m} = D_k \left[\frac{\partial Q \hat{T}_0}{\partial c_m} \right] - D_0 \left[\frac{\partial Q \hat{T}_k}{\partial c_m} \right] \quad (2.12)$$

Thus a desired solution with respect to δc_m is found by minimizing:

$$\sum_{u,v} \left| E + \sum_m \frac{\partial E}{\partial c_m} \delta c_m \right|^2 \quad (2.13)$$

This means that we need to solve a matrix equation:

$$\mathbf{A} \cdot \delta\mathbf{c} + \mathbf{b} = 0, \quad (2.14)$$

where

$$\mathbf{A} = \begin{pmatrix} \frac{\partial E}{\partial c_1} | \frac{\partial E}{\partial c_1} & \cdots & \frac{\partial E}{\partial c_1} | \frac{\partial E}{\partial c_m} \\ \vdots & \ddots & \vdots \\ \frac{\partial E}{\partial c_m} | \frac{\partial E}{\partial c_1} & \cdots & \frac{\partial E}{\partial c_m} | \frac{\partial E}{\partial c_m} \end{pmatrix} \quad (2.15)$$

and

$$\mathbf{b} = \frac{1}{2} \begin{pmatrix} \frac{\partial L_M}{\partial c_1} \\ \vdots \\ \frac{\partial L_M}{\partial c_m} \end{pmatrix}, \quad (2.16)$$

here $(f|g) = \sum_{u,v} f g^*$ denotes the inner-product.

The approach described above is similar to a standard non-linear least-squares fitting technique as described in Press et al. (1986).

The expression Eq. 2.5 cannot be used directly to obtain the restored object because it gives an unlimited amplification of noise at high Fourier frequencies and needs an increased number of iterations for successful convergence. Therefore the observed data D_0 and D_k should be filtered beforehand with a spatial filter H (see Löfdahl & Scharmer (1994)):

$$H = 1 - \frac{\langle |H|^2 \rangle}{\langle |F_M|^2 (|T_0|^2 + \gamma |T_k|^2) \rangle} \quad (2.17)$$

In the presented technique it is assumed that the observed images are isoplanatic, i.e. t_0 and t_k do not vary over the FOV. However, the image formation through the Earth's atmosphere is strongly anisoplanatic, even after AO corrections. To avoid this, the described PD algorithm was separately applied to small subfields usually with a size of 5.3×5.3 arcsec² or 128×128 pixels, which can be considered isoplanar. A full restored image is then constructed by combining the subfields in a mosaic.

However, as pointed out by Löfdahl & Scharmer (1994), the PD method described above leads to good estimates of the wavefront parameters but in poor seeing the restored objects F_M are disturbed by artifacts: the low S/N ratio at isolated spatial frequencies causes a fringing pattern in the restored images. This happens if the optical transfer functions T_k have zeros or very low values at some u, v . These artifacts can be removed by combining the results of several atmospheric realizations J , i.e. J number of PD image pairs taken close in time so that the 'true' object can be assumed to be constant. Thus in this approach, called partitioned phase-diverse speckle (PPDS), the restored object looks as follows:

$$F_M = \frac{\sum_{j=1}^J D_{j0} \hat{T}_{j0}^* + \gamma \sum_{j=1}^J D_{jk} \hat{T}_{jk}^*}{\sum_{j=1}^J \left(|\hat{T}_{j0}|^2 + \gamma |\hat{T}_{jk}|^2 \right)} \quad (2.18)$$

Even better results are expected with a joint phase-diverse speckle (JPDS) technique (Paxman et al. 1992a, Paxman et al. 1996, Seldin & Paxman 1994) because the joint treatment constrains the wavefronts by requiring that the 'true' object is identical in all atmospheric realizations. A comparative study of the described methods applied to solar images obtained with the SST can be found in Löfdahl & Scharmer (2001).

In Löfdahl (2002) all possible variations, i.e. different number of atmospheric realizations J , diversity channels K , objects and wavelengths are combined into a complex approach in the form of linear equality constraints (LEC) (Kahaner et al. 1989). The LEC are given as the set of linear equations which aim at minimizing the number of unknowns c_{jkm} :

$$\mathbf{C} \cdot \mathbf{c} - \mathbf{d} = 0, \quad (2.19)$$

where \mathbf{C} is a $N_c \times N$ matrix, $N = KJM$ and $N_c < N$ number of constraints. The solution is:

$$\mathbf{c} = \bar{\mathbf{c}} + \mathbf{Q}_2 \cdot \boldsymbol{\beta}, \quad (2.20)$$

where $\bar{\mathbf{c}}$ is a particular solution and \mathbf{Q}_2 is a matrix of $N' = N - N_c$ column vectors which are the orthogonal basis of the null-space of \mathbf{C} . Equation 2.14 can then be presented as:

$$\mathbf{Q}_2^T \mathbf{A} \mathbf{Q}_2 \cdot \delta\boldsymbol{\beta} + \mathbf{Q}_2^T \cdot \mathbf{b} = 0 \quad (2.21)$$

Thus in the particular case of only one diversity channel, i.e. $K = 1$, we have to solve a Multi-Frame Blind Deconvolution (MFBD) problem (Schulz 1993). Under the Gaussian noise assumption the 'true' object estimation can be found as (see Löfdahl (2002) for details):

$$F_M = \frac{1}{\gamma_{obj} + \sum_j |S_j|^2} \sum_j^J S_j^* D_j \quad (2.22)$$

and the error metric as

$$L(\mathbf{c}) = \sum_{u,v} \left[\sum_j^J |D_j|^2 - \frac{|\sum_j^J D_j^* S_j|^2}{\gamma_{obj} + \sum_j^J |S_j|^2} \right] + \frac{\gamma_{wf}}{2} \sum_m^M \frac{1}{\lambda_m} \sum_j^J |\alpha_{jm}|^2, \quad (2.23)$$

where γ_{obj} has the effect of establishing stability with respect to perturbations in the object, γ_{wf} stabilizes the wavefront estimates and λ_m is the expected variance of mode m of the KL functions.

If $K > 1$ and $J = 1$ we have the easiest PD case, in which the LECs look like:

$$c_{1m} - c_{km} = 0; \quad k > 1, \forall m \quad (2.24)$$

If $K > 1$ and $J > 1$ we obtain a PDS case, in which the LECs are as follows:

$$\begin{aligned} \sum_{j,k} c_{jkm} &= 0; & m \in \{\text{tilt modes}\} \\ c_{jkm} - c_{j(k-1)m} &= c_{(j-1)km} - c_{(j-1)(k-1)m}; & j > 1, k > 1, m \in \{\text{tilt modes}\} \\ c_{j1m} - c_{jkm} &= 0; & \forall j, k > 1, m \in \{\text{tilt modes}\} \end{aligned} \quad (2.25)$$

Piston and tilts, i.e. the first three modes were excluded from the computations since they do not affect the error metric and thus cannot be estimated.

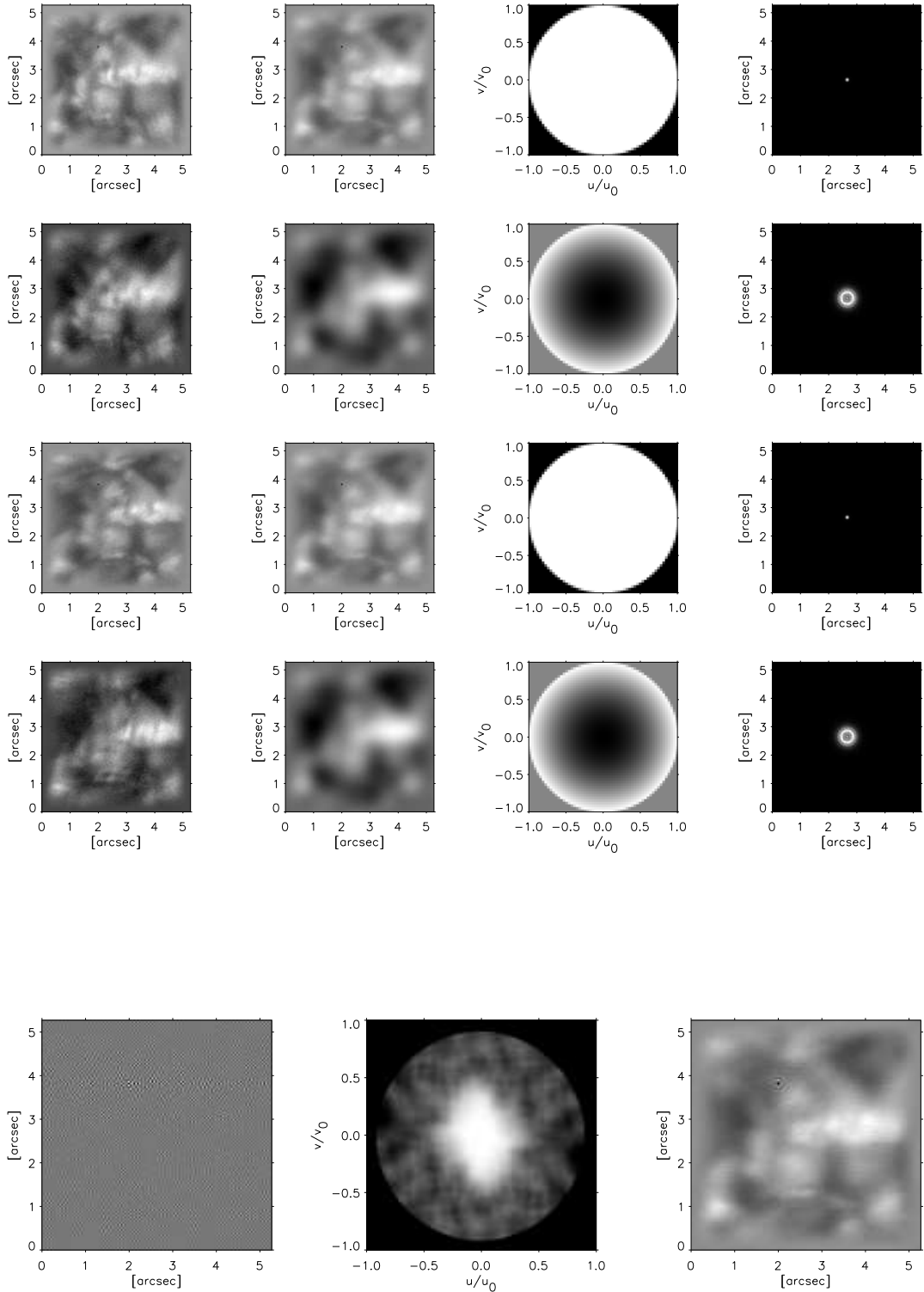


Figure 2.1: Example of PDS algorithm ($K = 2, J = 2$ case) at the 0-th iteration. The first and the third rows show focused channels, the second and the fourth the defocused channels, respectively. In each of these rows observed and Hanning windowed j, k image $\mathfrak{F}^{-1}(D_{jk})$, estimated j, k -th image $\mathfrak{F}^{-1}(HF_M T_{jk} + N_{jk})$, wavefront ϕ_{jk} at the exit pupil and the corresponding PSF are presented. Three bottom panels show not filtered 'true' object estimation before filtering $\mathfrak{F}^{-1}(F_M)$ (left panel), the noise filter H in Fourier domain (middle panel) and the estimated, filtered 'true' object $\mathfrak{F}^{-1}(F_M H)$ (right panel).

In this work we have used a MFBD/JPDS code developed by M. Löfdahl (Institute for Solar Physics, Sweden). For illustration in Fig. 2.1 an initial state of JPDS algorithm for a $K = 2$, $J = 2$ case and for one 128×128 pixels subfield is shown. Images were observed with the SST near $\lambda=430.5$ nm. The first and the third rows show focused channels, the second and the fourth the defocused channels, respectively. In each of these rows observed and Hanning windowed j, k image of the solar photosphere $\mathfrak{F}^{-1}(D_{jk})$, estimated j, k -th image $\mathfrak{F}^{-1}(HF_M T_{jk} + N_{jk})$, the initial estimate of the wavefront ϕ_{jk} at the exit pupil and the corresponding PSF are shown (\mathfrak{F} and \mathfrak{F}^{-1} denotes Fourier transform and the inverse Fourier transform, respectively). Three panels at the bottom show not filtered 'true' object estimation before filtering $\mathfrak{F}^{-1}(F_M)$ (left panel), the noise filter H in Fourier domain (middle panel) and the estimated, filtered 'true' object $\mathfrak{F}^{-1}(F_M H)$ (right panel). At this iteration, the error metric L has its maximum and hence the restored image has poor resolution. As seen from the bottom-left panel, the F_M is completely unusable without spatial filtering because of huge amplitudes at high spatial frequencies.

In Fig. 2.2 the final iteration of the algorithm for the same subfield as in Fig. 2.1 after successful convergence of L to the desired minimum is shown. The meaning of the panels is the same as in Fig. 2.1. Each individually estimated image $\mathfrak{F}^{-1}(HF_M T_{jk} + N_{jk})$ has now an intensity distribution close to the observed image d_{jk} . The JPDS restored image has a near diffraction limited spatial resolution (see at the spatial filter H) revealing structures unresolved in the raw observations.

2.2 Observations

Observations were carried out at the SST in September 2004. We have observed different active regions on the Sun near the disc center containing bright points (BPs) in three spectral domains.

In Fig. 2.3 a sketch of the optical setup used for the observations is shown. Beam splitters enabled simultaneous recordings in the three spectral regions. In the G-band and continuum channels the sunlight was split into two beams by a 50/50 nearly gray beamsplitter passing the light to the detectors. One CCD was located exactly at the focal plane of the telescope and another CCD with a 9.0 mm shift along the optical axis which roughly corresponds to approximately 1 wave phase shift at the entrance pupil (see Eq. 2.2). This enabled observations in two diversity channels, one focused and one defocused, in each spectral domain. Phase diversity image pairs in the G-band and in the blue continuum were recorded by two KODAK Megaplug 1.6 CCD (1536×1024 pixels with a pixel size of $9 \mu\text{m}$) cameras through narrowband interference filters centered at 430.5 nm and 436.4 nm respectively with a FWHM of 1 nm. Phase diversity image pairs in the CN band-head were recorded on a KODAK Megaplug 4.2 CCD camera (the FOV was reduced to 660×1050 pixels with a pixel size of $9 \mu\text{m}$) through a 0.8 nm wide interference filter centered at 387.9 nm. Detailed information about the filters can be found in Appendix A. Two diversity channels in the CN domain were provided by a combination of several prisms, which split the incoming beam into two with different optical paths leading to two images on the same CCD with a spatial separation (see in Fig. 2.3). Consequently one half of the CCD corresponds to the focused image and another half to the defocused image with an amount of defocus according to the optical path difference between the

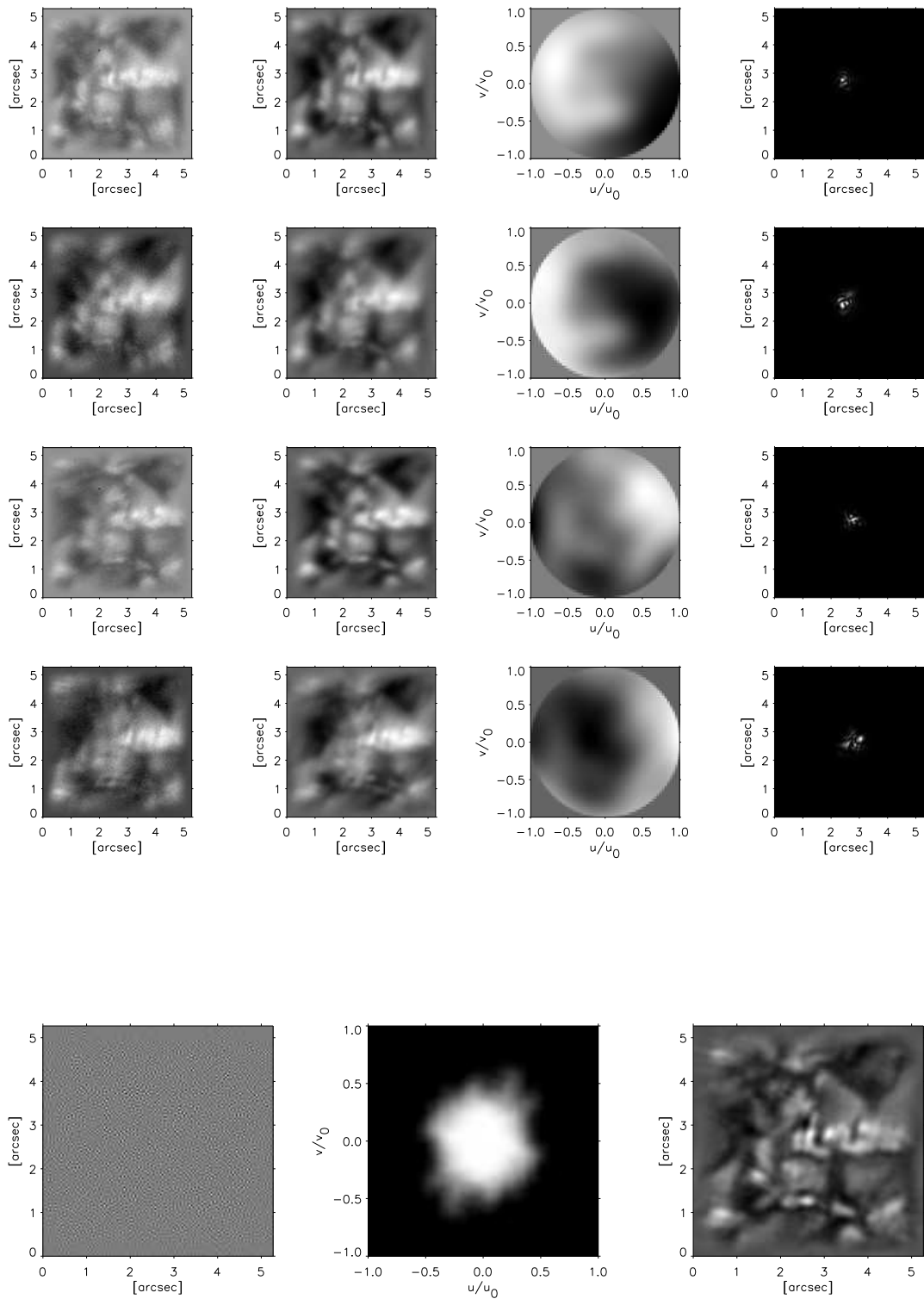


Figure 2.2: Example of PDS algorithm ($K = 2$, $J = 2$ case) after the final iteration. The annotation to panels is the same as in Fig. 2.1.

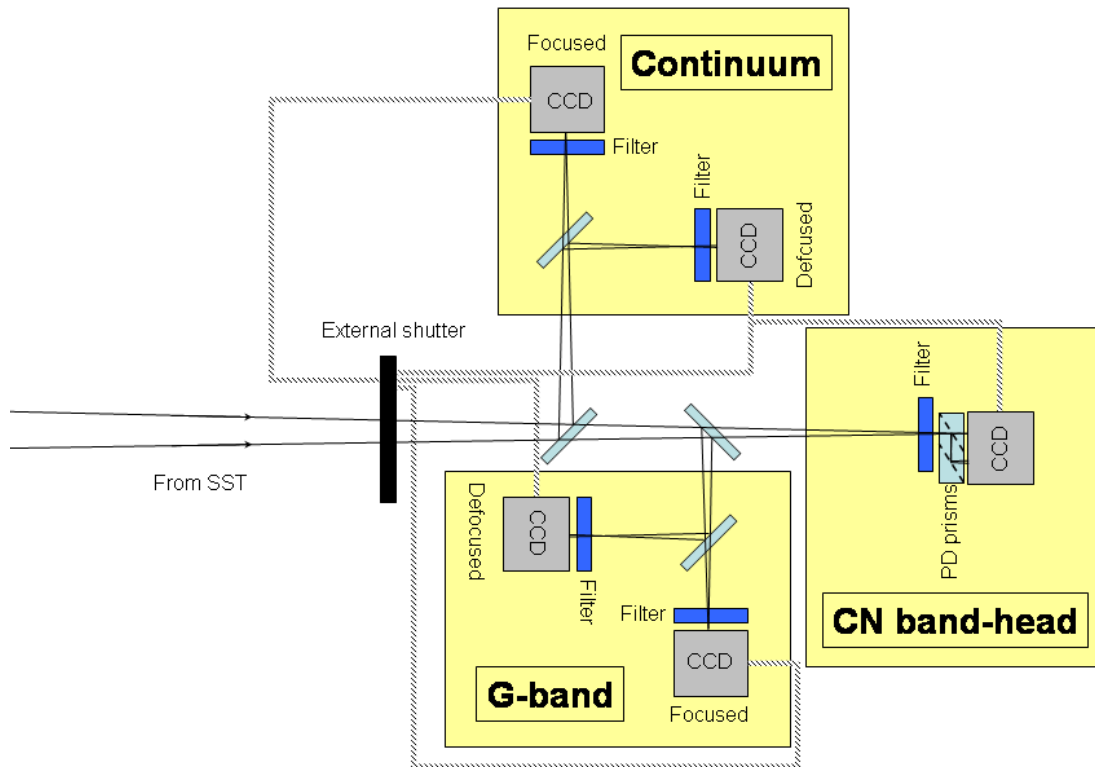


Figure 2.3: Optical setup for simultaneous PD imaging in G-band, CN band-head and blue continuum with SST. An external shutter triggers all CCD cameras to start the exposure at the same moment of time.

two beams, i.e. again 9 mm. All the science CCD detectors were triggered by an external shutter to secure simultaneous recordings in the three spectral regions. In our observations the exposure time was 12 ms for CN and 11 ms for G-band and blue continuum. In order to improve the quality of the obtained data tip-tilt and Adaptive Optics (AO) (Scharmer et al. 2003b) corrections during the observations were applied in real time .

2.3 Data reduction

2.3.1 Dark frame and flat field

The correction of the obtained images for dark signal and flat field of the CCD is an important part of the data reduction (see Chapter 3). As described in Chapter 3, the dark image was taken for each CCD with the same exposure time, CCD gain mode and the outdoor lighting as used in the imaging observations. The sunlight was blocked before the external shutter to exclude illumination of the CCDs. We have taken 100 dark images and averaged them to reduce any influence of the CCD read-out noise.

The CCD flat-field effects in the observed images coming from different photosensitivity of the CCD pixels also can be calibrated. For this purpose 400 images were obtained

at the same conditions as in the observations while the telescope pointing was randomly displaced near the disc center of the Sun avoiding active regions and then averaged. Thus even with the short exposure used here all details of the solar surface in the acquired flat-field image were smeared and it contains only a gain matrix of the CCD.

Using the additive property of the dark image and the multiplicative property of the flat field a reduced data image can be obtained as follows:

$$DATA_{reduced} = \frac{DATA_{observed} - DARKFRAME}{FLATFIELD - DARKFRAME} \quad (2.26)$$

However such an operation is not sufficient. Usually a CCD contains so-called dead pixels, i.e. corrupted pixels which deliver always the same signal, e.g. 0 or a maximum value, which does not depend on illumination. Dust particles on the CDD surface produce almost the same effect. In Fig. 2.2 an example of a dead pixel can be seen as a black dot in the observed focused image at a location (2.0,3.9) arcsec, which we left for illustration. The intensity in that pixel has a big contrast to the surroundings and thus affects the result of the PD reconstruction causing a characteristic circular fringe pattern in the restored data. To avoid this effect those pixels, whose contrast in the flat field exceeds a certain threshold (set manually) were replaced in the reduced image by the average intensity of the immediate surroundings. Of course the intensity values of such pixels in the PD restored image cannot be trusted, but at least no fringing pattern affected the brightness of nearby pixels.

2.3.2 JPDS reconstruction

The image scale at the focal plane of the SST is 0.0405 arcsec/pix at $\lambda=430$ nm. According to the Rayleigh criterion, the diffraction limit of the telescope with entrance pupil D at a certain wavelength λ is:

$$\alpha = 1.22 \cdot \frac{\lambda}{D}, \quad (2.27)$$

where α is the resolution in radian. Hence the diffraction limit of 0.114 arcsec, 0.103 arcsec and 0.116 arcsec in G-band, CN band-head and continuum channels corresponds to a sampling of around 2.8 pixels per resolution element on a CCD plane. This sampling is sufficient for a secure PD reconstruction.

For our observations the analysis of time sequences of the filtergrams did not show visible proper motions or structure changes of the BPs up to 130 km scales in less than 15 s, i.e. the Sun fulfills the requirement of a static scene. Therefore, to be conservative, we selected the set of 8 PD image pairs obtained within 10 s for further investigation which have the highest rms contrast. Thus in each spectral domain the JPDS code with $K=2$ and $J=8$ was applied to the observed data. All restored filtergrams used in the present work were co-aligned through a cross-correlation. Due to anisoplanar image formation individually restored subfields were slightly shifted with respect to each other so that co-alignment of a full reconstructed G band, CN band-head and continuum images varied over the FOV. To correct this the restored triplet of images was destretched using a 'local correlation tracking algorithm' (November et al. 1988).

The contrast of small-scale structures in an image is very sensitive to its spatial resolution. The unbiased comparison of the contrast values of BPs at different wavelengths

requires images with equally high spatial resolution in all three spectral regions (CN, G band and blue continuum). This is particularly problematic, since the magnitude of the atmospheric aberrations is wavelength dependent in an only approximately and statistically known fashion, but is known to increase towards shorter wavelengths. Additionally presence of photometric noise in the observed images impedes a correct estimation of the object and therefore only a near-diffraction limited resolution of JPDS restored images was achieved (see a spatial filter H in Fig. 2.2 for example). The different wavelengths were restored separately and have different amounts of residual aberrations after the JPDS processing. As a consequence JPDS restored images have different spatial resolution in three spectral channels. In order to equalize the spatial resolution of the restored CN, G-band, and blue continuum images the following technique was applied: In the last iteration of the JPDS reconstruction, for a given subfield, the final restored CN, G-band and continuum subfields were filtered with the same spatial filter. This filter was based on the cut-off frequencies, in the Fourier domain, of the worst image, which always was the CN filtergram, probably due to the lower S/N in the original images. This technique works if the sizes of the smallest structures lie below the spatial resolution. Tests using MHD simulations suggest that this is the case (see Chapter 4 or Shelyag et al. (2004)).

2.4 Results

In Fig. 2.4 the restored filtergrams in the blue continuum, G band and CN band-head are presented. All intensities were normalized to a mean intensity of the CN image. Intensities of BP pixels vary over a wide range. Often BPs or at least associated magnetic features are darker than granules (Langhans et al. 2002), (Shelyag et al. 2004). In order to allow a secure and automatic identification of BPs we use the technique of Berger et al. (1998), which consists of the subtraction of the continuum image from the corresponding image in the molecular band. Hence a BP mask at the left-bottom in Fig. 2.4 was computed as (compare with results in Chapter 3):

$$\begin{aligned} Mask &= 1; & \frac{I_{CNband-head}}{\langle I_{CNband-head} \rangle} - \frac{I_{cont}}{\langle I_{cont} \rangle} &> 0.15 \\ Mask &= 0; & \frac{I_{CNband-head}}{\langle I_{CNband-head} \rangle} - \frac{I_{cont}}{\langle I_{cont} \rangle} &\leq 0.15 \end{aligned} \quad (2.28)$$

The co-alignment of the three reconstructed filtergrams was assumed to be so perfect that the same BP-mask could be used in all of them. Although the obtained filtergrams reveal complex structure of the BPs, e.g. ribbons or "hot walls" pointed out by Berger et al. (2004), we do not provide an individual analysis of their intensity.

Fig. 2.5 shows the intensity variations along the same cut in a typical BP in the three spectral regions. The intensities are normalized to the average quiet Sun values. BPs in the CN band-head, as a rule, have the highest brightness excess with respect to the quiet Sun as compared to that in the G band and the blue continuum.

In Fig. 2.6 we present scatter plots of the normalized intensity in the molecular bands with respect to the normalized continuum. Two groups of photospheric features, BPs (red dots) and quiet granulation (black dots), show different brightness distributions in molecular bands as predicted by numerical simulations of Shelyag et al. (2004). The CN band-head distribution is in very good quantitative agreement with a similar analysis in Chapter 3.

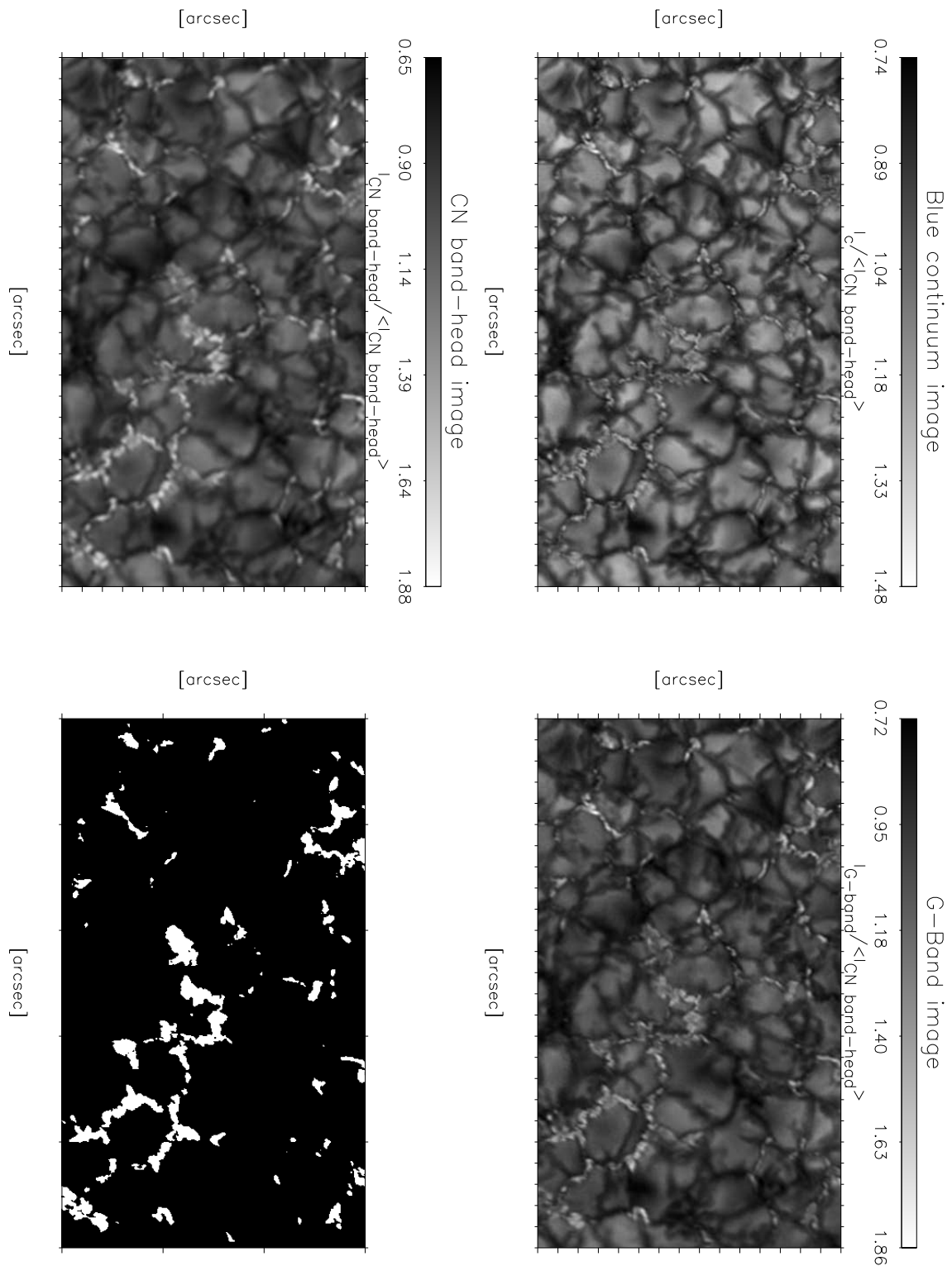


Figure 2.4: Joint phase diverse speckle reconstructed filtergrams of an active region NOAA0669, located at $\mu=0.97$ on 7 September, 2004 at 14:30 (UT), containing BPs taken in the blue continuum (436.5 nm), G-band (430.5 nm) and CN band-head (387.9 nm). Also shown (bottom-left) is the mask used to identify bright points. The presented images have not been filtered to equalize the spatial resolution.

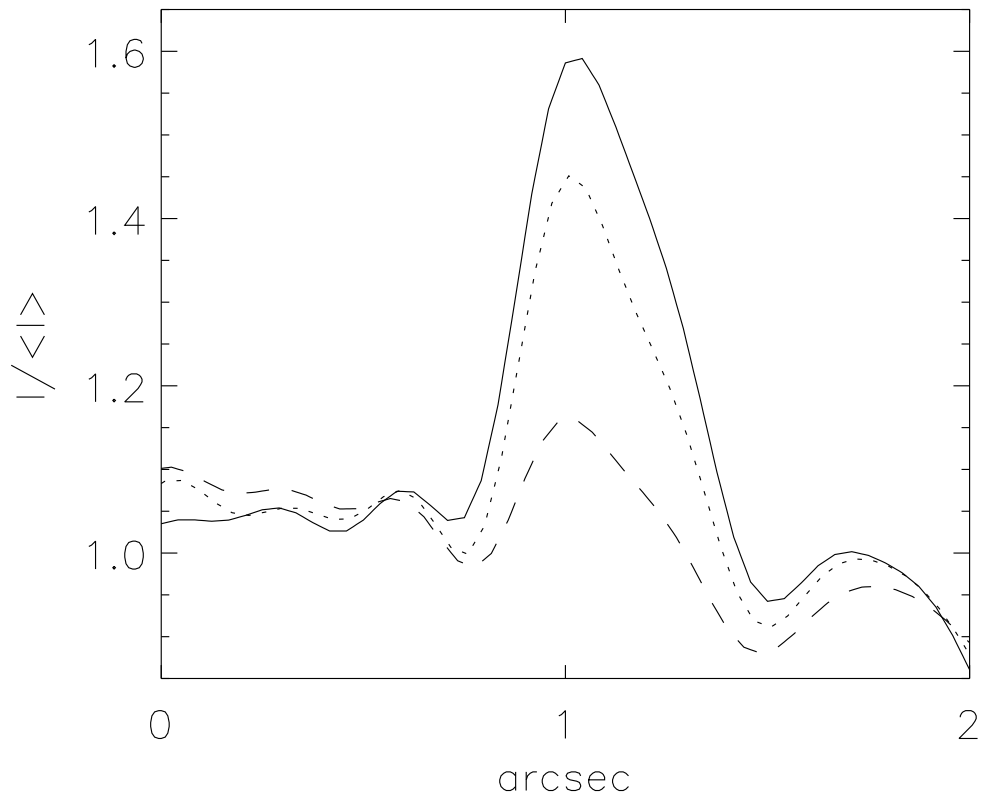


Figure 2.5: Intensity along a cut through a typical BP for the blue continuum (436.5 nm - dashed line), G band (430.5 nm - dotted line) and CN (387.9 nm - solid line).

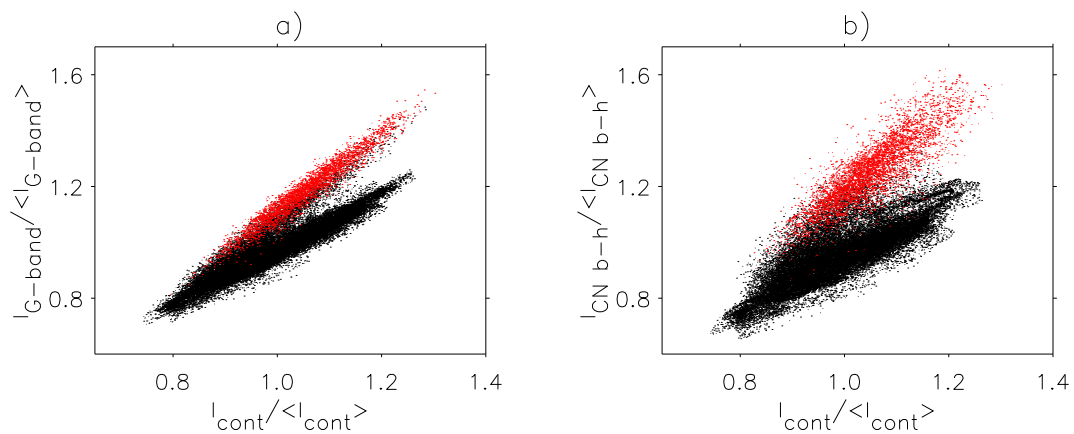


Figure 2.6: Normalized a) G band and b) CN band-head intensities dependence on the normalized intensity in the blue continuum measured in active region NOAA0669 located at $\mu=0.97$ on 7 September, 2004 at 14:30 (UT).

Spectral region	$\langle C \rangle$	$\langle C^{\text{JPDS}} \rangle$	$\langle C^{\text{JPDS+equ}} \rangle$	<i>rms</i>
Continuum	0.090	0.145	0.143	0.11
G band	0.218	0.341	0.340	0.12
CN band-head	0.311	0.481	0.481	0.12

Table 2.1: Observed contrast values of BPs with respect to the quiet Sun intensity within the G band at 430.5 nm, the violet CN band-head at 387.9 nm and blue continuum at 436.5 nm. $\langle C \rangle$, $\langle C^{\text{JPDS}} \rangle$ and $\langle C^{\text{JPDS+equ}} \rangle$ denote the contrast in the not reconstructed, JPDS reconstructed and JPDS reconstructed with resolution equalization images respectively. Rms contrasts are computed for the quiet Sun.

To quantify the brightness excess in BPs we define the contrast for a given pixel as:

$$C_\lambda = \frac{I_\lambda - I_{0,\lambda}}{I_{0,\lambda}}, \quad (2.29)$$

where I_λ denotes the intensity of the BP in a certain wavelength band λ and $I_{0,\lambda}$ is the mean intensity of the quiet Sun for the same wavelength.

The calculated mean contrast values of the BPs are presented in Table 2.1. The contrast of the BPs is higher in CN than in the G band, with the mean ratio $\langle C_{\text{CN}}/C_{\text{CH}} \rangle = 1.4$ over all BPs in the 27×43 arcsec² filtergram triplet. The mean BP contrast in CN band-head is $C_{\text{CN}}/C_{\text{cont}} \approx 3.4$ times higher than in the blue continuum. The contrast of BPs in the G band is $C_{\text{CH}}/C_{\text{cont}} \approx 2.4$ times higher than in the blue continuum. This is in reasonable agreement with simple theoretical predictions (Berdyugina et al. 2003, Kiselman et al. 2001).

According to Shelyag et al. (2004) those atmospheres which correspond to BPs have a mean temperature at the layer of the continuum intensity formation $\langle T(\tau_{\lambda=430 \text{ nm}} = 1) \rangle = 6500$ K. For this temperature from Berdyugina et al. (2003) we obtain:

$$C_{\text{CNband-head}}^{\text{theor}}/C_{\text{G-band}}^{\text{theor}}=1.4, C_{\text{CNband-head}}^{\text{theor}}/C_{\text{cont}}^{\text{theor}}=2.8 \text{ and } C_{\text{G-band}}^{\text{theor}}/C_{\text{cont}}^{\text{theor}}=2.0.$$

A statistical study of the brightness distributions of BPs in CN and CH filtergrams covering 81×43 arcsec² of active regions with the filling factor $\alpha \approx 0.03$ showed that the contrast ratio of the BPs in CN to CH decreases with increasing G-band brightness of the BPs as shown in Fig. 2.7. In this plot only a subset of the analyzed data is shown for a subfield, for which the alignment of the various images was particularly good.

Theoretically the relative brightness excess of BPs in CN band-head with respect to G band is due to a stronger decrease of the number density of the CN molecule with increasing temperature at the level of line-core formation, as compared to CH. We conclude that with increase of the BP intensity the absorption by CN lines decreases with respect to absorption by CH spectral lines. This is in agreement with our spectroscopic observations which we will present in the next Chapter.

Although the observed contrast ratios agree reasonably with model predictions, the absolute contrast values of observed BPs are lower than those in theoretical predictions based on the Kurucz model atmosphere (Kurucz 1993) with $T_{\tau=1} \approx 6500$ K by a factor of 5.

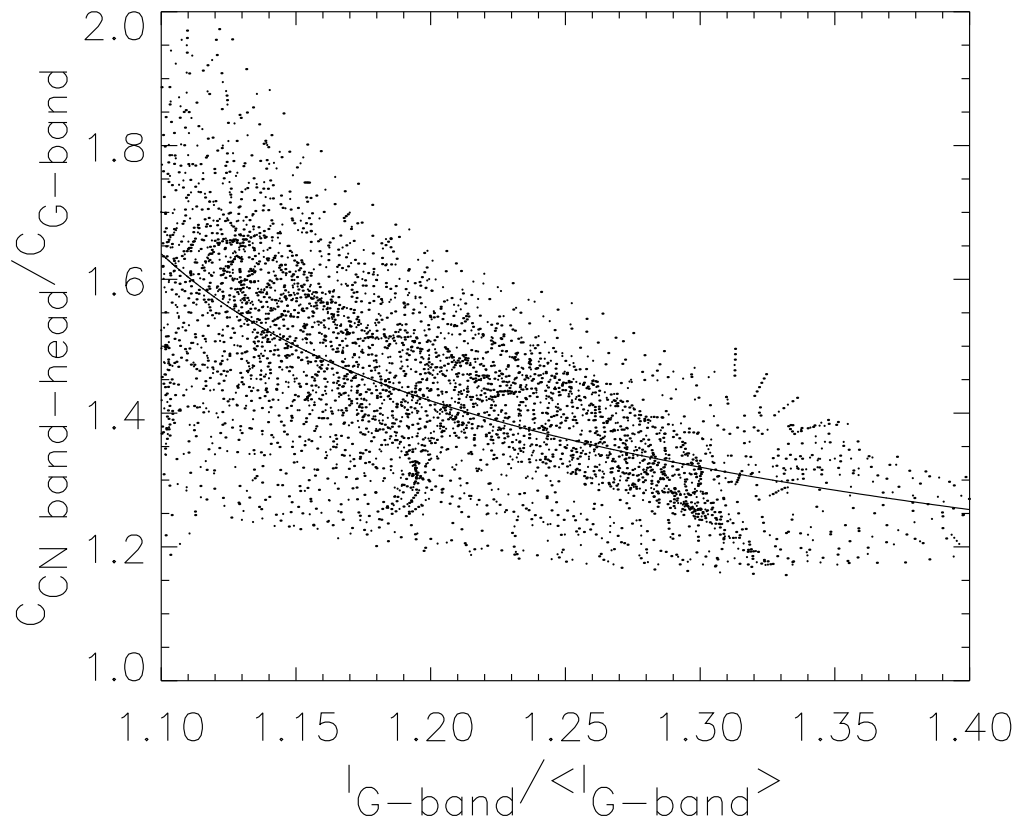


Figure 2.7: Scatter plots of the contrast ratio in CN band-head and G band vs. normalized G-band intensity. The solid line represents a 4-th order polynomial least squares fit to the data points.

The difference between the absolute contrasts found from the observations and computed by Berdyugina et al. (2003) can be attributed to several factors, of which the main ones are:

- the computed contrasts were calculated using a simple Kurucz model whose temperature stratification along τ differs from that of a flux-tube in the photosphere even if the temperatures at $\tau = 1$ are equal;
- the computed contrasts refer to an unlimited spatial resolution whereas our observed filtergrams are limited to a spatial resolution of 130 km;
- the observed contrast is further diminished by scattered light. Alternatively, the temperature contrast between magnetic BPs and the quiet Sun is lower.

The significantly higher contrast seen in the violet CN band-head compared with the G band makes it a promising wavelength band for solar high resolution studies, although there are factors making nowadays high-resolution ground-based solar observations in this wavelength more complex than in the G band:

- fewer photons are provided by the Sun;

- there is more scattered light;
- the spatial resolution is worse because of the stronger influence of the atmospheric aberrations (seeing).

Recently, Uitenbroek & Tritschler (2006 submitted.) presented results of the synthesis of the blue CN band-head and G band using 3-D MHD simulations. They present the comparison of the intensity contrast of BPs in synthetic CN band-head and G-band images. The result is $\langle C_{CN}/C_{CH} \rangle = 0.96$, which is in sharp contradiction with our observations. Moreover, their simulations yielded that this ratio is almost constant in the range of high G-band intensities of the BPs and decreases at low intensity. The Kurucz's models, however, gave opposite results where in the model with $T_{eff} = 6250$ K this ratio was computed as 1.35. They correctly pointed out that these models cannot be used to describe either granule's or BP's atmospheres. They found, also, that the BP brightness enhancement in molecular bands is due to partial evacuation in high field concentrations rather than due to non-linear dependence of the Planck function at short wavelengths which would lead to higher contrast in the CN.

Several possibilities to resolve this contradiction are at hand:

- Our estimated spatial resolution is not entirely correct and the CN band-head image is better resolved in our observations than the G-band. Alternatively, the amount of scattered light is larger in the G-band range than at the wavelength of the CN band-head.
- The continuum opacities used in simulations may be wrong.
- Before comparison with observations, the results of radiative transfer computations through MHD simulations should be convolved with the realistic PSF estimated from our observations by JPDS and the amount of scattered light should also be taken into account.
- The definition of a BP should be concretized, i.e. BP interior, ribbon structure, facula or evidence of the "hot walls", whose properties may be very different.

One way to distinguish between some of the above explanations would be to make a comparison of simulated CN and CH spectra with our spectroscopic observations including modelling the limited resolution, seeing and scattered light (see Chapter 3).

3 High resolution spectroscopy of the solar photosphere

In the previous chapter the brightness properties of the intergranular bright points (BPs) observed through narrow-band filters for G band, blue CN band-head and blue continuum were investigated. In this chapter, we present results of high-resolution spectroscopic observations of the small-scale magnetic activity manifestations in the solar photosphere with the spectrograph installed on the new 1-m Swedish Solar Telescope (SST). The results of simultaneous observations in two spectral regions in the blue and in the near UV containing absorption spectral lines of different species, e.g., CN, CH and many atoms, will be presented. Spectral properties of the BPs characterizing qualitatively the plasma state in the upper photospheric layers are investigated and compared with results obtained in Chapter 2.

We have observed and analyzed spectra in the blue CN band-head (387.588–388.473 nm) and in a blue region (436.1–436.9 nm) containing absorption lines of CH. Note that except for specifically mentioned cases all wavelengths we will use throughout the present chapter correspond to vacuum as follows from the wave number of the FTS atlas (Brault & Neckel 1987).

3.1 Observations

The SST spectrograph, designed on the basis of a Littrow system, has a 79 grooves/mm echelle grating with a blaze angle of $\beta=63.43^\circ$ and has a theoretical spectral resolving power of around 240000. The slit has a width of 25 μm which corresponds to 0.1143 arc-sec in the image plane and is etched on a glass plate with a reflecting layer of coated silver. The slit plate is mounted on the turnable slit holder which constitutes one wall of the slit box. The slit box also contains a corrector lens and mirrors that divert the outgoing beam into two exit ports labeled A and B where CCDs were mounted. This enabled to make spectroscopic observations in two spectral domains simultaneously. The optical setup used for observations is sketched in Fig. 3.1. Since there is no predisperser in the spectrograph itself, all spectral orders fall on top of each other on the CCD plane and to separate desired orders narrow-band interference filters were used. In Table 3.1 prefilters and CCDs used in the spectroscopic setup are listed. Unfortunately the high gain setting in the CCD at port A produced an increased noise level in recorded spectra with respect to the data collected at port B. This caused certain difficulties in the data reduction which will be discussed later. In order to identify the exact slit position on the Sun the light reflected by the slit box was used. The reflected light was refocused by a condensing

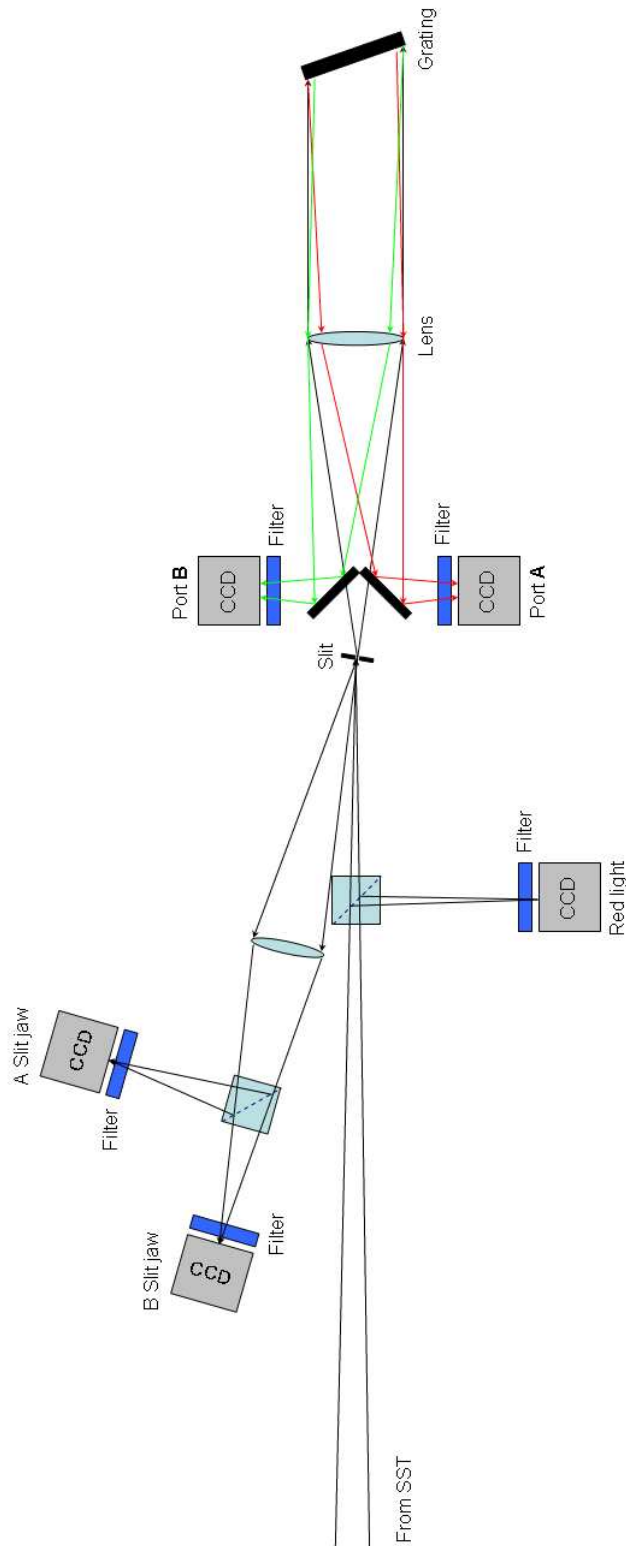


Figure 3.1: Optical setup for simultaneous spectroscopic observations in two spectral ranges, i.e. port A and port B. Additionally, cameras to record the corresponding slit jaw images and make short-exposure high-resolution images in the red continuum are sketched.

parameter	port A	port B
CCD type	Kodak Megaplug 1.6, 10 bit	Kodak Megaplug 1.6, 10 bit
CCD size	1536× 1024 pix × 9 μm	1536× 1024 pix × 9 μm
CCD gain	+6 dB	0 dB
prefilter	436.39 nm, 1.15 nm, 36.37% (air)	387.92 nm, 0.80 nm, 60.54% (air)
spectral range	436.085 nm < λ < 436.953 nm	387.590 nm < λ < 388.480 nm
spectral order	53	58
grating angle β − α	−0.71°	+0.13°
mean dispersion	15.5 mm/nm	15 mm/nm
spatial diffraction limit	0.11 arcsec	0.10 arcsec
exposure time	1500 ms	1500 ms
maximum intensity in continuum	947 counts	665 counts
spectral lines	CH, atomic	CN, CH, atomic

Table 3.1: Specification of instruments used in observations.

achromatic lens with a focal length of $F=25$ cm and split by a 50/50 beamsplitter passing the light to positions where slit jaw CCD cameras were installed. The exposure time for the slit jaw image was as long as the exposure time of the corresponding CCD collecting the spectra, to ensure that one achieves the same spatial resolution in both types of data to simplify identification of observed solar features. The main properties of the slit jaw

parameter	slit jaw A	slit jaw B
CCD type	Kodak Megaplug 1.6, 10 bit	Kodak Megaplug 1.6, 10 bit
CCD size	1536× 1024 pix × 9 μm	1536× 1024 pix × 9 μm
filter	430.513 nm - air, 1.18 nm, 46.37%	387.92 nm - air, 0.80 nm, 60.54%
spatial diffraction limit	0.11 arcsec	0.10 arcsec
exposure time	1500 ms	1500 ms

Table 3.2: Specification of observed slit jaw image data

detectors are listed in Table 3.2. Strong overexposure of the slit jaw cameras was compensated by neutral filters with high density. Exposure time in all four CCD cameras were synchronized by a trigger signal so that the complete dataset was recorded simultaneously.

In addition, high resolution images in a red continuum using a narrow-band interference filter were obtained (see Table 3.3) taking 10% of the total incoming sunlight by mounting a 90/10 beamsplitter in the light path before the spectrograph. These images are uncorrelated in time with the spectroscopic dataset and serve as high resolution, almost diffraction limited, intensity maps of the photosphere. The diffraction limit of the spatial resolution was achieved by means of Multi Frame Blind Deconvolution (MFBD) described in Chapter 2. Frame selection based on rms contrast measurements was applied

parameter	red light
CCD type	Kodak Megaplug 1.6, 10 bit
CCD size	1536 × 1024 pix × 9 μm
filter	705.7 nm - air, 0.71 nm, 45.37%
spatial diffraction limit	0.18 arcsec
exposure time	10 ms

Table 3.3: Specification of observed high resolution image data in a red continuum

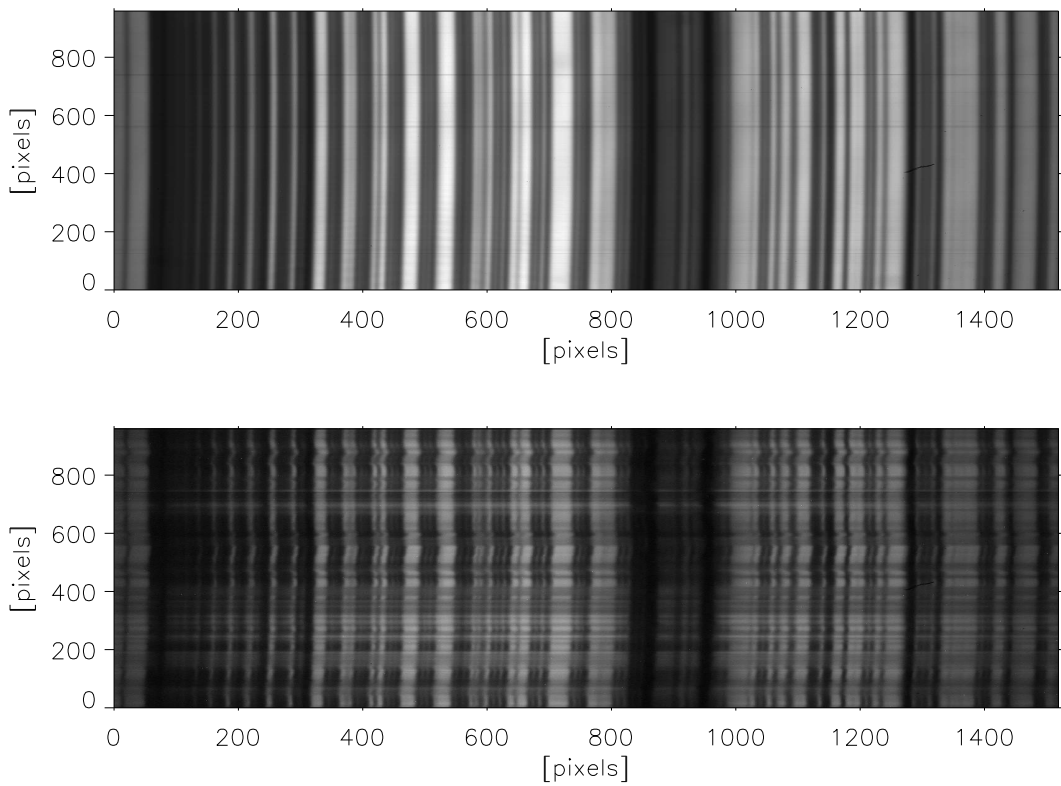


Figure 3.2: Example of a raw image of the flat field (top) and corresponding spectra (bottom) observed at the port B.

to choose 10 'Red' images with the best contrast during each 15 s time interval, which were stored to be processed by the MFBD routine.

3.2 Data reduction of the spectra

In figure 3.2 an example of the raw observed spectroscopic data at the port B (B-spectra) corresponding to the blue CN band-head spectral domain is shown. There are two characteristics of CCDs that must be considered in making an astronomical image: 1) since they

are electronic components CCDs are sensitive to heat within the camera as well as light from the object of interest and 2) the individual pixels in the CCD array may vary significantly in their sensitivity to both heat and light. The critical part of the data reduction is to diminish the effect of these two factors. It consists of dark frame subtraction and flat fielding, which will be explained in the following sections.

3.2.1 Dark frame

Astronomical CCDs are so sensitive that they can detect electronic noise generated by the CCD chip itself. This means that even without illuminating the CCD surface one gets a nonzero output signal. We call the output signal created by a CCD chip without exposure to photons a Dark Frame. It results from thermal electrons in the pixels, from voltage offsets in the CCD electronics and from noise produced by the electronics. The rate of thermal electrons depends on the temperature of the CCD and on the impurities of each pixel. Since the CCD pixels have different impurities, each element will accumulate electrons at a different rate. This can cause a faint pattern to form on images made with the CCD. Even though this pattern is not due to light, it is difficult to determine which pixel intensity was due to light and which was due to dark current when taking spectroscopic data. Luckily, for a given CCD temperature, the thermal electrons accumulate at a constant rate for each pixel. This means that this effect can be measured and its contribution can be subtracted from the recorded images. In practice, during the observations one should take a dark frame of the CCD under the same conditions as when taking spectroscopic data, with the only difference that the beam of sunlight is blocked somewhere in the optical path. This means that the chip temperature, exposure time, CCD operating mode as well as indoor lighting of the optical laboratory have to be equal to those used during observations. In order to reduce noise in the single dark frame usually 100 dark images were taken and subsequently averaged. The resulting dark frame is almost free of noise and contains only the information about the dark counts of each pixel of the CCD. Using the additive property of the latter, one removes it from the useful signal by subtraction of the averaged dark frame from the raw observed data. However, this method is not able to remove noise of the CCD and readout electronics in a single frame. The spectroscopic signal in our observations lies between 37 and 1024 counts whereas the typical count values of the dark frame lie around 29 counts, which is up to 78% of the useful signal. This means that dark frame subtraction is obligatory for reducing the spectroscopic data in order to get realistic values of spectroscopic line depression.

3.2.2 Flat field

First of all it should be mentioned that the flat fielding of observed spectroscopic data is much more complicated than for images. The flat field is a 2-dimensional gain matrix of the CCD. In a common image processing method a flat-field image should be made by taking a picture of an evenly illuminated scene which does not show any intensity variations. Obtained in that way the flat-field image shows only the inherent variances in intensity value across the CCD array due to differences in photosensitivity or to dust specks on the CCD surface or vignetting in the optical system. Using the multiplicative property of the flat field one divides the raw data image, already corrected for the dark frame, by the flat-

field image, which should be also corrected for the dark frame, and achieve the reduced data image with a 'true', accurate to the noise level, brightness distribution independent of the optical setup and CCD.

$$DATA_{reduced} = \frac{DATA_{observed} - DARKFRAME}{FLATFIELD - DARKFRAME} \quad (3.1)$$

In solar observations the homogeneous illumination of the detector is achieved by a rapid random swinging of the telescope by around 10 arcmin in all directions so that the field of view moves around the solar disc center avoiding sunspots and pores. By collecting many images on the CCD during this time but followed by averaging them one expects to smear any information about the solar surface and to have a pure gain matrix of the CCD (CCD flat field). It is very important to take flat fields when the CCD is in the same position in the optical setup as in the observations to avoid flatfielding artifacts on the dust particles on the CCD surface because of a different beam cone. In our observations a flat-field image consists of 400 averaged frames. On the top in Fig. 3.2 the observed averaged flat field is shown. It does not contain any spatial information of the solar features along the slit of the spectrograph, but the averaged spectrum of the solar photosphere near its disc center. In order to obtain the gain matrix of the CCD itself the following procedure has been applied:

Step 1. As one can see from Fig. 3.2 the observed spectra reveal a small inclination of the spectral lines and their no-rectilinear shape. Compressing the flatfield in the spatial direction by averaging each spectrum along the slit we got a reference 1-dimensional spectrum. Using the algorithm of cross correlation, spectra of all positions along the slit were co-aligned to a reference and divided by it. At the same time the corresponding vector of dispersion shifts was created. The latter was used to align the observed spectra along the dispersion axis. The observed spectra show not only a tilt of the spectral lines, but also distortions. This is inherent in grating spectrographs and is partly due to the fact that the spectrograph has an off-plane design which causes pincushion and barrel deformations of the spectra. Also, some image distortion is caused by the corrector lens. Such image distortions make the reference 1-dimensional spectrum slightly blurred and dividing flatfield spectra by it produces artifacts on the edges of the spectral lines. Therefore, to improve the quality of the result, the observed flatfield image was binned into 3 intervals in the spatial direction where the line distortion can be neglected and the afore mentioned algorithm was applied separately to each bin. The resultant CCD flat field is shown on the bottom in Fig. 3.3 where broad, slanting lines are interference fringes produced by the prefilter and the entrance window of the CCD.

Step 2. As opposed to narrow-band spectroscopy the transmission profile of the prefilter should also be taken into account. Unfortunately it is not possible to use a filter curve delivered by the manufacturer since the transmission of an interference filter depends strongly on its temperature, humidity and on the angle of inclination. In order to compute the filter transmission curve the reference 1-dimensional spectra of the observed flat field corrected for the dark frame and CCD flat field was computed in the same way as in Step 1 and compared with the high resolution Fourier Transform Spectrometer (FTS) atlas (Brault & Neckel 1987) for the photosphere in exactly the same spectral region. In case of B-spectra observations two fiducial wavelength positions at 387.588 nm (beginning of observed spectra) and at 388.473 nm (end of the observed spectra), corresponding

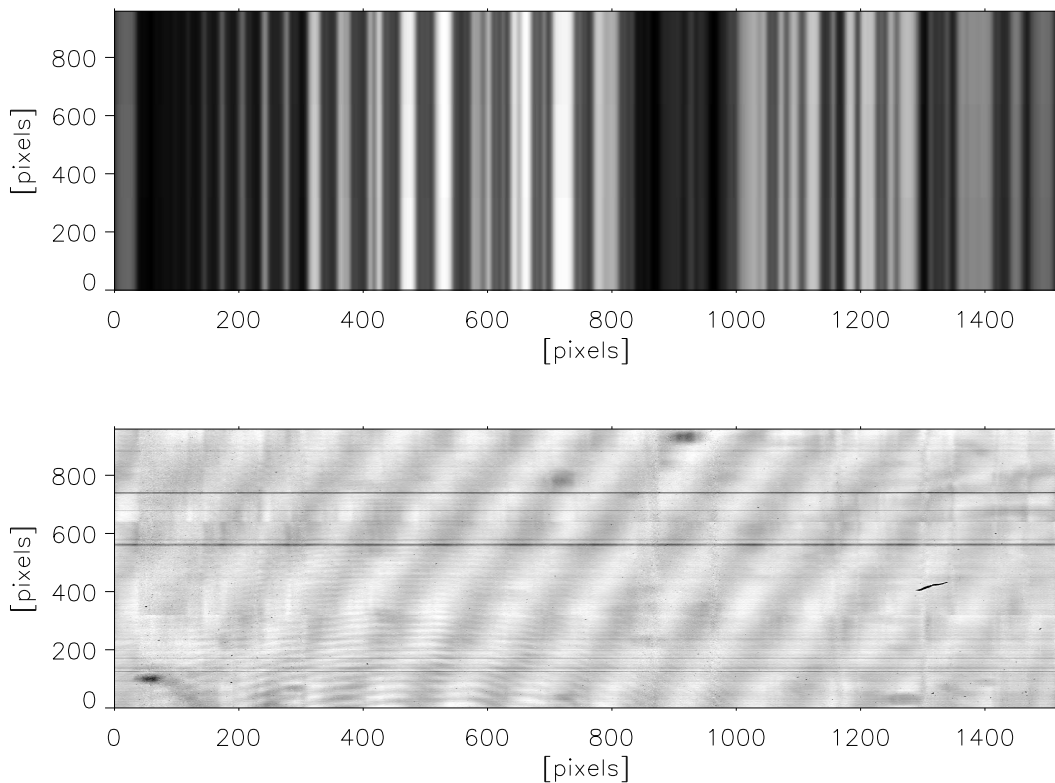


Figure 3.3: Observed flat field corrected for the dark frame, tilt and curvature of the spectral lines (top); computed gain matrix of the CCD (bottom).

to Fe I and CN absorption lines respectively were selected. Here and later we will use vacuum wavelengths, as given by wave numbers in the FTS atlas. It is important that both, our flatfielded mean spectrum and the corresponding spectrum provided by the FTS atlas were taken at the same disc position on the Sun, i.e., disc center, to avoid any differential center-to-limb variation effects (Langhans et al. 2004). The linear dispersion in the spectral plane is defined as :

$$\frac{dx}{d\lambda} = f_s \cdot \frac{d\beta}{d\lambda} = f_s \cdot \frac{m}{a \cdot \cos(\beta)}, \quad (3.2)$$

where $f_s=1500$ mm is the focal length of the Littrow lens, $d\lambda$ is a wavelength change and $d\beta$ is a corresponding angle of reflection change, a is the grating constant and β is the angle of reflection. From equation 3.2 it is evident that the linear dispersion of observed spectra shows a monotone increase when going from long to short wavelengths. In the case of B-spectra the linear dispersion varies from 14.94 mm/nm to 15.07 mm/nm, corresponding to fiducial wavelengths mentioned above. The values of dispersion for the A-spectra are 15.39 mm/nm and 15.55 mm/nm, respectively. To linearize the linear dispersion in the observed data the latter have been linearly interpolated between these two values on the whole observed spectral region and the spectra were destretched accordingly. The difference of the spectral resolution of the FTS atlas and of the obtained A- and B- spectra, which was lower than that of the FTS, is one cause for the slight dif-

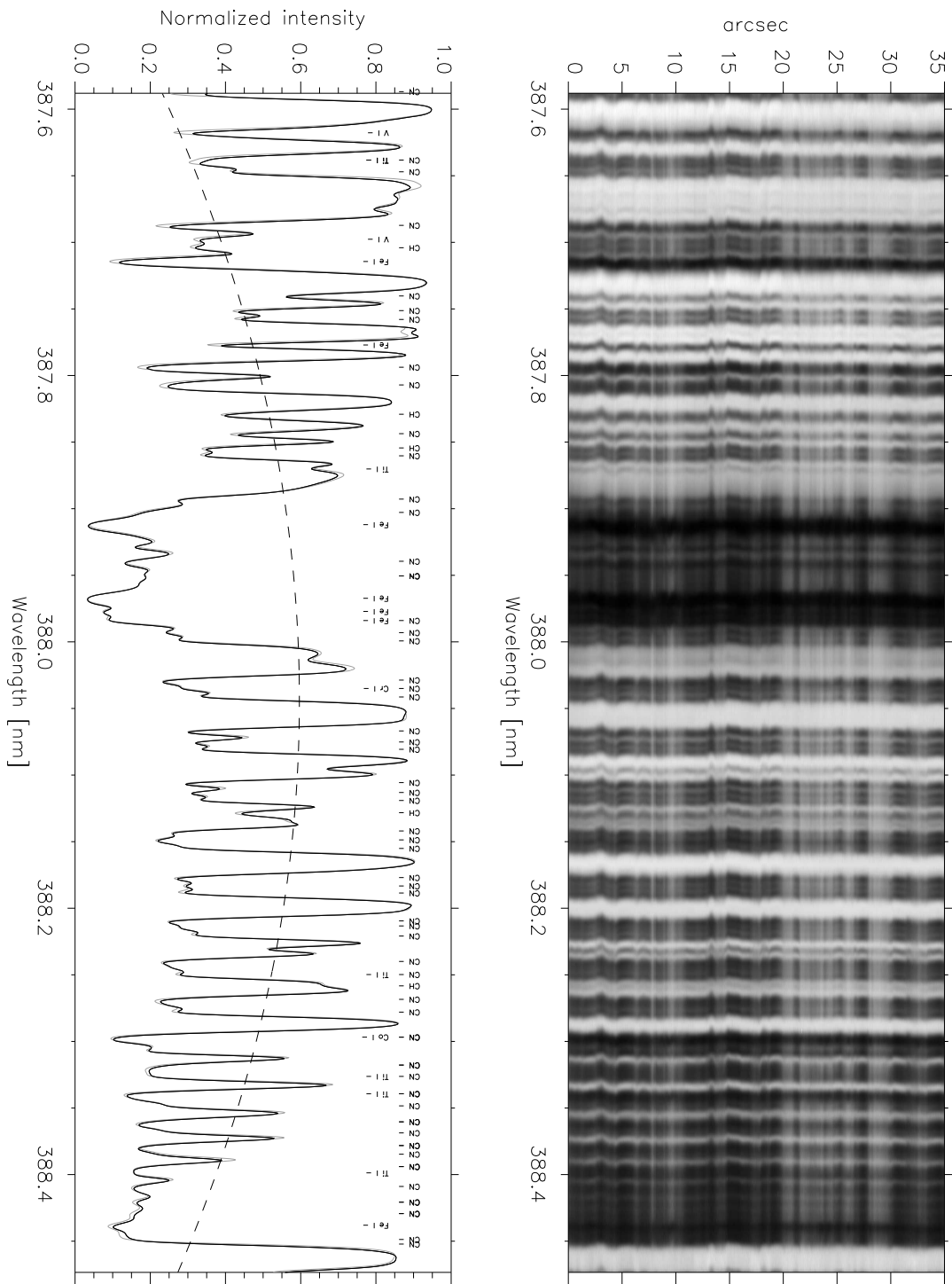


Figure 3.4: Example of a reduced B-spectrum corrected for dark frame, flat field and filter transmission profile (right). At the left we plot the mean observed photospheric spectrum (black line) corrected for dark frame, CCD flat field, filter curve (dashed line) and scattered light. We also plot the FTS spectrum (gray line) in the same spectral region.

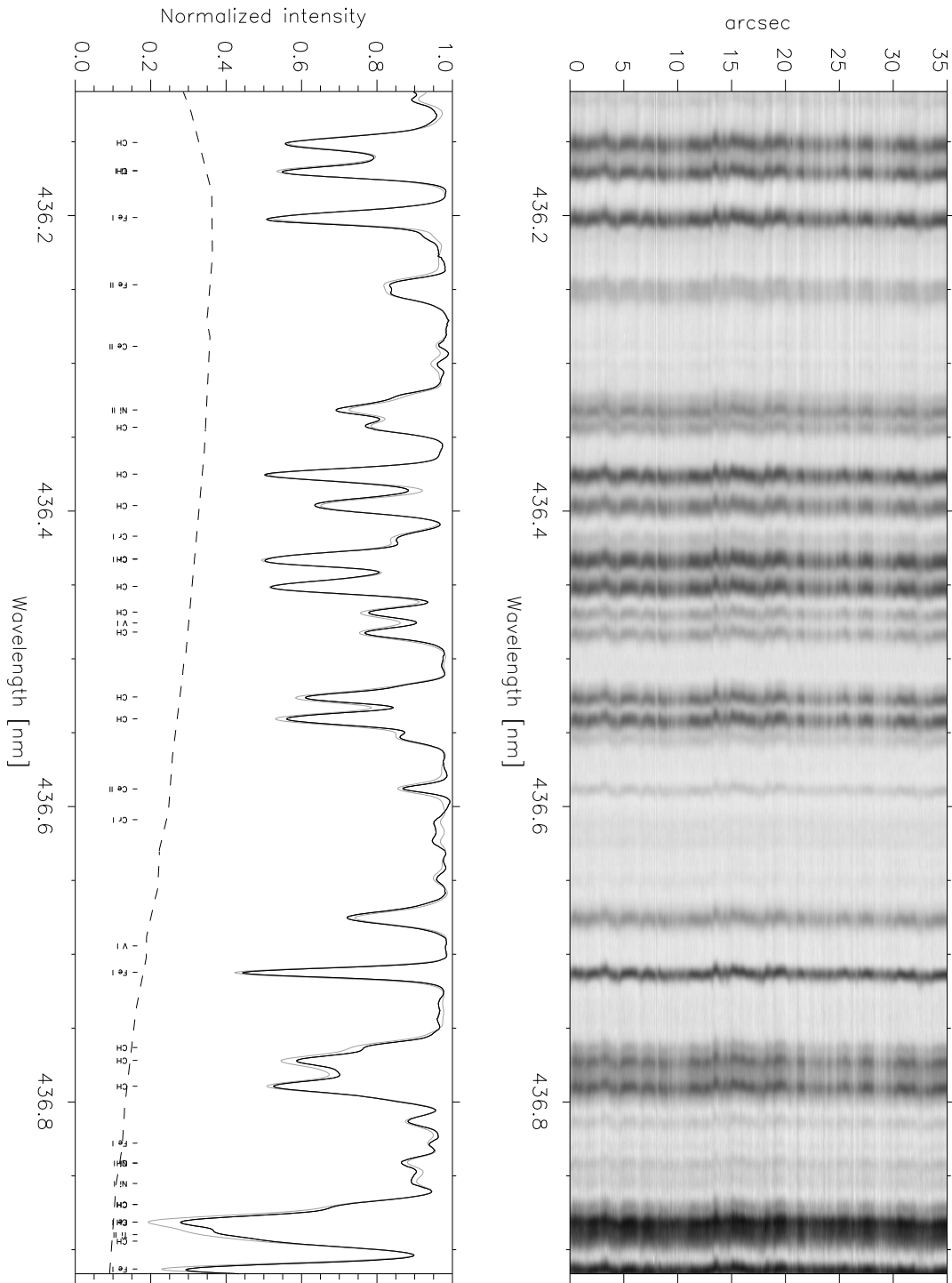


Figure 3.5: Example of a reduced A-spectrum corrected for the dark frame, flat field and filter transmission profile (right). At the left the mean photospheric spectrum taken from an observed flat field (black line) corrected for dark frame, CCD flat field, filter curve (dashed line) and scattered light is plotted, together with the FTS spectrum (gray line) corresponding to the same spectral region.

ference in profiles of corresponding spectral lines. Also spectral stray light in the SST spectrograph, which is absent in the FTS, causes these differences. To compute the transmission curve of the prefilter windows, parts of spectra relatively free of absorption were selected, at which the intensity is least influenced by the difference in spectral resolution. The prefilter curve is calculated by dividing the 1-dimensional reference spectra by the FTS intensity at these wavelengths and then polynomially interpolated on the whole observed spectral domain. Comparison of flatfielded reference spectra with FTS, which are assumed to be free of spectral scattered light, enables us to estimate the scattered light in the obtained data:

$$\begin{aligned} I_{\lambda}^{FTS} &= I_{\lambda} \otimes d_{FTS} \\ I_{\lambda}^{SST} &= I_{\lambda} \otimes d_{SST} + I_{scatter}, \end{aligned} \quad (3.3)$$

where d_{FTS} and d_{SST} are instrumental profiles of the FTS and the SST spectrograph respectively, I_{λ} is the 'true' infalling intensity, I_{λ}^{FTS} and I_{λ}^{SST} are detected intensities, $I_{scatter}$ means the level of the scattered light in the spectrograph and the symbol '*' denotes convolution. Narrow spectral lines are more sensitive to the spectral resolution than broader ones, whereas the scattered light intensity offset is expected to be the same for all of them. By varying the FTS spectral smearing by convolving with a Gaussian function and varying $I_{scatter}$ the optimal combination of these quantities was found showing the best coincidence with the observed 1-dimensional reference spectra, corrected for the prefilter profile.

parameter	A-spectra	B-spectra
spectral range	436.085 nm < λ < 436.953 nm	387.590 nm < λ < 388.480 nm
spectral sampling	5.59211 mÅ/pix	5.82236 mÅ/pix
dispersion	15.47 mm/nm	14.98 mm/nm
resolving power	76360	129170
scattered light	4.1 %	4.7 %
estimated spatial resolution	0.25 arcsec	0.25 arcsec

Table 3.4: Specification of calibrated spectral data

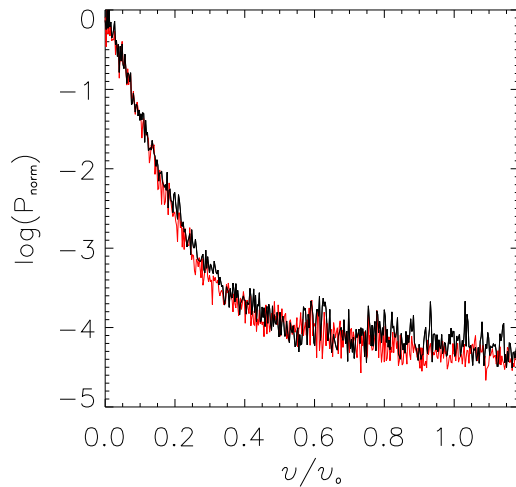
In Table 3.4 the properties of the reduced A-spectra and B-spectra are shown. It should be mentioned that the spectral resolution was estimated from the mean spectra produced as described above as the amount of smearing, which applied to the FTS spectra to get an optimum match.

An empirical diffraction limit of a telescope with entrance pupil D at a certain wavelength λ is given by the Rayleigh criterion:

$$\alpha = 1.22 \cdot \frac{\lambda}{D}, \quad (3.4)$$

where α is the resolution in radian. The spatial resolution of the obtained spectral data depends on several factors like atmospheric and fixed aberrations, exposure time, CCD focusing errors. Due to the λ dependence of seeing one would expect the A-spectra to

Figure 3.6: Normalized power spectra at local 'quasi'-continua I_{cont}^B (black) and I_{cont}^A (red). Spatial frequencies ν were normalized to frequency ν_0 for the diffraction limit of the SST at $\lambda=388$ nm.



have a higher spatial resolution as compared to the B-spectra. However, as a result of the high gain option for CCD in the port A the accuracy of focusing the CCD on the spectrograph slit was lower, than in the port B. This explains the decreased spectral resolution of the A-spectra as well. The refractor system of the SST suffers from residual chromatic aberration after the corrector lens, which makes a small shift of the focal plane along the optical axis when observing at A and B wavelengths. Hence the slit of the spectrograph cannot be located exactly on the focal plane for the two wavelengths. However, the seeing, i.e. contrast reduction, blurring and distortion of observed images due to atmospheric distortions of the wavefront, appears to be the dominant factor. Therefore, as discussed in Chapter 2 the blue B-spectra should have a higher amplitude of aberrations and consequently lower spatial resolution than the A-spectra. The spatial resolution, taking into account all factors listed here, is not linearly dependent on the spectral resolving power. This means that due to the discussed slit defocusing the position of the CCD giving the highest contrast of the spectral lines, i.e. perfectly focused spectra, does not necessarily correspond to the optimum position to obtain highest contrast in a spatial domain.

In Fig 3.6 the normalized power spectra in logarithmic scale of local continuum intensities I_{cont}^B -black and I_{cont}^A -red are shown. The abscissa is scaled to the spatial frequency ν_0 corresponding to Rayleigh's diffraction limit, i.e. 0.098 arcsec, of the SST at $\lambda=388$ nm. The power decrease is almost identical for both A and B data, which points to a similar spatial resolution. At approximately $0.4 \cdot \nu_0$, where the noise level dominates over useful signal of the small scale solar structures, the slope of the power spectra diminishes notably. This spatial frequency corresponds to the spatial resolution presented in Table 3.4 and is nearly equal in A and B spectral datasets.

3.2.3 Doppler shift and line width

The velocity of plasma motions can be calculated from Doppler shift $\Delta\lambda_D$ measurements of spectral lines:

$$\Delta\lambda_D = \frac{\lambda \cdot v}{c}, \quad (3.5)$$

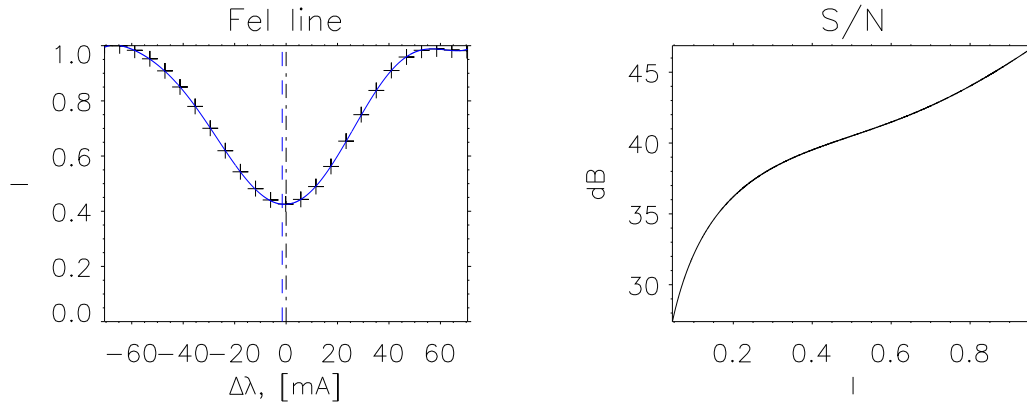


Figure 3.7: Left - an example of $\lambda_{I=min}$ determination using a 4-th order polynomial fit (blue line) to the observed profile of the Fe I line; right - estimated signal-to-noise ratio of B-spectra along several line profiles near 387.777 nm.

where v is velocity, c is the speed of light, λ is the wavelength of the line center. Since different spectral lines are formed at different heights in the photosphere, the knowledge of their Doppler shifts provides information of photospheric velocity stratifications. As shown in Appendix B the contribution function for a given spectral line varies when going from its line-core to the wings. Therefore, the analysis of Doppler shifts at different positions of the line profile also gives information about velocities at different heights. Since all lines in the observed 387.588–388.473 nm spectral region are blended by others, their 'true' profile could not be estimated easily. Therefore we restrict ourselves to investigating Doppler shifts at the line core: $\Delta\lambda_D = \lambda_{I=min} - \lambda_{I=min}^{ref}$, where $\lambda_{I=min}^{ref}$ is a reference wavelength. The reference $\lambda_{I=min}^{ref}$ is the line-core wavelength of the spatially averaged spectral line profile along the slit for which the velocity is assumed to be 0 m/s, since the absolute velocity values are not of particular interest. Before investigating the velocity signature of the solar features, an evaluation of accuracy of the Doppler measurements is essential. If one computes the line shift as the difference between the positions of minimum intensity of the line with respect to the reference position (peak-to-peak method) then an accuracy of ≈ 215 m/s corresponding to a spectral sampling of observed spectra of $5.822 \cdot 10^{-4}$ nm is expected. Fortunately the observed spectral lines are broad enough to contain a sufficient number of pixels so that it is possible to fit the line profile with the polynomial approximation.

In Fig. 3.7 (right) an example of the determination of $\lambda_{I=min}$ in the line-core of Fe I (387.777 nm) using a 4-th order polynomial approximation of the line profile is shown. The presence of noise in the observed data distorts the line profile and introduces an additional error in the approximation. In order to quantify the accuracy of this method and compare it with the others, the amount of noise in the flatfielded spectra was estimated by analyzing their power spectra. The signal-to-noise ratio (SNR) was computed as:

$$SNR[dB] = 10 \cdot \log_{10} \left(\frac{P_{signal}}{P_{noise}} \right) = 20 \cdot \log_{10} \left(\frac{I_{signal}}{I_{noise}} \right), \quad (3.6)$$

where P is average power and I intensity. In Fig. 3.7 (right) the SNR dependence on intensity I , normalized to continuum of a part of the B-spectrum around the Fe I spectral

line is shown. Knowing the noise level all possible distortions of an artificial spectral line were simulated. The result of the simulations showed that $\lambda_{I=min}$ measurements using a 4th order polynomial approximation have a maximum deviation of 43 m/s and a rms-value of 32 m/s, whereas the cross correlation method yields a maximum deviation of only 27 m/s and 24 m/s rms-value. Therefore we have used the latter in our data reduction. Taking into account that flatfielded spectra contain the same line shift errors as the cross correlation method the total error of velocity measurements is estimated to be 54 m/s. We have calculated velocities from Doppler shifts for three species: Fe I at $\lambda_{FeI}=387.777$ nm, CH and CN. To be precise the V_{CH}^B and V_{CN}^B were averaged over speed profiles measured at $\lambda_{CN}=387.844$ nm, $\lambda_{CN}=387.740$ nm and $\lambda_{CH}=387.829$ nm, $\lambda_{CH}=388.124$ nm respectively. In the present chapter the upflows, i.e. blue shifts, were assigned to negative velocities and downflows, i.e. red shifts, to positive velocities.

In addition to the Doppler shifts the full line width at half-minimum or FWHM of the spectral line provides information on the line broadening caused by many factors. The most pertinent for such measurements is the width of the Fe I (387.777 nm) line as its profile is least distorted by blends. The undistorted line profile was reconstructed by subtracting a linear interpolation between two quasi continuum positions at the line borders from the line profile. Using a 4-th order polynomial fit to the line the FWHM is measured. The simulations of such measurements of the artificial spectral line disturbed by known noise, as explained above, gave a maximum deviation of 2 mÅ.

3.2.4 Slit position

Refraction in the terrestrial atmosphere introduces a small shift on the focal plane of the telescope between images taken at different wavelengths in a direction vertical with respect to the horizon. Such a difference is minimum at noon, when the Sun's elevation is largest and maximum when the Sun is located at the horizon. The slit orientation of the SST's spectrograph is parallel to the horizon, which means that the impact of the mentioned effect is maximum and the spectra in port A and in port B are taken at slightly different slit positions on the solar surface. By analyzing A- and B-slit jaw images the spatial shift could be derived.

time, UT [hh:mm:ss]	Δx [arcsec]
14:56:20	0.0553
15:28:40	0.0623
15:49:20	0.0658

Table 3.5: Displacement of the image position on a slit for A-spectra and B-spectra observed on 8 April 2005.

In Table 3.5 the image displacement on a slit at the times, when the data were collected, is presented. For comparison the slit width amounts to around 0.12 arcsec. As one can see from Table 3.5 the difference in image positions on a slit is 0.061 arcsec on

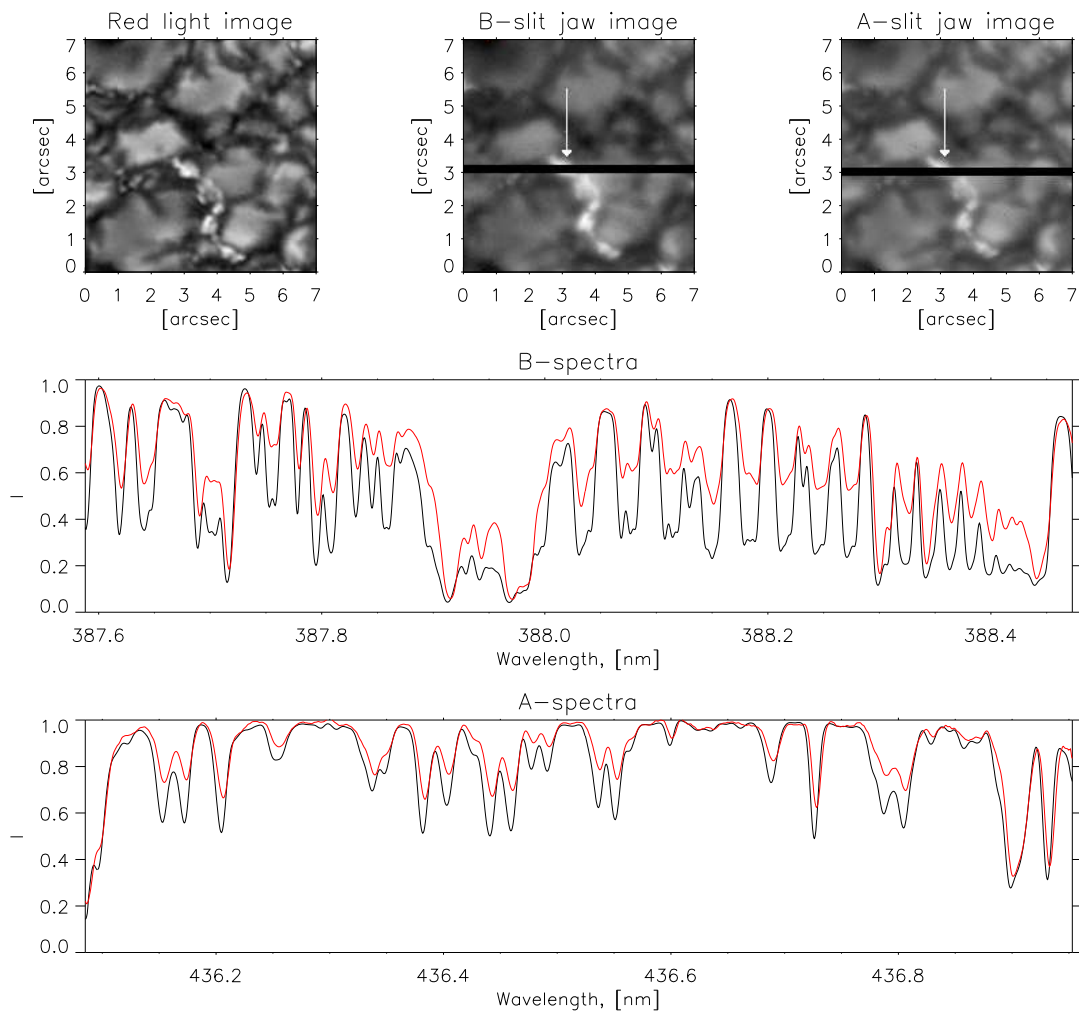


Figure 3.8: Example of B- and A- spectra of a BP (red line) in active region NOAA0753 at $\mu=0.97$ observed on 14 April 2005 at 15:00:45 (UT) and of the quiet Sun (black line). 'Red', B- and A- slit jaw images with a white arrow marking the BP are also provided.

average. Since we do not possess full two-dimensional spectral scans over a solar region but only one-dimensional spectra at single slit positions the accuracy of the comparison between A-spectra and B-spectra is decreased by this systematic error. Consequently for a precise investigation of the spectral properties of photospheric features A-spectra and B-spectra were studied separately. Since the B-spectrum covers spectral lines of all desired species (i.e. Fe, CH, CN) we give its analysis the highest priority.

3.2.5 Intensity

In Fig. 3.8 two samples of observed A- and B-spectra are presented. In BPs both spectra show a considerable decrease in depression of absorption lines of CN and CH molecules and of many atomic lines as well.

The intensity contrast C_λ at the line core was defined as:

$$C_\lambda = \frac{I_\lambda - \langle I_\lambda \rangle}{\langle I_\lambda \rangle}, \quad (3.7)$$

In the present analysis the line-core intensities I_{CH}^A of a CH line at 436.396 nm, I_{CH}^B of a CH line at 387.829 nm, I_{FeI}^B of an Fe I line at 387.777 nm and I_{CN}^B of a CN line at 388.188 nm were measured. The main properties of the transitions corresponding to these lines are given in Table 3.6 and in Table 3.7.

Element	Wavelength vacuum, [nm]	Wavelength air, [nm]	Branch	Oscillator strength	System
CH (A-spectra)	436.396	436.272	'P'	0.281E-02	A-X 0-0
CH (B-spectra)	387.829	387.719	'R'	0.230E-02	B-X 0-0
CN (B-spectra)	388.188	388.009	'P'	0.345E-01	Violet 0-0
CN* (B-spectra)	387.844	387.734	'P'	0.345E-01	Violet 0-0

Table 3.6: Properties of molecular transitions of CH and CN lines used in the present investigation. The CN line marked with * is used for Doppler measurements and line depression study.

Wavelength vacuum, [nm]	Wavelength air, [nm]	Transition	E_u [eV]	E_l [eV]	$\log(gf)$
387.7769	387.6670	$5D^0 - a^3P^2$	5.4763	2.2788	-2.808

Table 3.7: Atomic transition parameters for the Fe I line used in observations.

The fact that many spectral lines are blended with each other, which changes the line-core intensity, was not taken into account when computing the contrasts. This means that models must be used to compute the spectrum with all the blended lines prior to the comparison with the observations. The total A-spectra and B-spectra intensity were calculated by integration over λ of the whole obtained spectral domain multiplied with a prefilter curve representative of the filters used for imaging (see Chapter 2). Unfortunately the B-spectrum does not reach the pure continuum in the whole spectral range. Therefore the intensity over two positions of 'quasi'-continuum at 388.202 nm and 388.161 nm was averaged, which corresponds to a 'quasi'-continuum brightness I_{cont}^B at ≈ 388.18 nm with an FTS atlas value of 0.894. The A-spectrum has much less spectral lines and includes almost clear continuum regions with an FTS atlas value of 0.987. The I_{cont}^A intensity was averaged over four positions at 436.131 nm, 436.186 nm, 436.221 nm and 436.272 nm, corresponding to a mean wavelength of ≈ 436.202 nm. The above 'quasi'-continuum wavelengths were selected such that the absolute intensity at these positions showed the smallest rms along the slit in the observed spectra. This means that it is least affected by the spectral lines whose depression varies in a wide range depending on the solar feature.

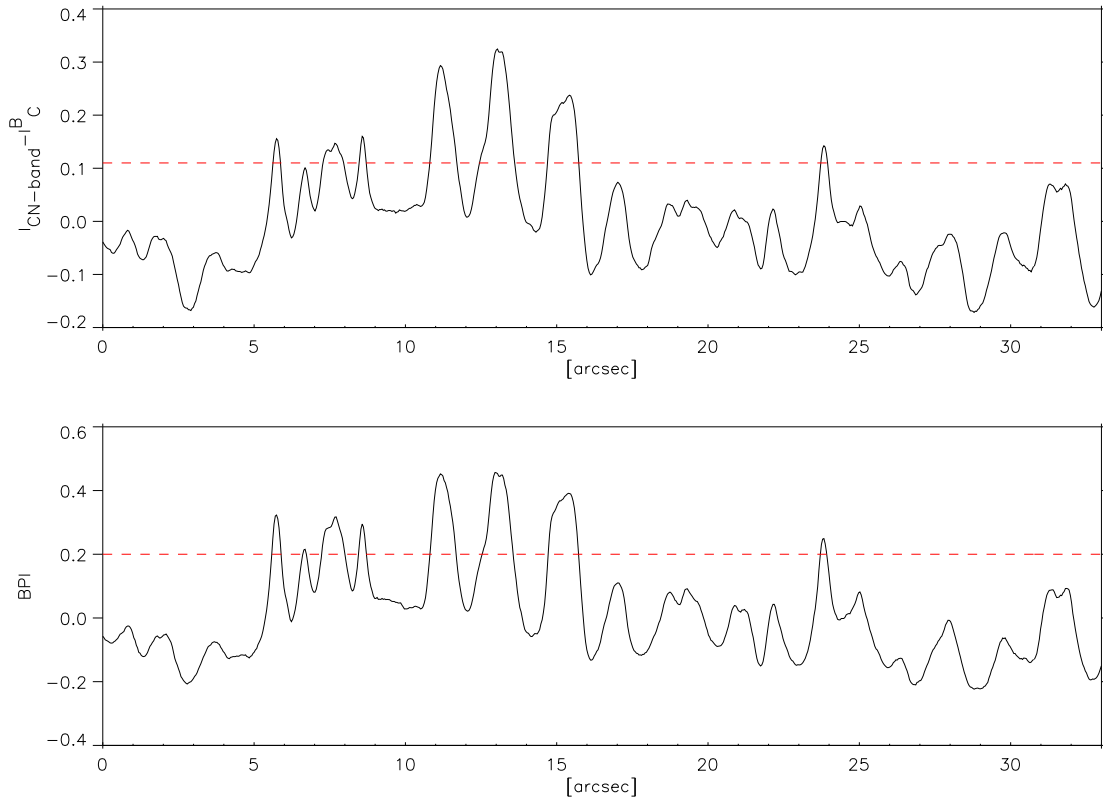


Figure 3.9: Coincidence of two methods of automatically discerning magnetic bright features from the non-magnetic features. Top - local continuum intensity subtracted from CN-band intensity; bottom - BPI. The dashed red line represents the threshold.

3.2.6 Bright Point Index

The Bright Point Index (BPI) was introduced by Langhans et al. (2001) in order to determine the positions of bright small-scale magnetic features and automatically distinguish them from the non-magnetic bright features. BPI calculations are based on the fact that in a BP the weakening of CH-line depression is stronger than that of atomic lines. Assuming that CN absorption lines behave similarly the BPI was computed as follows:

$$BPI = \frac{I_{cont} - I_{atom}}{\langle I_{cont} - I_{atom} \rangle} \cdot \frac{\langle I_{cont} - I_{CN} \rangle}{I_{cont} - I_{CN}} - 1, \quad (3.8)$$

where I_{cont} is a local continuum intensity (see previous section), I_{atom} is the line-core intensity of an atomic line and I_{CN} line-core intensity of a CN line. Following Langhans et al. (2001) all intensities were normalized to a 'quasi'-continuum atlas intensity $I_a = 0.894$. Not all atomic lines conform to the assumption above. Analysis of BP spectra revealed that the Fe I line at 387.912 nm has a very small amplitude of change in line depression over non-magnetic and magnetic, e.g. BPs, features and thus was used for the BPI determinations. The conformity of the BPI method and the difference of normalized to the mean intensities at local continuum in the CN-band is presented in Fig. 3.9. The criterion $BPI \geq 0.2$ is used to separate magnetic bright features from the non-magnetic

ones. This criterion according to Fig. 3.9 corresponds to $\left[\frac{I_{CN-band}}{\langle I_{CN-band} \rangle} - \frac{I_{cont}}{\langle I_{cont} \rangle} \right] > 0.11$ which can be applied when analyzing the filtergrams (see chapter 2). Fig. 3.9 is a vivid demonstration of the adaptability of the photospheric bright points detection technique introduced by Berger et al. (1998) using continuum and molecular band filtergrams taken simultaneously. Due to the absence of appropriate atomic spectral lines in the A-spectra the BPI was not calculated in that spectral domain.

3.2.7 Line depression

As mentioned above, the difference in image position on a slit in a vertical direction for both observed spectra complicates direct comparison and study of their relation in a certain solar feature. Fortunately the observed B-spectra contain several CH lines. Thus it is possible to avoid this problem. The CH line most favorable for the further investigation is situated at 387.829 nm and corresponds to the B-X system. This absorption line is still blended mainly by the blue wings of the Fe I (387.912 nm) and Fe I (387.968 nm) spectral lines. In the BPs these strong atomic lines insignificantly change their depression at the line-core, but absorption in the wings is weakening in a quite wide range up to 20%. As a consequence the shape of the CH line is distorted in a hardly predictable way. In order to improve the precision of computation of the CH line depth, the contribution of the wings of these atomic lines was estimated by linear interpolation between the values at 387.874 nm and 387.820 nm, i.e. local spectral maxima, which we consider as an attenuated continuum, and subtracted from its profile. Here we assume that the mentioned molecular line is never saturated. Deviations of the line-core depression in a certain photospheric feature were calculated as follows:

$$\Delta D_{\lambda} = \frac{I_{\lambda}/I_{cont} - I_{\lambda}^{quietSun}/I_{cont}^{quietSun}}{I_{\lambda}^{quietSun}/I_{cont}^{quietSun}}, \quad (3.9)$$

Among the almost free from undesirable blending CN lines the observed B-spectra possess a CN line at 387.844 nm which is positioned very close to the selected CH line and consequently is also blended by the blue wings of the same atomic lines as that. Thus the accuracy of line depression calculations was verified by comparison of the variation in line depression of the deblended (by deblending method described above) CN line at 387.844 nm and almost undisturbed (since they are far away from strong atomic lines with wide wings) CN lines at 388.188 nm, 388.183 nm and 388.178 nm. The results of such tests yielded that the deviation of two computed values is less than 3% throughout the observed data, which is acceptable for the present investigation.

3.3 Spectroscopy of small-scale magnetic features at the disc center

3.3.1 Main properties

In this section the common spectral properties of the photospheric bright points and other manifestations of the small-scale magnetic activity of the Sun are investigated. The quan-

titative analysis of the behavior of the spectral lines of CH, CN and Fe I will be presented in Section 3.3.5.

Fig. 3.10 and Fig. 3.11 show one example of a calibrated spectroscopic dataset of an active region NOAA07353 observed on 14 April 2005 at 14:56:19 (UT) at disc position $\mu = \cos(\theta) = 0.97$, where θ is the heliocentric angle. The first two images in Fig. 3.10 show an intensity map in 'Red' and the B-slit jaw image used to assign identified solar features to the spectra. The first two panels in Fig. 3.11 show a 'Red' image and an A-slit jaw image respectively. The brightness scales are not plotted since the slit jaw images were not used for intensity analysis. The horizontal black lines (Fig. 3.10 b) and Fig. 3.11 b)) mark the position of the slit. The seeing conditions were good enough to provide MFBF restored 'Red' images at the diffraction limit. The exposure time of 1.5 s is long enough to assume that the high frequency atmospheric aberrations of the wavefront had randomly distributed intensity over the whole FOV which, therefore, allow us to assume it as isoplanar. This means that A-, B-spectra and A-, B-slit jaw images and also 'Red' images have constant spatial resolution without any distortions. All three images as well as the spatial domain of A- and B- spectra were coaligned by means of cross correlation.

In Fig. 3.10 c) and in Fig. 3.11 c) the profiles of the local continuum contrast (i.e. at $\lambda_{cont}^B=388.18$ nm and $\lambda_{cont}^A=436.202$ nm respectively) along the slit obtained from B- and A-spectra respectively are plotted (red line). In the same panels the black line represents the contrast of intensity integrated over the whole B and A spectral regions labeled I_{int}^B and I_{int}^A . It is easy to see that I_{int}^B which could be roughly associated with intensity in the blue CN band-head observations described in Chapter 2 reveals strong brightness excess at the BPs positions in comparison with the local continuum intensity. Unfortunately the observed spectral region of A- and B-spectra does not fully cover the total pass-band of the filters used in imaging observations (see Chapter 2). This makes the direct comparison of spectroscopically obtained contrast values with results of the imaging observations impossible. At the same time many photospheric structures showing low BPI have almost everywhere reduced I_{int}^B comparing to the continuum one. A similar behavior was found for I_{int}^A and its 'quasi' continuum, although with a much lower separation between them.

Target	$\text{rms}(I_{cont}^B)$	$\text{rms}(I_{cont}^A)$	$\text{rms}(I_{int}^B)$	$\text{rms}(I_{int}^A)$	$\text{rms}(I_{CN}^B)$ $\lambda=388.188$	$\text{rms}(I_{CH}^B)$ $\lambda=387.829$	$\text{rms}(I_{FeI}^B)$ $\lambda=387.777$
Quiet Sun	0.097	0.075	0.091	0.070	0.178	0.100	0.066
Active area	0.099	0.093	0.142	0.090	0.355	0.179	0.115

Table 3.8: RMS contrasts of 'quasi' continuum intensities I_{cont}^B and I_{cont}^A ; integrated brightness I_{int}^B and I_{int}^A ; line-core intensities I_{CN}^B , I_{CH}^B and I_{FeI}^B observed at $\mu=0.97$ in active region NOAA0753 and nearby quiet Sun areas on 14 April 2005 at 14:56:19 (UT).

The corresponding rms contrast values of line-core, integrated and 'quasi' continuum intensities are presented in Table 3.8. The result is a product of analysis of spectrograms from 10 different image positions across the observed active region. In the 'Red' image the variety of the magnetic solar features of different scales catches one's eye. The

3.3 Spectroscopy of small-scale magnetic features at the disc center

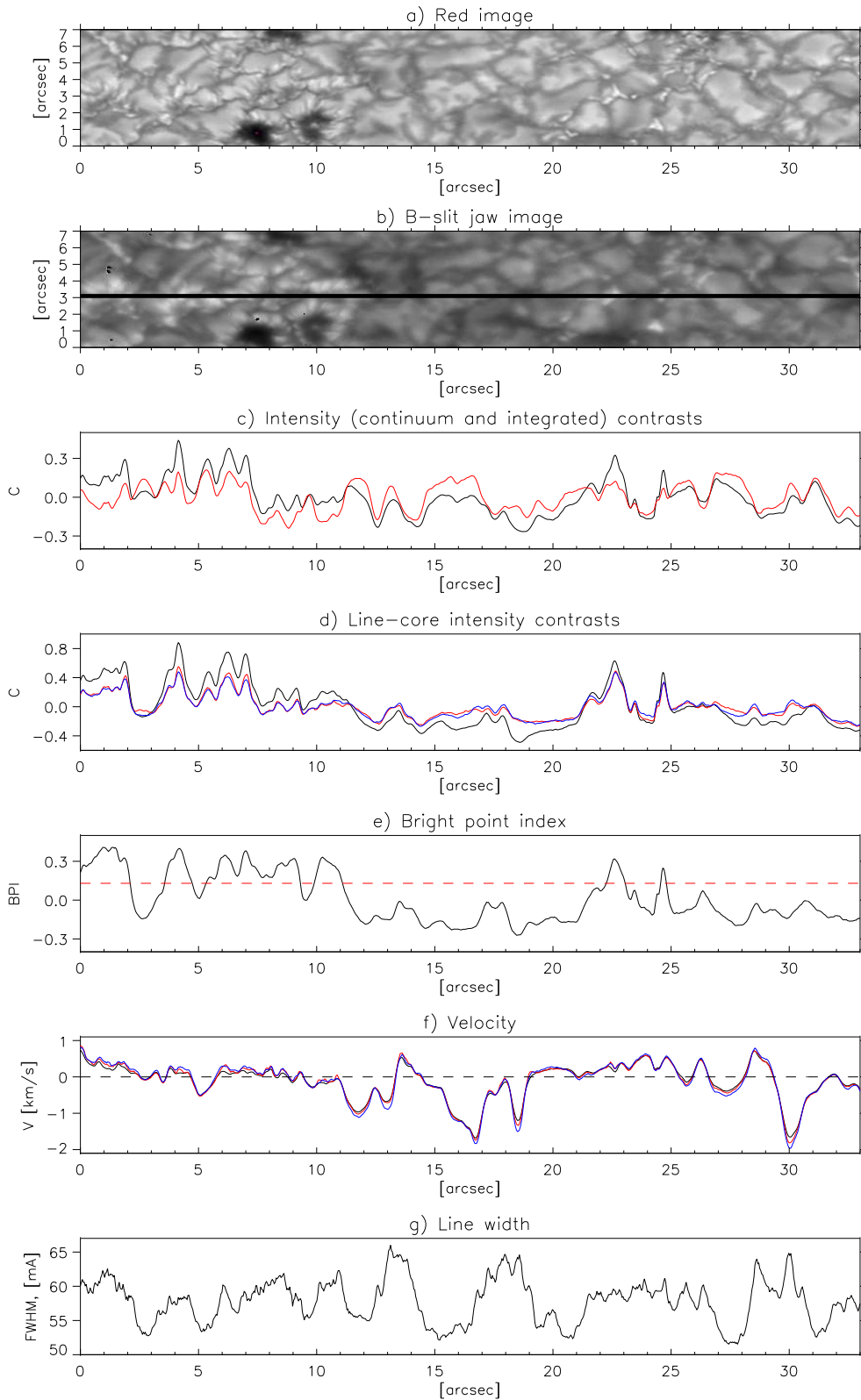


Figure 3.10: Spectroscopic data observed in the active region NOAA0753 at $\mu=0.97$ on 14 April 2005 at 14:56:19 (UT) : a) Reference image; b) B-slit jaw image; c) integrated and continuum intensity contrasts $C(I_{int}^B)$ - black, $C(I_{cont}^B)$ - red; d) line-core intensity contrasts $C(I_{CN}^B)$ - black, $C(I_{CH}^B)$ - red, $C(I_{FeI}^B)$ - blue; e) BPI; f) velocities V_{CN}^B - black, V_{CH}^B - red, V_{FeI}^B - blue; g) line width of Fe I line.

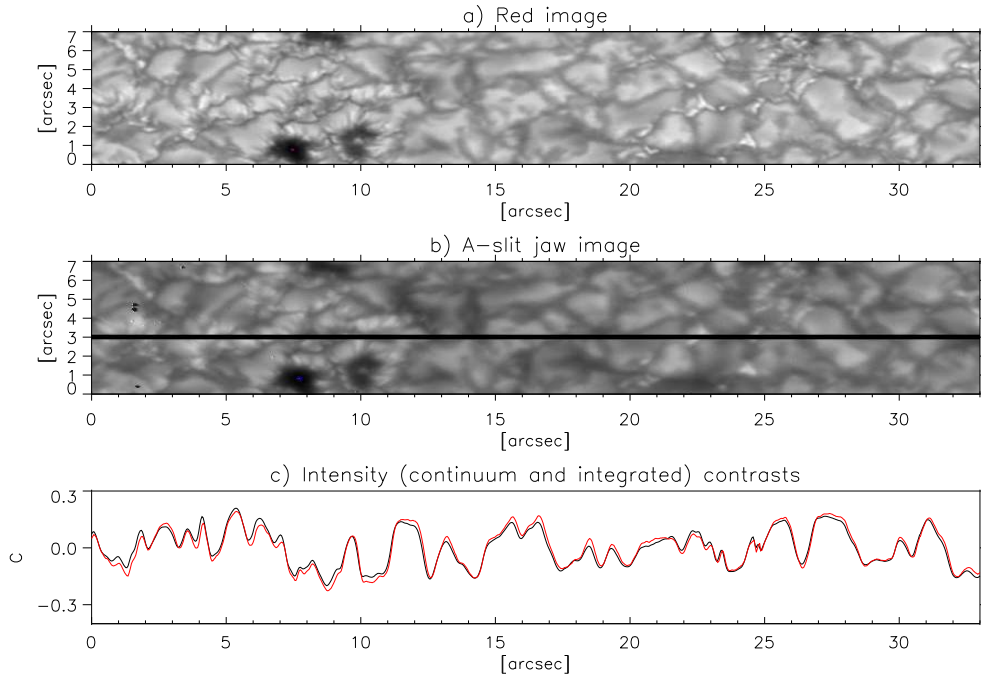
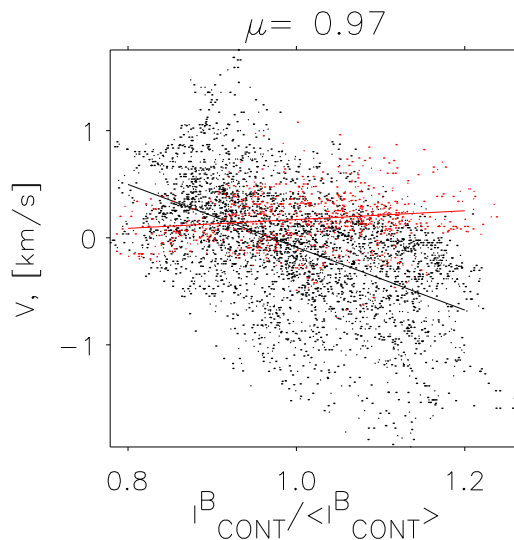


Figure 3.11: Spectroscopic data observed in the active region NOAA0753 at $\mu=0.97$ on 14 April 2005 at 14:56:19 (UT) : a) Reference image; b) A-slit jaw image; c) intensity contrasts (I_{int}^A) - black, (I_{cont}^A) - red.

presence of pores indicates an area with high magnetic activity. The not cropped slit jaw image (not shown in the figure) reveals that these pores are situated on the intersection of so-called supergranular cells. It is remarkable that the bright points near the pores look like solar facular structures as observed closer to the solar limb at very high spatial resolution. The physical origin of solar faculae will be discussed in more detail in Chapter 4. Here we just mention that solar faculae and BPs, are manifestations of small-scale magnetic concentrations in the photosphere. In the case of faculae the LOS is inclined to the magnetic field vector, which one assumes to be parallel to a flux-tube axis. The intensity enhancement corresponds to a "hot wall" of a granule located behind the flux-tube (see Section 4.6). The main marking of facular brightenings is the distinctive monotone brightness rise of the granule in a certain direction which drops abruptly at the edge with a thin dark lane just before the next granule. Such an appearance of the granulation is clearly seen in Fig. 3.10 a) at 4–12 arcsec. Therefore we propose that the active region observed at $\mu=0.97$ has an inclined magnetic field near the pores. The integrated intensity of the faculae I_{int}^B also shows a higher contrast than I_{cont}^B . It is remarkable that the line-core contrasts (Fig. 3.10 b) at 4–12 arcsec) reveal increased excess of I_{CN}^B and I_{CH}^B contrasts. This result is in good agreement with results obtained outside of the disc center (see Section 3.4).

Notice that the original A- and B-spectra were longer than presented here and the zero-velocity, however, was determined from the full spectra. The flow velocities presented in Fig. 3.10 f) vary in a wide range and are slightly different for CN, CH and Fe I spectral lines. Concerning the whole spectroscopic data obtained at $\mu=0.97$ the upflow velocity was observed to be up to ≈ -1950 m/s in the bright granules whereas the maximum

Figure 3.12: Scatter plot of flow velocity vs. continuum intensity I_{cont}^B observed at $\mu=0.97$. Red color corresponds to BPs and black to granulation and the lines are the corresponding linear fits to the data.



detected downflow velocity is only +1700 m/s in the dark intergranular areas. Large downflows are also very rare compared with large upflows.

Spectral line	$N_{downflow}/N_{total}$	N_{upflow}/N_{total}
CH	48.4 %	51.6 %
CN	48.6 %	51.4 %
Fe I	47.4 %	52.6 %

Table 3.9: Number of pixels along the slit showing downflows and upflows, with respect to the total number, measured for CN, CH and Fe I spectral lines (B-spectra) at $\mu=0.97$. Measurements from many spectrograms from different image positions were used.

Although, as summarized in Table 3.9, the mean velocity along the slit was set to 0 m/s the number of pixels, along the slit, which show downflow and upflow is not exactly the same. The low spectroscopic signal of narrow and dark intergranular lanes, which show downflows, is obscured by intense spectra of the nearby bright granulation, which show upflows. Consequently at limited spatial resolution, spectra showing blue shifts are more often observed as the downflow spectra. This explains the difference in numbers seen in Table 3.9.

In Fig. 3.12 the dependence of velocity on the continuum intensity I_{cont}^B observed at $\mu=0.97$ using spectrograms from 10 image positions is presented. The black and red pixels refer to the non-magnetic and the bright point (with the $BPI \geq 0.2$) areas respectively. The scatter plot shows that the downflow velocity of non-magnetic features decreases with increasing continuum brightness eventually becoming a sizable blue shift. This tendency confirms observations of Nesis et al. (1992). However, they used another spectral line for velocity measurements. The non-BP features cover mostly the whole range of measured velocities. In contrast, most BPs display almost constant velocity slightly increasing with

the rise of I_{cont}^B and cover the 0–300 m/s range. The uncertainty of the velocity 0-reference definition does not allow to make a statistically precise analysis of the velocity distribution and the diagram 3.12 should be considered as qualitative behavior.

The FWHM of the Fe I line shown in Fig. 3.10 g) reveals small changes with an amplitude up to 12% around the mean value. However, no clear correlation with velocity or intensity profiles was found. Inspecting the scatter plot of the FWHM versus velocity V_{FeI}^B at the corresponding heliocentric angle (Fig. 3.13 left, upper panel), no clear tendency of Fe I line broadening when going from upflow to downflow motions is seen. The areas related to the photospheric brightenings: BP's and faculae, marked with a red color, display an almost constant value of FWHM at around 62 mÅ.

3.3.2 Individual cases

In this section we will consider some properties of particular photospheric features in more detail.

1. In Fig. 3.10 and 3.11 the BP at 22.7 arcsec is a typical G-band bright point, of quite small size, located in the intergranular region. It is embedded in the dark intergranular furrow, which divides it from adjoining granules on each side. Almost no variation of FWHM, whose value amounts to 59 mÅ, was found within the error bars. The velocity shows a minutely enhanced downflow in the dark lane to the left of the BP and to its right. The local peak of negative velocity does not lie at the minima of intensities I_{cont}^B , I_{CN}^B , I_{CH}^B or I_{FeI}^B , but is shifted toward the BP center by around 0.25 arcsec. The BP itself reveals a slightly smaller downflow by ≈ 200 m/s as compared to the immediate surrounding downflow peaks of the intergranular lanes. At the center of the BP the contrast of I_{FeI}^B is slightly lower than those of I_{CH}^B and much less than that of I_{CN}^B . A very faint BP to the right centered at 24.75 arcsec is also surrounded by dark lanes, which appear to be more prominent. This BP has a clear 'embedded in the downflow' structure. The plasma downflow motions are gradually increasing when going from the BP center, where it reaches 350 m/s, to the right dark lane up to 500 m/s. When going to the left from the center of the BP the velocity decreases down to 200 m/s and starts to increase again in the left dark lane, reaching a maximum of 600 m/s. As in the previous case local extrema of the BPI correspond exactly to those of the contrast profiles. Also, in the discussed regions, the velocity profiles obtained for different lines are equal.

2. In Figs. 3.14 and 3.15 the BP centered at 23.9 arcsec does not show a clear 'embedded in the downflow' velocity distribution. The center of this BP has a downflow value of $V_{CH}^B = V_{CN}^B \approx 300$ m/s and $V_{FeI}^B \approx 400$ m/s which is somewhat larger than in its immediate surrounding to the right. The right side of this BP borders on the quite extensive intergranular dark region where downflow velocity increases up to $V_{CH}^B = V_{CN}^B \approx 800$ m/s and $V_{FeI}^B \approx 1000$ m/s at 24.8 arcsec on the slit, after a narrow slump of 250 m/s near the BP. Thus at the location of this velocity slump the BPI is less than 0.2 and the 'Red' image together with $C(I_{CN}^B)$ does not show any brightness excess there. From these examples we conclude that the dark intergranular lanes could have various velocities which are not necessarily higher than those of the embedded BP. It is remarkable that the intensity I_{CN}^B contrast profile has a distance between the minima, assigned to the intergranular dark region, bigger than the same for I_{cont}^B . This fact could be explained by the expansion of the flux tube with height in the photosphere.

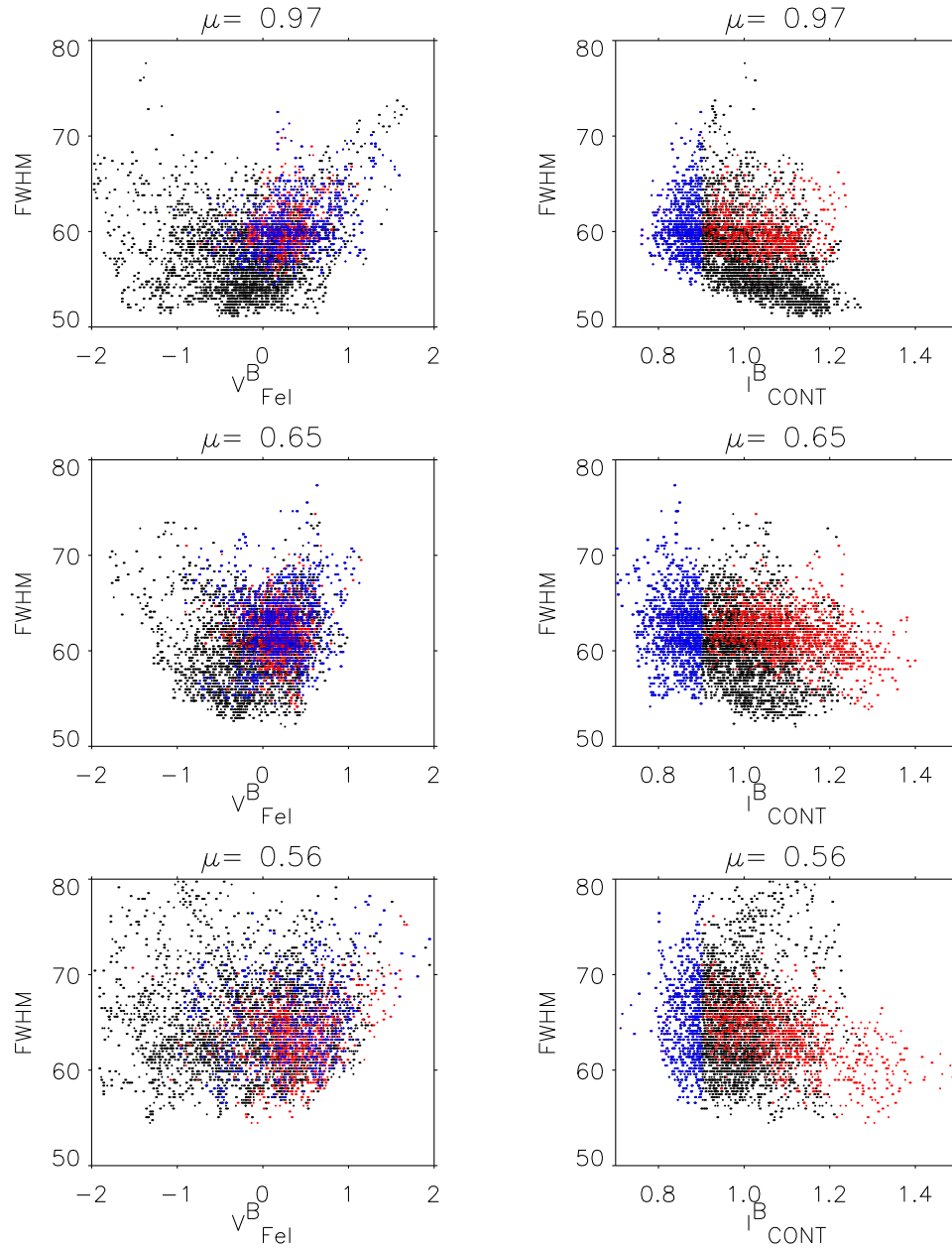


Figure 3.13: Fe I line FWHM plotted versus flow velocity measured for this line (left panels) and versus normalized continuum intensity (right panels) at different heliocentric angles. Data marked with black, red and blue colors correspond to granules, **BPs** (BPI ≥ 0.2 for $\mu=0.97$ and BPI ≥ 0.13 for $\mu = 0.65$ and $\mu = 0.56$, and **intergranular lanes**, where $I_{\text{cont}}^B < 0.9$, respectively.

3 High resolution spectroscopy of the solar photosphere

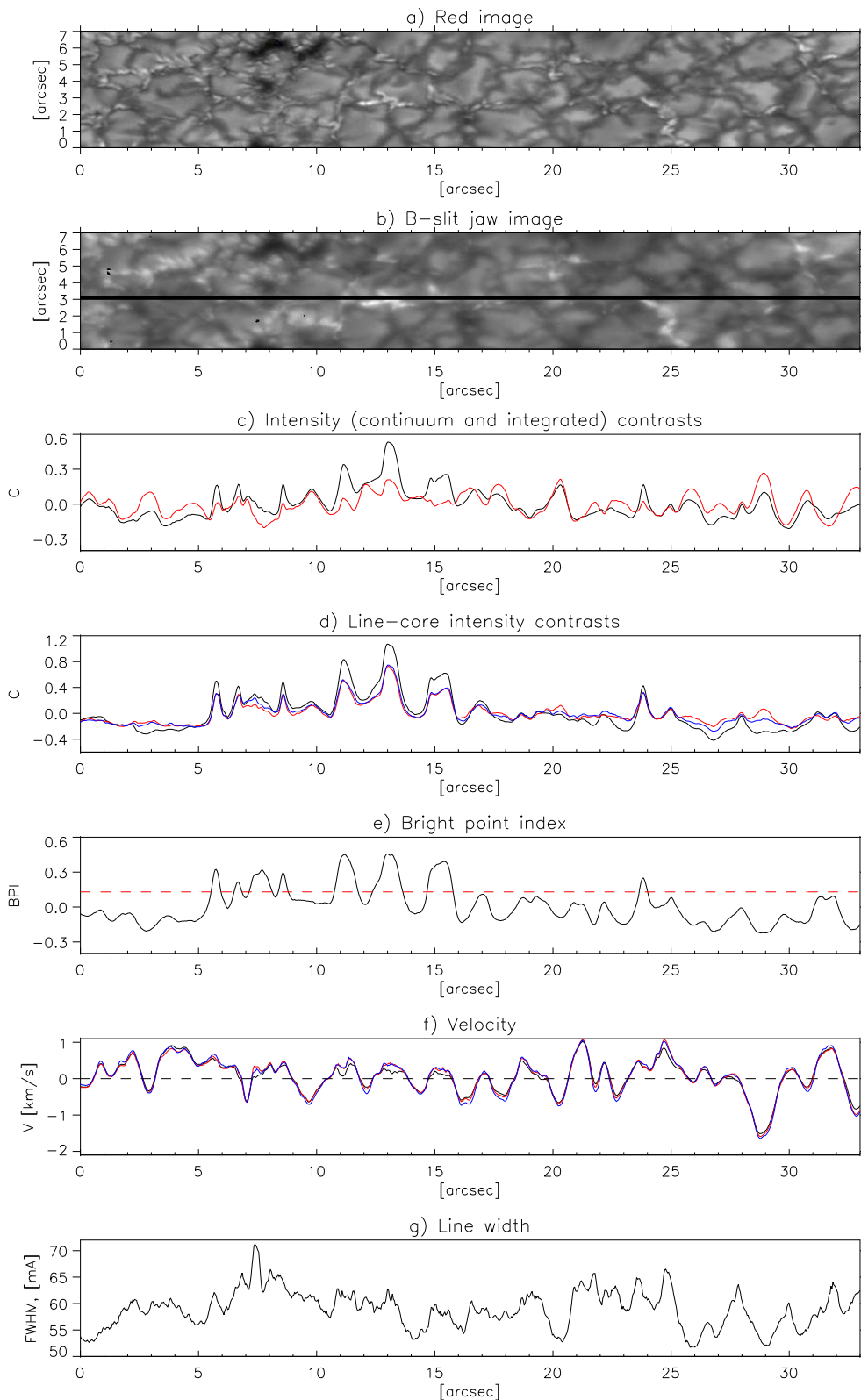


Figure 3.14: Spectroscopic data observed in the active region NOAA0753 at $\mu=0.97$ on 14 April 2005 at 14:56:19 (UT) : a) Reference image; b) B-slit jaw image; c) integrated and continuum intensity contrasts $C(I_{int}^B)$ - black, $C(I_{cont}^B)$ - red; d) line-core intensity contrasts $C(I_{CN}^B)$ - black, $C(I_{CH}^B)$ - red, $C(I_{FeI}^B)$ - blue; e) BPI; f) velocities V_{CN}^B - black, V_{CH}^B - red, V_{FeI}^B - blue; g) line width of Fe I line.

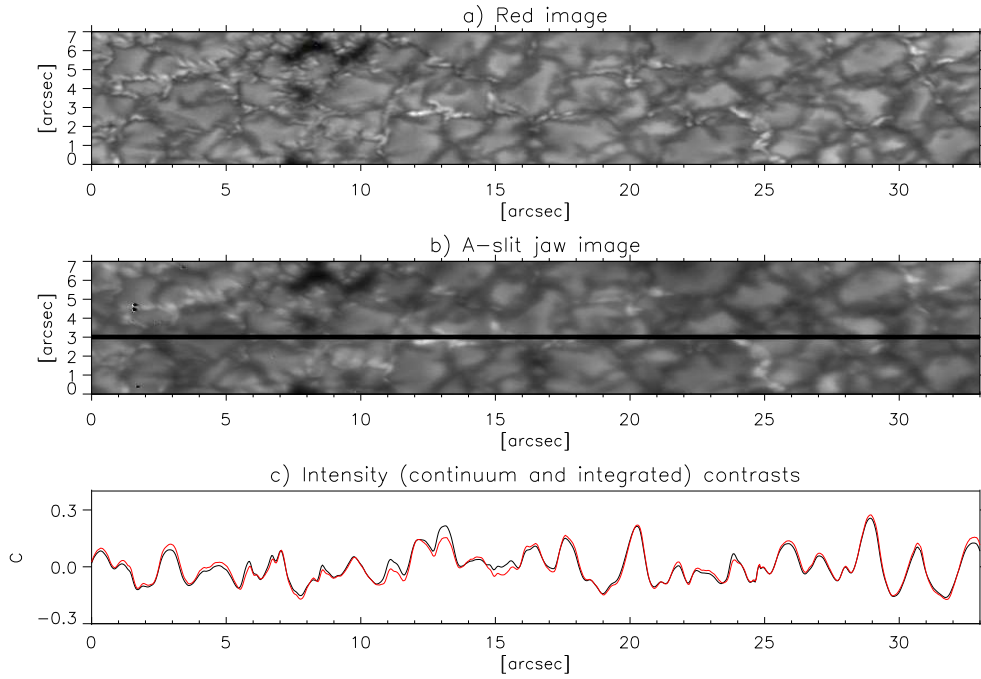


Figure 3.15: Spectroscopic data observed in the active region NOAA0753 at $\mu=0.97$ on 14 April 2005 at 14:56:19 (UT) : a) Reference image; b) A-slit jaw image; c) intensity contrasts (I_{int}^A) - black, (I_{cont}^A) - red.

3. The continuum contrast of I_{cont}^B and I_{cont}^A shows almost zero or even negative values for some BPs. In the 'Red' image such BPs appear bright or sometimes darker than granules. A good example of such a structure is a BP at 11.1 arcsec in Figs. 3.14 and 3.15. The velocity V_{CN}^B differs from V_{CH}^B and V_{FeI}^B by ≈ 250 m/s in the center of the BP. Nevertheless the shape of velocity profiles across the BP is similar for all three spectral lines and shows a clear 'embedded in the downflow' contour. However, the BPI fulfills the criteria of photospheric BP even at the local minima around observed BP. Thus this BP should be ≈ 1 arcsec wide for a certain slit position. The high value of the BPI=0.47 at the center of the BP, i.e. peak of $C(I_{CN}^B)$, $C(I_{CH}^A)$ points to a stronger decrease of absorption in CN and probably CH spectral lines there, due to the high temperature, in comparison to a 'normal' BP. The difference between velocities in the core of the BP and in the bordering dark lanes is 200 m/s and 300 m/s to the left and to the right of the BP respectively. Outside of the dark lanes velocities $V_{CN}^B=V_{CH}^B=V_{FeI}^B$ become negative monotonely in the neighboring granules, reaching highest values at the location of their maximum intensity. The contrast of I_{int}^B is above those of I_{cont}^B , the same as for I_{int}^A and I_{cont}^A , not only within the BP interior but also in dark furrows. The physical explanation of this phenomenon will be presented in Section 3.6.1. The FWHM with local minima of 58 mÅ and 59 mÅ on the BP edge, where $V_{CN}^B=V_{CH}^B=V_{FeI}^B=0$ m/s, is slightly larger, than 62 mÅ in-between.

4. Another example of wide, dark BPs situated at 14.4–15.9 arcsec position is on the same plots as above. This BP has quite diffuse borders with adjacent granulations with narrow dark lanes on the edges. The intensity across this BP remains flat with a slump at the edges. As follows from the BPI profile the size of this BP is ≈ 1.15 arcsec if it is not

an unresolved agglomeration of smaller BPs. It is similar to a wide 'ribbon-like' structure observed by Berger et al. (2004). The FWHM shows again a ≈ 6 mÅ leap inside the BP. The contrast difference between I_{int}^B and I_{cont}^B reaches a value of 0.23, which is bigger than for a 'normal' BP and similar to the dark BP from example 3. The velocity profiles have no local perturbations and increasing, as a downflow up to $V_{CN}^B = V_{CH}^B = V_{FeI}^B \approx 300$ m/s in the BP center, monotonely from its sides. Thus, in contrast to the previous examples, this BP has no visible 'embedded in the downflow' structure and is located in a strong downflow as the whole.

Topka et al. (1992) report that in the active regions away of sunspots or pores there are significant amounts of magnetic flux concentrations that are neither dark or bright in continuum relative to the non-magnetic photosphere. We conclude that examples 3 and 4 can be classified to this case. Of course, magnetograms are needed to decide this point.

5. A typical example of a dark intergranular lane is located between 29.9 arcsec and 30.8 arcsec with minimum intensity at 30.0 arcsec in Fig. 3.14 and 3.15. The 'Red' and A-, B- slit jaw images do not show any evidence of small-scale magnetic activity, e.g. BP. The adjacent granules have higher contrast of the 'quasi' continuum I_{cont}^B and I_{cont}^A in comparison with contrasts of I_{int}^B and I_{int}^A respectively. The granule to the left shows the highest continuum intensity excess compared to the slightly fainter granule to the right. The peaks of maximum intensity correspond exactly to the local minimum of the BPI, which reaches -0.22 and -1.4 for the left and right granules, respectively. The minimum of I_{int}^B is shifted by 0.1 arcsec to the right with respect to position where I_{cont}^B has its local minimum. The BPI is increasing when going from the left granule towards the right and reaches a maximum value of -0.08 corresponding to a local extremum of I_{cont}^B and then decreases again. Such small increase of the BPI is a sign of a strong absorption of CN, and probably CH, molecules in that place. This is well seen even in the behavior of the contrast curves of I_{int}^B and I_{cont}^B ; I_{int}^A and I_{cont}^A . The line-core contrasts display a considerable difference of those for the different species. At the right and left granules the contrast of I_{CH}^B accounts to 0.07 and to -0.11 in the granules with a minimum of -0.21 at the core. The same values for the Fe I line-core are -0.09 , -0.11 and -0.22 respectively. It is remarkable that the I_{FeI}^B and I_{CH}^B still have a 'normal' shape of granule-intergranular lane-granule structure. The contrast of I_{CN}^B has almost the same value -0.11 at the right granule, but is strongly decreased to -0.30 and -0.31 for the lane-core and the left granule with an almost horizontal distribution between them. Such a case is an indication of a so-called reversed granulation pattern (Berger et al. 2004, Janssen & Cauzzi (in press.), Leenaarts & Wedemeyer-Böhm 2004, Rutten et al. 2003), usually observable in the line-core of strong atomic lines whose level of the line-core formation lies very high in the photosphere, or even at the bottom layers of the chromosphere. This phenomenon is caused by the temperature stratification of expanding granular gas. The main cause for $I_{CN}^B < I_{FeI}^B < I_{CH}^B$ in the granule, although according to the Stokes-I contribution functions (see Appendix B) of the line-core formation and $(\tau^{FeI} = 1) < (\tau^{CN} = 1) < (\tau^{CH} = 1)$, is the difference in temperature sensitivity of these species. However, a non-monotonic temperature gradient in the height range accessible to observations or a presence of unresolved fine structures can also produce this effect. In this sense inversion computations of the observed spectrum would be useful. The FWHM has a very strong jump from 52 mÅ, at the left granule, up to 60 mÅ in the center of the dark lane and decreasing down to 54 mÅ when reaching the right granule. The velocity profiles show a huge upflow of $V_{CN}^B = V_{CH}^B = -1500$ m/s

and $V_{FeI}^B = -1720$ m/s, as expected, at the right granule, which becomes a downflow of $V_{CN}^B = V_{CH}^B = 250$ m/s and $V_{FeI}^B = 300$ m/s in the dark core of the lane and finally an upflow again of $V_{CN}^B = V_{CH}^B = -240$ m/s and $V_{FeI}^B = -360$ m/s at the center of the right granule.

6. Another example of the dark intergranular lane is located between 25.8 arcsec and 26.95 arcsec in Figs. 3.10 and 3.11. The character of continuum contrast profiles $C(I_{cont}^B)$ and $C(I_{cont}^A)$ remains almost the same as in example 5. The special property of this type of dark intergranular channel is the behavior of absorption by molecules and atoms inside it. Examining the contrast curves of I_{int}^B and I_{int}^A one notices that, again, in the neighboring granules the corresponding continuum intensity dominates. However, in-between, where the dark lane itself is located, the I_{int}^B shows higher contrast than I_{cont}^B by a factor of 0.5. The same tendency have $C(I_{int}^A)$ and $C(I_{cont}^A)$. The BPI never reaches the 0.2 threshold but is nevertheless higher than for a 'normal' intergranular lane: 0.08 in the core and -0.06 , -0.08 at the maximum of I_{cont}^B in the granules. We suppose that such dark regions have an increased concentration of magnetic field. The reason why such structures are not bright, like a photospheric bright point is concealed, probably, in the geometry of an embedded flux tube and its thermal and density structure. This is possible an example of a so-called micropores (Bercik et al. 2003), (Berger & Title 2001), (Berger et al. 2002) - a dark area with magnetic flux concentrations. However, without corresponding magnetic field measurements this statement is only a presumption. The small brightness of a micropore was explained by low temperature inside it relative to the surrounding granulation. The low temperature of a micropore interior is due to the quenching of convection by the field inside it.

7. A possibility to verify the last statement in example 6 is to search for similar structures in magnetically very active part of the photosphere. A spectacular example of micropore structures is in Figs. 3.10 and 3.11 situated between 8.9 arcsec and 10.3 arcsec. This area is most probably penetrated by strong magnetic flux (see Section 3.6.1 suggesting the discussed feature to be magnetic). The contrast profile of I_{int}^B in that region lies everywhere above I_{cont}^B . The line-core intensities of all three spectral lines (Fig. 3.10 c) have a brightness excess across the whole dark feature with maximum contrast values: $C(I_{CN}^B) = 0.22$, $C(I_{CH}^B) = 0.062$ and $C(I_{FeI}^B) = 0.063$ at the middle of the micropore. This means that the micropore appears brighter than many surrounding granules when observed in the line-core. The contrasts are decreasing down to $C(I_{CN}^B) = -0.029$, $C(I_{CH}^B) = -0.063$, $C(I_{FeI}^B) = -0.063$ and to $C(I_{CN}^B) = 0$, $C(I_{CH}^B) = 0$, $C(I_{FeI}^B) = 0$ at the center of adjacent granules to the left and to the right respectively. The difference in the contrasts of CN and CH reaches 1.62. For comparison such big separation was never observed in BPs. The BPI even exceeds the threshold of 0.2 and reaches its maximum value of 0.312, which is already comparable with that for 'normal' BPs, at that point (10.3 arcsec), where the continuum intensity I_{cont}^B has its minimum. The velocity profiles show that the whole discussed dark feature has a minor, fairly constant upflow with mean velocities $V_{CN}^B = V_{CH}^B = -110$ m/s and $V_{FeI}^B = -220$ m/s. This feature is embedded in big upflows of $V_{CN}^B = V_{CH}^B = -940$ m/s and $V_{FeI}^B = -1100$ m/s at the right granule and $V_{CN}^B = V_{CH}^B = V_{FeI}^B = -270$ m/s at a very narrow edge of the left granule. The FWHM has, again, a strong increase by 6 mÅ on average over the micropore and reaches a maximum of 62 mÅ also at 10.9 arcsec.

It is important that for this kind of solar features the definition of the photospheric G-band brightening cannot be applied, mainly because of significantly low continuum

and consequently line-core intensities. Although the BPI and $I_{CN-band}/\langle I_{CN-band} \rangle - I_{cont}/\langle I_{cont} \rangle$ as well yield a sure reference on the photospheric brightening of a small-scale magnetic nature.

8. The last type of small-scale photospheric features we would like to discuss in detail is facular structures, particularly at the disc center. A good example of such a structure we found in the same figures as above, between 5.75 arcsec and 7.8 arcsec. On the 'Red' image one can see that the right side of the granule has a typical facular brightening which is even prominently seen on the A- and B-Slit jaw images. At that place the granule does not possess a homogeneous brightness, but a characteristic wavy-like pattern with alternate light and dark stripes parallel to each other (compare with imaging observations and corresponding simulations near the limb presented in Chapter 4). The $C(I_{cont}^B)$ reaches 0.2 in the center of the facula, which was observed only at the brightest granules or BPs. The line-core intensity I_{CN}^B repeats the curvature of I_{cont}^B contrast, but its contrast is everywhere higher than that of the continuum. The positions of local peaks of $C(I_{cont}^B)$ and $C(I_{int}^B)$ are almost equal. However, it should be mentioned that the contrast excess for I_{int}^B and I_{cont}^B is only about 1.7, which is less than the same for 'normal' bright points. The difference between contrasts of I_{CN}^B and I_{CH}^B reaches 0.26 at the brightest parts of the facula, which is much more than usually observed in the BPs. The BPI has quite low values, reaching a maximum of 0.38 and decreases down to 0.2 at the dark stripe of the facula. At 7.0 arcsec, the center of the bright stripe of the facula, the BPI has a local maximum, whereas its other local maximum at 6.1 arcsec does not correlate with an intensity peak of another bright stripe and is shifted to the left by around 0.27 arcsec. The investigation of velocity yields that there is a quite small downflow which counts to $V_{CN}^B = V_{CH}^B = 170$ m/s $<$ $V_{FeI}^B = 300$ m/s.

3.3.3 Intensity contrast

In Fig. 3.16 the normalized intensity of CN line-core I_{CN}^B - a), 'quasi' CN band-head I_{int}^B - b), CH line-core I_{CH}^B - c) and CH line-core I_{CN}^A - d) versus normalized continuum brightness I_{cont}^B are drawn. Intensities where $BPI \geq 0.2$ and $BPI < 0.2$, i.e. BPs and granulation, are presented as red and black dots, respectively. Additionally we designate those data points where $BPI < 0.2$ and $I_{int}^B > I_{cont}^B$ by green. Dark magnetic structures discussed in Examples 6,7 in section 3.3.2, for instance, fulfill this criterion. A similar behaviour is seen in Berger et al. (2004) for the G band and the blue continuum at $\lambda = 436.4$ nm intensities across both BPs and micropores. Therefore we call these points a "transition region" between BPs and non-magnetic granulation. However, except for identifying BPs the BPI is not so well suited to identify other solar features like granules, intergranular lanes or micropores. In particular a certain amount of data points in this "transition region" corresponds to some less prominent BPs which were neglected by the general criterion $BPI \geq 0.2$. This means that the definition of a BP should be substantiated more precisely which probably will lead to their manual selection. Simultaneous observations of at least spectra and magnetograms are needed to clarify this problem.

The prevailing number of bright granules reveals a very small elevation of CN line-core brightness whereas the continuum intensity changes in the whole observed range. In the upper left panel of Fig. 3.16 BPs are completely separated from the granulation and reach intensities from 1.08 up to 2.15. As expected the split between two branches in

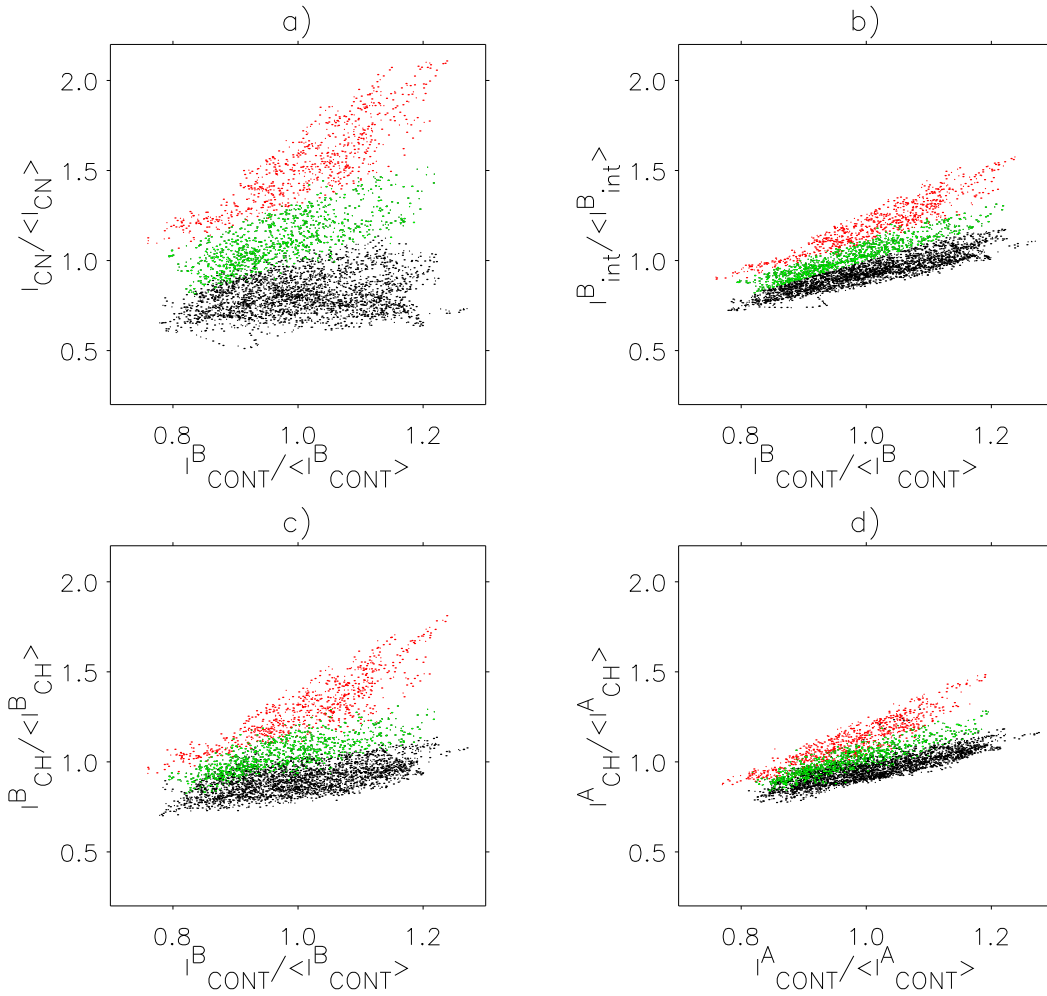


Figure 3.16: Normalized line-core I_{CN}^B - a), 'quasi' CN band-head I_{int}^B - b), CH line-core I_{CH}^B - c) and I_{CH}^A - d) intensities versus normalized continuum brightness I_{cont}^B measured at $\mu=0.97$. Red, black and green points denote structures such as BPs, where $BPI \geq 0.2$, granulation, where $BPI < 0.2$, and "transition region", where $BPI < 0.2$ & $I_{int}^B > I_{cont}^B$.

panel b) is much less, than in panel a) due to the finite density of CN absorption spectral lines, presence of lines of other, less sensitive to temperature species and consequently lower brightness excess in BPs. The graph b) is in a very good quantitative agreement with Fig. 2.6. I_{CH}^B and I_{CH}^A both exhibit a less prominent BP intensity separation as compared to the CN line-core, but still bigger than in the I_{int}^B case. This fact confirms the behavior of the corresponding contrast courses discussed in Section 3.3.1 and with the rms values listed in Table 3.8. A plausible explanation of the sharp distinction between c) and d), which were obtained for the same molecule CH and should therefore be identical, is that the measured spectral lines belong to different electronic transitions of the CH molecule, namely the B-X and the A-X systems, respectively (see Table 3.6). These two electronic levels may have a different sensitivity to temperature fluctuations in the photosphere. Radiative transfer computations are needed to verify this statement and to carry out a quantitative analysis. The difference in spatial resolution of A- and B-spectra and the small difference between I_{cont}^B and I_{cont}^A (see Section 3.5) also contribute to this

effet.

The next graph 3.17 (top panel) shows how the contrast of CN and CH line-core intensities obtained from the B-spectra changes with the contrast of the 'quasi' CN band-head intensity normalized to its mean value $I_{int}^B / \langle I_{int}^B \rangle$. The bright points exhibit an evident decrease of the ratio C_{CN}^B / C_{CH}^B with increasing continuum brightness. This result is in a qualitative agreement with Fig. 2.7 presented in Chapter 2. A quantitative comparison is not possible since in the present study we can analyze only line-core intensities rather than intensities integrated over the whole band-head, which have different densities of spectral lines. Thus on average we have obtained $\langle C_{CN}^B \rangle / \langle C_{CH}^B \rangle = 1.9$ which is higher than obtained from the imaging observations. This result is again in contradiction with numerical simulations by Uitenbroek & Tritschler (2006 submitted.).

3.3.4 Bright point index

The scatter plot 3.18 shows how velocity V_{CN}^B , the width of the Fe I line, contrast of I_{cont}^B , I_{CN}^B , I_{CH}^B and I_{int}^B vary with the BPI. Again the red, black and green color mark BPs, granulation and the "transition region". The blue line in each panel represents the average dependency. Qualitatively these results are very similar to those obtained by Langhans et al. (2004) in the G band. However, in our observations many BPs show higher continuum contrast, which is comparable with that for brightest granules. This could be due to a higher intensity of BPs relative to granulation when observing at shorter wavelengths. Also the obviously higher spatial resolution of our observed spectra than of those of Langhans's data boosts the contrast of small-scale BPs.

The continuum intensity shows a separation into two populations: BPs, where I_{cont}^B increases with increase of the BPI, and all other features whose I_{cont}^B decreases with increase of the BPI. The difference between the graphs of C_{CN}^B , C_{CH}^B and C_{int}^B lies in the steepness of the dependence on the BPI. The "transition region" features show rather constant I_{cont}^B dependence of the BPI.

The maximum upflow velocity $V_{CN}^B \approx -1000$ m/s corresponds to the lowest value of the BPI and decreases rapidly down to 0 m/s at BPI around -0.05 . For BPI > 0 velocity, on average, becomes positive and nearly constant. The FWHM is the lowest at the granules, which, as the rule, have the smallest BPI and increases gradually by 10 mÅ becoming, as the velocity, almost constant for all photospheric magnetic brightenings.

In the upper-right panel of Fig. 3.13 we plot the Fe I line width versus $I_{cont}^B / \langle I_{cont}^B \rangle$. Here, additionally, we designate intergranular dark lanes, using the criterion $I_{cont}^B / \langle I_{cont}^B \rangle < 0.9$, as blue dots. In this plot it is seen that the brighter the granules are, the lower the line broadening they show. BPs and intergranular lanes have very similar FWHM values, with an average of 60 mÅ. In contrast, the granules have 58 mÅ mean FWHM. The darkest intergranular lanes reveal 10 mÅ line width excess as compared to the brightest granules. This result is in good agreement with observations near disc center by Nesis et al. (1992), Holweger & Kneer (1989) and with numerical simulations by Solanki et al. (1996). Nesis et al. (1992) report 15 mÅ FWHM excess, detected for the Ni I line at $\lambda = 491.23$ nm, in the dark lanes. They argue that the enhanced line broadening is caused by increased turbulence introduced by the shocks that brake the horizontal transonic flows back into the subsonic regime. Solanki et al. (1996) provided alternative explanations of the observations as a physical structure of the downflow lanes themselves.

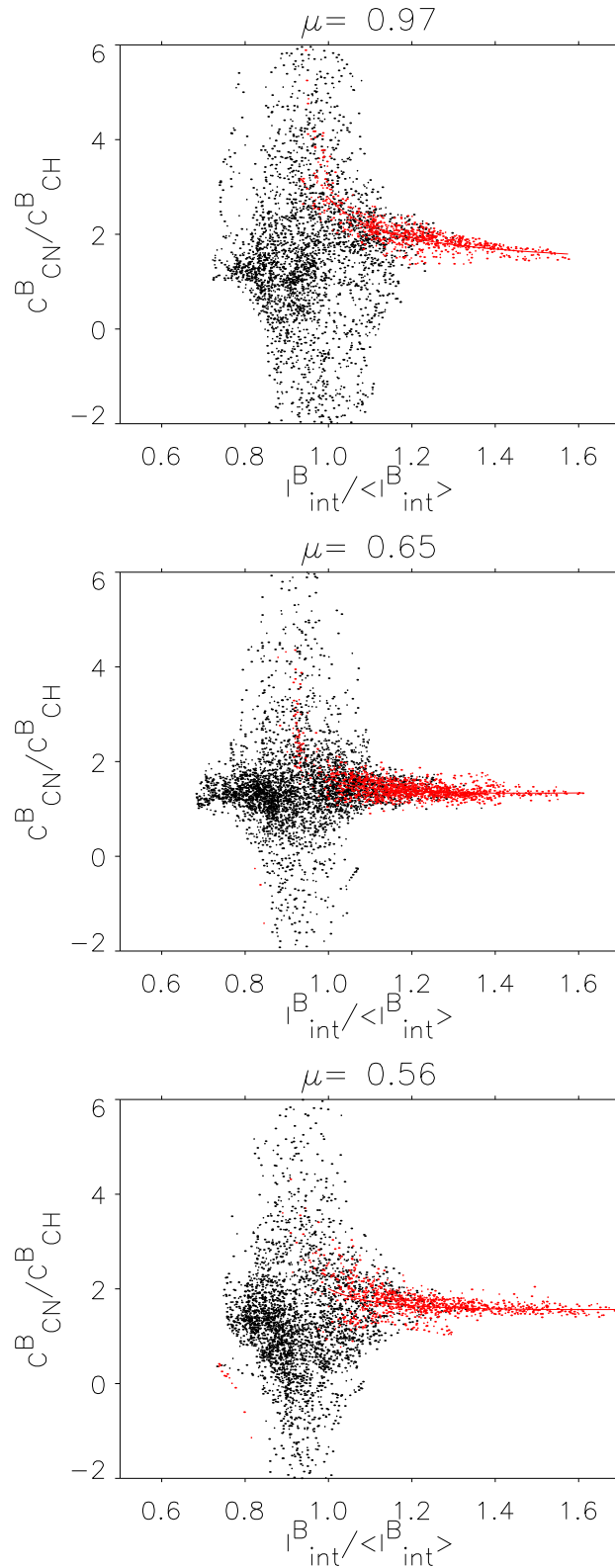


Figure 3.17: Dependence of the ratio of the contrast of CN and CH line-core intensities C_{CN}^B , C_{CH}^B on the integrated 'quasi'-CN band-head intensity C_{int}^B observed at three heliocentric angles.

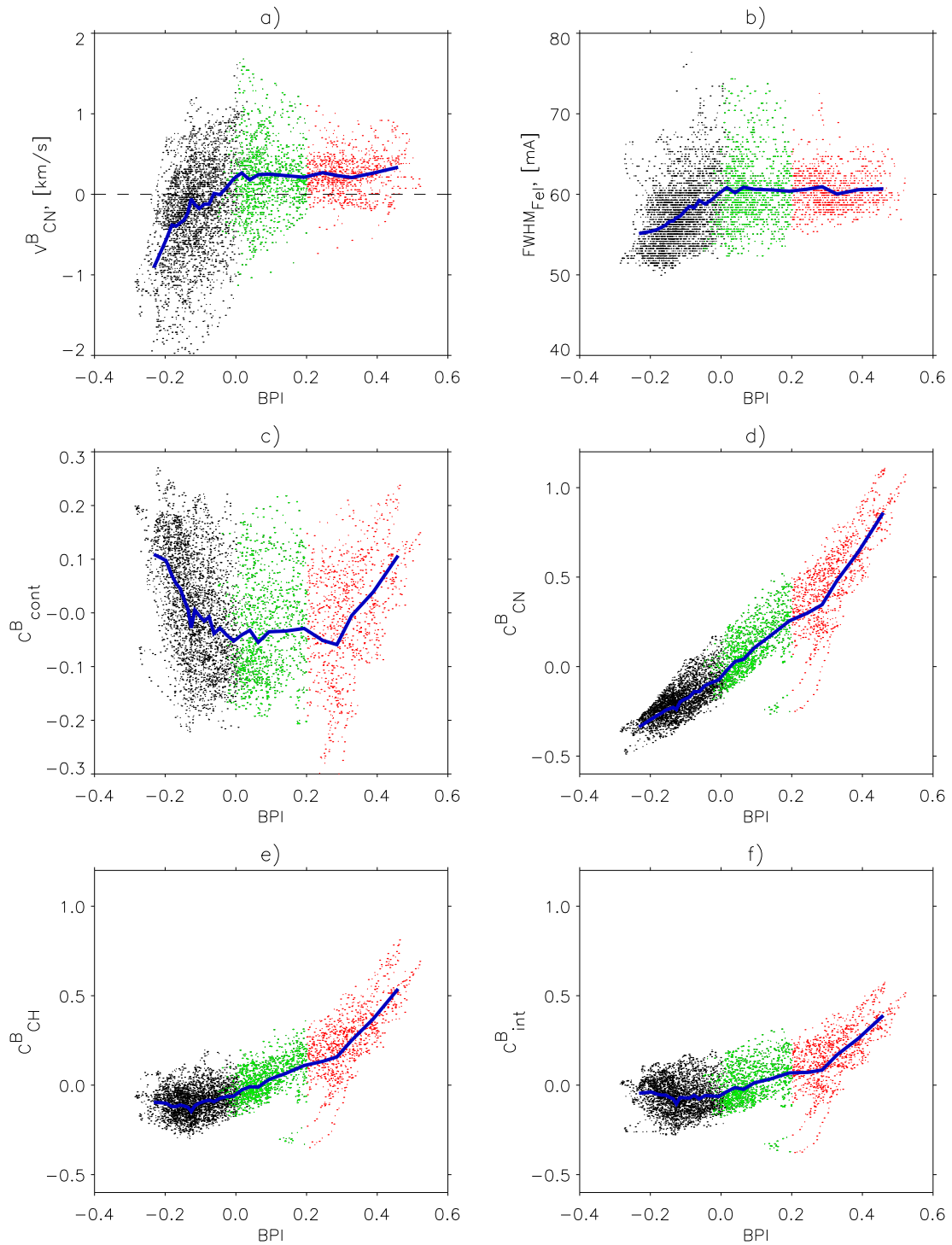


Figure 3.18: Velocity V_{CN}^B - a), FWHM - b), 'quasi' continuum intensity contrast C_{cont}^B - c), CN line-core intensity contrast C_{CN}^B - d), CH line-core intensity contrast C_{CH}^B - e) and "quasi" CN band-head intensity contrast C_{int}^B versus BPI observed at $\mu=0.97$. A blue line is the average dependency. **Red**, black and **green** points denote structures such as **BPs**, where $BPI \geq 0.2$, granulation, where $BPI < 0.2$, and "transition region", where $BPI < 0.2$ & $I_{int}^B > I_{cont}^B$.

According to our FWHM measurements at disc center, velocity measurements near the limb (see Section 3.4) and investigation of absorption in spectral lines, which will be presented in Section 3.6.1, we admit to several scenarios of line broadening:

- broadening due to turbulent flows in cool downflow regions,
- broadening due to presence of shock-waves in the upper photosphere.

3.3.5 Line depression

Feature	$\langle \Delta D_{CN}^B \rangle$ $\lambda = 387.844$	$\langle \Delta D_{CH}^B \rangle$ $\lambda = 387.829$	$\langle \Delta D_{CH}^A \rangle$	$\langle \Delta D_{FeI}^B \rangle$	V_{CN}^B [m/s]	V_{CH}^B [m/s]	V_{FeI}^B [m/s]	$FWHM$ [mÅ]
BPs	-0.410	-0.321	-0.289	-0.308	101	137	198	60
FC	-0.400	-0.291	-0.275	-0.261	86	114	202	60

Table 3.10: Mean change in line-core depression of CN, CH, Fe I lines from B-spectra and CH line from A-spectra for BPs and faculae (FC) showing a $BPI \geq 0.2$ with respect to those observed in the quiet Sun; flow velocities computed for the given lines and the FWHM for Fe I line observed at $\mu=0.97$.

In Table 3.10 the averaged line-core depressions of deblended CH ($\lambda = 387.829$ nm) and CN ($\lambda = 387.844$ nm), and Fe I spectral lines measured from B-spectra and additionally of the CH line from A-spectra are listed. Corresponding mean velocities and FWHM of the Fe I line were also computed. Separation between faculae and BPs was done by hand following the 'Red' and B-slit jaw images.

From these results it follows that, on average over the BPs, the CN line is weakening $\langle \Delta D_{CN}^B \rangle / \langle \Delta D_{CH}^B \rangle = 1.28$ times more than the CH spectral line and $\langle \Delta D_{CN}^B \rangle / \langle \Delta D_{FeI}^B \rangle = 1.33$ times more than the Fe I line concerning the line-core intensities. For facular structures the same weakening ratios are 1.38 and 1.53, respectively.

Each BP, however, is an individual case of a small-scale magnetic phenomenon on the Sun and therefore the above analysis does not reflect such an individuality. In order to investigate the behavior of line depression in somewhat more detail, we provide a similar analysis as in Sections 3.4.3 and 3.3.3, but concerning the line-core depression instead of the contrast. Here we restrict ourselves to the study of the properties only of the CN line at 387.844 nm and of the CH line at 387.829 nm measured in B-spectra to exclude possible inaccuracies related to the spatial problems (resolution and image displacements in two spectroscopic channels).

The corresponding scatter plots of variations in a line-core depression for CH and CN lines ($\Delta D_{CN}^B, \Delta D_{CH}^B$) and their quotient, calculated for the active region at $\mu=0.97$, depending on the I_{int}^B are shown in the two left panels in the top of Fig. 3.19. The red color labels the BPs and faculae, here we do not separate between them, and the black color designates all other features. The curvature of both ΔD_{CN}^B and ΔD_{CH}^B reveals a

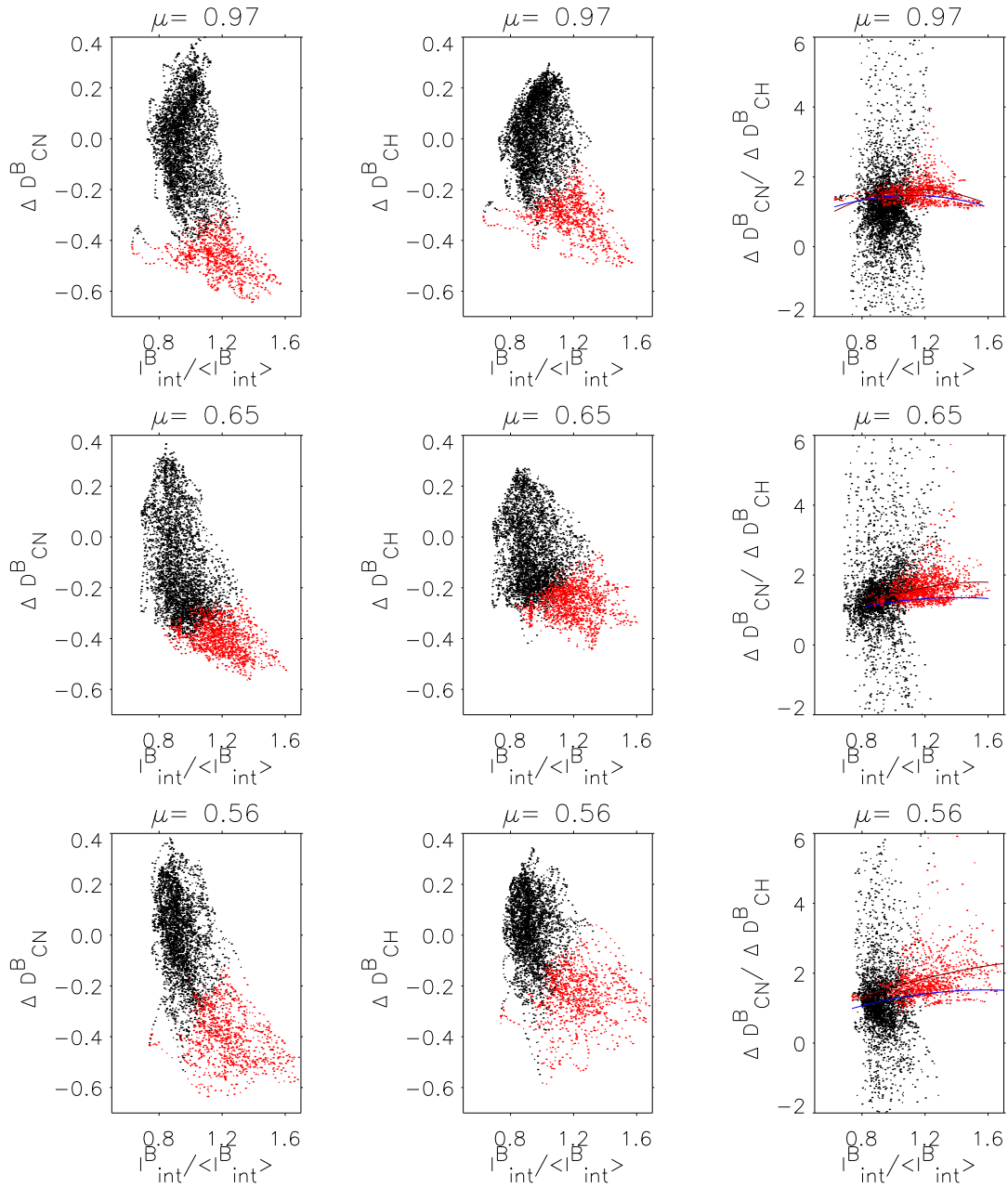


Figure 3.19: Change in line-core depression of CN and CH spectral lines depending on 'quasi' CN band-head intensity and their ratio observed at three disc positions. Blue and red lines are least square fits to this ratio considering blended and deblended line depths respectively.

peculiar bow-shaped profile, with convex to the left. From these graphs it is evident that the depth of the line core changes in a wide range not only in the BPs, but also in the granulation, intergranular regions etc.

In granulation the variation of ΔD_{CN}^B is notably higher than that of ΔD_{CH}^B . In these regions the depression of CH changes from $(\Delta D_{CH}^B)_{max} = 0.297$, at the peaks of the brightest granules, up to $(\Delta D_{CH}^B)_{min} = -0.376$ with a mean value of $\langle \Delta D_{CH}^B \rangle = 0.019$ which is, as expected, around zero. The analogous magnitudes for CN were found as 0.432, -0.413 and -0.017 , respectively. A small difference in ΔD_{CH}^B and ΔD_{CN}^B at some points along the slit produces huge values, positive and negative, in the $\Delta D_{CN}^B / \Delta D_{CH}^B$ dependence (Fig. 3.19 top - right). With decreasing granular intensity the CH and, less prominent, the CN line-core depression has a tendency to increase from negative values to 0 and then to increase further with increasing I_{int}^B .

In areas corresponding to BPs and facular brightenings the situation is opposite, i.e. $(\Delta D_{CH}^B)_{max} = -0.091$, $(\Delta D_{CH}^B)_{min} = -0.502$, $\langle \Delta D_{CH}^B \rangle = -0.306$, and $(\Delta D_{CN}^B)_{max} = -0.275$, $(\Delta D_{CN}^B)_{min} = -0.643$, $\langle \Delta D_{CN}^B \rangle = -0.466$. Taking into consideration this relatively small change of depression with continuum intensity we explain it by a lower temperature fluctuation within the BPs as compared to those in granulation, intergranular lanes etc.

In the right panel (Fig. 3.19 top) the corresponding ΔD_{CN}^B and ΔD_{CH}^B show a very good correlation in the whole presented intensity range of the BPs. Here the red line represents a least-square fit to the data points. In addition, in the same graph the least-square fit to $\Delta D_{CN}^B(\text{orig}) / \Delta D_{CH}^B(\text{orig})$ is presented as the blue line, where index 'orig' means depression of the spectral line without deblending correction. As expected, the difference between red and blue fits increases with increasing BP intensity.

From this result we conclude that for BPs the temperature deviations near $\tau_{CN} = 1$ are comparable to those at $\tau_{CH} = 1$ (since its gradient is small). However, the CN molecule, which is more sensitive to the temperature perturbations, as compared to CH (Berdyugina et al. 2003), has a slightly higher amplitude of ΔD than that for the CH molecule. The ratio of line-core depression in CN and CH has a minimum of 1.05 and the maximum equals to 3.96, but has a rather flat dependence from I_{int}^B with a mean value of 1.52. Even at peaks of brightest BP intensity the CN line weaken 1.26 times more than the CH lines.

3.4 Spectroscopy of small-scale magnetic features near the limb

3.4.1 Main properties

Unfortunately poor statistics does not allow us to provide a detailed spectroscopic investigation of the center-to-limb variation of small-scale magnetic phenomena. It is important, however, to study the specific and individual character of the observed active regions, especially near the solar limb. In this section we will describe the main properties of two active regions : NOAA0752 at $\mu=0.65$ and a small plage at $\mu=0.56$.

Two exceptional samples of reduced spectroscopic data obtained from observations in these two active regions are presented in Figs. 3.20, 3.21, 3.22 and 3.23, respectively.

3 High resolution spectroscopy of the solar photosphere

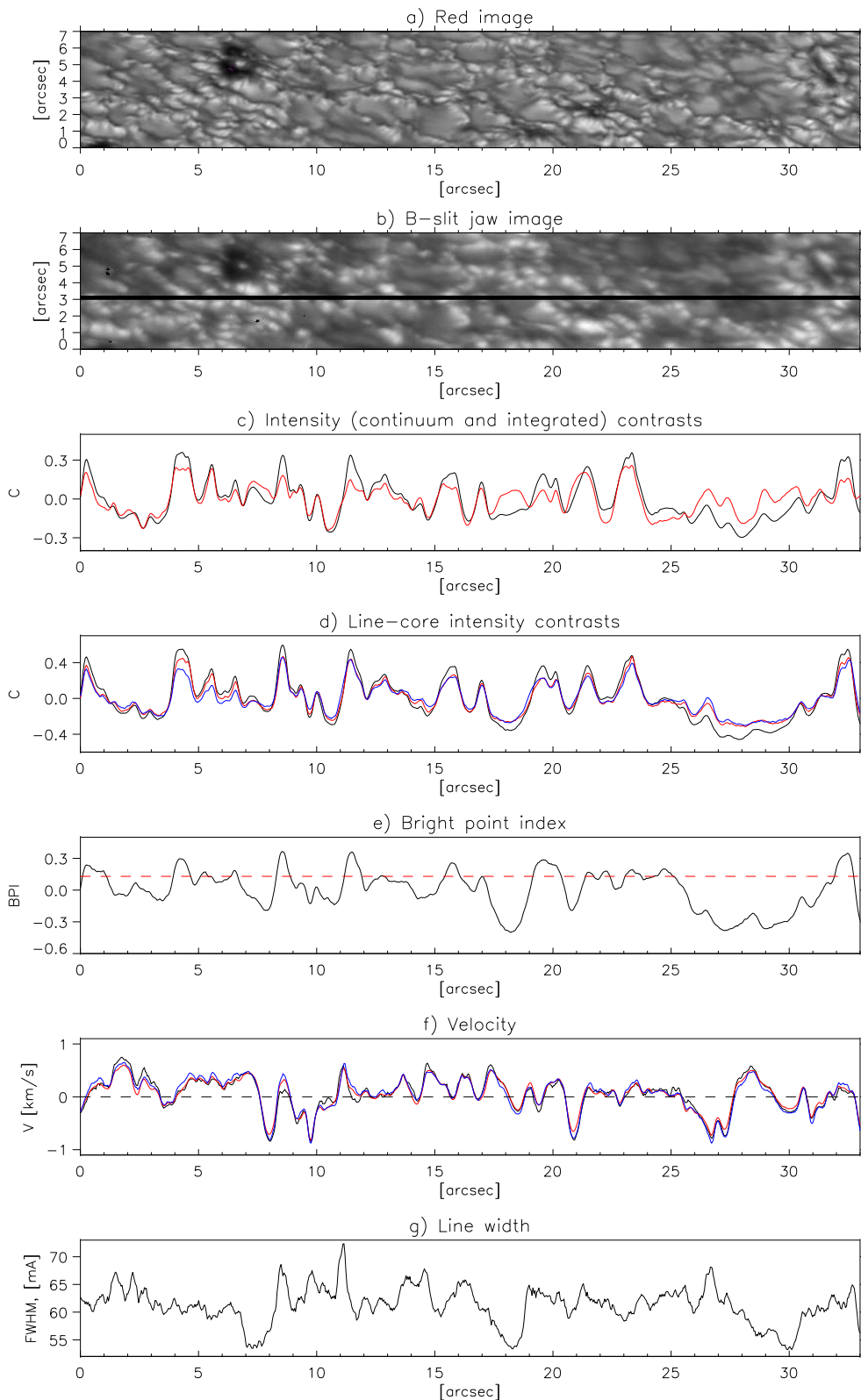


Figure 3.20: Spectroscopic data observed in the active region NOAA0752 at $\mu=0.65$ on 14 April 2005 at 15:28:52 (UT) : a) Reference image; b) B-slit jaw image; c) integrated and continuum intensity contrasts $C(I_{int}^B)$ - black, $C(I_{cont}^B)$ - red; d) line-core intensity contrasts $C(I_{CN}^B)$ - black, $C(I_{CH}^B)$ - red, $C(I_{FeI}^B)$ - blue; e) BPI; f) velocities V_{CN}^B - black, V_{CH}^B - red, V_{FeI}^B - blue; g) line width of Fe I line.

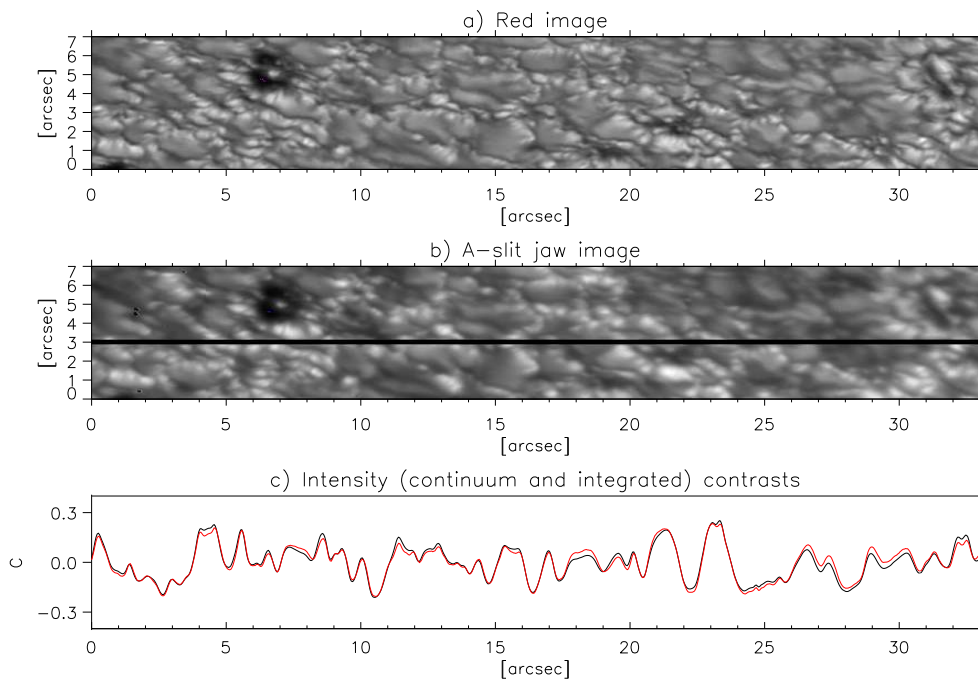


Figure 3.21: Spectroscopic data observed in the active region NOAA0752 at $\mu=0.65$ on 14 April 2005 at 15:28:52 (UT) : a) Reference image; b) A-slit jaw image; c) intensity contrasts (I_{int}^A) - black, (I_{cont}^A) - red.

In general, the brightness properties of the faculae are very close to those observed at the disc center. However, in this case we see much more of them which appear as prominent features. Hence we do not provide a detailed analysis of individual features, but rather restrict ourselves to a study of their main properties.

The integrated intensity I_{int}^B shows in many pixels along the slit higher contrast as compared to that of I_{cont}^B . As the rule, these pixels correspond to faculae. Only in quiet Sun areas, like at positions 26–31 arcsec in Fig. 3.20 and in non-magnetic features, e.g. granules, the continuum contrast dominates. We have noticed that the selection criteria by $BPI \geq 0.2$ is not satisfied for some faint faculae and the threshold of $BPI \geq 0.13$, which we have used for all data at $\mu=0.65$ and at $\mu=0.56$, looks more useful for their automated selection. One of the reasons for this is that many dark magnetic structures, micropores for example, appear bright near the limb (see discussion in Chapter 4). Thus the horizontal dashed line in Fig. 3.20 - e) and in Fig. 3.22 - e) designates this threshold.

The velocity distribution reveals an interesting fact. In Fig 3.20, i.e. at $\mu=0.65$, velocity amplitudes are reduced, if one compares them with those obtained at the disc center, and do not exceed upflows of $V_{CN}^B < -850$ m/s, $V_{CH}^B < -830$ m/s, $V_{FeI}^B < -870$ m/s and downflows of $V_{CN}^B > 750$ m/s, $V_{CH}^B > 600$ m/s, $V_{FeI}^B > 660$ m/s. At even bigger heliocentric angle $\theta \approx 56^\circ$, in Fig 3.22, the measured velocities are higher than at $\mu = 0.65$ and similar to those observed at the disc center. Their magnitude reaches $V_{CN}^B \approx -2030$ m/s, $V_{CH}^B \approx -1880$ m/s, $V_{FeI}^B \approx -1900$ m/s in the upflows and $V_{CN}^B \approx 1550$ m/s, $V_{CH}^B \approx 2090$ m/s, $V_{FeI}^B \approx 1660$ m/s in the downflows, which were found mostly in the brightest faculae. Obviously horizontal and vertical gas motions contribute to this effect.

3 High resolution spectroscopy of the solar photosphere

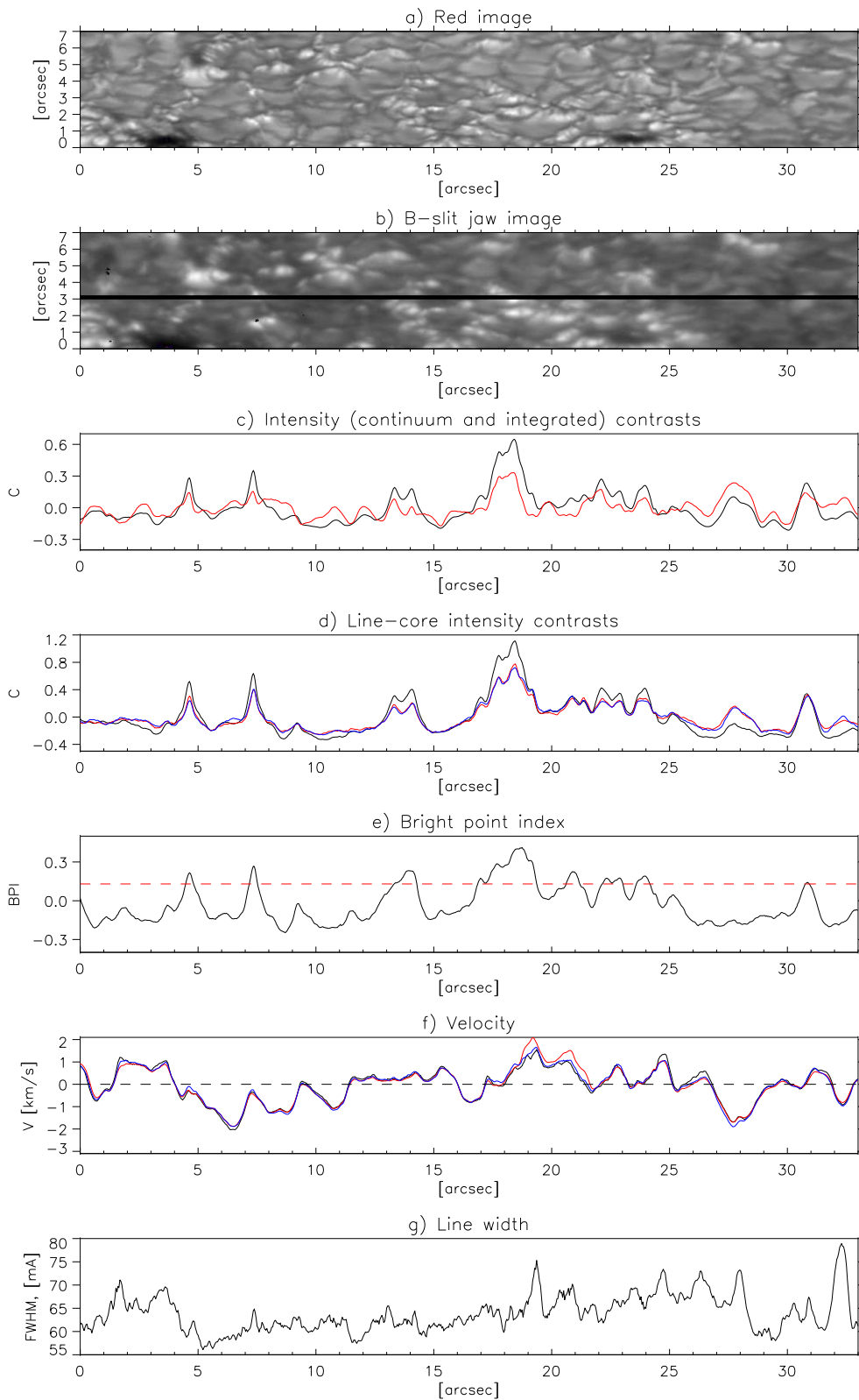


Figure 3.22: Spectroscopic data observed in an active region at $\mu=0.56$ on 14 April 2005 at 15:49:05 (UT) : a) Reference image; b) B-slit jaw image; c) integrated and continuum intensity contrasts $C(I_{int}^B)$ - black, $C(I_{cont}^B)$ - red; d) line-core intensity contrasts $C(I_{CN}^B)$ - black, $C(I_{CH}^B)$ - red, $C(I_{FeI}^B)$ - blue; e) BPI; f) velocities V_{CN}^B - black, V_{CH}^B - red, V_{FeI}^B - blue; g) line width of Fe I line.

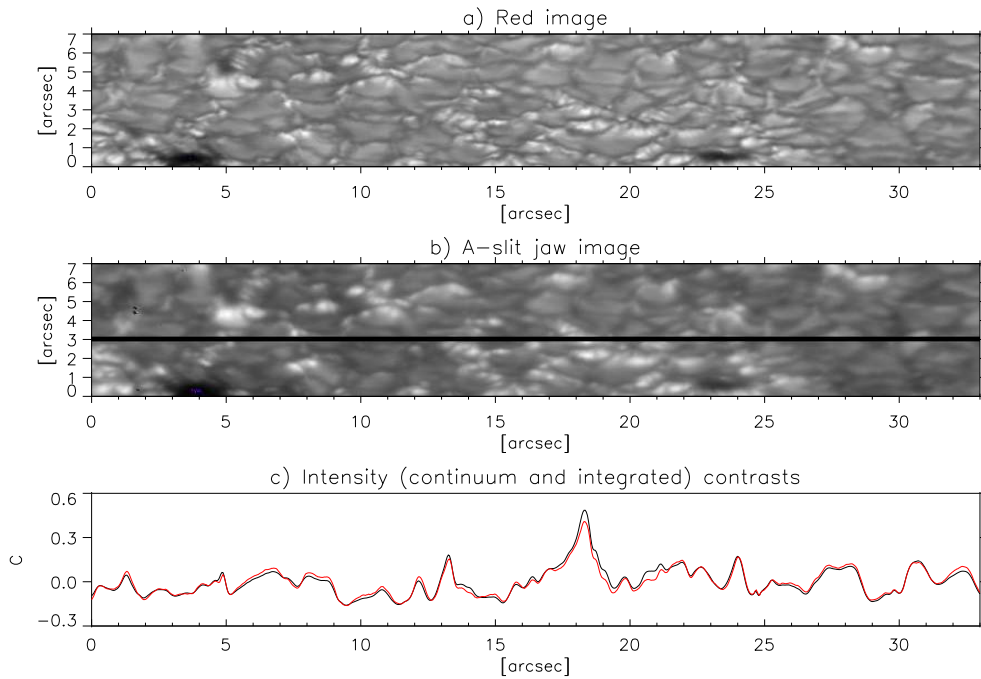


Figure 3.23: Spectroscopic data observed in an active region at $\mu=0.56$ on 14 April 2005 at 15:49:05 (UT) : a) Reference image; b) A-slit jaw image; c) intensity contrasts (I_{int}^A) - black, (I_{cont}^A) - red.

Figure 3.24: Scatter plot of flow velocity vs. continuum intensity I_{cont}^B observed at $\mu=0.65$. Red color corresponds to faculae and black to granulation and the lines are linear fits to the data.

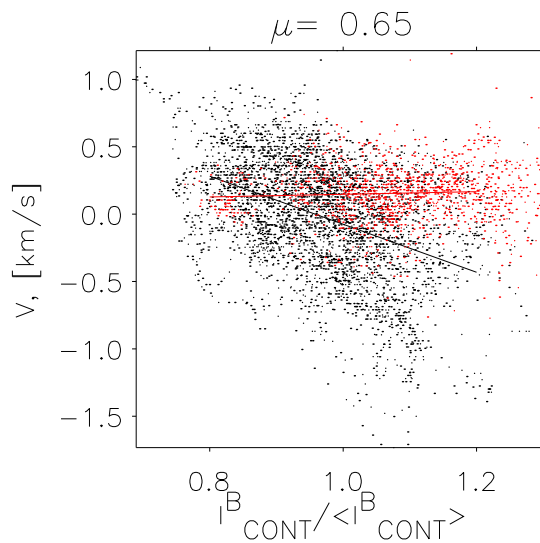
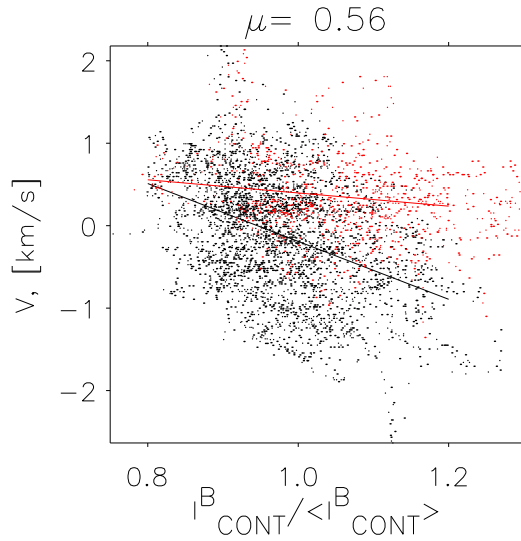


Figure 3.25: Scatter plot of flow velocity vs. continuum intensity I_{cont}^B observed at $\mu=0.56$. Red color corresponds to faculae and black to granulation and the lines are the corresponding linear fits to the data.



On the one hand strong peaks of velocity profiles observed near several faculae (for example at 19.2 arcsec in Fig. 3.22) could be a manifestation of shock waves in the upper photosphere, which were found in numerical simulations by Solanki et al. (1996). On the other hand, if we consider the velocity distribution of the granulation in Fig. 3.24 and in Fig. 3.25, it could be an evidence of supersonic, parallel to the surface plasma motions pointed by Nesis et al. (1992) which appear more prominent at $\mu = 0.56$ than at $\mu = 0.65$ and in these particular active regions.

In Fig. 3.22 at 19.1 arcsec the CH line-core velocity shows a significant excess over V_{CN}^B by -540 m/s and over V_{FeI}^B by -430 m/s. This location corresponds to a tiny bright dot very close nearby to the black dot in the intergranular lane. Such an isolated speck, embedded in the intergranular lane, is something special, which does not conform to a definition of faculae. The maxima of V_{CN}^B and of V_{FeI}^B in that position are shifted by 0.16 to the right with respect to the maximum downflow in V_{CH}^B , which could be a sign to rightward inclination of the flow.

The brightest facula in the same figure at 18.65 arcsec reveals a very clearly decreased downflow velocities V_{CN}^B and V_{CH}^B demonstrating again an 'embedded in the downflow' bright structure. However, the CH velocity only slightly drops at that point. Also as in the case of the disc center faculae, almost everywhere along the slit the contrasts of I_{CH}^B and of I_{FeI}^B , are very close to each other, whereas $C(I_{CN}^B)$ is always higher at the facular regions and lower in the granulation.

3.4.2 Intensity contrast

In Figs. 3.26 and 3.27, analogically to Fig. 3.16, the distribution of the line-core and integrated intensities versus continuum, normalized to the mean value are presented. At these disc positions three types of brightness, i.e. BPs, granulation and "transition region" features, are distributed closely to each other. The CN line-core intensity distribution of granules and non-magnetic intergranular lanes looks inclined to the X-axis. Such qualitative differences from results obtained at $\mu = 0.97$ find a possible explanation in the

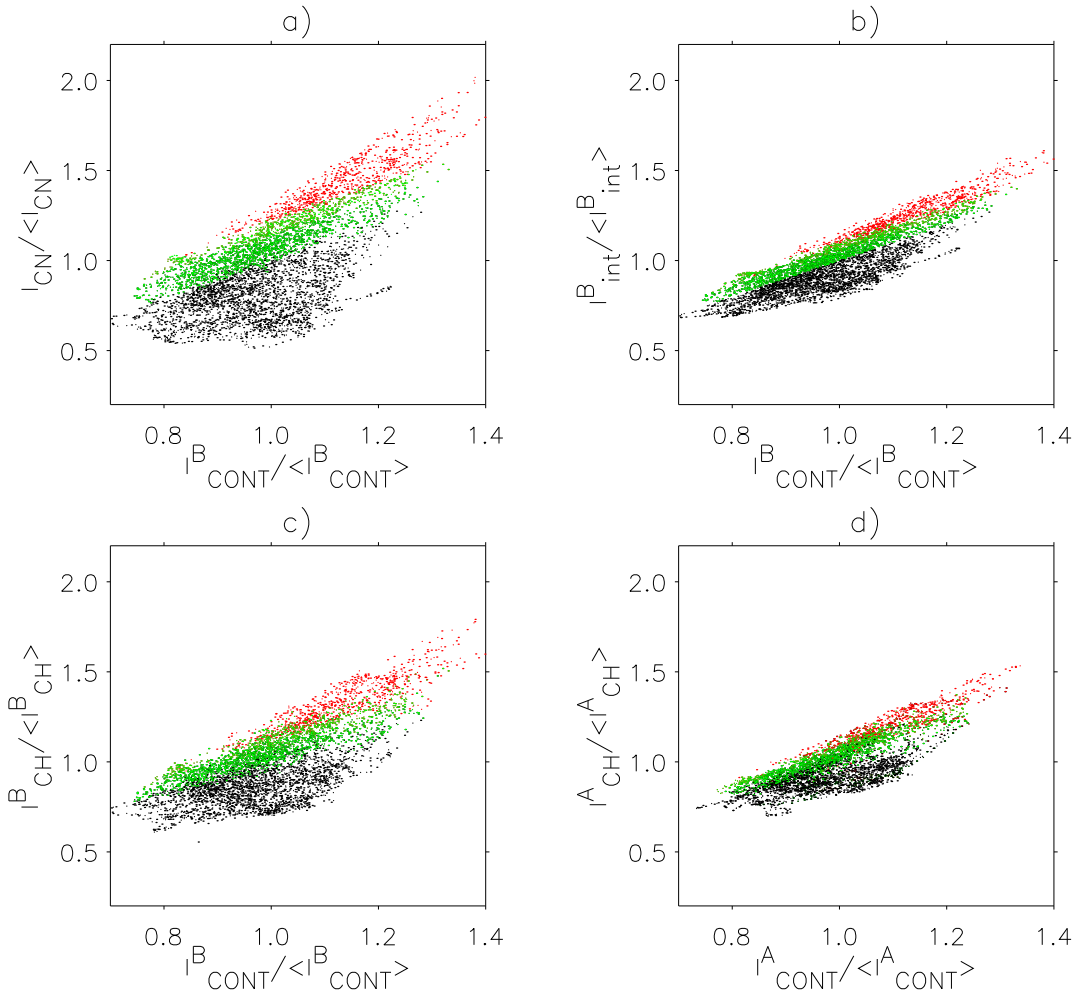


Figure 3.26: Normalized line-core I_{CN}^B - a), 'quasi' CN band-head I_{int}^B - b), CH line-core I_{CH}^B - c) and I_{CN}^A - d) intensities versus normalized continuum brightness I_{cont}^B measured in plage at $\mu=0.65$. Red, black and green points denote structures such as BPs, where $BPI \geq 0.13$, granulation, where $BPI < 0.13$, and "transition region", where $BPI < 0.13$ & $I_{int}^B > I_{cont}^B$.

Eddington-Barbier relation:

$$I_{\lambda}(\mu) = S_{\lambda}(\tau_{\lambda} = \mu) \quad (3.10)$$

It says that the scale of optical depth τ_{λ} shifts downwards when looking at increasing heliocentric angle θ . In the upper photosphere, the temperature gradients could be flatter due to the effect of reversed granulation. Thus temperature deviations near $\tau_{cont}=1$ and $\tau_{CN}=1$ of the quiet granulation drop down when approaching the solar limb.

Corresponding rms contrasts of line-core, integrated and local continuum intensities are presented in Table 3.11. Comparing these results with those obtained at the disc center we conclude that the rms contrast of active areas and of quiet Sun regions in continuum increases near the limb. Contrary to this, the rms contrast in molecular bands, as expected (Hirzberger & Wiehr 2005), increases slower than that in continuum. However, at $\mu=0.56$ the rms values measured in the quiet Sun are considerably smaller than the correspond-

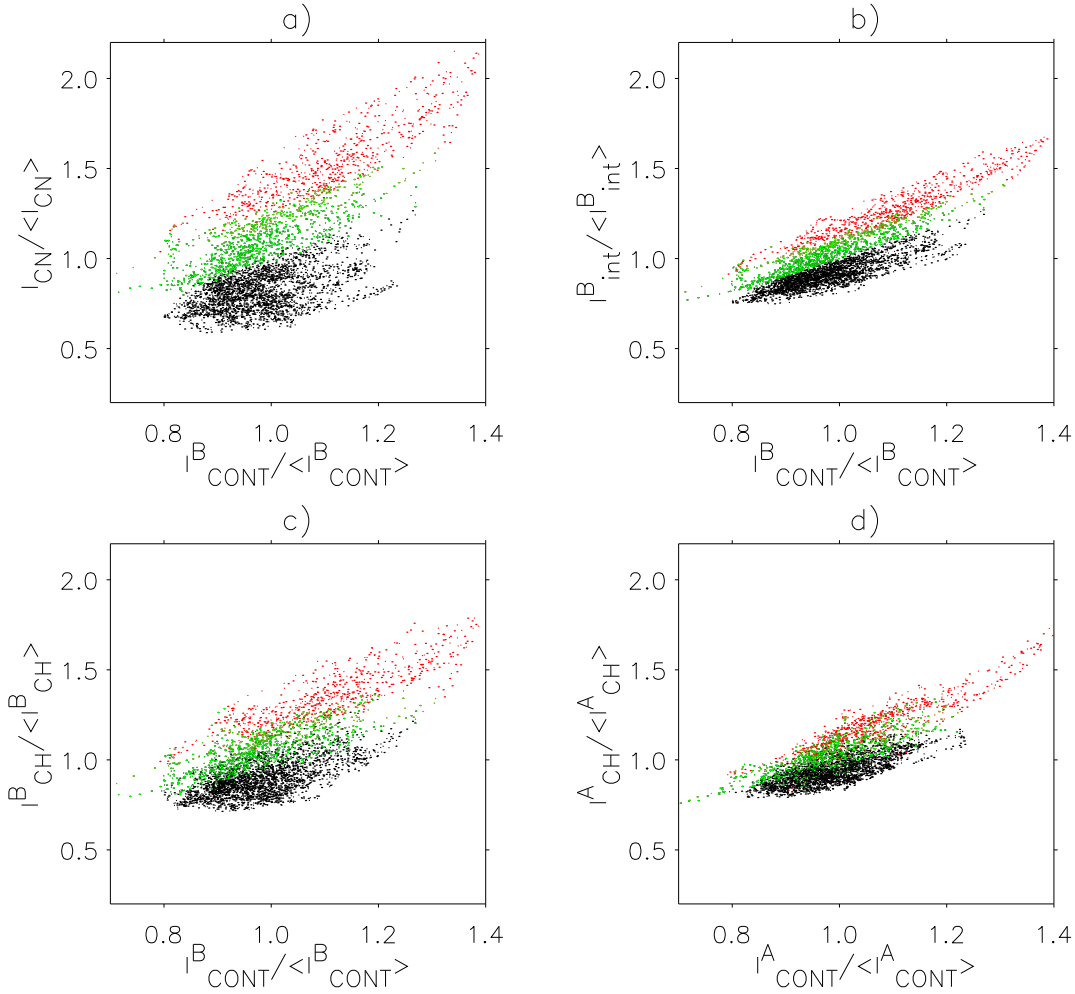


Figure 3.27: Normalized line-core I_{CN}^B - a), 'quasi' CN band-head I_{int}^B - b), CH line-core I_{CH}^B - c) and I_{CN}^A - d) intensities versus normalized continuum brightness I_{cont}^B measured in plage at $\mu=0.56$. Red, black and green points denote structures such as BPs, where $BPI \geq 0.13$, granulation, where $BPI < 0.13$, and "transition region", where $BPI < 0.13$ & $I_{int}^B > I_{cont}^B$.

ing measurements at $\mu=0.65$ and even at $\mu=0.97$. One of the possible reasons for this observable fact could be the lack of sufficient large quiet Sun regions in our observations at $\mu=0.56$ and $\mu=0.65$ in statistical sense and too few slit positions covering an extremely limited area of the solar surface. The variable spatial resolution during the observations also has an effect.

3.4.3 Bright point index

From Figs. 3.28 and 3.29 we see a very similar dependence of V_{CN}^B , FWHM, $C(I_{CN}^B)$, $C(I_{CH}^B)$ and $C(I_{int}^B)$ on the BPI as those obtained at the disc center. However, the main difference between limb and disc center positions shows the continuum contrast $C(I_{cont}^B)$ distribution, where the granulation fraction has in general a reduced contrast with a minimum of -0.3 at $BPI = -0.07$ (see Fig. 3.28). Contrary to the disc center case the $C(I_{CH}^B)$

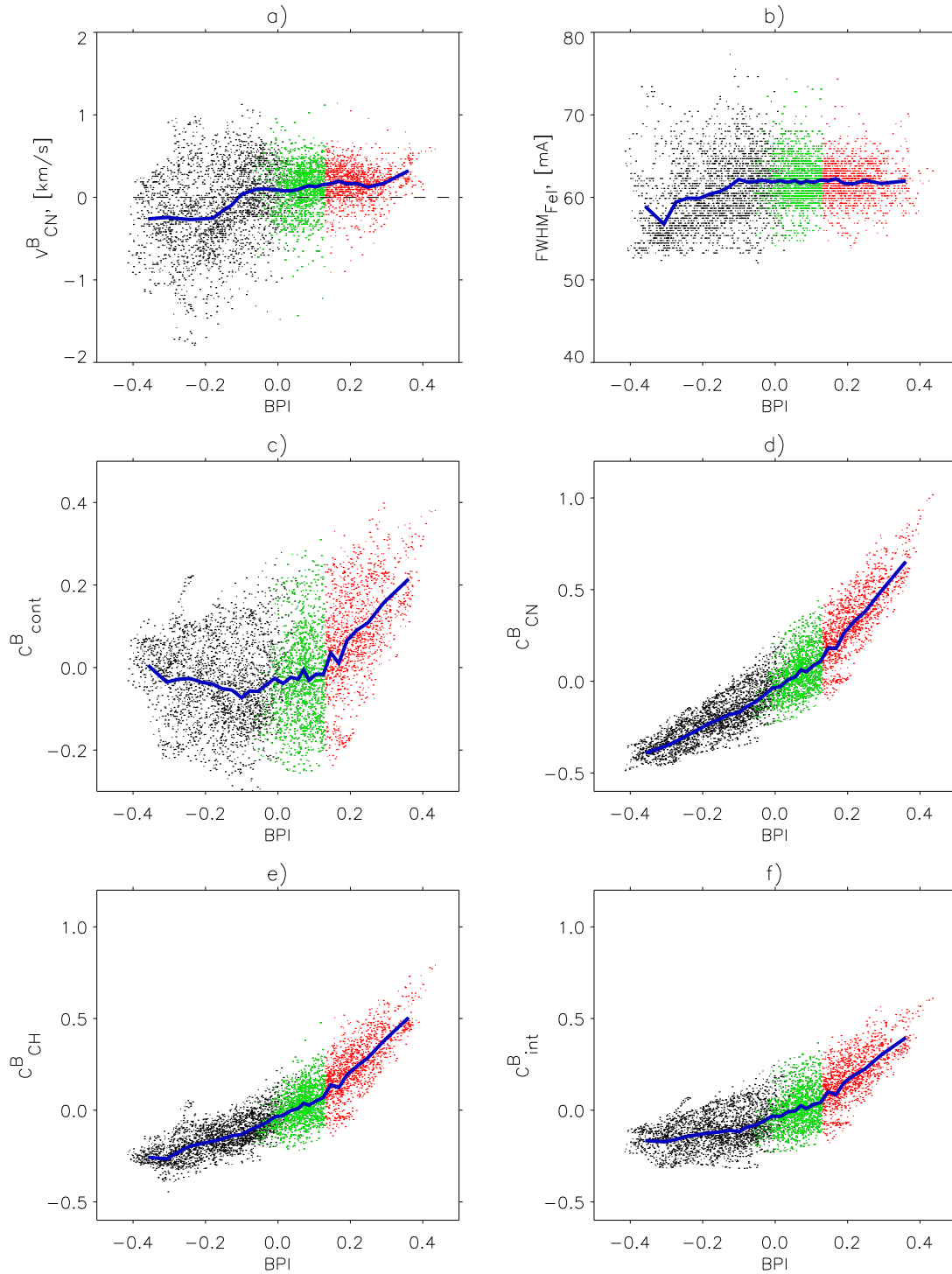


Figure 3.28: Velocity V_{CN}^B - a), FWHM - b), 'quasi' continuum intensity contrast C_{cont}^B - c), CN line-core intensity contrast C_{CN}^B - d), CH line-core intensity contrast C_{CH}^B - e) and "quasi" CN band-head intensity contrast C_{int}^B versus BPI observed at $\mu=0.65$. A blue line is the average dependency. **Red**, black and **green** points denote structures such as **BPs**, where $BPI \geq 0.13$, granulation, where $BPI < 0.13$, and "transition region", where $BPI < 0.13$ & $I_{int}^B > I_{cont}^B$.

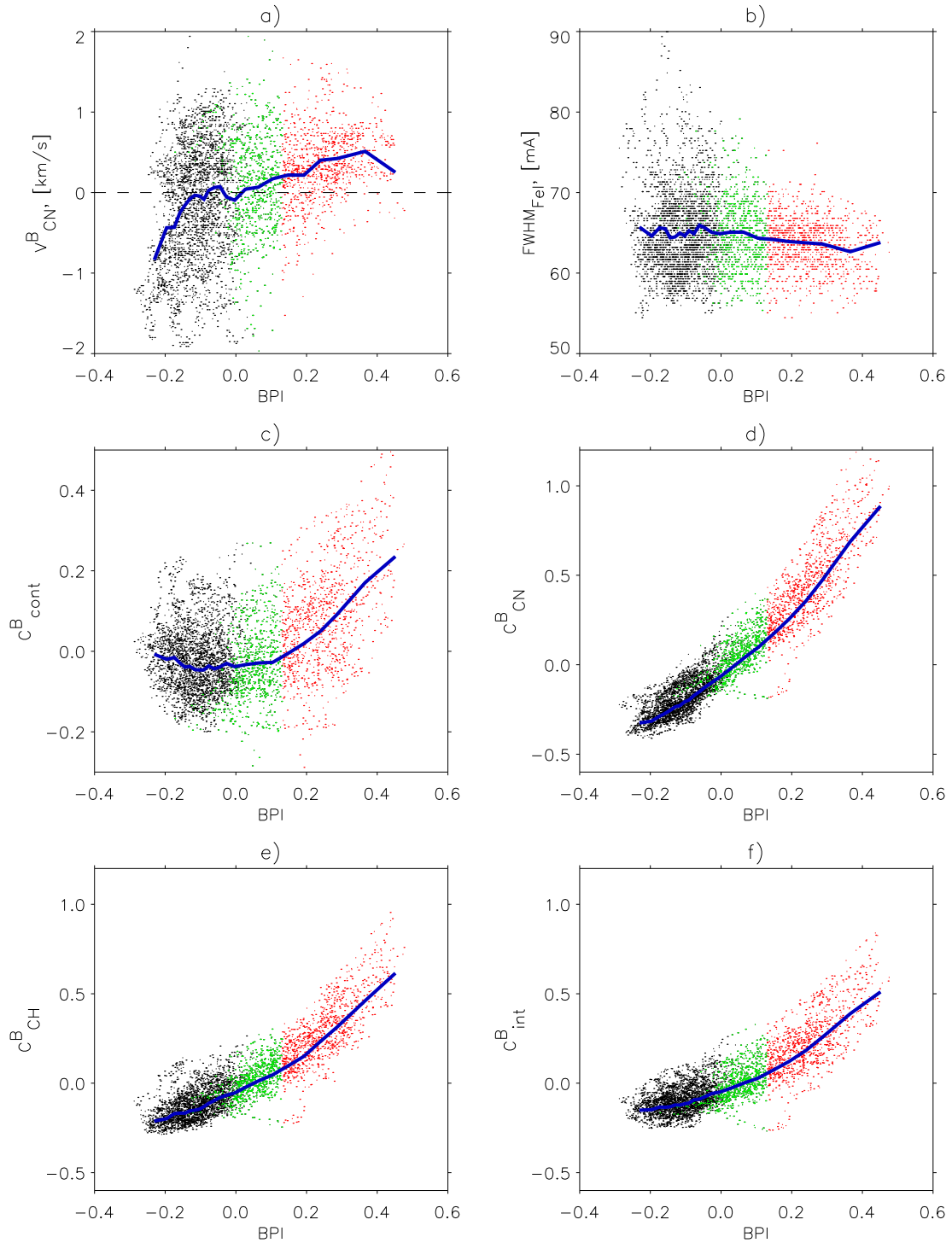


Figure 3.29: Velocity V_{CN}^B - a), FWHM - b), 'quasi' continuum intensity contrast C_{cont}^B - c), CN line-core intensity contrast C_{CN}^B - d), CH line-core intensity contrast C_{CH}^B - e) and "quasi" CN band-head intensity contrast C_{int}^B versus BPI observed at $\mu=0.56$. A blue line is the average dependency. **Red**, black and **green** points denote structures such as **BPs**, where $BPI \geq 0.13$, granulation, where $BPI < 0.13$, and "transition region", where $BPI < 0.13$ & $I_{int}^B > I_{cont}^B$.

3.4 Spectroscopy of small-scale magnetic features near the limb

Target	rms(I_{cont}^B)	rms(I_{cont}^A)	rms(I_{int}^B)	rms(I_{int}^A)	rms(I_{CN}^B) $\lambda=387.844$	rms(I_{CH}^B) $\lambda=387.829$	rms(I_{FeI}^B) $\lambda=387.777$
Quiet Sun at $\mu=0.65$	0.119	0.083	0.110	0.079	0.188	0.138	0.091
Active area at $\mu=0.65$	0.119	0.102	0.167	0.106	0.372	0.201	0.141
Quiet Sun at $\mu=0.56$	0.072	0.060	0.073	0.061	0.134	0.089	0.083
Active area at $\mu=0.56$	0.108	0.093	0.172	0.099	0.410	0.203	0.145

Table 3.11: RMS contrasts of 'quasi' continuum intensities I_{cont}^B and I_{cont}^A ; integrated brightness I_{int}^B and I_{int}^A ; line-core intensities I_{CN}^B , I_{CH}^B and I_{FeI}^B observed at $\mu=0.65$, in active region NOAA0752, $\mu=0.56$ and nearby quiet Sun areas respectively.

and $C(I_{CH}^B)$ dependencies on the BPI are more linear when observing near the limb. This causes a flattening of the ratio $C(I_{CN}^B)/C(I_{CH}^B)$ in the middle and bottom panels in Fig. 3.17 for faculae and is more concentrated for granules.

Note that due to the lowered BPI threshold to separate faculae the "transition region" spans a shorter range of BPI near the limb. Velocities at $\mu=0.65$ and $\mu=0.56$ positions reveal a more flat dependence and reach 0 m/s already at a BPI=-0.11 and BPI=-0.13, respectively. The FWHM at $\mu=0.65$ is almost constant over majority of structures with a small decrease near low BPI by 3 mÅ. In the $\mu=0.56$ case we have detected even a small increase of the line broadening below BPI=-0.1. It is interesting to note that the BPI at $\mu=0.65$ and $\mu=0.56$ varies in the same range as at the disc center with a small shift to high values. This suggests that at given height in the photosphere turbulent motions have comparable amplitude at these disc positions. According to Fig. 3.13 we expect black data points to show the highest FWHM to represent intergranular lanes.

3.4.4 Line depression

In this section we provide an analysis of the relative line-core depressions of deblended CH ($\lambda=387.829$ nm) and CN ($\lambda=387.844$ nm) lines, the Fe I line from B-spectra and additionally of the CH line from A-spectra measured in two active regions located at $\mu=0.65$ and at $\mu=0.56$. Results represent average values over 10 image positions in each active region.

Mean line depressions in faculae are listed in Table 3.12. In faculae at $\mu=0.65$ the depression of the CN line core is $\langle \Delta D_{CN}^B \rangle / \langle \Delta D_{CH}^B \rangle = 1.32$ and $\langle \Delta D_{CN}^B \rangle / \langle \Delta D_{FeI}^B \rangle = 1.61$ times stronger than that of the CH and Fe I lines respectively. The same for the $\mu=0.56$ case yields $\langle \Delta D_{CN}^B \rangle / \langle \Delta D_{CH}^B \rangle = 1.46$ and $\langle \Delta D_{CN}^B \rangle / \langle \Delta D_{FeI}^B \rangle = 1.48$. CN and CH line-core depressions at $\mu=0.65$ and $\mu=0.56$ are, as the rule, 1.16 and 1.17 times smaller than those observed in the faculae at $\mu=0.97$.

Contrary to the disc center case, the ratio of CN, CH line depressions in faculae near

3 High resolution spectroscopy of the solar photosphere

Feature	$\langle \Delta D_{CN}^B \rangle$ $\lambda = 387.844$	$\langle \Delta D_{CH}^B \rangle$ $\lambda = 387.829$	$\langle \Delta D_{CH}^A \rangle$	$\langle \Delta D_{FeI}^B \rangle$	V_{CN}^B [m/s]	V_{CH}^B [m/s]	V_{FeI}^B [m/s]	$FWHM$ [mÅ]
Faculae at $\mu=0.65$	-0.340	-0.258	-0.211	-0.201	98	160	173	62
Faculae at $\mu=0.56$	-0.349	-0.238	-0.222	-0.236	172	278	286	64

Table 3.12: Mean change in line-core depression of CN, CH, Fe I lines from B-spectra and CH line from A-spectra for faculae showing $BPI > 0.13$ with respect to those observed in the quiet Sun; flow velocities computed for the given lines and the FWHM for Fe I line observed in two active regions located at $\mu=0.65$ and $\mu=0.56$.

Feature	$(\Delta D_{CH}^B)_{max}$ $\lambda=387.829$	$(\Delta D_{CH}^B)_{min}$ $\lambda=387.829$	$(\Delta D_{CN}^B)_{max}$ $\lambda=387.844$	$(\Delta D_{CN}^B)_{min}$ $\lambda=387.844$
Granulation at $\mu = 0.65$	0.270	-0.418	0.366	-0.441
Faculae at $\mu = 0.65$	-0.06	-0.442	-0.236	-0.563
Granulation at $\mu = 0.56$	0.343	-0.582	0.383	-0.537
Faculae at $\mu = 0.56$	0.040	-0.586	-0.129	-0.635

Table 3.13: Change of the line-core depression of CN, CH spectral lines, corrected for the blending effect, observed in two active regions located at $\mu=0.65$ and $\mu=0.56$. Two types of structures are presented: granulation with $BPI < 0.13$ and faculae with $BPI \geq 0.13$.

the limb tend to increase, as seen from the right panels in Fig. 3.19, with an increase of the integrated intensity.

3.4.5 Strong velocity shifts seen in upper photosphere

We have detected a remarkable behavior of the strong atomic lines Fe I at 387.912 nm and at 387.968 nm in the active region at $\mu=0.56$. The corresponding 'Red' image, B-slit jaw image and fragment of the B-spectra, containing these lines, along the slit are presented in Fig. 3.30. At, for example, 3.2 arcsec, which corresponds to a very faint facula, these spectral lines have a strong red-shift of the line-core. At the same time all other lines presented in B-spectra show only a very small red shift in that place. Because of the circumstance that the Fe I lines at 387.912 nm and 387.968 nm are strongly blended by many atomic and some CN lines, the measurement of their Doppler shifts is complicated. Nevertheless, using cross-correlations we have estimated these shifts as flows of about

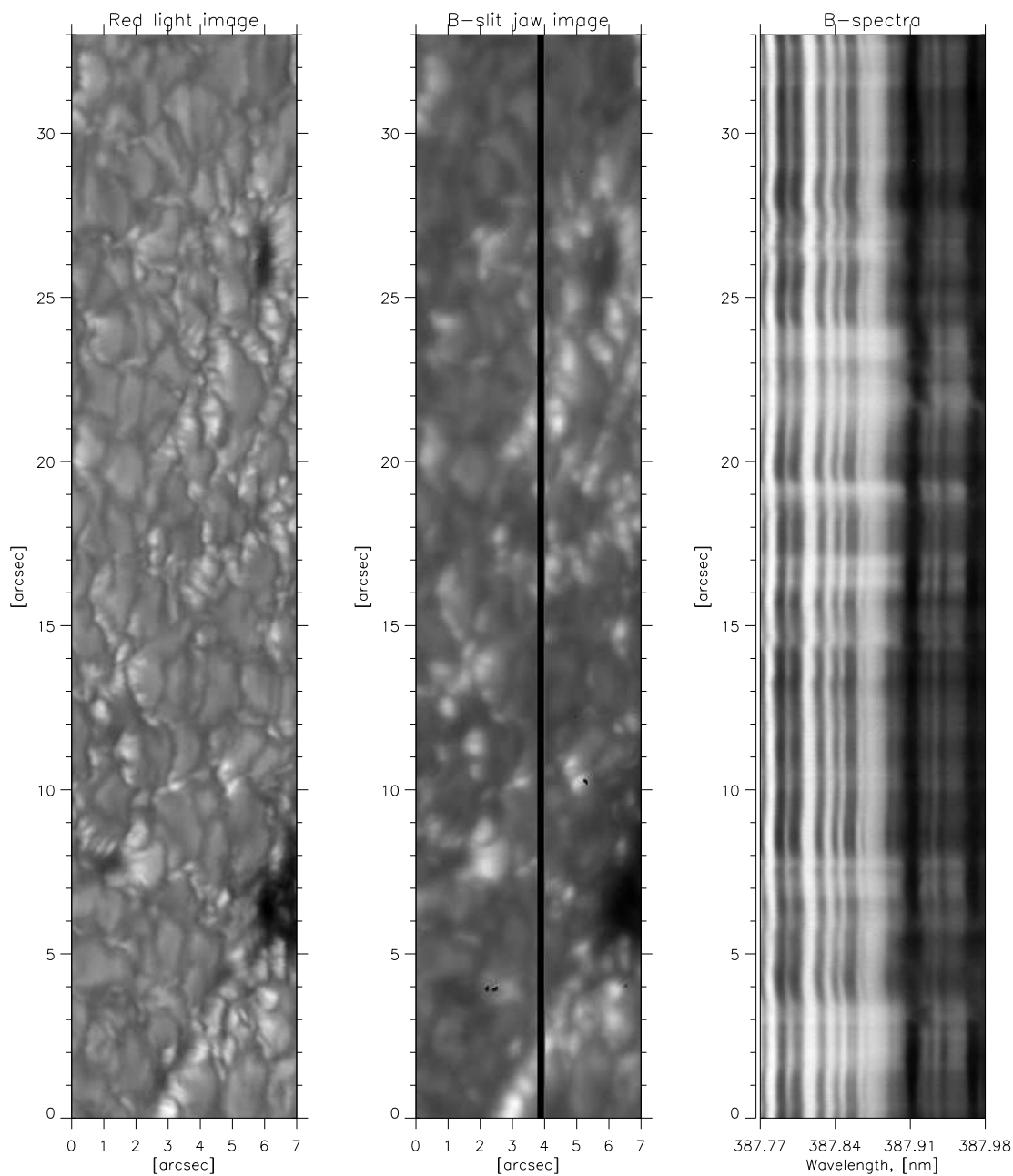


Figure 3.30: High resolution 'Red' image, B-slit jaw image and section of B-spectrum near 387.9 nm observed in the active region at $\mu=0.56$ on 14 April 2005 at 14:49:19 (UT).

1800 m/s. Usually, the above mentioned atomic lines show lower velocities than standard CN, CH or Fe I lines by a factor of 1.7 possibly because they are formed high in the atmosphere (see Appendix B). However, at this location $V_{CN}^B=620$ m/s, $V_{CH}^B=980$ m/s and $V_{FeI}^B=830$ m/s. Thus we can conclude that near the limb in the high photosphere strong plasma flows exist. If we assume that the flow follows the field lines and that they are more or less vertical, then the true velocity is $1800/\mu \approx 3200$ m/s. Since the magnetic features are likely to be spatially unresolved this is actually a lower limit to the true velocity. On the other hand, the true inclination of the magnetic field vector at this location is not known, so that further interpretation of such velocities is speculative.

3.5 Continuum intensity

An important factor in intensity contrast calculations in molecular bands is the local continuum intensity. In order to provide a quantitatively precise comparison of the brightness distribution observed in any particular spectral line or in the whole molecular band one should know how the continuum intensities at that wavelengths relate to each other. Here we compare the measurements of local 'quasi' continuum I_{cont}^B (at $\lambda_{cont}^B=388.18$ nm) and I_{cont}^A (at $\lambda_{cont}^A=436.20$ nm) in all observed active regions. An aggregate of negative factors, like spatial displacement of the images on a slit in two observed spectra, probably their still different spatial resolution and uncertainty in the determination of the 'true' local continuum in the B-spectra reduces the value of the quantitative results of the present analysis in a hardly controlled way.

Scatter plots of I_{cont}^B versus I_{cont}^A for three heliocentric angles are presented in Fig. 3.31. The red and black colors designate the BPs and other features, respectively. The dependence is almost linear. However, a small separation of intensity group corresponding to the BPs is seen. This small split is evidence of higher continuum intensity of the BPs at $\lambda_{cont}^B=388.18$ nm than that at $\lambda_{cont}^A=436.202$ nm. The quotient of rms contrasts of I_{cont}^B and I_{cont}^A amounts to 1.07 at $\mu=0.97$, 1.17 at $\mu=0.65$ and 1.16 at $\mu=0.56$. Evidently the continuum at λ_{cont}^B shows higher amplitude than at λ_{cont}^A and increases the difference of the total contrast of the BPs observed in CN band-head and G band. However, this result cannot be assumed to be statistically significant and observations covering more active regions at different μ should be done. In particular, this result depends strongly on the relative spatial resolution and scattered light in both spectral channels.

3.6 Spectroscopy of large-scale magnetic phenomena

3.6.1 Pore

Pores, by definition, are small, mainly of size of several granules and their appearance is similar to sunspots which have no penumbra.

In Figs. 3.32 and 3.33 spectroscopic observables of a pore of 2 arcsec size at $\mu=0.97$ are presented. This pore is surrounded by facular-like structures and by a disturbed granulation pattern. This appearance of strongly disturbed granulation indicates large amount of magnetic flux in that region. The magnetic field influences hydrodynamic evolution and causes fuzzy or so-called "abnormal" granulation (Dunn & Zirker 1973, Ramsey et

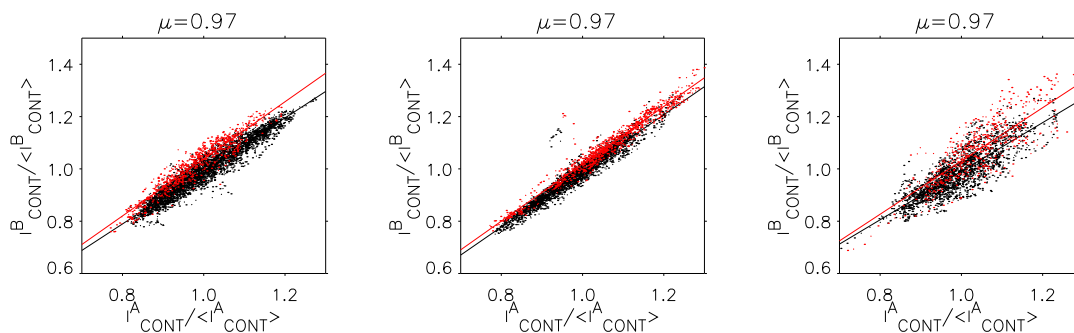


Figure 3.31: Scatter plot of normalized continuum intensities at 388.18 nm and 436.202 nm of active regions at $\mu=0.97$ (left), $\mu=0.65$ (middle) and $\mu=0.56$ (right). Red and black colors mark BPs and other features, respectively. The lines represent a linear fit to the data points.

al. 1977, Koschinsky et al. 2001). Granulation is clearly perturbed in regions where magnetic flux is emerging (Brants & Steenbeck 1985). The contrast of I_{int}^B is in the pore interior 1.25 times higher than that of I_{cont}^B . At the same time the BPI at the edges of the pore reaches up to 0.33 and decreases down to 0.13 towards its center. Also, the contrast of I_{CN}^B is higher than that of I_{CH}^B . Such a situation is comparable to the case of the dark magnetic concentrations or micropores discussed in Section 3.3.2.

In order to inspect changes in the absorption of spectral lines, which could be an indirect proxy to thermal conditions there, we plot B- and A-spectra in Fig. 3.34 which were averaged over structures of different types and normalized to a continuum value of unity. Black, green, blue and red colors signify mean spectra of the quiet Sun, brightest granules, intergranular dark lanes and the pore interior, respectively. In contrast with BP spectroscopy (see Fig. 3.8) we find that line depths of not only molecular, but also of atomic lines presented in Fig. 3.34 change in a wide range. Even strong atomic lines at 387.968 nm and 387.912 nm show an evidently variable line depression, although this variation is smaller than of molecular lines.

Feature	$\langle \Delta D_{CH}^B \rangle$ $\lambda=387.829$	$\langle \Delta D_{CN}^B \rangle$ $\lambda=387.844$	$\langle \Delta D_{FeI}^B \rangle$ $\lambda=387.777$	$\langle \Delta D_{FeI}^B \rangle$ $\lambda=387.912$
Granules	0.193	0.202	0.174	0.021
Intergranular lanes	-0.160	-0.156	-0.184	-0.009
Pore	-0.301	-0.411	-0.282	-0.031
BPs	-0.306	-0.466	-0.289	-0.020

Table 3.14: Change relative to the quiet Sun of the line-core depression of CN, CH and Fe I spectral lines, corrected for the blending and Fe I line at $\lambda=387.912$ nm without deblending correction, observed in an active region at $\mu=0.97$.

In Table 3.14 mean line-core depressions of deblended CN and CH lines and Fe I line at $\lambda=387.844$ nm, $\lambda=387.829$ nm and $\lambda=387.777$ nm respectively are listed. In addition,

3 High resolution spectroscopy of the solar photosphere

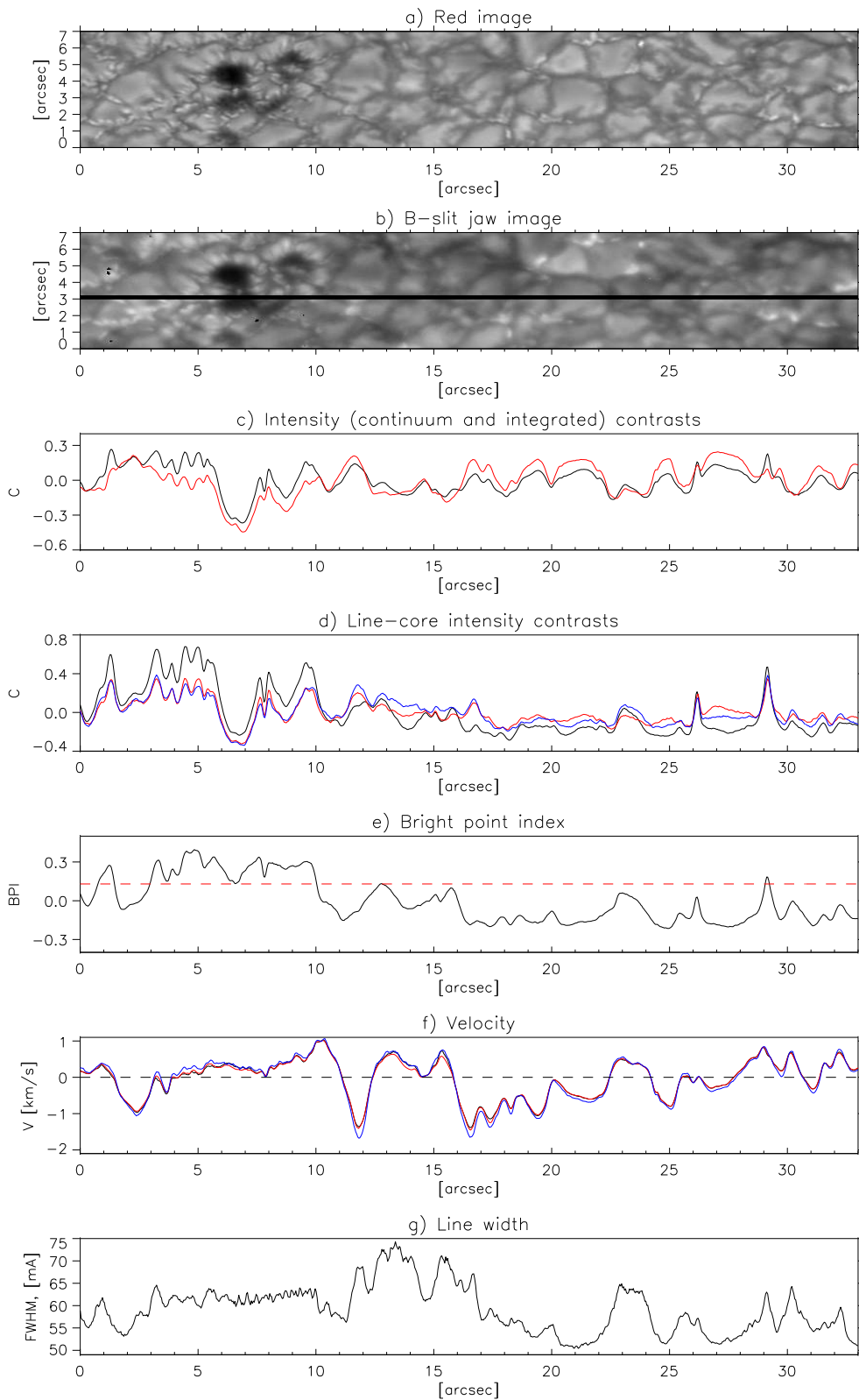


Figure 3.32: Spectroscopic data observed in the active region NOAA0753 at $\mu=0.97$ on 14 April 2005 at 14:56:19 (UT) : a) Reference image; b) B-slit jaw image; c) integrated and continuum intensity contrasts $C(I_{int}^B)$ - black, $C(I_{cont}^B)$ - red; d) line-core intensity contrasts $C(I_{CN}^B)$ - black, $C(I_{CH}^B)$ - red, $C(I_{FeI}^B)$ - blue; e) BPI; f) velocities V_{CN}^B - black, V_{CH}^B - red, V_{FeI}^B - blue; g) line width of Fe I line.

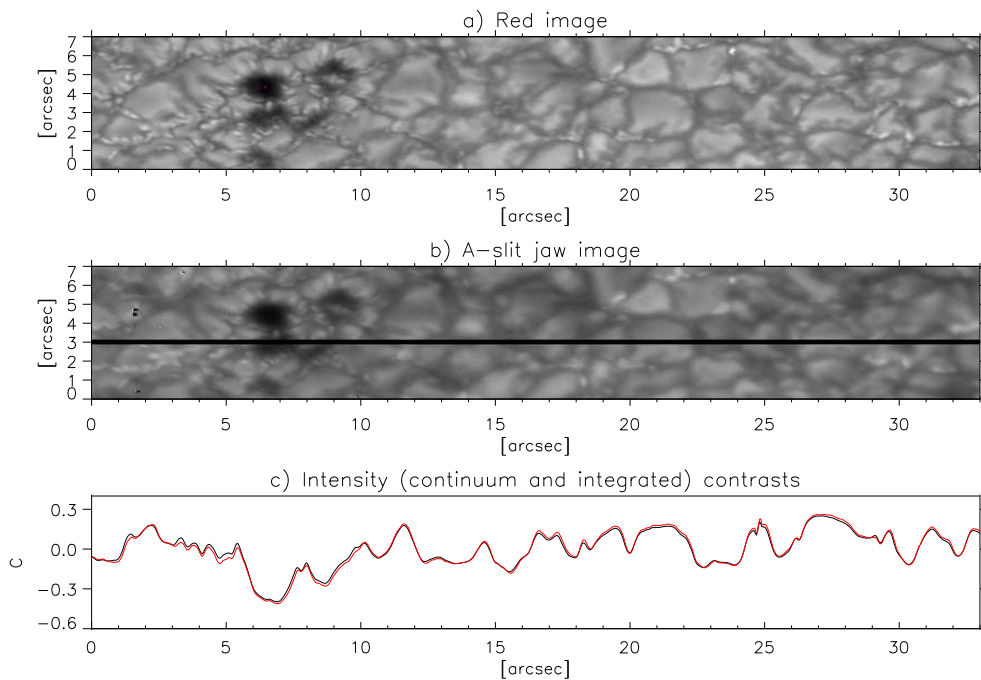


Figure 3.33: Spectroscopic data observed in the active region NOAA0753 at $\mu=0.97$ on 14 April 2005 at 14:56:19 (UT) : a) Reference image; b) A-slit jaw image; c) intensity contrasts (I_{int}^A) - black, (I_{cont}^A) - red.

the measurements for the strong Fe I line at $\lambda=387.912$ nm are also given, although this line was not cleaned from blending effects because of the obvious difficulty. As expected, BPs (compare with Fig. 3.8) have the faintest molecular absorption. However, the pore also reveals a very feeble absorption by diatomic molecules. The CN line is 1.13 times and CH line only 1.02 times deeper in the pore compared with BPs. At the same time very deep Fe I line at 387.912 nm is 1.6 times less deep in the pore as in BPs. Taking the line-core intensity as a proxy for the temperature we conclude that the temperature of upper photospheric layers, where atomic line $FeI_{\lambda=387.912}$ is formed should be higher in the pore than that in BPs. Near $\tau_{CN}=1$ BPs are on average slightly hotter than the pore and near $\tau_{CH}=1$ their temperatures are almost equal. We conclude that in the pore, as an extreme case of evacuated magnetic flux tube, the temperature gradient in a vertical direction should be lower as in the BP between $\tau_{FeI,\lambda=387.912}=1$ and $\tau_{CH}=1$ if we assume that both types of features are completely spatially resolved. This is problematic since the BPs, probably, are incompletely resolved. The pore, in turn, is affected by scattered light. A similar analysis concerning intergranular lanes leads to a statement that in these formations gas is colder than in a BP's flux tube at mid photospheric heights. Granules have even stronger absorption in all lines than intergranular regions, which is a clear manifestation of 'reversed granulation' phenomena, caused by their steeper vertical thermal gradient.

The velocity inside the pore is non-zero and is around 300 m/s. It drops down to 200 m/s at the borders. This is in contradiction with observations reported by Sankarabramanian and Rimmele (2003), Tritschler et al. (2002), Hirzberger (2003). Even if we assume that the velocity inside the pore is zero we have not detected any evidence of

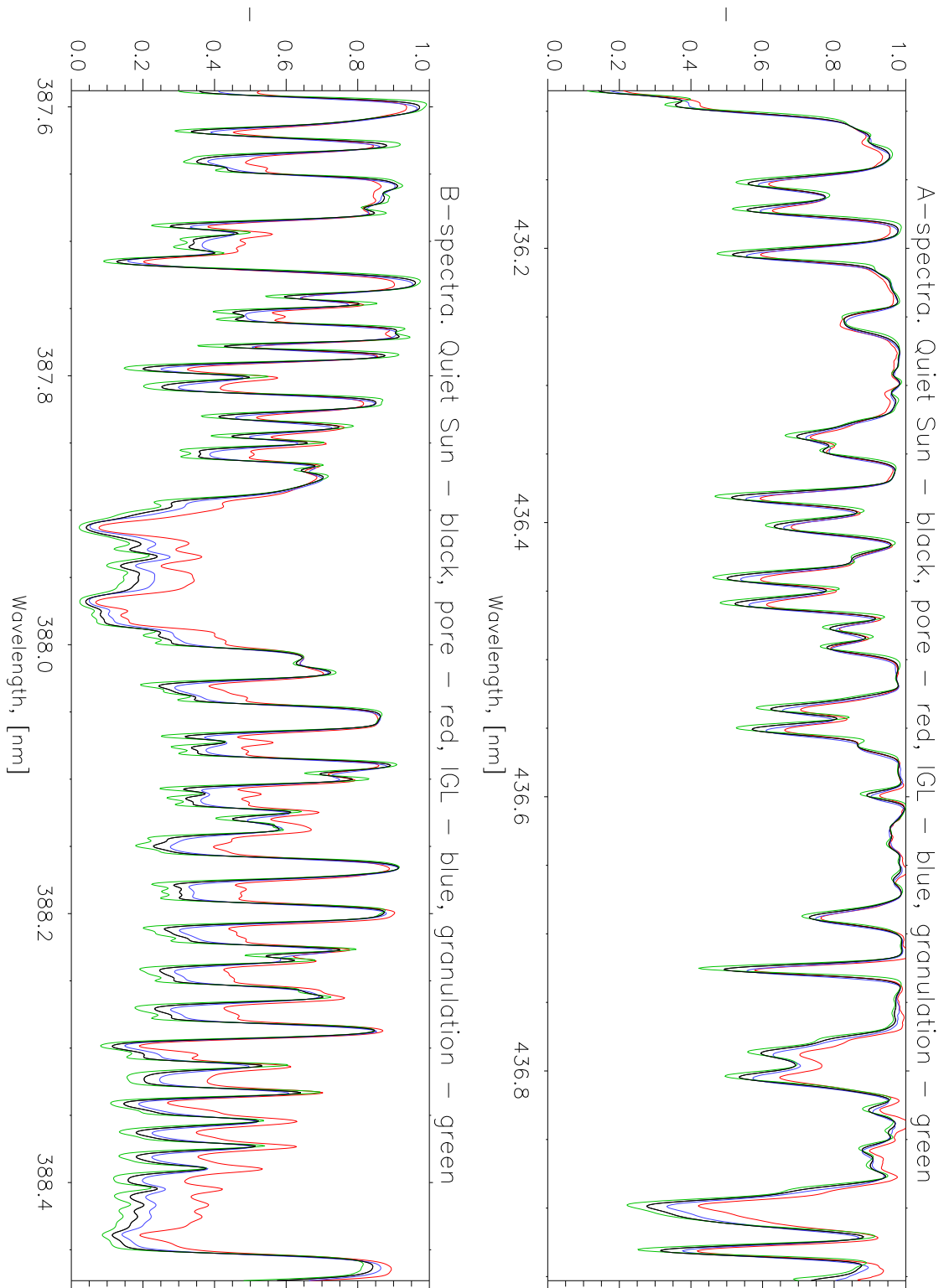


Figure 3.34: Example of A- and B-spectra of the pore in active region NOAA0753 at $\mu=0.97$ on 14 April 2005 at 14:53:14 (UT). Black, red, blue and green lines represent spectra of the quiet Sun, pore, intergranular dark lane (IGL) and top of the granules respectively.

a strong and narrow downflow around it, which was observed by them. However, needle-like structures, reported by Sankarasubramanian and Rimmele (2003), around the pore were detected where a head of the needle shows an upflow (see position 7.67 arcsec in Fig. 3.32 f) for example).

3.6.2 Sunspot

In Fig. 3.35 and Fig. 3.36 reduced spectral data obtained from B- and A-spectra respectively of an active region NOAA0750, containing a sunspot, observed on 14 April 2005 at 15:08:25 (UT) at $\mu=0.79$ are shown. In the 'Red' image an umbra and a well developed penumbra of the sunspot are seen. The umbra in Fig. 3.35 a) reveals a number of umbral dots, indicating its complex thermal structure. Even A- and B-slit jaw images show the brightest of them. In plots of the intensity contrast along the slit, c) and d) in Fig. 3.35 and c) in Fig. 3.36), at 8.9 arcsec the most prominent umbral dot is seen. In general their spectroscopic properties are close to those of penumbral filaments, i.e. strong decrease of BPI by 0.25 and a very faint downflow of 180 m/s with respect to the umbral velocities. It is remarkable that the sunspot interior, penumbra and quiet Sun area to the left show almost everywhere higher intensity contrast in continuum I_{cont}^B , I_{cont}^A than that in I_{int}^B and I_{int}^A , respectively. This fact suggests that the temperature gradient at $-2 < \log(\tau) < 0$ in a sunspot's atmosphere could be similar to that in the quiet Sun. Unfortunately the signal-to-noise ratio in the recorded spectroscopic data is too low within the umbra which makes it impossible to produce a detailed quantitative analysis of its brightness distribution. The area to the right of the spot (1–5 arcsec in Fig. 3.35) possesses almost no visible penumbral filaments but rather "abnormal granulation" like that seen near the pore. In the presented figure the solar limb direction is to the top and facular brightenings on the centerward side of the granules are clearly seen. The contrast of I_{int}^B has larger values with respect to those of I_{cont}^B not only in faculae, but also in a dark regions between the rest of granules (1.3 arcsec and 2.55 arcsec positions in Fig. 3.35). Also the BPI reaches almost 0.4 in those locations. The edge of the umbra at 6.0 arcsec as seen from a) and b) images corresponds to a steep slope of the contrast profiles whereas the BPI is still higher than 0.35 and decreases down to 0.2 only at 6.6 arcsec along the slit, i.e. well inside the umbra. This means that the thermal structure of the atmosphere near the steep "wall" of the umbra is similar to the pore's atmosphere, discussed in Section 3.6.1. In support of this statement the contrast of I_{int}^B is still higher near the left border of the umbra than that of I_{cont}^B . In the umbra, penumbra and quiet Sun areas where $BPI < 0$ the contrast of I_{int}^B is always below the contrast of I_{cont}^B .

3.6.3 Velocity reference

Since we have not measured an absolute velocity standard, we are limited to relative velocity measurements. From the mass conservation it follows that the mean speed of the quiet Sun granulation motions must be zero. When observing the solar surface from the Earth many factors play a role in the velocity determination. To mention some of them, systematic blue shift of around 200–300 m/s, gravitational red shift (Dravins 1999, Lites et al. 1989), solar oscillations, Earth's rotation, solar rotation and thus different disc position of observed feature etc. In the framework of the present research we content ourselves

3 High resolution spectroscopy of the solar photosphere

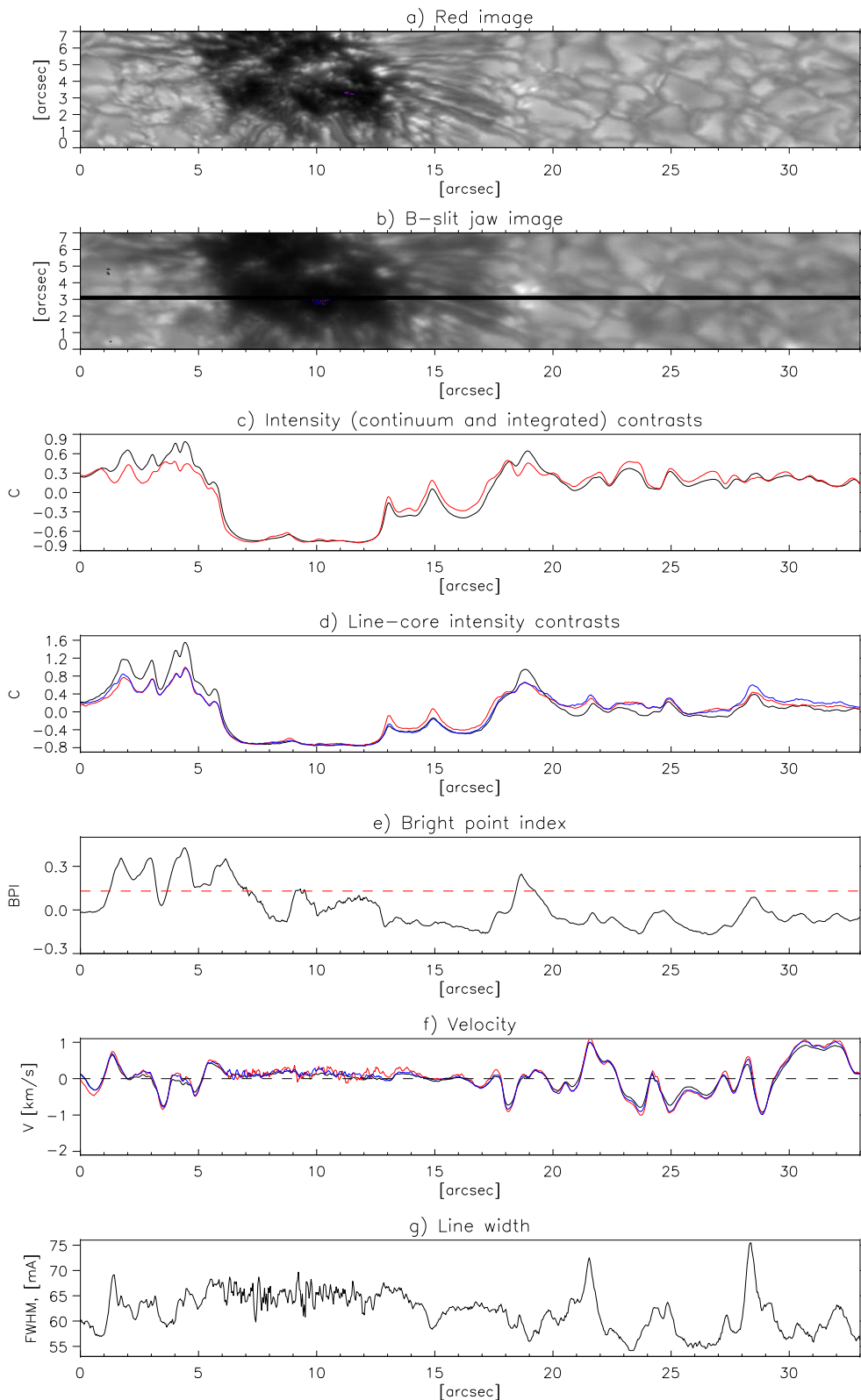


Figure 3.35: Spectroscopic data observed in the active region NOAA0750 at $\mu=0.79$ on 14 April 2005 at 15:08:25 (UT) : a) Reference image; b) B-slit jaw image; c) integrated and continuum intensity contrasts $C(I_{int}^B)$ - black, $C(I_{cont}^B)$ - red; d) line-core intensity contrasts $C(I_{CN}^B)$ - black, $C(I_{CH}^B)$ - red, $C(I_{FeI}^B)$ - blue; e) BPI; f) velocities V_{CN}^B - black, V_{CH}^B - red, V_{FeI}^B - blue; g) line width of Fe I line.

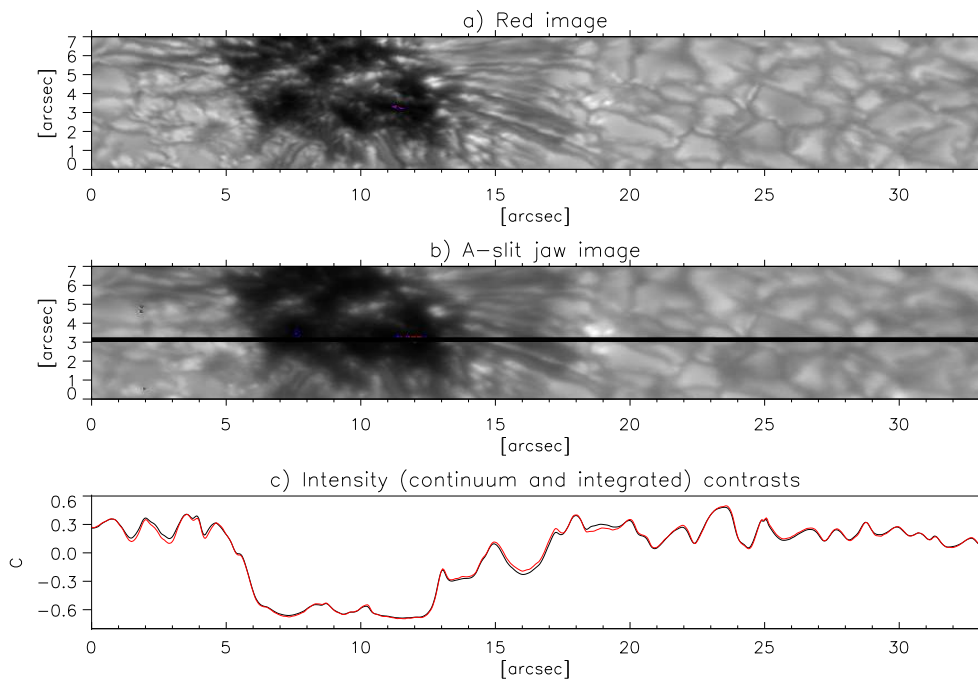


Figure 3.36: Spectroscopic data observed in the active region NOAA0750 at $\mu=0.79$ on 14 April 2005 at 15:08:25 (UT) : a) Reference image; b) A-slit jaw image; c) intensity contrasts (I_{int}^A) - black, (I_{cont}^A) - red.

to investigating velocity changes along the slit of the spectrograph, where its mean value was set to 0 m/s for each spectral line. Under this assumption velocity measurements for two different image positions on the slit cannot be compared quantitatively, since the 0-reference is not exactly the same even if the slit in both positions covers only a quiet Sun area at the same μ . However, it is possible to estimate the order of these deviations if we use observations of the sunspot. The sunspot consists of penumbra and dark umbra. The latter is commonly believed to be at rest except for oscillatory effects (Mathew et al. 2003), (Schmidt & Balthasar 1994). In the particular example shown in Fig. 3.35 the slit covers at the same time umbra and quiet Sun. This enables to calibrate velocities of the granular fraction and estimate its typical offset. The total observations cover a quiet Sun area of $7 \times 13 \text{ arcsec}^2$ and different parts of the umbra simultaneously, which allows velocity measurements with good statistical significance.

It must be noticed that the results of error estimations described in Section 3.2.3 relate to the case of relative high intensities like granules, bright features and intergranular lanes. In case of a very dark solar features like umbra of the sunspots the S/N ratio is so low that the accuracy of velocity measurements degrades dramatically up to 250 m/s and even more. As a consequence no quantitative investigation of umbral flow velocities at high spatial resolution is possible.

The velocity averaged over the whole umbra was compared with the mean velocity measurements in the quiet Sun for three spectral lines.

The results are presented in Table 3.15. We obtain a relatively good estimation of the 0-level in our Doppler measurements. Locally, the values of the differences in LOS velocity may change due to solar oscillations which we did not take here into account.

$V_{CH}^{umbra} - V_{CH}^{qs}$ [m/s]	$V_{CN}^{umbra} - V_{CN}^{qs}$ [m/s]	$V_{FeI}^{umbra} - V_{FeI}^{qs}$ [m/s]
75	97	133

Table 3.15: Umbral LOS velocities differences to the quiet Sun velocity observed at $\mu=0.79$ in active region NOAA0750 on 14 April 2005 between 15:05:56 (UT) and 15:11:07 (UT).

4 Radiative MHD Simulations

4.1 MHD model

Realistic solar magneto-convection simulations aim at representing the radiative and magnetohydrodynamical processes in the solar photosphere and in the uppermost layers of the convection zone, so that the results can be compared with the observations. Here, results of ab-initio three-dimensional simulations of non-grey radiative magneto-convection in the solar surface layers carried out with the MURaM code have been analysed. The MURaM (MPS/University of Chicago Radiative MHD) code has been developed by the magneto-hydrodynamic (MHD) simulation groups at the Max-Planck-Institut für Sonnensystemforschung in Katlenburg-Lindau by Vögler A., Shelyag S., Schüssler M. and at the University of Chicago by Cattaneo T., Emonet Th., Linde T. (Vögler & Schüssler 2003, Vögler et al. 2003, Vögler 2003, Vögler et al. 2005). The MURaM code solves the time-dependent MHD equations for a compressible and partially ionized plasma including a non-grey Local Thermodynamic Equilibrium (LTE) radiative transfer based on multigroup frequency binning. The computational box of the analysed runs corresponds to a small part of a unipolar plage region on the Sun, extending 1400 km in the vertical direction (roughly covering the range between 800 km below to 600 km above the visible solar surface) and 6000 km in both horizontal directions, with grid spacing of 14 km and 21 km, respectively. Such a model box corresponds to an area of $8.28 \times 8.28 \text{ arcsec}^2$ on the Sun. In the simulation runs that we consider in the present investigation, the box is penetrated by a fixed amount of vertical magnetic flux corresponding to an average vertical magnetic field strength (flux density) of 50 G (5 mT), 200 G (20 mT) and 400 G (40 mT). In addition a 0 G model representing a pure hydrodynamical (HD) case was used. This HD model was assigned to the quiet solar photosphere. In the MURaM code the entropy density of the fluid in the computational box was chosen to be uniform across the upflow regions at the lower boundary and independent of magnetic field. The entropy of inflowing material was calibrated such that the radiative energy flux of the nonmagnetic run on average equals the solar value $F_{\odot} = 6.3 \cdot 10^{10} \text{ erg cm}^{-2}\text{s}^{-1}$. We have used snapshots taken after a statistically stationary state of the simulated radiative magneto-convection had developed. The produced array of $288 \times 288 \times 100$ mesh pixels consists of the following physical quantities for each pixel:

- Temperature T [K]
- Pressure P [$\text{g cm}^{-1} \text{ s}^{-2}$]
- Horizontal velocity components V_x, V_y [cm/s]
- Vertical velocity component V_z [cm/s]
- Internal energy per unit volume [erg cm^{-3}]

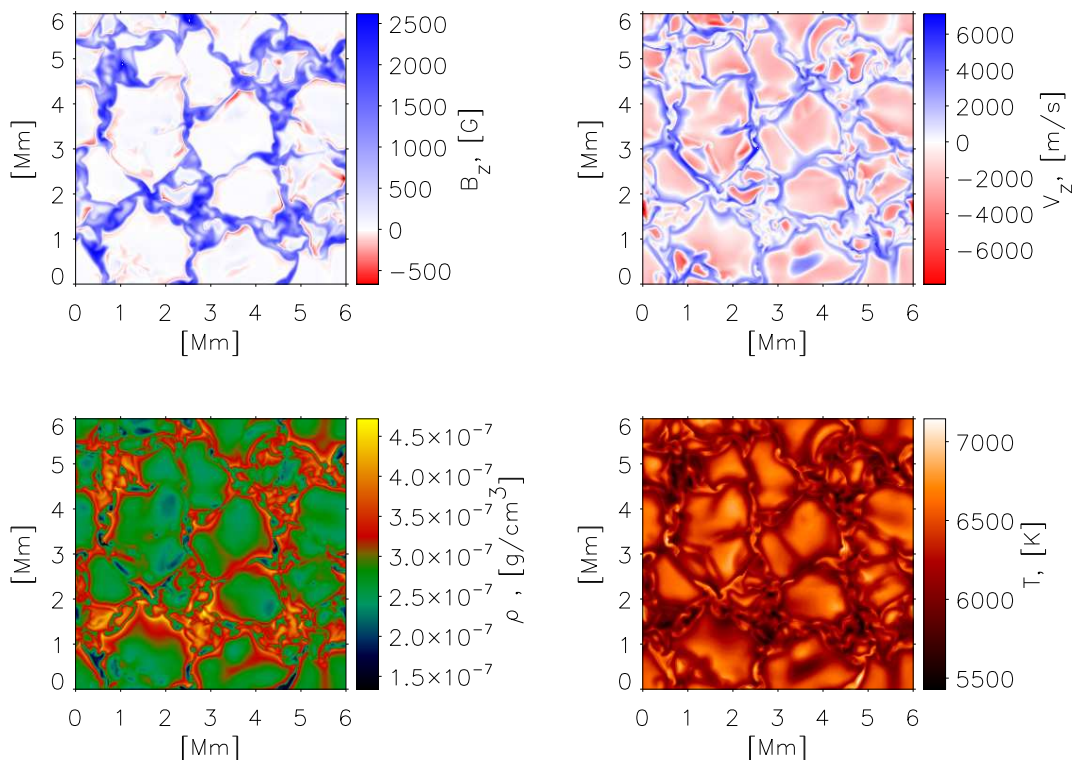


Figure 4.1: Snapshot of the MHD model with 400 G mean vertical magnetic field. Top left - longitudinal component of the magnetic field \mathbf{B} at the level of $\tau_{705nm}=1$, positive and negative values are represented by blue and red colors, respectively. Top right - vertical component of the velocity vector \mathbf{V} also at the level $\tau_{705nm}=1$, red color corresponds to downflows and blue to upflows. Bottom left - mass density at $\tau_{705nm}=1$. Bottom right - the temperature distribution at $\tau_{705nm}=1$ which is similar to the relative continuum brightness at $\lambda = 705$ nm.

- Horizontal magnetic field components B_x, B_y [G]
- Vertical magnetic field component B_z [G]

In Fig. 4.1 a roughly horizontal slice of the MHD model with the 400 G averaged magnetic field uncovers the two-dimensional distribution of the vertical component of magnetic field, flow velocity, mass density and temperature at the height corresponding to an optical depth $\tau=1$, computed for the continuum at $\lambda = 705$ nm. This wavelength has been chosen, since high-resolution observations are available with which the simulations are compared in Section 4.6.1. As seen from this figure the major part of magnetic flux is concentrated in the intergranular downflow regions which form a network pattern. There the field strength \mathbf{B} reaches values up to 2570 G. The magnetic pressure $|\mathbf{B}^2/8\pi|$ in such small-scale concentrations, known as evacuated magnetic flux tubes, reduces the internal gas pressure P_{gas} since the total pressure should be in balance with the surroundings (Spruit 1976, Deinzer et al. 1984, Knölker et al. 1991, Vögler & Schüssler 2003). As a result the density in the flux tubes is significantly reduced. This leads to the inflow of excess radiation through the walls of these structures, which heat up and become bright.

For the narrower magnetic structures this also produces a heating throughout their interior. This leads to the formation of photospheric bright points.

4.2 Radiative transfer and line synthesis

In this section we briefly describe the procedure of numerical solution of the radiative transport in the model. A forward spectral synthesis of the Stokes parameters of atomic transitions will be discussed.

Let us denote the Stokes vector as $\mathbf{I} = (S_I, S_Q, S_U, S_V)^T$ with S_I denoting total intensity and S_V - circularly polarized component. Following the formulation of Rees et al. (1989) the radiative transfer equation for the Stokes vector is as follows:

$$\frac{d\mathbf{I}}{dz} = -\mathbf{K}\mathbf{I} + \mathbf{j}, \quad (4.1)$$

where \mathbf{K} is the total absorption matrix,

$$\mathbf{K} = \kappa_c \mathbf{1} + \kappa_0 \mathbf{\Phi} \quad (4.2)$$

and \mathbf{j} is the total emission vector,

$$\mathbf{j} = \kappa_c S_c e_0 + \kappa_0 S_l \mathbf{\Phi} e_0. \quad (4.3)$$

Here $\mathbf{1}$ is the unit 4×4 matrix, $e_0 = (1, 0, 0, 0)^T$, and κ and S_c are the opacity and source function in the unpolarized continuum. Assuming gas at LTE, the source function was set to $S_c = B_\lambda(T_e)$, i.e. the Planck function at the local electron temperature T_e . The line center opacity κ_0 (for zero damping, zero magnetic field and corrected for stimulated emission) and the line source function S_l depend only on the total populations of the upper and lower levels of the transition. In the LTE regime $S_l = S_c$. In Fig. 4.2 the xyz coordinate frame in which the Stokes parameters are defined is shown. The z -axis is toward the observer. The line absorption matrix $\mathbf{\Phi}$ is:

$$\mathbf{\Phi} = \begin{pmatrix} \phi_I & \phi_Q & \phi_U & \phi_V \\ \phi_Q & \phi_I & \phi'_V & -\phi'_U \\ \phi_U & -\phi'_V & \phi_I & \phi'_Q \\ \phi_V & \phi'_U & -\phi'_Q & \phi_I \end{pmatrix}, \quad (4.4)$$

where

$$\begin{aligned} \phi_I &= \frac{1}{2} \phi_p \sin^2 \gamma + \frac{1}{4} (\phi_r + \phi_b) (1 + \cos^2 \gamma), \\ \phi_Q &= \frac{1}{2} \left[\phi_p - \frac{1}{2} (\phi_r + \phi_b) \right] \sin^2 \gamma \cos 2\chi, \\ \phi_U &= \frac{1}{2} \left[\phi_p - \frac{1}{2} (\phi_r + \phi_b) \right] \sin^2 \gamma \cos 2\chi, \\ \phi_V &= \frac{1}{2} (\phi_r - \phi_b) \cos \gamma, \\ \phi'_Q &= \frac{1}{2} \left[\phi'_p - \frac{1}{2} (\phi'_r + \phi'_b) \right] \sin^2 \gamma \cos 2\chi, \\ \phi'_U &= \frac{1}{2} \left[\phi'_p - \frac{1}{2} (\phi'_r + \phi'_b) \right] \sin^2 \gamma \cos 2\chi, \\ \phi'_V &= \frac{1}{2} (\phi'_r + \phi'_b) \cos \gamma. \end{aligned} \quad (4.5)$$

Generalized absorption and anomalous dispersion profiles are denoted by $\phi_{p,b,r}$ and $\phi'_{p,b,r}$, respectively. For a normal triplet, the indices p , b and r refer, respectively, to the unshifted π component and the *blue*- and *red*-shifted σ components of the line profile.

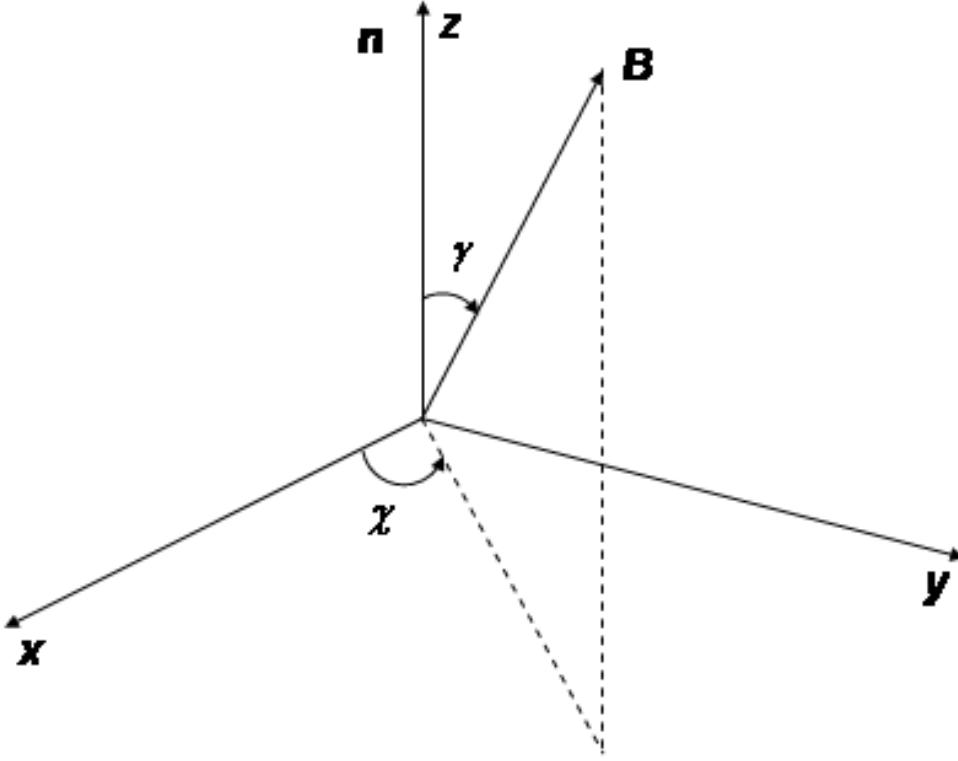


Figure 4.2: Reference frame in which the Stokes vector I and magnetic vector B are defined.

For anomalous splitting we denote the numbers of Zeeman components of each type with $N_{p,b,r}$, governed by the selection rules,

$$\Delta M = M_u - M_l = \begin{cases} +1 \equiv b, \\ 0 \equiv p, \\ -1 \equiv r, \end{cases} \quad (4.6)$$

where M_u and M_l are the magnetic quantum numbers of the Zeeman levels in the upper and lower states of the line transition, i.e. with $M\hbar$ eigenvalues of the z -component of the total angular momentum. Each level $k(=u,l)$ with quantum numbers S_k , L_k , J_k , i.e. describing spin, orbital angular momentum and the total angular momentum of the atom, and Landé factor:

$$g_k = \frac{3}{2} + \frac{S_k(S_k + 1) - L_k(L_k + 1)}{2J_k(J_k + 1)} \quad (4.7)$$

splits into $2J_k + 1$ Zeeman sublevels $M_k = -J_k, \dots, +J_k$. The Zeeman wavelength shift of the i_j component is:

$$\Delta\lambda_{i_j} = \frac{e\lambda_0^2 |\mathbf{B}|}{4\pi m_e c^2} (g_l M_l - g_u M_u)_{i_j}, \quad (4.8)$$

where e , m , c have their usual meanings, λ_0 is the wavelength of the unsplit line, $j =$

p, b, r and $i_{p,b,r} = 1, \dots, N_{p,b,r}$. The strength of the component i_j is S_{i_j} , and

$$\sum_{i_j=1}^{N_j} S_{i_j} = 1, \quad j = p, b, r. \quad (4.9)$$

The generalized profiles (see Rees et al. (1989)) ϕ_j for $j = p, b, r$ in turn are:

$$\phi_j = \sum_{i_j=1}^{N_j} S_{i_j} H(a, v - v_{i_j} + v_{los}), \quad (4.10)$$

and

$$\phi'_j = 2 \sum_{i_j=1}^{N_j} S_{i_j} F(a, v - v_{i_j} + v_{los}), \quad (4.11)$$

where $H(a, v)$ and $F(a, v)$ are the Voigt and Faraday-Voigt functions respectively:

$$H(a, v) = \frac{a}{\pi} \int_{-\infty}^{\infty} \frac{e^{-y^2}}{(v - y)^2 + a^2} dy \quad (4.12)$$

and

$$F(a, v) = \frac{1}{2\pi} \int_{-\infty}^{\infty} \frac{(v - y)e^{-y^2}}{(v - y)^2 + a^2} dy. \quad (4.13)$$

Here the parameters are expressed in units of the Doppler width $\Delta\lambda_D$, i.e.:

$$a = \Gamma\lambda_0^2/4\pi c\Delta\lambda_D, \quad (4.14)$$

where Γ is the line damping parameter,

$$v = (\lambda - \lambda_0)/\Delta\lambda_D, \quad (4.15)$$

λ is the wavelength in the line,

$$v_{i_j} = \Delta\lambda_{i_j}/\Delta\lambda_D, \quad (4.16)$$

and the Doppler shift induced by a macroscopic velocity field \mathbf{v}_{mac}

$$v_{los} = \lambda_0 |\mathbf{v}_{mac}| \cos\gamma / c\Delta\lambda_D, \quad (4.17)$$

with γ denoting here the angle between \mathbf{v}_{mac} and the LOS.

The STOPRO (STokes PROfiles) code developed by C. Frutiger, S.K. Solanki and S. Berdyugina (Solanki 1987, Solanki et al. 1992, Frutiger et al. 2000 & Berdyugina et al. 2003), which solves the Stokes vector radiative transport (RT) equation 4.1 in a given atmospheric model, was used to compute normalized Stokes parameters I and V for atomic and molecular lines in LTE as well as the absolute continuum intensity. The input quantities used by the STOPRO code are as follows:

- Continuum optical depth $\log \tau$
- Height z [cm]

- Temperature T [K]
- Gas pressure P [$\text{g cm}^{-1} \text{s}^{-2}$]
- Electron pressure P_e [$\text{g cm}^{-1} \text{s}^{-2}$]
- Continuum absorption coefficient κ [g^{-1}]
- Mass density ρ [g cm^{-3}]
- Magnetic field strength $|\mathbf{B}|$ [G]
- Micro-turbulence velocity [$\text{cm} \cdot \text{s}^{-1}$]
- LOS velocity [$\text{cm} \cdot \text{s}^{-1}$]
- γ (angle between \mathbf{B} and LOS) [deg]
- χ (azimuthal angle of \mathbf{B}) [deg]

With the aim to obtain the quantities, which are not provided by the MURaM code, the MODCON subroutine was used. This code computes the ionization equilibrium for a given chemical composition, electron pressure P_e , continuum optical depth τ_λ and continuum absorption coefficient κ_λ .

Parameters of atomic and molecular transitions required as an input for the STOPRO routine are listed in Tables 4.1 and 4.2. Radiative transfer computations were carried out along rays passing through each surface pixel of the model separately and collected for further analysis with the LINE code, developed by Shelyag S. (2004).

The validity of the described MHD models, together with Stokes radiative transfer computations to reproduce and explain many observable features in the solar photosphere at disc center was shown by Shelyag et al. (2004), Shelyag S. (2004). In the present study, we extend this work to investigations of the center-to-limb variation of continuum intensity and Stokes profiles and to computations of CN molecular lines.

4.3 Center-to-limb variation

The position of any feature on the visible solar disc can be characterized in terms of its $\mu = \cos(\theta)$ value, where θ is the heliocentric angle of the feature varying from 0° at the disc center till 90° at the limb. With the aim to study the center-to-limb variation (CLV) of emitted radiation, i.e. the radiation coming from different disc positions, resulting from the MHD simulations we need to compute the atmospheric variables along rays inclined by the desired θ between the LOS and the normal of the visible solar surface (X-Y plane).

The geometry of the radiative transfer computations is illustrated schematically in Fig. 4.3. The grid of the MHD model corresponds to the white dots in Fig. 4.3. Red lines represent the emerging rays that are inclined by θ . The grid step along the LOS was fixed to $\Delta z=14$ km to keep the accuracy of subsequent RT calculations roughly the same as in the $\mu=1$ case. Thus the red points correspond to an inclined atmospheric box. The new Z' -axis of the model is parallel to the LOS. Some physical parameters of the model were linearly interpolated in a horizontal direction between neighboring points of the source. Since the density ρ , pressure P and internal energy E drop exponentially with height a logarithmic interpolation in a vertical direction was applied. The original MHD model has periodic boundary conditions in the horizontal direction, resulting in a repetition of the pattern with a period of 288 pixels. Therefore those rays which reach the edge of the model were shifted back by 288 pixels horizontally. Consequently the obtained box, used as an input for STOPRO, appears as an array of $288 \times 288 \times 100/\mu$ mesh points.

N	Variable	Description	Dimension
1	NLINES	Number of lines	[-]
2	WLREF	Reference wavelength (line center)	[Å]
3	WL1 WL2 NWL	wavelength grid $\lambda_i = WLREF - WL1 + i \frac{WL2 - WL1}{NWL}$, $i = 1, \dots, NWL$	[Å]
4	NATOM	Atomic number, e.g. Fe=26	[-]
5	ION	Ionization state. 1-neutral, 2=+, ION ≥ 3 is not allowed	[-]
6	ALOGGF	$\log_{10}(gf)$, where g - statistical weight of the lower level and f - oscillator strength	[-]
7	ABUND	Elemental abundance on a log scale, on which A(H) = 12.0	[-]
8	EPOT	Energy of the lower level	[eV]
9	IPOT1	First ionization potential $X \rightarrow X^+$	[eV]
10	IPOT2	Second ionization potential $X^+ \rightarrow X^{++}$	[eV]
11	RMASS	Atomic mass	[amu]
12	DMPEMP	Empirical damping enhancement factor, see Simmons & Blackwell (1982)	[-]
13	LANDEC	$\begin{cases} =0: g_u \text{ and } g_l \text{ are calculated from L,J,S} \\ =1: g_u \text{ and } g_l \text{ are taken from input (see 18)} \end{cases}$	[-]
14	CFGL	Configuration/term description of the lower level (from Kurucz CD-ROM)	[-]
15	$2S_l + 1$ L_l J_l	Standard term description of the lower level $^{2S_l+1}L_l$	[-]
16	CFGU	Configuration/term description of the upper level (from Kurucz CD-ROM)	[-]
17	$2S_u + 1$ L_u J_u	Standard term description of the upper level $^{2S_u+1}L_u$	[-]
18	GL	Landé factor of the lower level g_l (used if LANDEC=1, see 13)	[-]
19	GU	Landé factor of the upper level g_u (used if LANDEC=1, see 13)	[-]

Table 4.1: The description of atomic data, required by STOPRO.

In Fig. 4.4 an example of cuts along the LOS of the temperature are shown, once for a vertical viewing angle (corresponding to disc center) and once for an inclined viewing angle (corresponding to a location close to the limb).

N	Variable	Description	Dimension
1	NLINES	Number of line blends	[-]
2	WLREF	Reference wavelength (line center)	[Å]
3	WL1 WL2 NWL	wavelength grid $\lambda_i = WLREF - WL1 + i \frac{WL2 - WL1}{NWL}$, $i = 1, \dots, NWL$	[Å]
4	NMOLEC	Notation in the form of an integer comprising the numbers of the atoms in the molecule, e.g. 601=CH and 607=CN	[-]
5	ABUND1 ABUND2	abundances of the atoms comprising the molecule	[-]
6	BRANCH	branch name='R','P','Q'	[-]
7	IU, IL	upper and lower multiplet sublevels = 1,2,3,...	[-]
8	JL	lower rotational number = 0,1,2,3,... or 0.5,1.5,2.5,...	[-]
9	VU, VL	upper and lower vibrational levels = 0,1,2,3,...	[-]
10	FVV	band oscillator strengths	[-]

Table 4.2: The description of molecular data record, required by STOPRO.

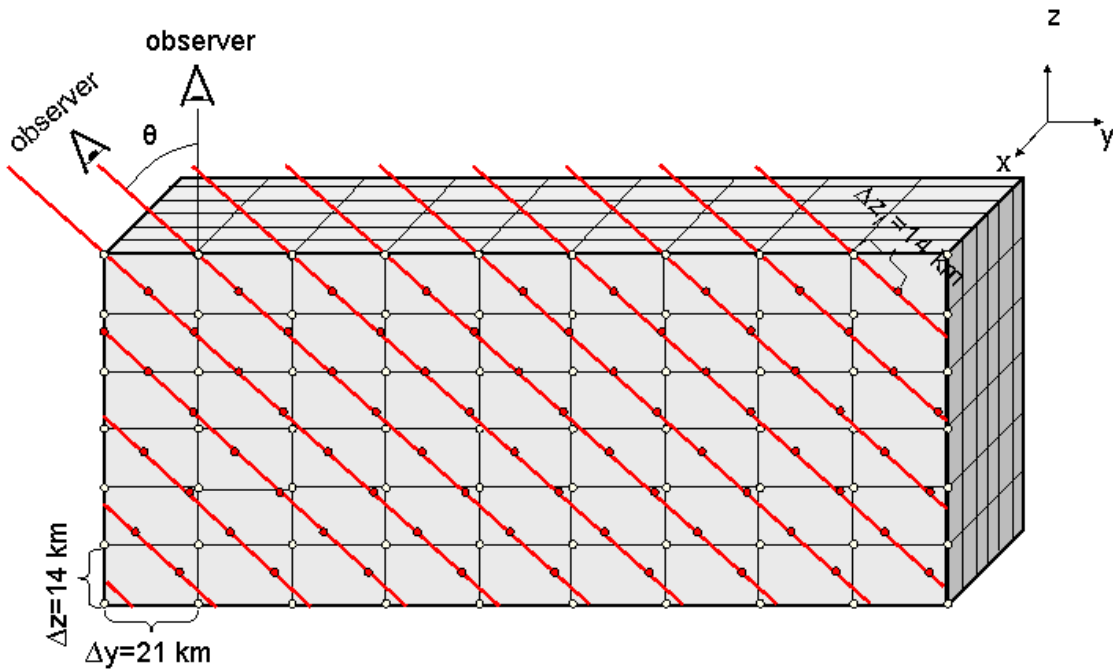


Figure 4.3: Skewing of the MHD model for a certain $\mu = \cos(\theta)$ value

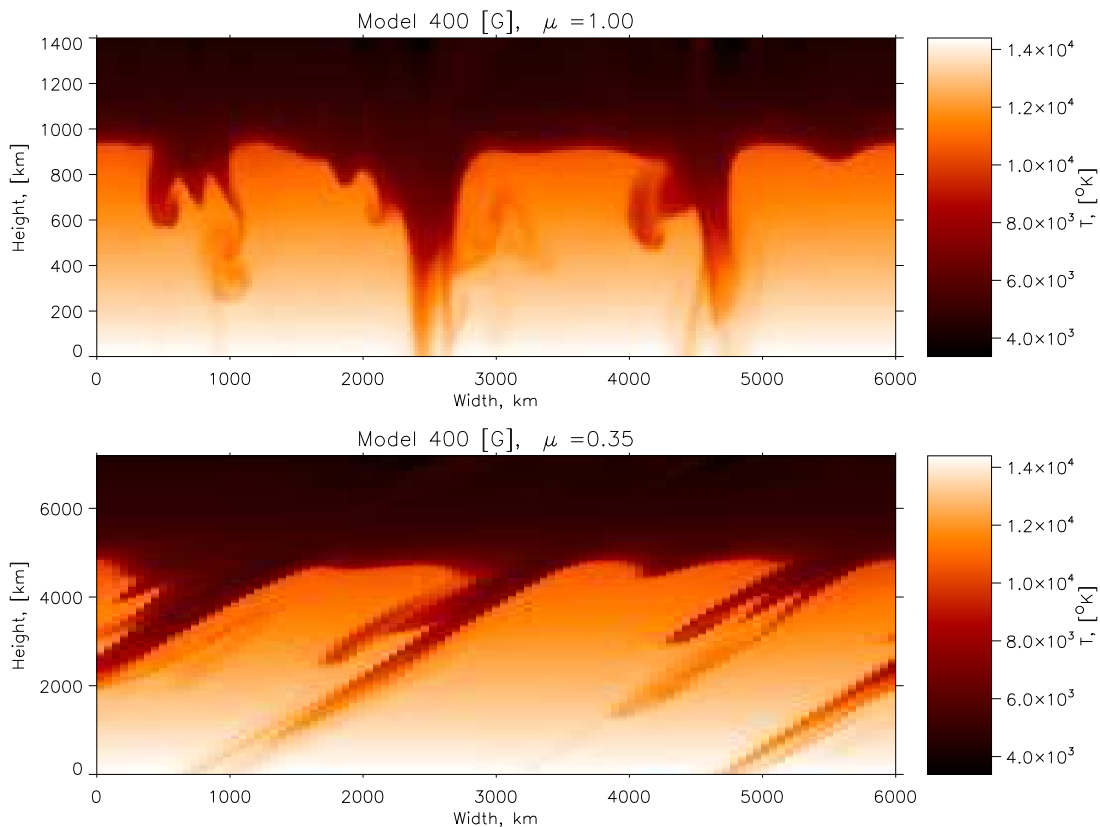


Figure 4.4: Example of a vertical cut of the temperature after interpolation to the LOS grid for $\mu=1.0$ and $\mu=0.35$

4.4 Results of radiative simulations at low resolution

In Fig. 4.5 a sample of computed intensity maps in the continuum at $\lambda = 676.8$ nm for snapshots with different amount of magnetic flux and at different μ are presented. The brightness of each image, assigned to a certain model, was normalized to the mean intensity at disc center. In the following section we will discuss the brightness properties of simulated images depending on B and μ .

4.4.1 Limb darkening

A first direct piece of evidence for the existence of a temperature gradient in the solar atmosphere is the limb darkening effect. At disc centre the Sun appears brighter as compared to its intensity near the limb (see Fig. 4.5). In the first case one looks deeper into the photosphere where the gas is hotter while when observing near the limb we sample shallower depths. We have calculated the continuum intensity at $\lambda = 676.8$ nm for a 0 G model, assumed to represent the quiet Sun, and for the other models in the range of $0.2 \leq \mu \leq 1.0$ with a 0.1 step in μ .

Neckel & Labs (1994) reported measurements of the limb darkening effect in the continuum in a wide spectral range observed at the National Solar Observatory/Kitt Peak, utilizing the McMath Solar Telescope with high accuracy. They derived coefficients of

4 Radiative MHD Simulations

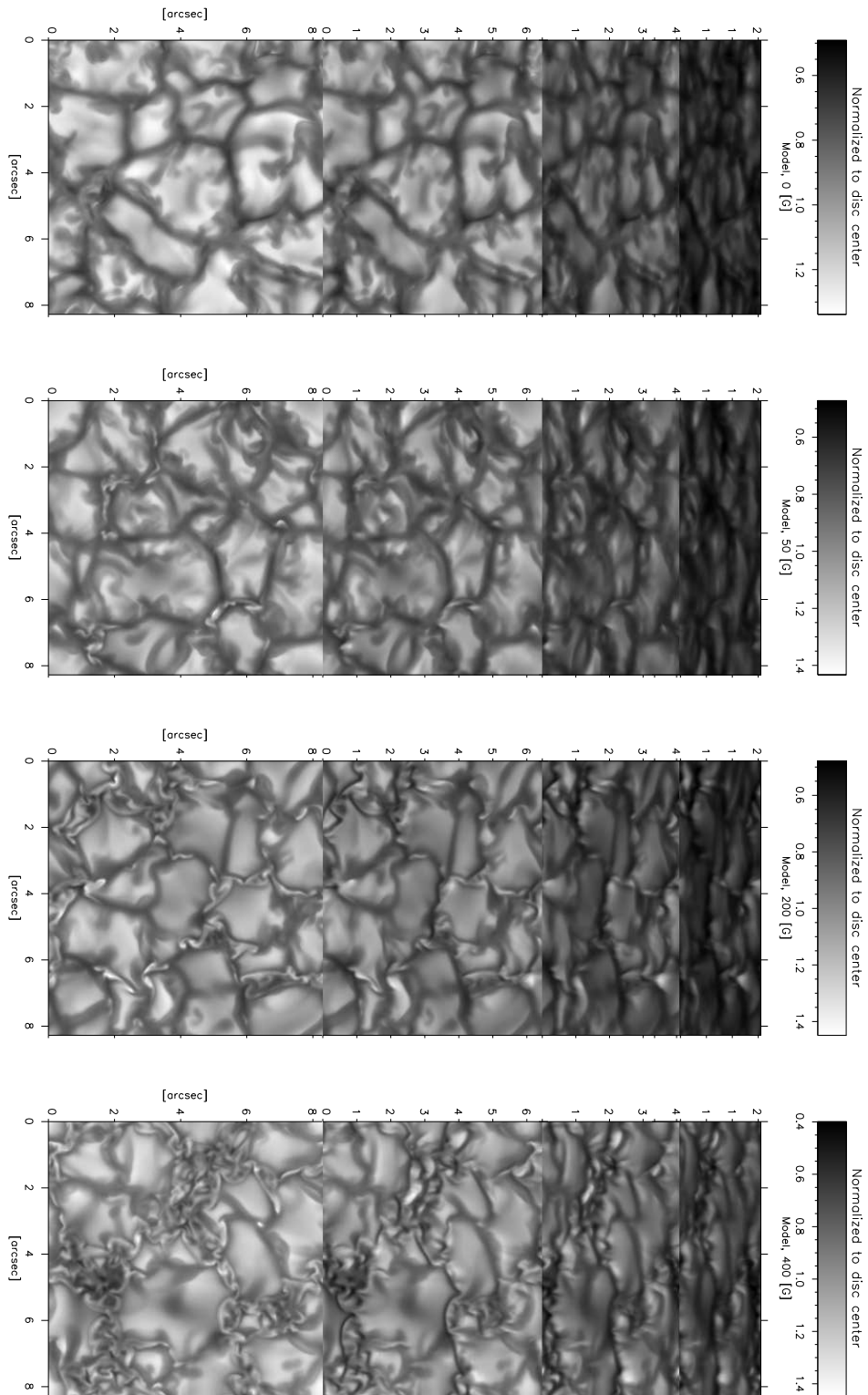


Figure 4.5: 2-D continuum maps at $\lambda = 676.8$ nm computed for 0 G, 50 G, 200 G and 400 G models at (from left to right) $\mu=1.0$; 0.8; 0.4 and 0.2. For each model, the brightness of each image was normalized to that at disc center. The effect of the limb darkening is evident.

fifth-order polynomial fit by the r.m.s. method to observed limb darkening profiles:

$$\frac{I_\lambda(\mu)}{I_\lambda(\mu=1)} \equiv P_5(\mu) = A_0 + A_1 \cdot \mu + A_2 \cdot \mu^2 + A_3 \cdot \mu^3 + A_4 \cdot \mu^4 + A_5 \cdot \mu^5 \quad (4.18)$$

Here A_0, \dots, A_5 are wavelength-dependent coefficients. The 5-th order polynomials were chosen, because this type of function had provided the best representation in the former reductions by Pierce & Slaughter (1977) and Pierce et al. (1977). Later the same authors argued, however, that these 'purely mathematical' fits are not the functions with the optimum physical reliability (Kourganoff 1949), small errors in the coefficients may cause huge, unrealistic fluctuations in the corresponding τ -dependence of the source function. Therefore, in order to obtain a per se 'reasonable' τ -distribution of the source function, they provided 'physically realistic' fits to their data and described limb darkening of intensity by the following function:

$$\frac{I_\lambda(\mu)}{I_\lambda(\mu=1)} \equiv L_n(\mu) = c_0 + (1 - c_1) \mu + \sum_{i=2}^n c_i \psi_i(\mu). \quad (4.19)$$

A description of the deviation functions ψ_j and the determination of correct wavelength-dependent coefficients c_j can be found in Neckel (1996). Although the question which of two functions, L_3 or L_4 , is 'more reliable' was left open, they preferred L_3 .

In Fig. 4.6 CLVs of simulated mean intensity for 4 different snapshots of each MHD model with average field strength of 0 G, 50 G, 200 G and 400 G are presented. The intensity of each model was normalized to the average intensity of that model at $\mu = 1$. In the same plot polynomial approximations P_5 , L_3 and L_4 linearly interpolated to $\lambda = 676.8$ nm from the data provided by Neckel (1996) for $\lambda = 669.400$ nm and $\lambda = 700.875$ nm are also shown. Our simulations conform with the well known fact that the continuum intensity CLV displays various slopes, depending on the amount of magnetic flux (e.g. Frazier 1971, Topka et al. 1997, Ortiz et al. 2002). The most 'bright' atmosphere in this presentation corresponds to the 400 G case and is 1.1 times brighter at $\mu=0.2$ as compared with the 'darkest' model. For $\mu \approx 0.6$ the 50 G model has a very good coincidence with observations, whereas the 200 G model is 1.5% brighter and the HD model is 0.7% darker than observations. With decreasing μ the observed CLV lies systematically above the 50 G case, lying closer to the 200 G model at $\mu = 0.2$. From the work of Khomenko (2005) & Trujillo Bueno et al. (2004) we expect the best correspondence with the 50 G (or an even weaker field) model. There are different possible reasons for the dependence.

- The quiet Sun contains more magnetic flux at higher layers than suggested by the models.
- The thermal structure of the models is slightly different from the real Sun. At $\mu = 0.2$ the 50 G model is 2% too dark, implying a too low temperature near $\tau = 1$ by around 120 °K.
- Neckel & Labs (1994) included some plage in their measurements. This would have the largest effect at small μ and make their measured curve too bright there.

In Table 4.3 the coefficients of the 5-th order polynomial approximation based on the least-squares minimization method of the continuum intensity dependence on μ are listed.

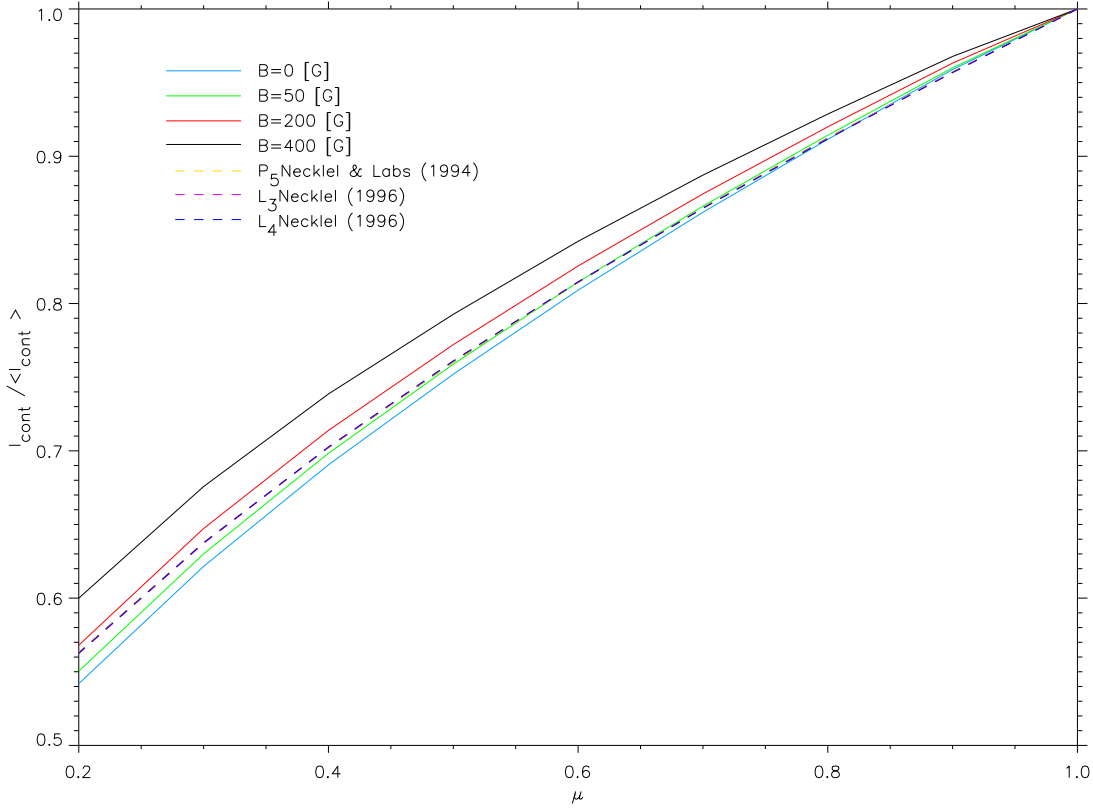


Figure 4.6: Limb darkening in continuum at $\lambda = 676.8$ nm computed for 0 G, 50 G, 200 G and 400 G models and corresponding 5-th order polynomial estimation P_5 and polynomials L_3 , L_4 linearly interpolated to $\lambda = 676.8$ nm from coefficients at $\lambda = 669.400$ nm and $\lambda = 700.875$ nm provided by Neckel & Labs (1994), Neckel (1996).

Model	A_0	A_1	A_2	A_3	A_4	A_5
0 G	0.33843	1.20224	-1.04388	0.60276	0.04617	-0.14566
50 G	0.34148	1.26031	-1.25274	0.92726	-0.21474	-0.06152
200 G	0.35373	1.31571	-1.42500	1.07999	-0.25095	-0.07341
400 G	0.38868	1.32212	-1.56988	1.29463	-0.39893	-0.03654
Neckel's P_5 $\lambda = 676.8$ nm	0.35437	1.34721	-1.96545	2.58538	-1.86123	0.53972

Table 4.3: Coefficients of 5-th order polynomial fit to simulated CLVs for 0 G, 50 G, 200 G and 400 G models at $\lambda = 676.8$ nm and those derived by Neckel & Labs (1994) for the same wavelength.

Additionally, for reference, the coefficients estimated by Neckel & Labs (1994) are also given.

Our simulations showed that Neckel's continuum limb darkening at $\lambda = 676.8$ nm can be roughly represented by an average of those computed for HD and 200 G models. Since the 200 G model could represent the network and weak plage, this does not appear totally impossible, although we expect a lower filling factor for this than 50%.

4.4.2 CLV of intensity contrast

In the previous section it was shown that the limb darkening effect is different for the various models.

In Fig. 4.7 individually normalized continuum images computed for various models and at different heliocentric angles are presented. The models which possess stronger magnetic flux concentrations are brighter near the limb than models with less magnetic field. This suggests, that small-scale concentrations of magnetic flux influence the thermal structure of the atmosphere in such a way that at low μ hotter parts become visible (see also Section 4.6.1).

In Fig. 4.8 the CLVs of continuum intensity deviations from the quiet Sun, i.e. 0 G model, for 11 different snapshots are presented. Each intensity assigned to a certain μ is the average over 1, 2, 4 and 4 snapshots of HD, 50 G, 200 G and 400 G models, respectively and is related to the non-magnetic case as follows:

$$C_{\lambda}(\mu) = \frac{I_{\lambda}(\mu) - I_{\lambda,0}(\mu)}{I_{\lambda,0}(\mu)} \quad (4.20)$$

However, the correctness of such a comparison is limited by the brightness distribution over the granulation in individual snapshots, which can fluctuate significantly from one snapshot to another. Nevertheless this analysis showed, that all magnetic models deliver less radiation at the disc center than the HD ones. The 400 G model is significantly darker at the disc center, meaning that the magnetic flux is so big, that it causes formation of larger and darker flux concentrations. The extreme cases of such flux concentrations appear as micropores (Vögler 2003), which are easy to see at (4.7,1.8) arcsec or (6,7) arcsec positions in Fig. 4.7 bottom-left. Therefore this model becomes as bright as the HD one only at $\mu=0.63$ whereas 50 G and 200 G models have a brightness crosstalk at $\mu=0.82$ and $\mu=0.92$ respectively. At $\mu \leq 0.41$ the 400 G snapshot displays the largest contrast and would contribute appreciably to the total solar irradiance, when such magnetic features were located near the limb.

As shown in Fig. 4.9 the RMS contrasts, computed as

$$C_{rms} = \sqrt{\left(\sum_{i=0}^N (I_i - \langle I \rangle)^2 \right) / N}, \quad (4.21)$$

of synthesized continuum images depend on the μ and magnetic field. At the disc center 0 G, 50 G and 400 G images have similar rms contrast, due to high amount of intensity gradients at the intergranular dark lanes and 'dark' flux tubes. The 200 G image shows a high number of photospheric bright points, which slightly reduces the total rms contrast by filling in the dark intergranular lanes. Since the τ scale shifts upwards when approaching the limb and due to the effect of reversed temperature in granules and intergranular lanes in the upper photospheric layers the observed continuum image for the 0 G case becomes smoothed and consequently its rms contrast is decreased dramatically. However, even at $\mu = 0.2$ the normal granulation pattern is still visible. The more magnetic flux penetrates the MHD box the shallower is the corresponding CLV of the rms contrast. The increase of rms due to the appearance of high contrast faculae competes with the decreasing rms contrast of non-magnetic features. In the 400 G case the rms contrast even increases with

4 Radiative MHD Simulations

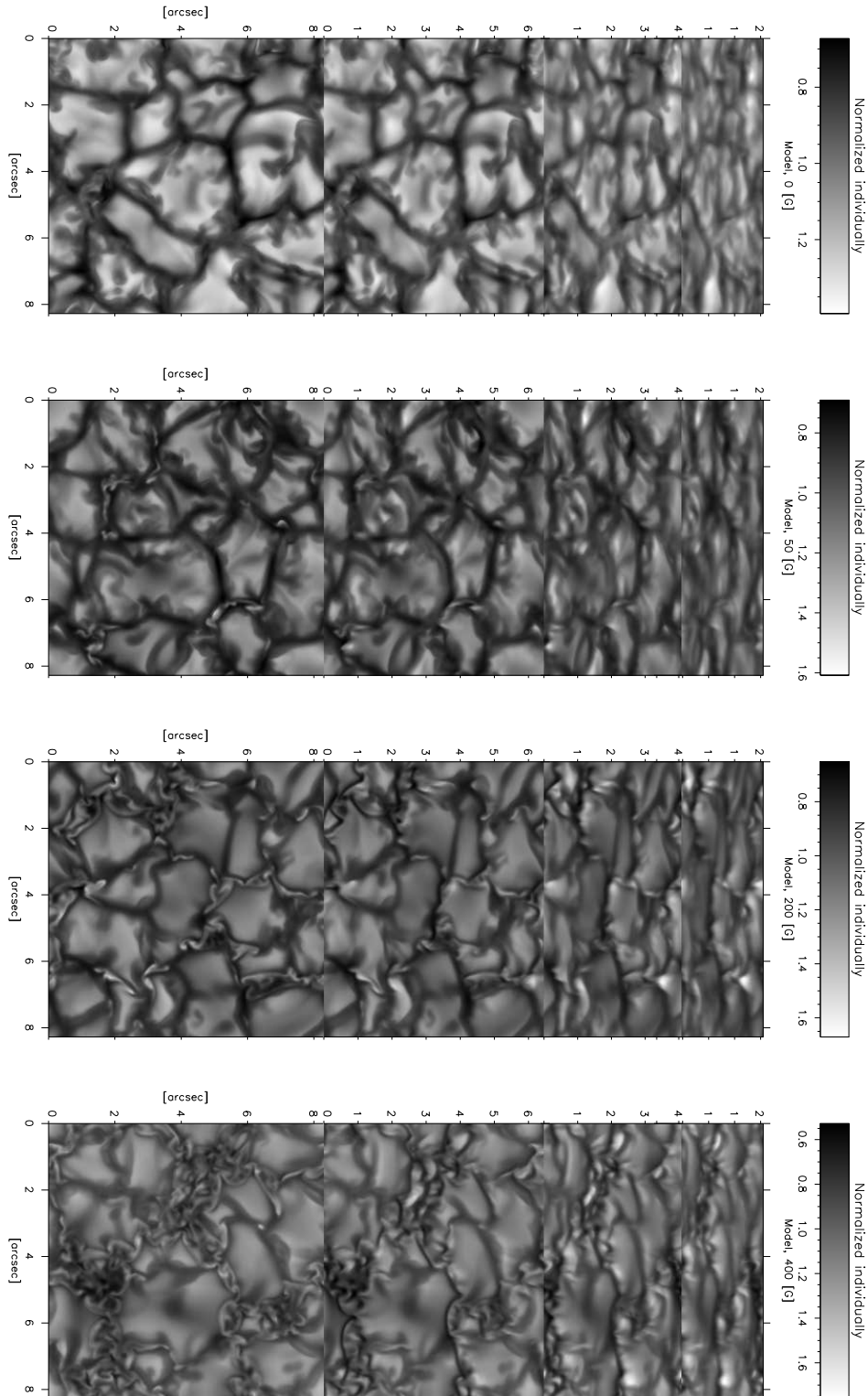


Figure 4.7: 2-D continuum maps at $\lambda = 676.8$ nm computed for 0 G, 50 G, 200 G and 400 G models at $\mu=1.0$; 0.8; 0.4 and 0.2. Each image (i.e. each model at each μ) was normalized to its mean separately. The appearance of faculae for magnetically active snapshots is evident.

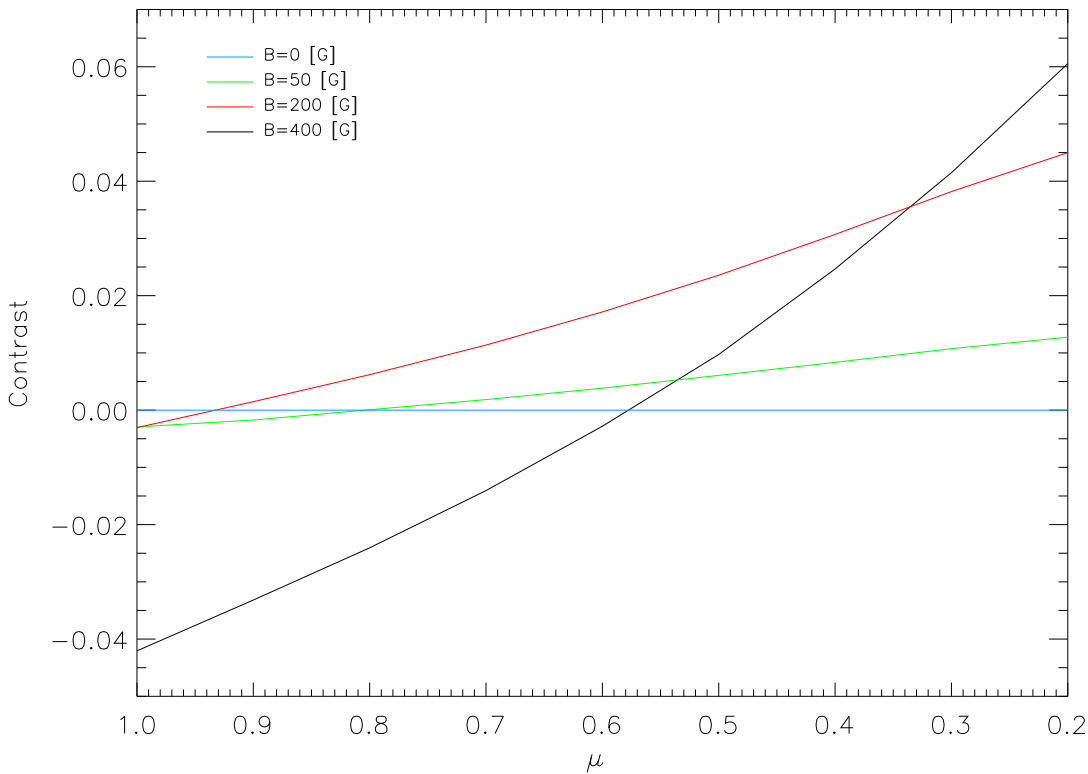


Figure 4.8: Contrast of continuum intensity relative to quiet Sun versus μ value calculated for 0 G, 50 G, 200 G and 400 G models.

μ due to the high number of facular brightenings visible near the limb and drops only below $\mu=0.3$

In the next section some important aspects of existing extraterrestrial solar observations will be touched in order to provide an adequate comparison with results of our simulations.

4.5 MDI observations

The most appropriate observations of the Sun in order to investigate its irradiance over the whole disc over a long period of time are measurements made by the Michelson Doppler Imager (MDI). The MDI instrument is a magnetograph installed on board of the SOHO spacecraft devoted to investigate the structure and dynamics of surface magnetic field and velocity in the Sun (Scherrer et al. 1995). This instrument makes it possible to obtain full disc images of the Sun on a 1024×1024 pixels CCD camera, which corresponds to a 2×2 arcsec² pixel size. Two tunable Michelson interferometers allow MDI to record very narrow-band filtergrams centered at five wavelength positions near the Ni I absorption line at 676.8 nm, equally spaced by 75 mÅ. In Fig. 4.10 the transmission profiles of the five filters labeled as F_0 , F_1 , F_2 , F_3 and F_4 as well as the Ni I line profile, taken from the FTS atlas (Brault & Neckel 1987), are presented. F_0 corresponds to the nearby

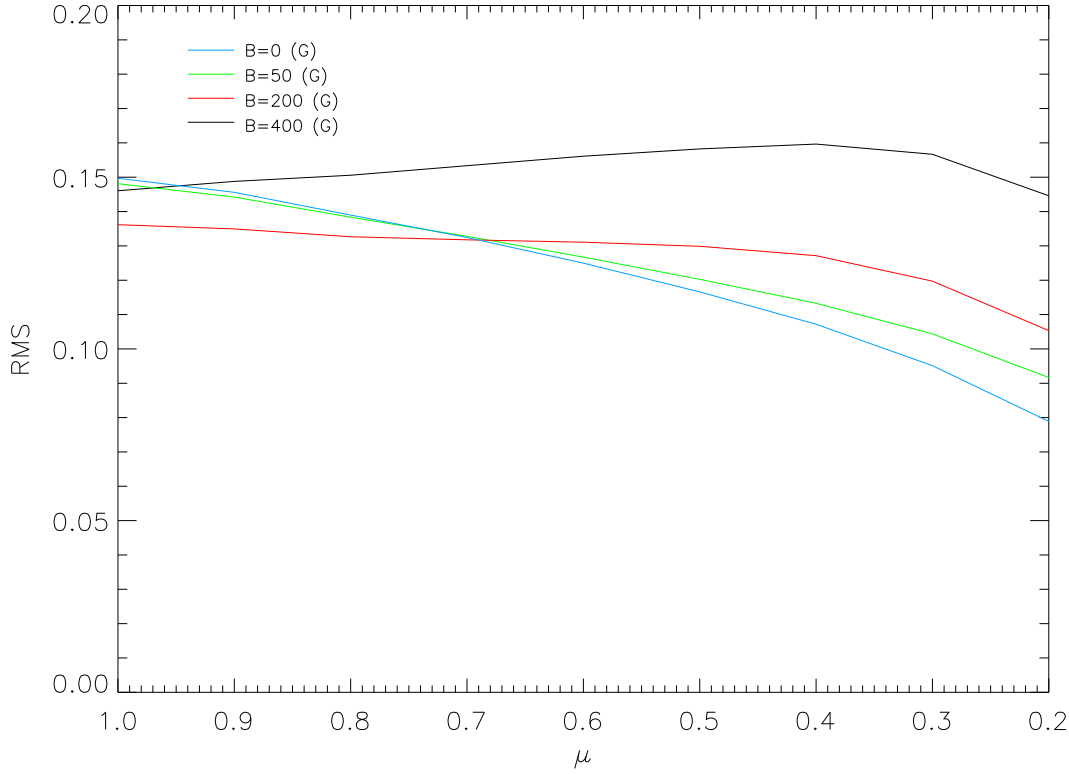


Figure 4.9: RMS contrast dependence on the μ value calculated for 0 G, 50 G, 200 G and 400 G models.

continuum, F_1 and F_4 are centered on the wings and F_2 and F_3 are centered about the core of the center-of-disc Ni I line. From the filtergrams, MDI obtains the following observables: continuum intensity, line depth, longitudinal magnetic field, LOS velocity and limb position. However, due to limitations in the telemetry rate to SOHO not all these parameters are available for a given data set. MDI derives an estimate of the LOS velocity from a ratio of differences of filtergrams F_1 through F_4 :

$$\alpha = \frac{I_1 + I_2 - I_3 - I_4}{I_1 - I_3}, \text{ if numerator} > 0$$

$$\alpha = \frac{I_1 + I_2 - I_3 - I_4}{I_4 - I_2}, \text{ if numerator} \leq 0 \quad (4.22)$$

where I_1, \dots, I_4 are intensities detected through the F_1, \dots, F_4 filters.

With the help of a 15-bit lookup table (see Fig. 12 in Scherrer et al. (1995)), constructed from their simulations, MDI calculates the LOS Doppler velocity. They expect the range of α to be limited to ± 2 which corresponds to a velocity range of ± 4000 m/s.

The continuum intensity was computed using all five filtergrams in order to cancel systematic errors introduced by Doppler shifts caused by any solar velocity:

$$I_c = 2 \cdot I_0 + I_{depth}/2 + I_{aver}, \quad (4.23)$$

where $I_{depth} = \sqrt{2 \cdot [(I_1 - I_3)^2 + (I_2 - I_4)^2]}$ is the line depth and I_{aver} is the average over I_{1-4} . Thus the resultant I_c is believed to be free from Doppler crosstalk at the 0.2%

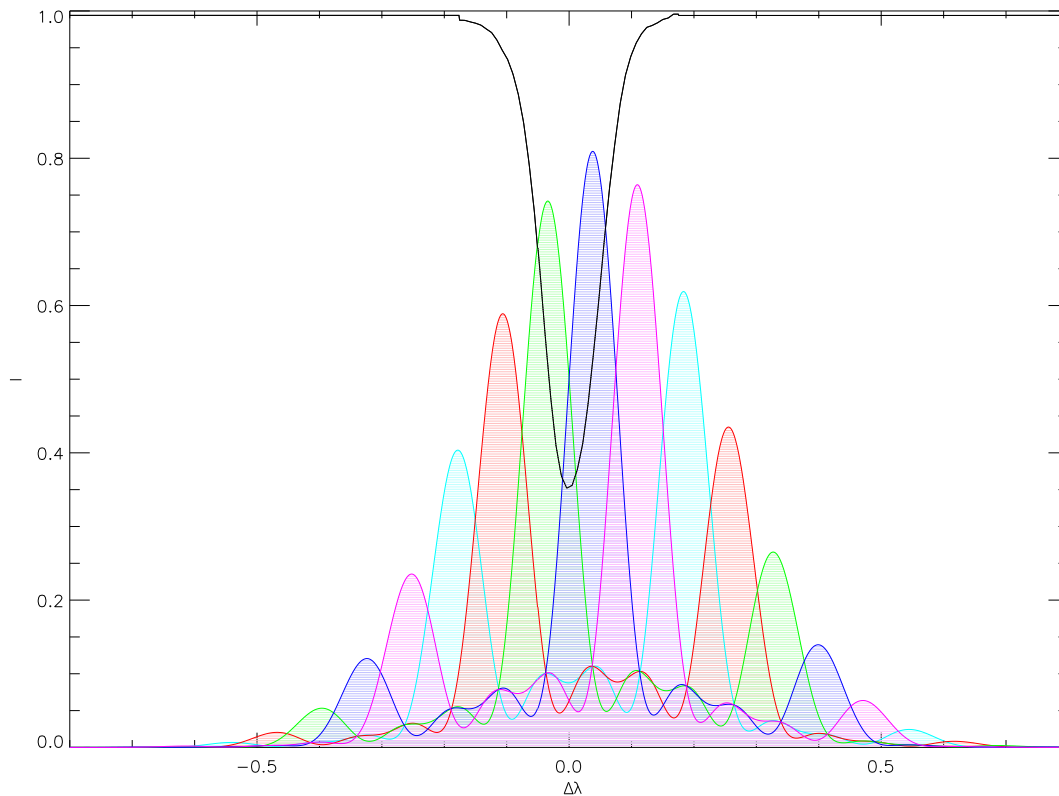


Figure 4.10: Filter profiles for the F_0 , F_1 , F_2 , F_3 and F_4 filters used in observations with MDI.

level. The longitudinal magnetogram is constructed by measuring the Doppler shift separately in right and left circularly polarized light, which is equivalent to a measurement of the Zeeman splitting via some sort of center-of-gravity method:

$$B = \frac{V_{right} - V_{left}}{2.84}, \text{ [G]}, \quad (4.24)$$

where V_{left} and V_{right} are measured velocities in circularly left and right polarized light respectively. B is roughly proportional to the LOS component of the magnetic field averaged over the resolution element.

The main advantages of these measurements as compared with ground-based observations are:

- seeing effects due to the Earth's turbulent atmosphere are avoided,
- the 20-min averaged MDI magnetograms have a reasonably low noise level,
- the characteristics of the instrument and obtained data sets are well known and stable,
- magnetograms and continuum intensity images are obtained regularly by the same instrument with exactly the same spatial resolution.

In the framework of the present investigation, analysis of the full disc magnetograms and continuum intensity images obtained by MDI at different disc positions carried out by Ortiz et al. (2002) are of special interest. They measured the MDI continuum contrast of photospheric bright features as a function of heliocentric angle and magnetogram

signal. The main disadvantage of such a study is the quite poor spatial resolution of MDI observables in its full disc mode.

4.5.1 Radiative simulations

In order to be able to compare the results of the CLV computations using 3-D MHD models, presented in Section 4.4.2, with observations, we need to reproduce MDI measurements taking into account the technical aspects of that instrument. For the MDI measurements the Ni I spectral line was used to measure the magnetic field. In order to be consistent we also compute this line for each snapshot an μ value for which the continuum intensity is determined.

Wavelength [nm]	Transition	E_u [eV]	E_l [eV]	g_{eff}	χ_e [eV]	$\log(gf)$
676.7768	$z^3P^0 - a^1S$	3.6576	1.8262	1.426	1.826	-2.170

Table 4.4: Atomic transition parameters for the Ni I line used for the radiative diagnostics.

The main properties of the corresponding transition are given in Table 4.4 (Bruls 1993). The polarized radiative transfer equations for the Ni I line through the MHD models with averaged magnetic field in the range of 0-400 G for a heliocentric angle from $\mu=1.0$ to $\mu=0.2$, with a grid-step of 0.1 were solved by means of the MODCON and STOPRO routines. To improve the statistics, 1,2,4 and 4 snapshots of 0 G, 50 G, 200 G and 400 G models, which correspond to different moments of time of the MHD model evolution, respectively, were taken. The time step was around 5 min which is a reasonable interval to obtain relatively independent 2-D configurations of the granulation and other features. Additionally for $\mu \neq 1$ each snapshot was analysed from four mutually perpendicular directions in its X-Y plane, which allows to include in our investigation geometrical inhomogeneities of magnetic features and hence make it even more statistically weighted. Thus our analysis comprised 44 different snapshots in total covering an area of 54.9×54.9 arcsec² at disc center of the Sun. The products of RT computations were continuum intensity I_c at $\lambda = 676.8$ nm and Stokes profiles S_I and S_V for the Ni I spectral line. These quantities were smeared down to the 2×2 arcsec² spatial resolution of MDI. To compute MDI-like Doppler shifts and MDI-like continuum, simulated spectra were multiplied with the MDI filter profiles (see Fig. 4.10). The resultant filtergrams I_{0-4}^{sim} were used to produce MDI-like observables. The LOS component of the magnetic field B was calculated using formula 4.24 :

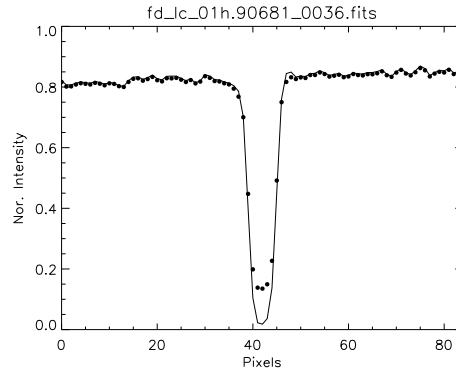
$$B_z = \frac{\Delta\lambda}{4.67 \cdot 10^{-13} \cdot g_{\text{eff}} \cdot \lambda^2} \equiv \frac{V(\alpha[S_I + S_V]) - V(\alpha[S_I - S_V])}{2.84}, \quad (4.25)$$

where g_{eff} is the effective Landé factor of the transition, defined as

$$g_{\text{eff}} = \frac{1}{2}(g_l + g_u) + \frac{1}{4}(g_l - g_u)(J_l(J_l + 1) - J_u(J_u + 1)). \quad (4.26)$$

Here the g_u , g_l , J_u and J_l are the Landé factors and total angular momenta of the upper and lower states of the transition, respectively.

Figure 4.11: Stray light during a mercury transit across the solar disc observed with MDI in 2003. The dots represent the observed continuum intensity which is non-zero at Mercury disc center. This plot has been kindly provided by S. Mathew (private communication)



The observed signal of the longitudinal magnetic field drops down to 0 G at the limb, even though the local magnetic field is non-zero. This is a consequence of the property of magnetograms to be sensitive only to the line-of-sight component of the magnetic field whereas the magnetic vector \mathbf{B} of facular fields is roughly perpendicular to the solar surface. Thus, to compensate for this we have considered B/μ instead of B .

The MDI instrument possesses a certain amount of stray light, which has been estimated by Mathew et al. (in preparation). They analysed the Mercury transit across the solar disc recorded by MDI in 2003 and produced a plot presented in Fig. 4.11. From this graph we obtain that MDI measures intensities with about 18% contribution from scattered light. This quantity affects mainly the continuum intensity measurements which reduces the calculated contrasts. Mathew has estimated the convolution function which is needed to fit the amount of stray light in MDI observations. This function is the sum of four components, three Gaussians and one Lorentzian:

$$f(r) = a_1 e^{-(r/b_1)^2} + a_2 e^{-(r/b_2)^2} + a_3 e^{-(r/b_3)^2} + \frac{1 - a_1 - a_2 - a_3}{r^2 + b_4^2}, \quad (4.27)$$

where a_1 , a_2 and a_3 are the weight for the Gaussian functions, b_1 , b_2 and b_3 are the widths of the Gaussians and b_4 is the width of the Lorentzian. We have used the function $f(r)$ with the weight and width parameters obtained by Mathew, which give the best fit to their observations, to convolve with the simulated MDI-like continuum intensity I_c^{STOPRO} , i.e. $I_c^{MDI-like} = I_c^{STOPRO} \otimes f(r)$.

Following Ortiz et al. (2002) the continuum contrast of the faculae in each resolution element was defined as:

$$C_{fac} = \frac{I_c(x, y) - \langle I_c^{qs}(\mu) \rangle}{\langle I_c^{qs}(\mu) \rangle}, \quad (4.28)$$

where $\langle I_c^{qs}(\mu) \rangle$ is an averaged quiet Sun continuum intensity for a given heliocentric angle.

4.5.2 Results of simulations and comparison with MDI observations

In this section we study the simulated faculae and network contrast dependence on μ and the corresponding magnetic field signal. A comparison of computed data with observations will be presented.

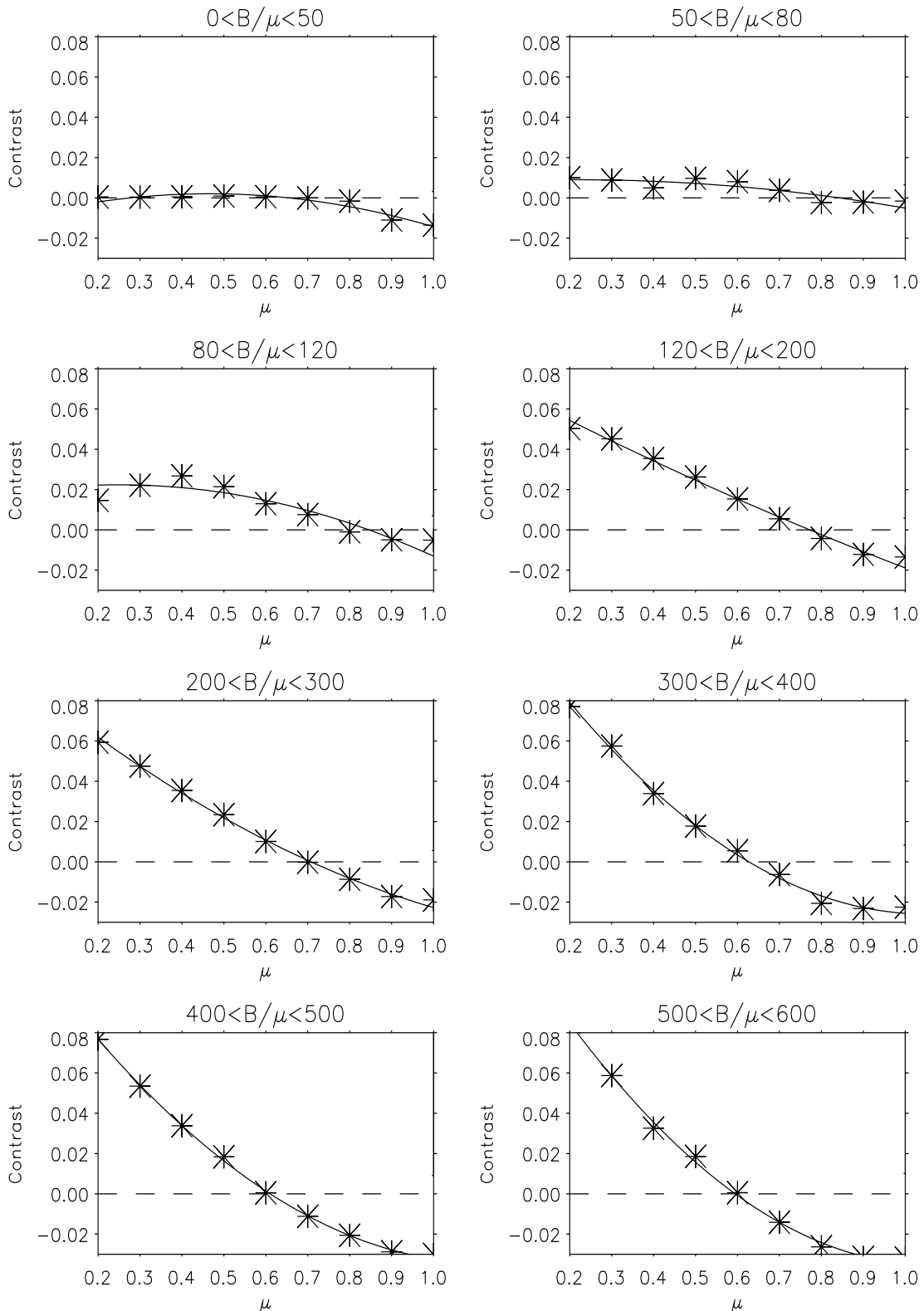


Figure 4.12: Computed center-to-limb variation of MDI-like continuum contrast from MHD simulation. The stars are binned values based on data taken from the MHD models with average vertical fields of 0 G, 50 G, 200 G and 400 G at the solar surface. The B/μ values have been obtained from the longitudinal MDI-like magnetogram signal as described in the text.

We present two plots in analogy to research by Ortiz et al. (2002). Fig. 4.12 displays the computationally produced MDI-like continuum contrast C_{fac} of the faculae as a function of the computed MDI-like magnetogram signal divided by μ , i.e. B/μ . The B/μ values have been binned into eight intervals from the threshold level of 0 G to 600 G, although these intervals of magnetic field do not contain an equal number of data points. In Fig. 4.12 each data point represents an average C_{fac} binned over all computed contrasts for a given μ and B/μ range. Data points from different models enter into a given frame, since the B/μ assigned to a certain data point is obtained from the magnetogram signal consistently computed for each grid point as described in Section 4.5.2. A least-squares quadratic fit to the data points is depicted in Fig. 4.12 as black solid lines.

The various panels in Fig.4.12 reveal significantly different CLV behavior of the contrast. At the disc center and in its immediate vicinity small C_{fac} is produced by regions with low magnetic flux (e.g. quiet areas), whereas approaching the limb the contrast of active region faculae (large magnetic flux) dominates. Network features (see top-left panel in Fig.4.12) show low contrast, which increases from the minimum value -0.005 at the disc center up to 0 near the limb, whereas a very steep CLV of the contrast was detected at high magnetic signals ($400 \text{ G} < B/\mu < 500 \text{ G}$ and $500 \text{ G} < B/\mu < 600 \text{ G}$). Intermediate cases reveal the progressive increase of the contrast towards the limb and an increasingly pronounced CLV. The stronger the B/μ the lower the C_{fac} at the disc center, which for $B/\mu > 200 \text{ G}$ appears negative. This general behaviour of the computed curves is in good qualitative agreement with the observations of Ortiz et al. (2002) and with results presented in Section 4.4.2. However one remarkable feature of the obtained CLV curves is their property of steadily increasing towards the limb from magnetogram signals of $B/\mu > 120 \text{ G}$. Thus the position μ_{max} characterizing the peaks of the contrast corresponds to 0.46 and 0.2 for the first two B/μ intervals and lies at $\mu < 0.2$ for the others. This fact is partly in discordance with the observational results of Ortiz et al. (2002), where the μ_{max} was measured in a range from 1. to 0.2 in all concerned intervals $B/\mu < 500 \text{ G}$. Possibly the 400 G models which mainly contribute to the CLV in the last three bins are hotter than the real photosphere. It may also be that a better treatment of the stray light is needed to improve the correspondence. Another possibility is that there could be a possible error in the continuum intensity determination in MDI observations made near the limb at low latitudes. Due to the rotation of the Sun the observed Ni I line gets an additional Doppler shift such that the filter F_0 does not lie in the nearby continuum but at the wing of the line. Consequently Eq. 4.23 gives lower continuum intensity than expected. This effect becomes important near the limb at low latitudes where v_{rot} is big. Numerical simulations of this effect to estimate the order of the error of continuum intensity determination should be carried out. Another possible explanation for the discrepancy with the observations lies in the rather limited statistics of the simulations compared with the observations. The visible surface of the model decreases proportionally to μ and hence near the limb the number of simulated points corresponding to the MDI pixel size of $2 \times 2 \text{ arcsec}^2$ is extremely small.

In Fig. 4.13 the contrast as a function of B/μ , for 9 disc positions from $\mu=1.0$ to $\mu=0.2$ is presented. The centres of the μ -bins in a similar plot made by Ortiz et al. (2002) roughly correspond to our μ grid. Again, the second order polynomial fit was used to visualize the character of the computed dependences on B/μ . In Fig. 4.13 all data points corresponding to 50 G, 200 G and 400 G models are designated with the green, red

4 Radiative MHD Simulations

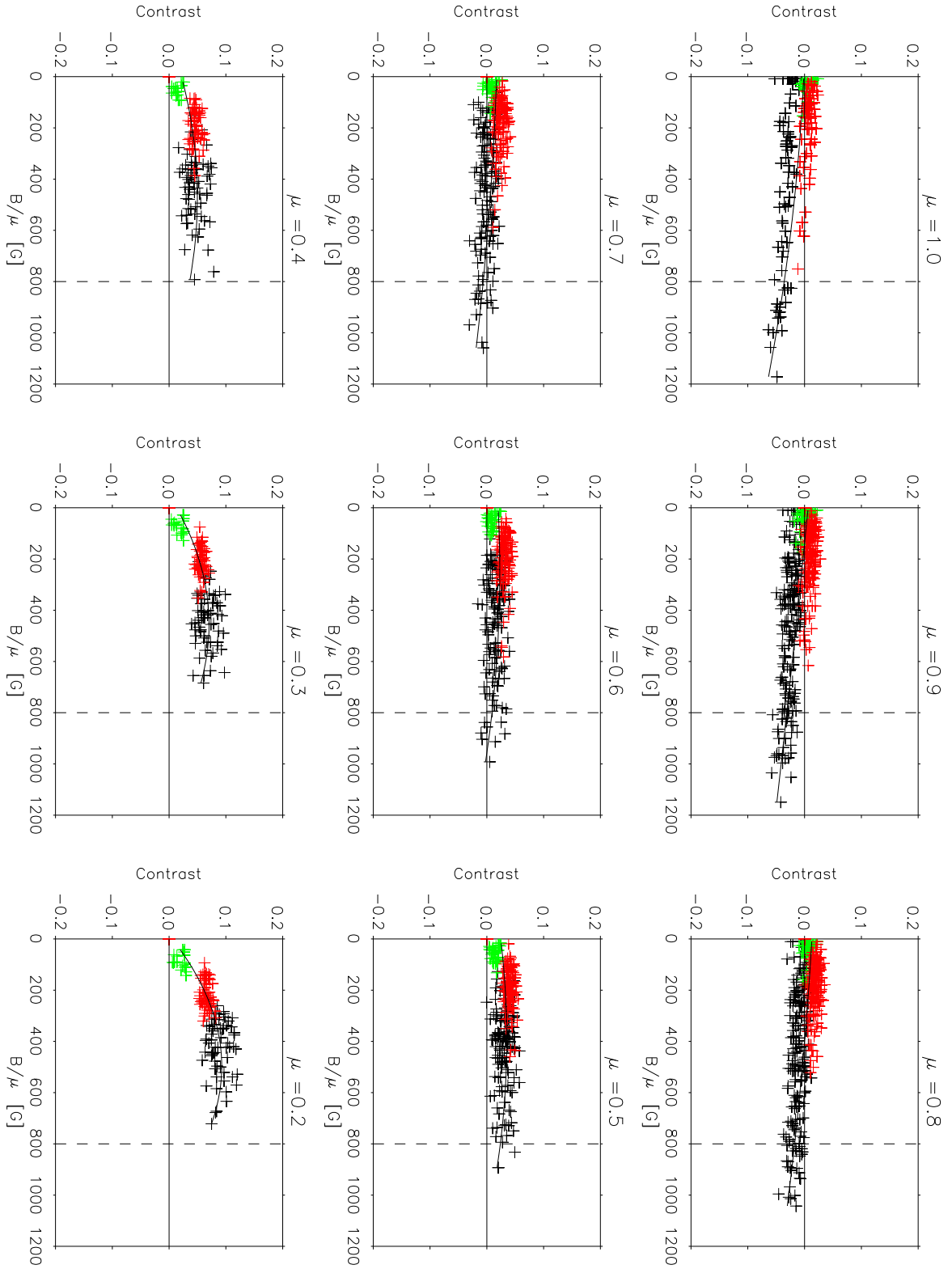


Figure 4.13: Computed center-to-limb variation of continuum contrast using 0 G, 50 G, 200 G and 400 G MHD models depending on the longitudinal "quasi" MDI magnetic field strength.

and black colors, respectively. We have not binned 40 data points with neighbouring B/μ values together, as was done by observers, since we have far fewer points. We also wanted to show the true scatter. Nevertheless, a certain overcrowding of the data points in our plots is present. This figure shows that initially, for $\mu \leq 0.6$, the contrast increases with B/μ before decreasing again. The range of computed magnetogram signals was widened up to 1200 G, since many areas deliver signals stronger than 800 G. This may have to do with the lack of proper scattered light treatment in the computations. The decreasing of the contrast continues with increasing B/μ also for $B/\mu > 800$ G where many of the data points correspond to micropores and dark magnetic structures. This circumstance agrees with the prediction by Ortiz et al. (2002). Note, however, that the observed data sets include the even stronger magnetic field concentrations, i.e. pores and sunspots, which were excluded in the analysis of Ortiz et al. (2002). Near the disc center, i.e. at $1.0 < \mu < 0.7$, the initial increase is not detected, so that the contrast decreases with magnetic field for all B/μ values. In contrast, at $\mu \leq 0.6$ the initial increase is clearly visible and the B/μ value at which the contrast has its maximum, $(B/\mu)_{max}$ shifts towards higher B/μ with decreasing μ . Points with large B/μ show negative contrast at $\mu=1.0$ while at the limb almost all computed contrasts are positive.

The range of the simulated magnetogram signals stretches even beyond the 1200 G level near the disc center. Gradually with decrease of μ the detected range of B/μ converges down to 740 G at $\mu=0.2$. We expect, that at even smaller μ values the maximum of measured longitudinal magnetic field strength will continue decreasing. On the one hand this happens due to the decrease of Stokes S_V near the limb since the Ni I line is then formed higher in the atmosphere where the magnetic flux is lower. On the other hand, as proposed by Van Ballegooijen (1985) and shown by Solanki et al. (1998) in their CLV simulations of the plane-parallel models of a flux tube, observed at an angle of the axis of an isolated thin flux tube, the amplitude of S_V should be much lower than in the plane-parallel case. Highly inclined rays, i.e. at low μ , pass through flux tubes and the intermediate non-magnetic gas where the polarized signal S_V is greatly reduced due to absorption (Audic 1991).

μ	1.0	0.9	0.8	0.7	0.6	0.5	0.4	0.3	0.2
$P_2^{max}(C_{fac})$ simulated	-0.001	0.007	0.013	0.018	0.022	0.035	0.050	0.070	0.092
$P_2^{max}(C_{fac})$ Ortiz's	0.081	0.012	0.019	0.029	0.038	0.045	0.046	0.047	-
$B/\mu(P_{max})$ simulated	8	9	11	12	235	393	476	466	507
$B/\mu(P_{max})$ Ortiz's	68	144	189	250	332	392	419	594	-

Table 4.5: Dependence of maximum of the 2-nd order polynomial fit to the simulated data points $P_2^{max}(C_{fac})$ and $B/\mu(P_{max})$ on μ .

Values of the contrast C_{fac} synthesized for the MHD models appear again higher than observed by Ortiz et al. (2002). The maximum of the contrast fit $P_2^{max}(C_{fac})$ and corresponding $B/\mu(P_{max})$ for various μ obtained from our simulations and from Ortiz's

observations are summarized in table 4.5.

4.6 High resolution structure of the solar surface near the limb

In this section the morphology of observed high-resolution images of the photosphere away from the disc center will be studied. The results of high resolution simulations will be presented and analysed. The relation between the main observed small-scale features with their analogues in the simulated images will be provided and their physical origin will be discussed.

4.6.1 High resolution observations

In Fig. 4.14 an exceptionally sharp MFBD reconstructed image of an active region NOAA587 observed with the SST on 8 April 2004 at 14:01:57 (UT) near $\mu=0.35$ using an interference filter centered at 705.7 nm and with a FWHM of 0.7 nm is presented (filter profile is presented in Appendix A). The exposure time was set to 10 ms and the recordings were made using a KODAK Megaplug 1.6 CCD camera. MFBD restoration was implemented on 8 single frames recorded within a 10 s time interval and corrected for the flat field and dark frame (for the details of image processing see Chapter 2). The image covers an area of 59.4×38 arcsec² and has a spatial resolution of 0.2 arcsec what corresponds to 145 km on the solar surface. The considered spectral region contains many absorption lines of the TiO molecule. Due to their great temperature sensitivity the spectral lines become appreciable only in the coolest parts of the photosphere, namely in sunspot umrae (Berdyugina and Solanki 2002). Therefore, possibly apart from the darkest features assigned to pores, Fig. 4.14 represents the pure continuum brightness distribution at the stated wavelength. The limb direction in Fig. 4.14 is marked by the white arrow and white contour lines mark areas selected for the further analysis. Even with such a small field of view μ varies from 0.384 to 0.314, with $\mu = 0.35$ at the center of the image. This gradient is enough to notice a slight limb darkening of the quiet Sun areas when going from the lower right to the upper left on the image. The topology of the observed area shows photospheric phenomena of different scales, e.g. faculae, granulation, pores, and reveals the complexity of their structure at high spatial resolution. The solar surface at such μ makes the impression of a three-dimensional appearance as if certain 'sculptured' granules were illuminated by a big lamp from the centerward direction. This property of the solar granulation observed near the limb was also reported by Lites et al. (2004) on the basis of high spatial resolution observations. A close examination of the image reveals a very different manifestation of the three-dimensional effect which is stronger near the pores, i.e. in active regions, than far outside it, i.e. in quiet areas. This suggests that the magnetic field plays a key role in this effect. Indeed the detailed analysis of the 3-D granular pattern in active regions leads to the following summary of its main properties:

- The centerward part of the granules has brightness enhancements, i.e. faculae.
- Often faculae appear to extend over about 0.5 arcsec.

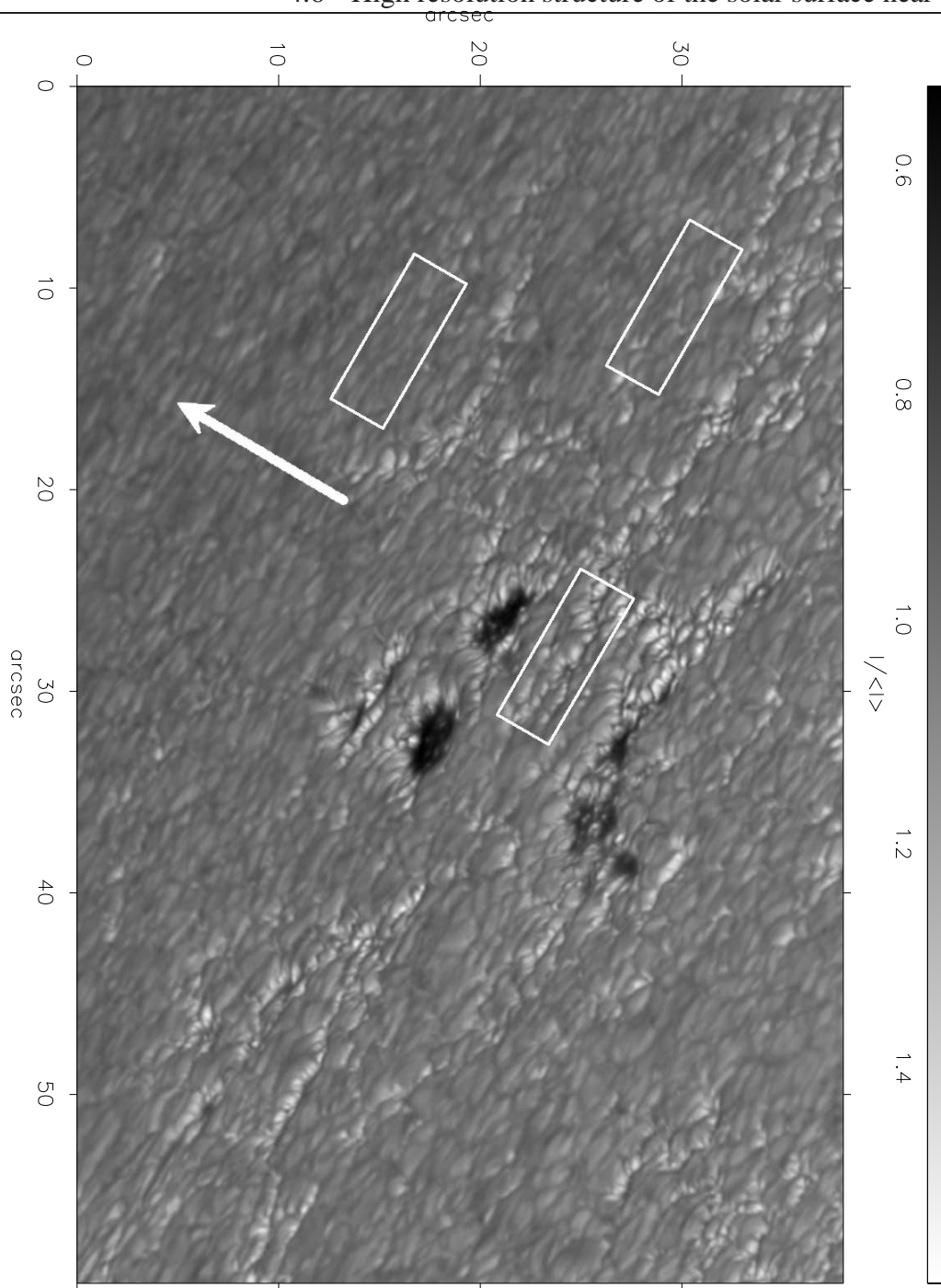


Figure 4.14: Active region NOAA587 observed with the SST on 8 April 2004 at 14:01 (UT) at $\mu=0.35$ at 705.7 nm covering the red band of TiO absorption spectra. Over the whole observed area this wavelength band corresponds to a pure continuum, except possibly in the darkest features assigned to big pores. The image was reconstructed with MFBF using 8 single frames. White contours designate subframes used in further analysis.

- The intensity is decreasing gradually from centerward to limbward sides of granules, which contain a facula.
- The facular elements are often preceded by a narrow, dark lane just centerward of them.
- Facular chains form a cell-like pattern, elongated perpendicularly the disc center radius-vector.
- Quiet Sun granulation and intergranular lanes have lower intensity contrast as compared to the disc center case.
- Relatively small granules are partly or almost completely covered by the facular brightenings (e.g. the (30,24) – (35,32) region in Fig. 4.14).
- The pores have a sharp edge on the centerward side and quite extend granulation area accompanied by a very bright faculae on the limbward side.

4.6.2 Simulated faculae

In this section, in analogue to the research of Keller et al. (2004), the results of continuum RT computations for different MHD models 'observed' at the same heliocentric angle as the observations illustrated in Fig. 4.14 will be presented and compared with the latter. We have used MHD models resulting from the MURaM code presented in Section 4.1. However, in the present study we used those MHD models which were computed assuming that not the entropy, but the internal energy per unit mass for the inflowing gas ϵ_0 be constant. The parameter ϵ_0 is used to control the net vertical energy flux through the computational domain and to make sure that the time-averaged value of the radiation flux density leaving the box is equal to the solar value $F_{\odot} = 6.34 \cdot 10^{10} \text{ erg s}^{-1} \text{ cm}^{-2}$.

In Fig. 4.15 (left panels) the synthesized, by means of the STOPRO code, normalized continuum intensity maps at $\lambda = 705.7 \text{ nm}$ and $\mu = 0.35$ resulting from the MHD models with 10 G, 200 G and 400 G averaged magnetic field are shown. In the same figure (right panels) small sub-frames of an observed active region at the same heliocentric angle (see areas marked with white contours in Fig. 4.14) are plotted. These sub-images were chosen to show different amounts of faculae and different appearance of 3-D granulation pattern. The numerical results match the appearance of the high-resolution observations and reproduce qualitatively all features seen in the observations. However the spatial resolution of the simulations, i.e. 0.029 arcsec or 20.8 km on the Sun, does not conform to that of the observed data. This partly explains the noticeable difference between the brightness scales of the two types of images. The magnetic field is known to be vastly involved in the formation of the faculae, as intensity boost in comparison with the surrounding granules. This also finds confirmations if one examines non-magnetic and magnetic simulated cases. The effect of three-dimensional granulation was not so clearly evident, but still present, in the 10 G computations than in the 200 G and 400 G cases. The successive intensity increase in the three presented simulated images is caused by faculae which agrees with the observed ones and with the results of the low-resolution investigation in Section 4.4. Later a similar numerical modeling was carried out in the G band by Carlsson et al. (2004) which revealed similar results.

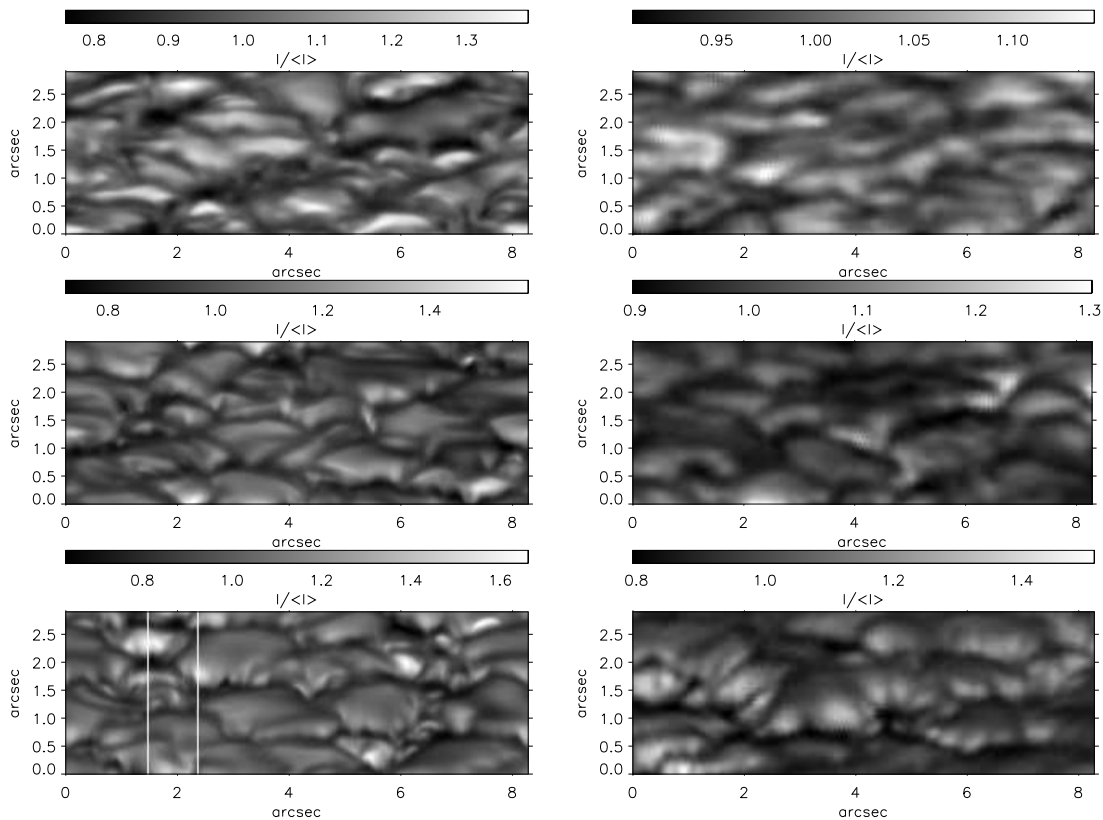


Figure 4.15: Left panels: simulated continuum images at 705.7 nm of models with average magnetic field of 10 G (top-left), 200 G (middle-left) and 400 G (bottom-left). Right panels: sub-frames of observed plage and quiet Sun at $\mu=0.35$ and 705.7 nm with increasing amount of plage from top to bottom. The spatial resolution of simulated and observed images is not exactly the same.

4.6.3 Origin of faculae and narrow, dark lanes

Here we restrict ourselves to a qualitative investigation of the configuration of the physical parameters in the photosphere which lead to the appearance of the phenomena discussed in Section 4.6.1. As the prototype of a facula let us consider a structure situated at (2.4,1.75) arcsec in Fig. 4.15 bottom-left (the 400 G model). The corresponding limbward vertical cuts through the facular atmosphere are shown in Fig. 4.16 left. The top panel gives the profile of continuum intensity along the cut, normalized to the mean intensity for the whole computed MHD box. Vertical slices of various physical quantities, i.e. temperature T (3300–14000, K), LOS component of magnetic field strength B_z (0–3500, G) and mass density variations $\delta\rho$ ($\pm 2 \cdot 10^{-7} \cdot \text{g} \cdot \text{cm}^{-3}$ from their mean, for the 400 G model) are shown in the other panels, respectively. The total emerging continuum intensity, at a frequency ν , at the solar surface is defined as:

$$I_\nu(0, \mu) = \frac{1}{\mu} \cdot \int_0^\infty S_\nu(\tau_\nu) \cdot e^{-\frac{\tau_\nu}{\mu}} d\tau_\nu, \quad (4.29)$$

where τ is the optical depth, μ is the heliocentric angle and S_ν is the source function, which in LTE is equal to the Planck function,

$$S_\nu = B_\nu(T(\tau_\nu)) = \frac{2h\nu^3}{c^2} \cdot \frac{1}{e^{h\nu/kT} - 1}, \quad (4.30)$$

where $h = 6.6262 \cdot 10^{-27}$ erg · s is Planck's constant, $c = 2.9979 \cdot 10^8$ cm · s⁻¹ is the speed of light and $k = 1.3807 \cdot 10^{-16}$ erg · K⁻¹ is Boltzmann's constant. The expression with the integral of Eq. 4.29 is called the contribution function, has a maximum at $\log(\tau)=0$ and gradually drops with optical depth. We have calculated the contribution function for each ray for a corresponding temperature profile in the model.

The dashed lines in Fig. 4.16 illustrate the range of heights where the contribution function of continuum I_c over optical depth reaches 10% and 90% of its full value. This means 80% of the total continuum intensity for a certain wavelength arise in the indicated region. The continuum intensity profile has an expansion corresponding to the facular brightening with peak brightness at 1.79 arcsec. The opacity in the magnetic flux concentration is strongly reduced owing to its low density, caused by the presence of magnetic pressure, and low temperature (at a given geometric level) and thus provides a clear sight straight through the flux tube onto the upper part of the 'hot wall' of the adjacent granule. The spatial extension of the facular brightening is determined, on the centerward side, by the point at which the continuum formation range becomes dominated by the cool gas in front and within the flux concentration, and, on the limbward side, by the point at which the boundary of the flux concentration no longer lies adjacent to the hot granule. As cooler gas above the top of the granule contributes more and more to the formation of the continuum intensity, the stronger the decrease of the brightness in the limbward direction. The excess brightness of the faculae comes from a thin layer (corresponding to a thickness of about 30 km), which is embedded in the steep density gradient at the interface between the magnetic and the non-magnetic atmosphere.

The right panels in Fig. 4.16 represent a vertical cut of the 400 G model through a very prominent dark lane located at 2.0 arcsec position which precedes a facula to its right. This cut differs from the one shown in the left panels in that there every major intergranular lane was occupied by a magnetic flux concentration, here there is only a single facula, with two downflow lanes immediately on its discward side, which merge to form a very broad intergranular lane on the discward side of the facula. As one approaches the flux concentration from the centerward side, the brightness drops sharply when the line of sight no longer crosses the 'top' of the adjacent granule, so that the range of continuum formation becomes dominated by the cool and dense downflowing material between the granule and the flux concentration. Somewhat more limbward, lines of sight traverse the flux concentration with lower density, so that the continuum formation range shifts downward towards the bottom of limbward wall of the flux concentration. The exact location of the intensity minimum varies between these two boundaries where the temperature is lower than the average temperature stratification at equal optical depth, explaining the brightness deficit. The continuum intensity in the dark lanes comes from an extended range along the line of sight, which can be as large as 340 km in the vertical direction.

Three factors are crucial for the appearance of faculae: the shape of the granule limbwards of the flux concentration, the size of the magnetic flux concentration and the field

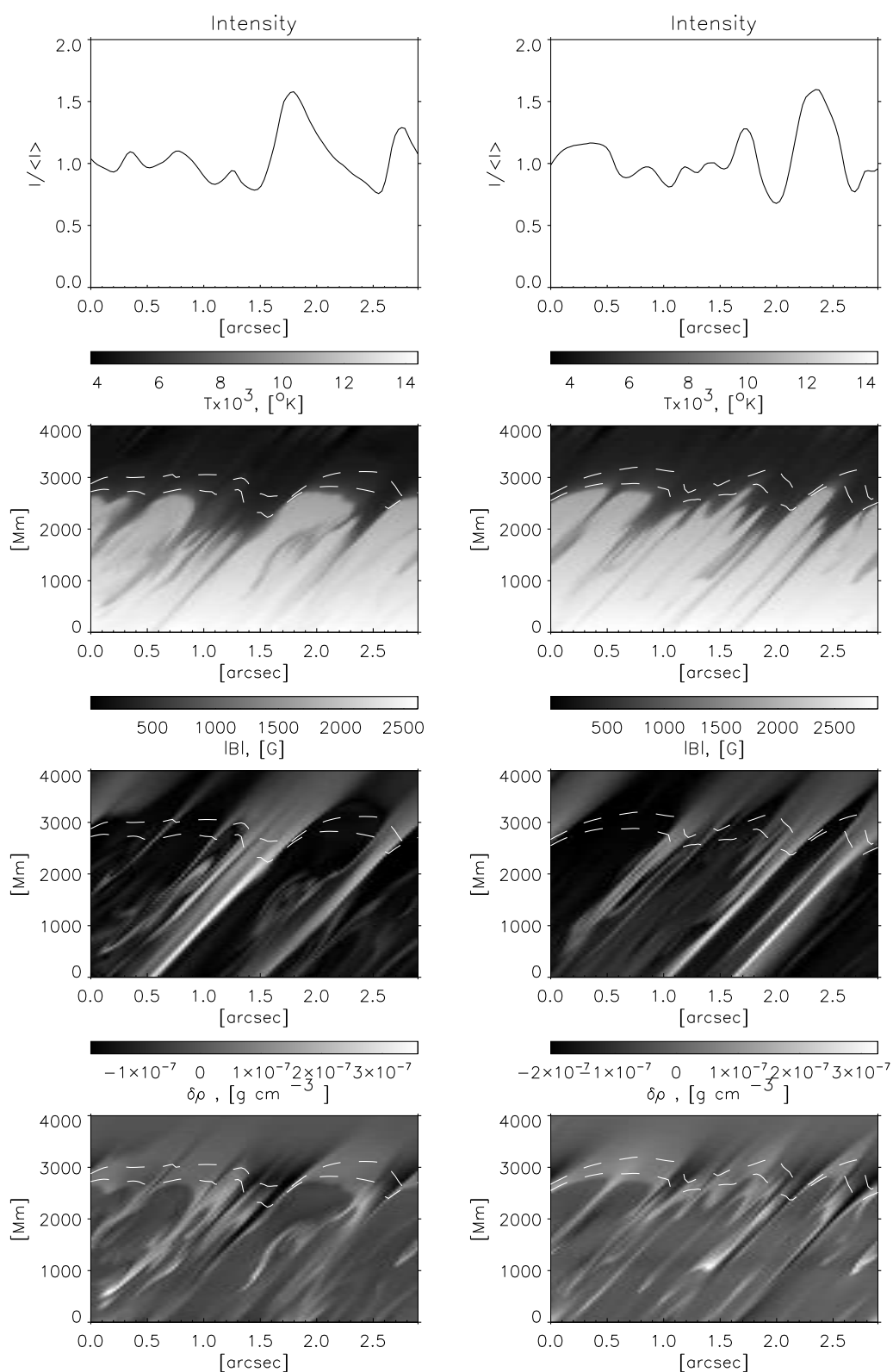


Figure 4.16: Example of a vertical cut of the 400 G MHD model at $\mu=0.35$ crossing a narrow dark lane on the limbward side of a granule. Dotted lines bracket the heights where $\approx 80\%$ of continuum intensity are formed.

strength centerwards of the facula.

If the flux concentration is too thin, e.g. in Fig. 4.17 right, or it is bright but the field strength is too small, e.g. in Fig. 4.17 left, the opacity reduction it produces is not sufficient along the line of sight to have the continuum intensity be formed almost exclusively in the hot granule. In Fig. 4.18 at location 1.0 arcsec the magnetic field is as big as in Fig. 4.16 left, but the neighboring granule is not well developed and thus the thermal conditions near $\tau=1$ prevent the formation of a facula.

Not only small-scale magnetic flux concentrations which are also associated with bright points at $\mu = 1$ produce faculae at small μ . In Figs. 4.18 and 4.19 vertical cuts, at $\mu = 1$ (left panels) and $\mu = 0.35$ (right panels), through a complex magnetic cluster exhibiting the properties of a micropore in the 400 G model and through a small pore in the MHD model by Cameron et al. (2004) respectively are shown. As we discussed in preceding sections both these types of structures appear darker than the quiet Sun near the disc center. This is in agreement with intensity profiles in the left panels of Figs. 4.18 and 4.19. However at $\mu=0.35$ both structures produce facular brightenings which in the case of the pore extend even over several granules owing to the big radial size of the pore. This explains why the 400 G model is the brightest at the limb and the darkest at the disc center. The property of pores to display several faculae on their limbward side finds support in observations (see Fig. 4.14).

We can conclude that we basically understand the cause of the facular brightening as well as of the narrow, dark lanes. Despite the excellent qualitative agreement between simulations and observations, there remain quantitative disagreements such as the peak brightness of faculae, which is substantially larger in the simulations as compared to the observations. It also appears that there are more very small brightenings in the observations as compared to the simulations. However the continuum intensity of simulated faculae is slightly higher than that of observed ones. These differences are not surprising due to the limited spatial resolution under which the observations were recorded. This includes the effect of scattered light which greatly reduces the contrast.

The explanation of facular brightenings given here is largely consistent with the "hot wall" model of Spruit (1976). Fig. 4.20 schematically shows a vertical cut through a typical magnetic flux tube. The dotted lines enclose the region where the dominant part (80%) of the continuum radiation is formed. The brightness enhancement of the facula mainly originates from a thin layer near the limbward interface between the magnetic flux concentration and the hot, non-magnetic granule. The intensity of the dark lane is formed in the relatively cool regions above the centerward granule and inside the flux concentration. The lines of sight for the facular brightening and for the dark, narrow lane are indicated with correspondingly shaded grey areas. Note that the magnetic flux concentration is usually observed on the centerward side of the facula. This agrees with high-resolution spectropolarimetric observations by Okunev & Kneer (2004).

Qualitatively similar features, e.g. dark lane followed by a more extended brightening on its limbward side, are already apparent in 2-D models (Deinzer et al. 1984a, Knölker & Schüssler 1988, Knölker et al. 1991, Steiner 2005).

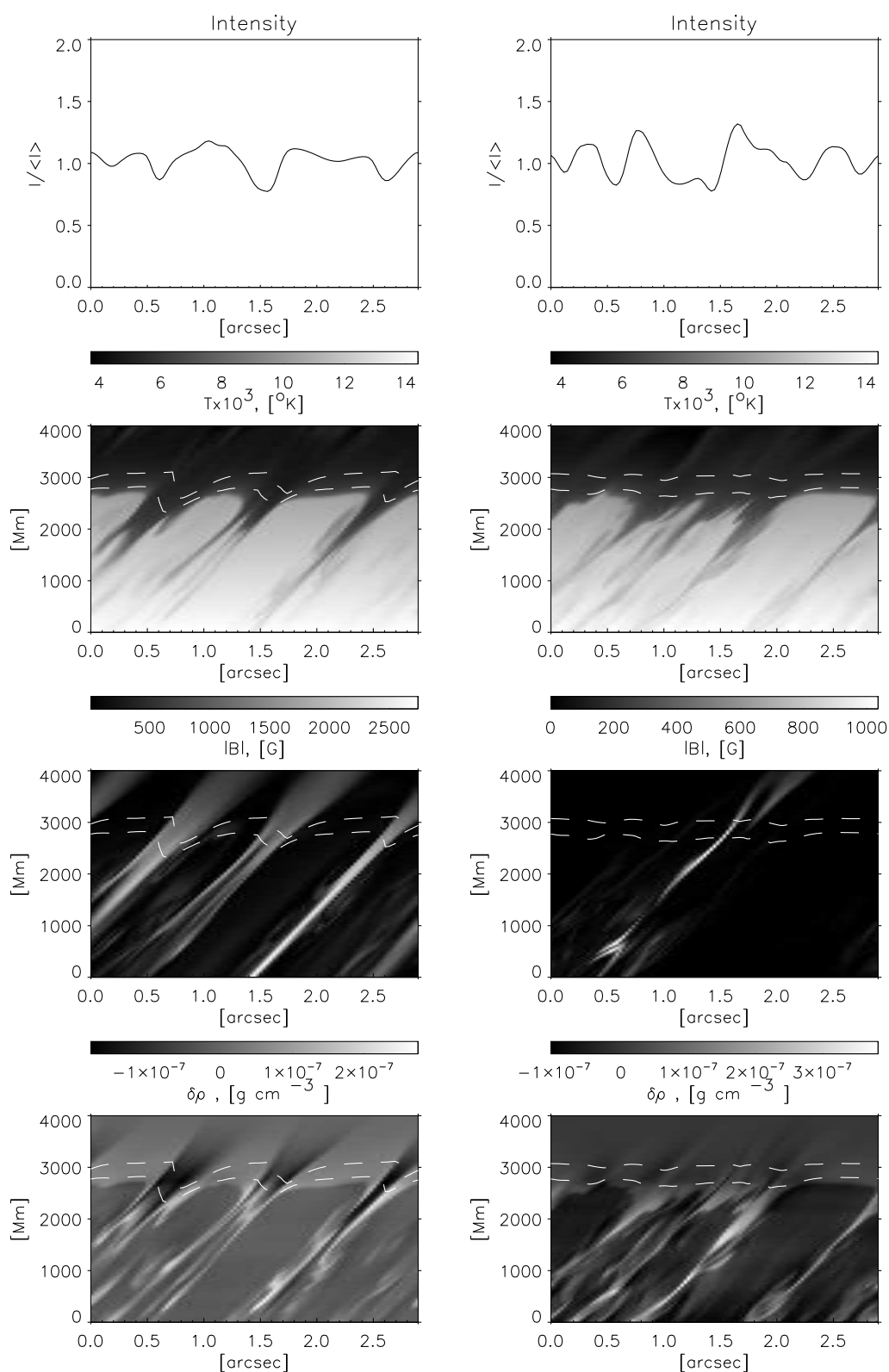


Figure 4.17: Example of a vertical cut of the 10 G MHD model at $\mu=0.35$ crossing a very weak (left) and thin (right) flux tube which do not cause the formation of strong faculae. The dashed lines bracket the heights where $\approx 80\%$ of the continuum intensity are formed.

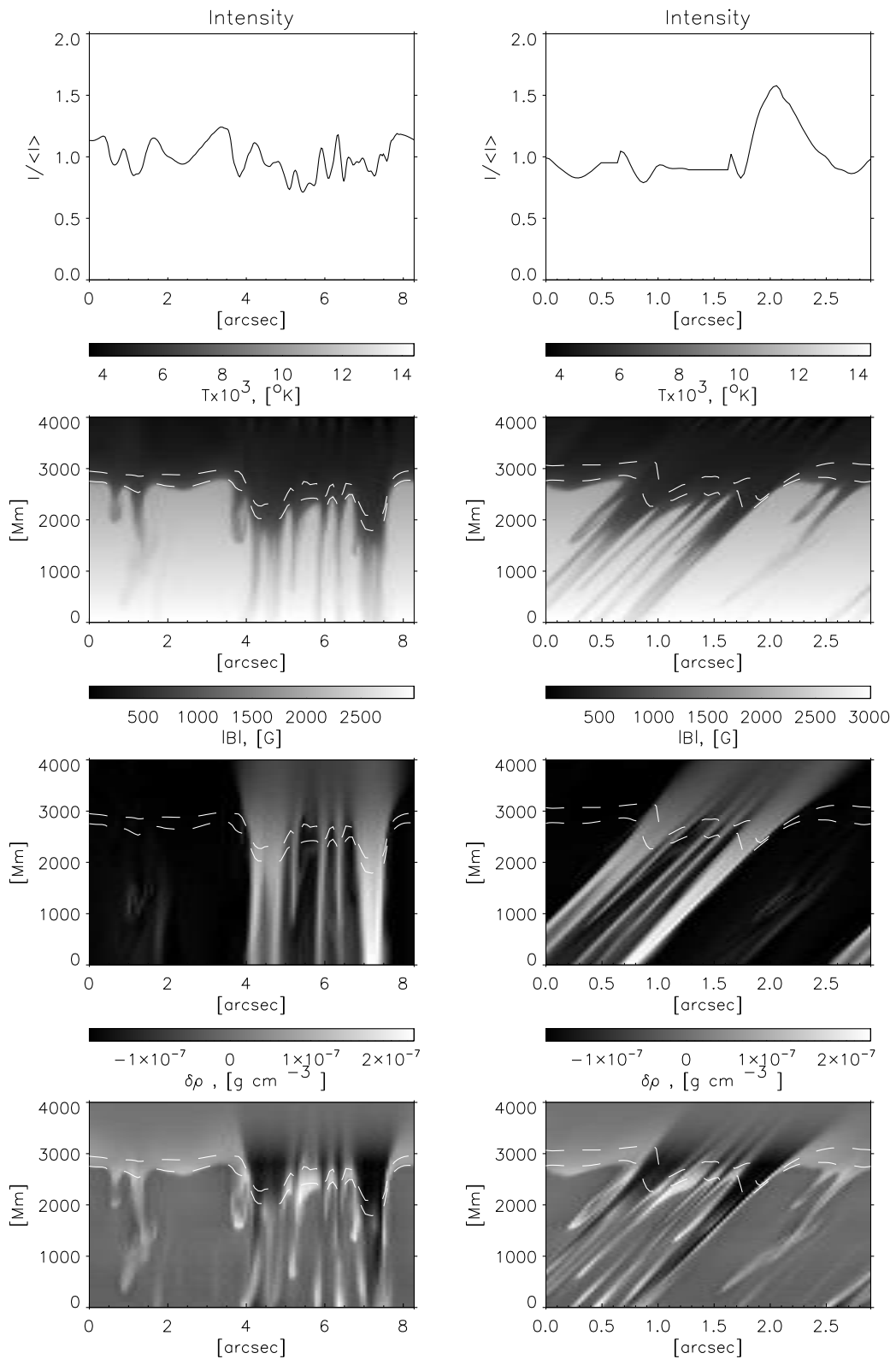


Figure 4.18: Example of a vertical cut of the 400 G MHD model at the disc center (left) and at $\mu=0.35$ (right) crossing a broad dark magnetic concentration, a micropore, which appears dark at the centre of the disc, but bright near the limb. The dashed lines bracket the heights where $\approx 80\%$ of the continuum intensity are formed.

4.6 High resolution structure of the solar surface near the limb

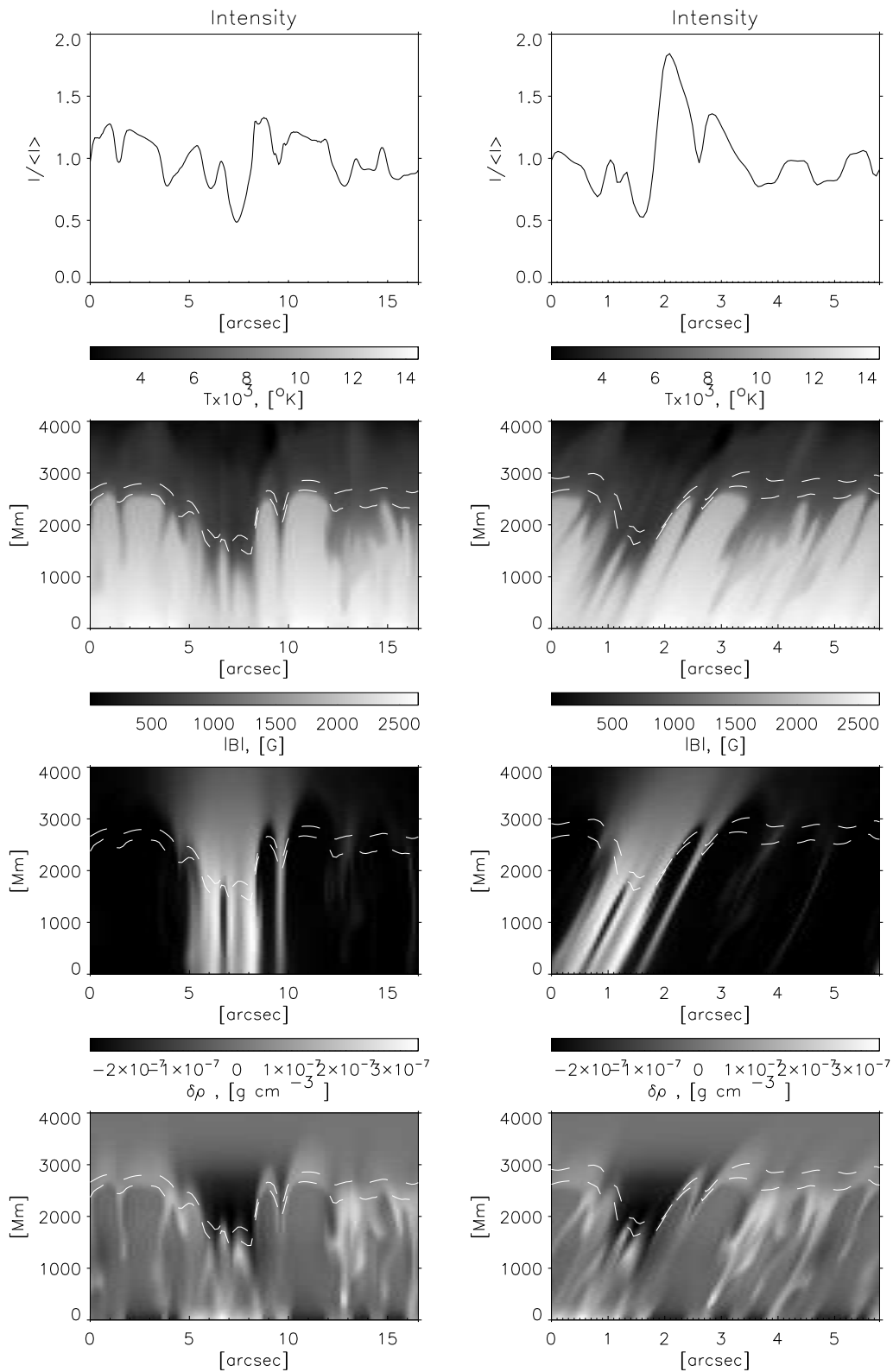
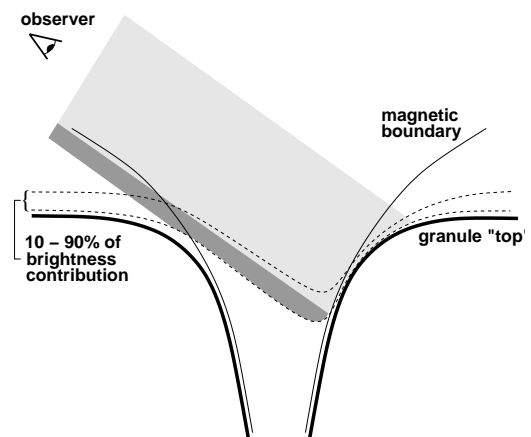


Figure 4.19: Example of a vertical cut of the 400 G MHD model at the disc center (left) and at $\mu=0.35$ (right) crossing a broad dark magnetic concentration, a pore, which appears dark at the centre of the disc, but bright at its limbward side near the limb. The dashed lines bracket the heights where $\approx 80\%$ of the continuum intensity are formed.

Figure 4.20: Schematic sketch of a magnetic flux concentration (region within the thin lines) and adjacent granules (thick lines), illustrating the origin of the facular brightening and the dark lane.



Conclusions and outlook

In this PhD thesis the structure and intensity properties of small-scale magnetic features on the Sun were studied by means of high spatial resolution observations and numerical simulations. For this purpose observations with the 1-m Swedish Solar Telescope (SST, La Palma) of active regions, plages and quiet Sun areas in the solar photosphere at different disc positions were carried out.

The first observational campaign was aimed at imaging observations in three narrow spectral bands, the blue continuum (436.4 nm), the G band (430.5 nm) and the violet CN band-head (387.9 nm), simultaneously. The unprecedented high spatial resolution of better than 0.18 arcsec, which corresponds to 130 km on the Sun, of the solar images in all three spectral bands was achieved by means of the Joint Phase Diverse Speckle image reconstruction method (see Sect. 2.1). Our investigation of the intensity contrast of photospheric bright points (BP - a class of small-scale bright structures, which show enhanced contrast in the G band as compared to that in the continuum) in the obtained filtergrams of active regions at disc centre showed that:

- On average over all bright points in the 27×43 arcsec² filtergram triplet the contrast of the BP intensity relative to intensity of the quiet Sun is 1.4 times higher in the blue CN band-head than that in the G band and it is 3.4 times higher in the blue CN band-head than that in the blue continuum. Analogically, in the G band the contrast of bright points is on average 2.4 times higher than in the blue continuum. This is in a reasonable agreement with the theoretical predictions by Kiselman et al. (2001) and Berdyugina et al. (2003). However, this is in sharp disagreement with the simulations by Uitenbroek & Tritschler (2006 submitted.). The possible reasons for this are discussed in Sect. 2.4.
- The ratio of the bright points contrast in the blue CN band-head to that in the G band decreases with increasing continuum intensity of the bright points. The minimum value of this ratio is 1.25 for the brightest BPs.

The high spatial resolution of the obtained filtergrams reveal a complex structuring of bright points. In particular, structures such as "hot walls" and "floors" of the magnetic flux tubes, ribbons etc. are clearly seen. A further detailed analysis of the intensity properties of such structures would be of particular interest, since it provides indirect information of the thermal structuring of small-scale concentrations of magnetic flux in the photosphere. In the present PhD work, however, we did not study them separately. The significantly higher contrast seen in the violet CN band-head compared with the G-band makes it a promising wavelength band for solar high resolution studies, although

there are factors making contemporary high-resolution ground-based solar observations in this wavelength more complex than in the G band:

- fewer photons are provided by the Sun,
- there is more scattered light,
- the spatial resolution is worse because of the stronger influence of the atmospheric aberrations (seeing).

The goal of the second observational campaign at the SST was to obtain highly spatially and spectroscopically resolved spectra of small-scale photospheric features, e.g. BPs and faculae. We have observed spectra of several solar active regions at different disc positions in the range of 387.588–388.473 nm with a resolving power of about 130000 and a spatial resolution of about 0.25 arcsec. This spectral band covers absorption spectral lines of both CH and CN molecules and many atomic lines as well. This enabled us to provide a quantitative comparison of their behavior, i.e. absorption, Doppler shift and line width, in the different photospheric features. Our analysis of obtained data yielded that:

- On average, over all BPs in the observed 33×14 arcsec² area at the disc centre, the change of the line-core depression in BPs relatively to the quiet Sun of a CN spectral line ($\lambda = 387.844$ nm vacuum) is 1.28 stronger than that of a CH spectral line ($\lambda = 387.829$ nm vacuum). In faculae at $\mu = 0.65$ and at $\mu = 0.56$ these values are 1.32 and 1.46, respectively.
- At the disc centre the CN line-core intensity for the same spectral lines has higher BP contrast than the contrast in the CH line-core by a factor of 1.9, and the ratio of these contrasts is decreasing with increasing continuum intensity. The minimum value of this ratio is 1.5 for the brightest BPs. This trend is similar to that obtained from filtergram observations although here we have analyzed individual spectral lines rather than the whole band and the CH line corresponds to another, i.e. the B-X, electronic system than CH lines from the G band.

We suppose that one of the cause of enhanced contrast of BPs in the blue CN band-head as compared to that in the G band is a higher temperature sensitivity of CN molecules and thus their more efficient dissociation in flux tubes than those of CH molecules. However we can not exclude the influence of other factors to this result.

A detailed synthesis of the spectra at these wavelengths using 3-D MHD simulations and a direct comparison with observed data would be of considerable interest. In particular, an inversion of observed CH and CN spectral lines is desired.

The third observational campaign was aimed at high resolution imaging observations of faculae near the limb. We have observed with the SST a plage region near $\mu = 0.35$ in the red continuum at 705.7 nm. The Multiframe Blind Deconvolution method allowed us to reach the diffraction limit of the telescope of 0.2 arcsec (145 km on the Sun) for this wavelength. An observed plage region showed many facular brightenings of a very complex structure. The granulation at some places gives the impression of a three-dimensional structure (see Sect. 4.6.1).

In order to understand the physics of such a structuring we have made continuum radiative transfer computations in realistic 3-D MHD models, at the same disc positions as in the observations. The analysis of our simulations revealed many qualitative similarities to the observed faculae and granulation pattern (see Sect. 4.6.2). We can explain many observational features, e.g. faculae, narrow dark lanes at the discward side of some granules, with a "hot wall" model of the magnetic flux tube.

The last part of this work consisted of radiative simulations of faculae in several snapshots of 3-D MHD models with a different amount of the mean magnetic field. We have found that the models with 0 G mean magnetic field appear brighter at $\mu = 1.0$ and darker near the limb than the models with a non-zero magnetic field. Comparing the synthesized limb darkening in continuum at $\lambda = 676.8$ nm with observations of Neckel (1996) at the same continuum wavelength we found that the 50 G models yield the best coincidence to his observational results (see Sect. 4.4.1).

The comparison of the center-to-limb variation (CLV) of the continuum intensity, depending on a computed magnetogram signal, in different models we found a good agreement with observations made by Ortiz et al. (2002) with MDI on board the SOHO spacecraft (see Sect. 4.5.2). However, our synthesized contrast values are slightly higher than the observed ones. The results of our simulations indicates that the CLV of the continuum contrast of magnetic features changes with their magnetogram signal. Stronger magnetogram signals correspond to wide flux tubes, which appear dark at the disc centre, but bright near the limb. Weak magnetogram signals usually correspond to narrow flux tubes and appear bright at the disc centre and near the limb. A typical CLV of the continuum contrast of faculae increases towards the limb reaching the maximum value at a certain μ_{max} and then decreases again. The value of μ_{max} decreases with an increase of the magnetogram signal.

The results of this investigation are useful in modeling of the variations of the total solar irradiance.

A Filter profiles

In Figs. A.1, A.2, A.3 and A.4 the transmission profiles of the blue CN band-head, G band, blue continuum and TiO narrow-band interference filters used in our imaging (Chapter 2) and spectroscopic (Chapter 3) observations are shown.

The main characteristics of these filters are presented in Table A.

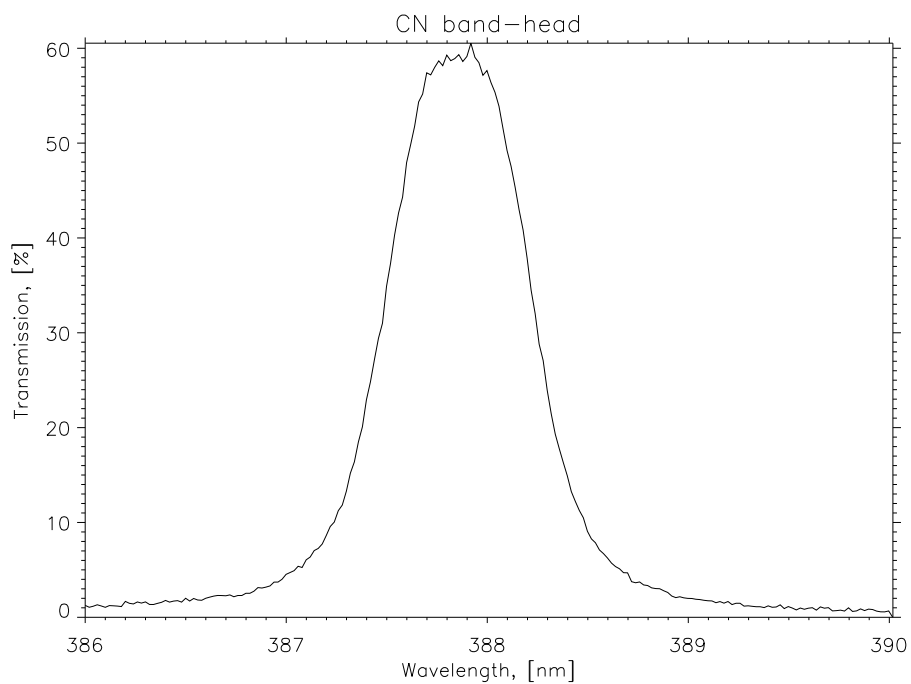


Figure A.1: Transmission profile of the CN band-head interference filter.

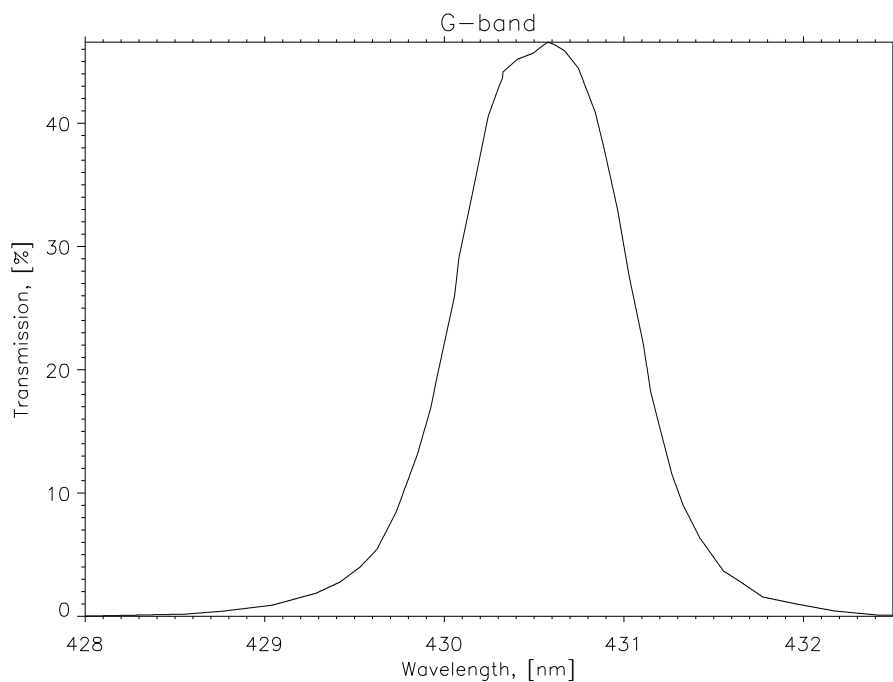


Figure A.2: Transmission profile of the G-band interference filter.

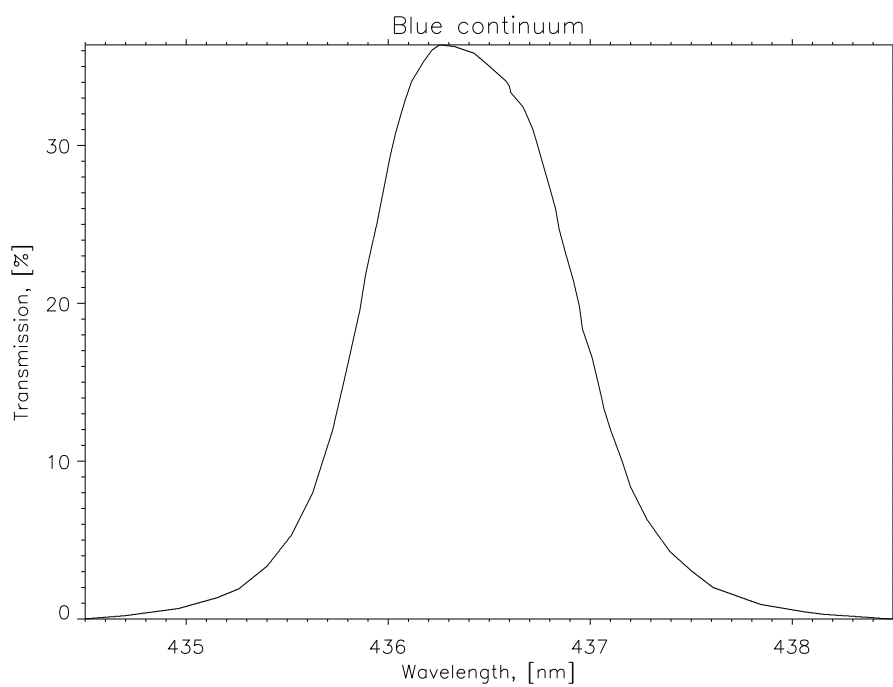


Figure A.3: Transmission profile of the blue continuum interference filter.

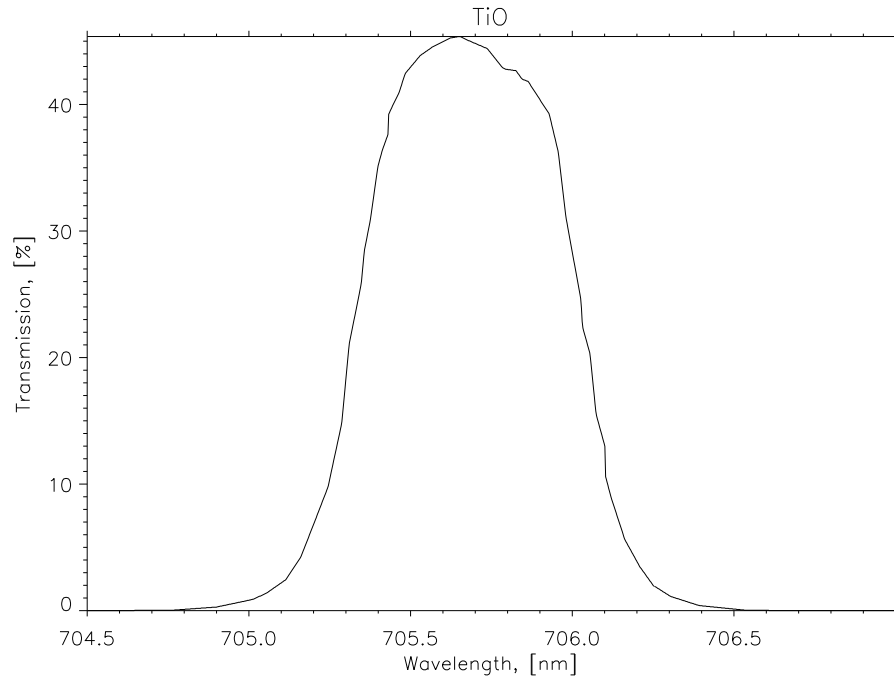


Figure A.4: Transmission profile of the TiO interference filter.

Name	Central wavelength	FWHM	Peak transmission
TiO	705.68 nm	0.71 nm	45.37%
Blue continuum	436.39 nm	1.15 nm	36.37%
G band	430.56 nm	1.08 nm	46.71%
CN band-head	387.919 nm	0.74 nm	60.54%

Table A.1: Technical data for the filters.

B Contribution functions

The range of heights over which a spectral line is sensitive to physical parameters of the atmosphere is an important quantity that needs to be known when using the spectral line to probe the solar photosphere. In order to quantify the depths of line formation usually two different approaches are used, a contribution function (CF) and a response function (RF). The CF represents a depth-dependent function showing the relative contribution of different layers to the formation of the line. The line depression CF for all Stokes components I , Q , U and V , assuming that there is no polarization in continuum can be written as:

$$\begin{aligned}
 \int_0^{\infty} CF_I(\tau_c) d\tau_c &= 1 - \frac{I(0)}{I_c(0)}, \\
 \int_0^{\infty} CF_Q(\tau_c) d\tau_c &= -\frac{Q(0)}{I_c(0)}, \\
 \int_0^{\infty} CF_U(\tau_c) d\tau_c &= -\frac{U(0)}{I_c(0)}, \\
 \int_0^{\infty} CF_V(\tau_c) d\tau_c &= -\frac{V(0)}{I_c(0)},
 \end{aligned}
 \tag{B.1}$$

where I_c is the continuum intensity and τ_c is the continuum optical depth. The RF illustrates the influence on the line profile of perturbations in a given atmospheric parameter at different depths and is used for empirical diagnostics of atmospheric parameters. An exhaustive description of Stokes CF and RF computations can be found in Grossmann-Doerth et al. (1988) and Solanki & Bruls (1994).

In Fig B.1 we present CFs of the Stokes-I line depression of the cores of molecular and atomic lines computed for the radiative equilibrium model atmosphere by Kurucz (1993) with $T_{eff} = 5750$ K, which represents the solar photosphere. The computations were carried out with the STOPRO code. From these calculations we obtain that the maximum of line-core formation for CN at $\lambda = 388.009$ nm, CH at $\lambda = 387.719$ nm ($A - X$ system), CH at $\lambda = 436.272$ nm ($B - X$ system), Fe I at $\lambda = 387.667$ nm and the strong Fe I line at $\lambda = 387.8018$ nm are located at depths, i.e. $\log(\tau_{387})$, equal to -1.412 , -0.929 , -1.169 , -1.528 and -5.592 , respectively. This corresponds to relative heights in the model of 152 km, 88 km, 120 km, 167 km and 654 km above $\tau_{387 \text{ nm}} = 1$. Here we have used the same spectral lines as employed in analysis in Chapter 3.

In Fig. B.2 we present CFs computed in the same Kurucz model for several wavelength positions of the Fe I line (line-core at $\lambda = 387.667$ nm). From this plot we obtain that the position of CF maximum varies depending on the wavelength, i.e. different part of the line profile are formed at different heights in the atmosphere.

B Contribution functions

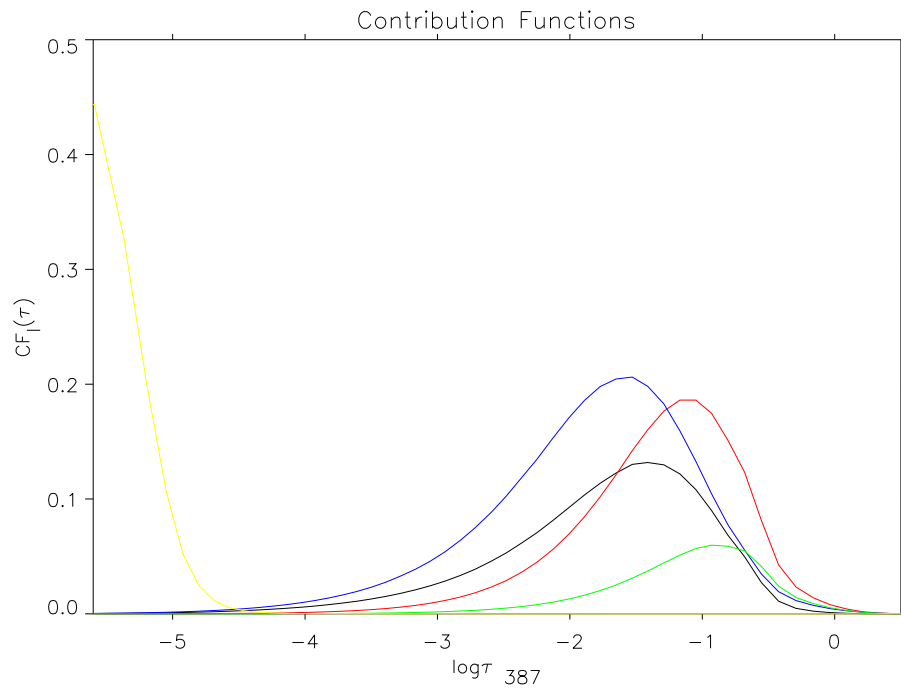


Figure B.1: Contribution functions for CN at $\lambda = 388.009$ nm (black), CH at $\lambda = 387.719$ nm (red), CH at $\lambda = 436.272$ nm (green), Fe I at $\lambda = 387.667$ nm (blue) and Fe I at $\lambda = 387.8018$ nm (yellow) dependence of optical depth $\log(\tau)$ computed for the continuum at $\lambda = 387$ nm.

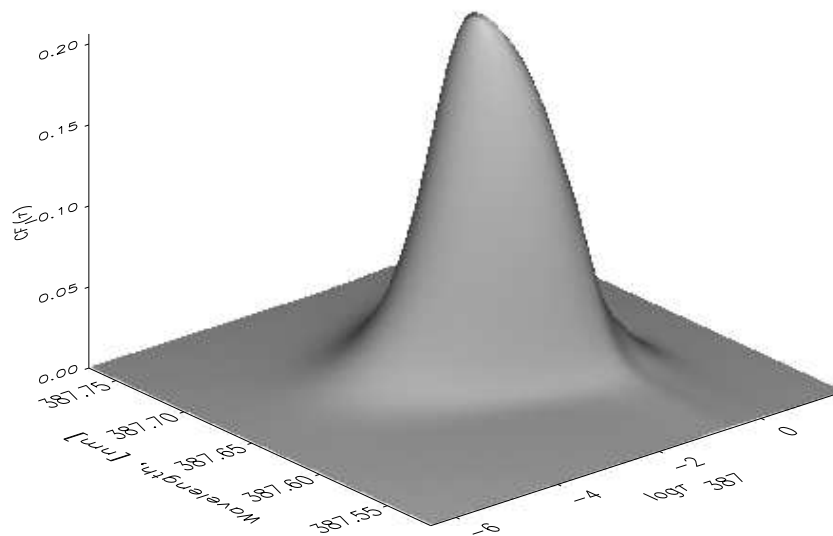


Figure B.2: Contribution functions of Fe I (387.667 nm) at different wavelength positions.

Bibliography

- Akimov, L. A., Belkina, I. L., Dyatel, N. P., & Marchenko, G. P. 1985, *Soviet Astron.*, 31, 64
- Atroshchenko, I. N., Gadun, A. S. 1994, *A&A*, 291, 635
- Audic, S. 1991, *Sol. Phys.*, 135, 275
- Auffret, H., Muller, R. 1991, *A&A*, 246, 264
- Van Ballegooijen, A. A. 1985, in *Measurements of Solar Vector Magnetic Fields*, ed. M.J., Hagyard, NASA Conf. Publ. 2374, p. 322
- Beckers, J. M., Schröter, E. H. 1968, *Sol. Phys.*, 4, 142
- Beckers, J. M. 1976, Sacramento Peak Observatory, AFGL-TR-76-0131
- Bellot Rubio, L. R., Ruiz Cobo, B., & Collados, M. 1998, *ApJ*, 506, 805
- Bercik, D. J., Nordlund, Å., Stein, R. F. 2003, In: *Proceedings of SOHO 12 / GONG+ 2002. Local and global helioseismology: the present and future*, 27 October - 1 November 2002, Big Bear Lake, CA, USA. Edited by H. Sawaya-Lacoste, ESA SP-517, Noordwijk, Netherlands: ESA Publications Division, ISBN 92-9092-827-1, 2003, p. 201 - 206
- Berdyugina, S. V., & Solanki, S. K. 2002, *A&A*, 385, 701
- Berdyugina, S. V., Solanki, S. K., & Frutiger, C. 2003, *A&A*, 412, 513
- Berger, T. E., Schrijver, C. J., Shine, R. A., Tarbell, T. D., Title, A. M., Scharmer, G. 1995, *ApJ*, 454, 531
- Berger, T. E., & Title, A. M. 1996, *ApJ*, 463, 365
- Berger, T. E., Title, A. M. 2001, *ApJ*, 553, 449
- Berger, T. E., Löfdahl, M. G., Title, A.M., & Shine, R. S. 1998, *ApJ*, 495, 973
- Berger, T. E., Löfdahl, M. G., Bercik, D. J. 2002, *American Astronomical Society, 200th AAS Meeting*, No. 91.01; *Bulletin of the American Astronomical Society*, vol. 34, p.953

- Berger, T. E., Rouppe van der Voort, Löfdahl, M. G., Carlsson, M., Fossum, A., Hansteen, V. H., Marthinussen, E., Title, A., & Scharmer, G. 2004, *A&A*, 428, 613
- Brants, J. J., Steenbeck, J. C. M. 1985, *Sol. Phys.*, 96, 229
- Brault J. W., Neckel H., 1987, *Spectral Atlas of Solar Absolute Disk-averaged and Disk-center Intensities from 3290 to 12510*
- Briand, C., Solanki, S. K. 1995, *A&A*, 299, 596
- Bruls, J. H. M. J. 1993, *Solar Physics*, 269, 509
- Bruls, J. H. M. J., Solanki, S. K. 1993, *A&A*, 273, 293
- Büntje, M., Solanki, S. K., Steiner, O. 1993, *A&A*, 268, 736
- Cameron, R., Vögler, A., Shelyag, S., Schüssler, M. 2004, *The Solar-B Mission and the Forefront of Solar Physics*, ASP Conference Series, Vol. 325, Proceedings of the Fifth Solar-B Science Meeting held 12-14 November, 2003 in Roppongi, Tokyo, Japan. Edited by T. Sakurai and T. Sekii. San Francisco: Astronomical Society of the Pacific, p.57
- Cannon, C. J. 1970, *ApJ*, 161, 255
- Carlsson, M., Stein, Robert F., Nordlund, Å.; Scharmer, G. B. 2004, *Multi-Wavelength Investigations of Solar Activity*, IAU Symposium, No 223, Edited by Alexander V. Stepanov and Elena E. Benevolenskaya and Alexander G. Kosovichev Cambridge, UK: Cambridge University Press, 233
- Cattaneo, F. 1999, *ApJ*, 515, 39
- Chapman, G. A. 1970, *Sol. Phys.*, 13, 78
- De Boer, C. R. 1993, PhD thesis, University of Göttingen, Germany
- De Pontieu, B. 2002, *ApJ*, 569, 474
- Deinzer, W., Hensler, G., Schüssler, M., Weisshaar, E. 1984, *A&A*, 139, 426
- Deinzer, W., Hensler, G., Schüssler, M., Weisshaar, E. 1984, *A&A*, 139, 435
- Domínguez Cerdeña, I., Sánchez Almeida, J., Kneer, F. 2003, *A&A*, 407, 741
- Domínguez Cerdeña, I., Sánchez Almeida, J., Kneer, F. 2006, *ApJ*, 636, 496
- Dravins, D. 1999, *Precise Stellar Radial Velocities*, ASP Conference Series 185, IAU Colloquium 170. Eds. J. B. Hearnshaw and C. D. Scarfe., 268
- Dunn, R. B., Zirker, J. B. 1973, *Sol. Phys.*, 14, 89
- Eker, Z. 2003, *Sol. Phys.*, 212, 277
- Emonet, T., Cattaneo, F. 2001, *ApJ*, 560,197

- Fligge, M., Solanki, S. K. 2000, *A&A*, 21, 275
- Fontenla, J., White, O. R., Fox, P. A., Avrett, E. H., Kurucz, R. L. 1999, *ApJ*, 518, 480
- Frazier, Edward N. 1971, *Sol. Phys.*, 21, 42
- Fraunhofer, J. 1817, *Denkschriften der Münch. Akad. der Wissenschaften*, 5, 193
- Fröhlich, C. 2002, *Adv. Space Res.*, 29, 1409
- Frutiger, C., Solanki, S. K., Fligge, M. & Bruls, J.H.M.J. 2000, *A&A*, 358, 1109
- Gadun, A. S., Hanslmeier, A. 2000, *Kinematika i Fizika Nebesnykh Tel*, 16, 130
- Gadun, A. S., Solanki, S. K., Johannesson, A. 1999, *A&A*, 350, 1018
- Gonsalves, R. A. 1982, *Optical Engineering*, 21, 829
- Goodman, M. K. 2004, *A&A*, 416, 1159
- Grossmann-Dörth, U., Larsson, B. & Solanki, S. K. 1988, *A&A*, 204, 266
- Grossmann-Dörth, U., Knölker, M., Schüssler, M., Weisshaar, E. 1989, in *Solar and Stellar Granulation*, ed. R. J. Rutten & G. Severino, Vol. 263, 481
- Hale, G. E. 1908, *ApJ.*, 28, 315
- Hasan, S. S., Kalkofen, W., Steiner, O. 1999, in *Solar Polarisation*, ed. K. N. Nagendra & J. O. Stenflo, *Astrophysics and space science library*, Vol.243, p. 409
- Hirzberger, J. 2003, *A&A*, 405, 331
- Hirzberger, J., Wiehr, E. 2005, *A&A*, 438, 1059
- Holweger, H., Kneer, F. 1989, *Solar and Stellar Granulation*, Proceedings of the 3rd International Workshop of the Astronomical Observatory of Capodimonte (OAC 3) and the NATO Advanced Research Workshop on Solar and Stellar Granulation, June 21-25, held at Capri, Italy., Dordrecht: Kluwer, 1989, edited by Robert J. Rutten and Giuseppe Severino. NATO Advanced Science Institutes (ASI) Series C, Volume 263, p.173
- Hu, Y. Q., Habbal, S. R., Chen, Y., Li, X. 2003, *J. Geophys. Res.*, 108, 1377
- Hirayama, T. 1978, *PASJ.*, 30, 337
- Janssen, K., Cauzzi, G. in press., *A&A*
- Jorgensen, U. G., Larsson, M., Iwamae, A., Yu, B. 1996, *A&A*, 315, 204
- Kahaner, D., Molker, C., & Nash, S. 1989, *Numerical Methods and Software*, Prentice Hall
- Keller, C. U. 1992, *Natur.*, 359, 307

- Keller, C. U., Stenflo, J. O., Solanki, S. K., Tarbell, T. D., & Title, A. M. 1990, *A&A*, 236, 250
- Keller, C. U., von der Lühe, O. 1992, *A&A*, 261, 321
- Keller, C. U., Schüssler, M., Vögler, A., Zakharov, V. 2004, *ApJ*, 607, 59
- Kiselman, D., Rutten, R. J., & Plez, B., 2001, *ASP Conf. Series 200, Recent Insights into the Physics of the Sun and Heliosphere*, ed. P. Brekke, B. Fleck & J.B. Gurman, 287
- Khomenko, E. V., Martínez González, M. J., Collados, M., Vögler, A., Solanki, S. K., Ruiz Cobo, B., & Beck, C. 2005, *A&A*, 436, 27
- Knölker, M., Schüssler, M. 1988, *A&A*, 202, 275
- Knölker, M., Schüssler, M., & Weisshaar, E. 1988, *A&A*, 194, 257
- Knölker, M., Grossmann-Doerth, U., Schüssler, M., Weisshaar, E. 1991, *Advances in Space Research*, 11, 285
- Koschinsky, M., Kneer, F., Hitzberger, J. 2001, *A&A*, 365, 588
- Kourganoff, V. 1949, *C.R. Acad. Sci. Paris* 228, 2011 (Countr. Inst. Astrophys. Paris A, No. 46)
- Krivova, N. A., Solanki, S. K., Fligge, M., & Unruh, Y. C. 2003, *A&A*, 399, 1
- Kurucz, R.L. 1993, *VizieR On-line Data Catalog*, VI/39
- Leka, K. D., Steiner, O. 2001, *ApJ*, 552, 354
- Leenaarts, J., & Wedemeyer-Böhm, S. 2005, *A&A*, 431, 687
- Langhans, K., Schmidt, W., Rimmele, T., & Sigwarth, M. 2001, *ASPC*, 236, 439
- Langhans, K., Schmidt, W., & Tritschler, A. 2002, *A&A*, 394, 1069
- Langhans, K., Schmidt, W., & Rimmele, T. 2004, *A&A*, 423, 1147-1157
- Lean, J. L., Cook, J., Marquette, W., & Johannesson, A. 1998, *ApJ*, 492, 390
- Lee, L., Vasudevan, G., Smith, E.H. 2003, in *Proc. of the SPIE, IR Space Telescopes and Instruments*, ed. John C. Mather, 4850, 441
- Löfdahl, M. G., Scharmer, G. B. 1994, *A&A*, 107, 243
- Löfdahl, M. G., Berger, T. E., Shine, R. S., & Title, A. M. 1998, *ApJ*, 495, 965
- Löfdahl, M. G., Berger, T. E., Seldin, J. H. 2001, *A&A*, 377, 1128
- Löfdahl, M. G. 2002, 'Multi-frame blind deconvolution with linear equality constraints', in *Proc SPIE, Vol. 4792, pp. 146-155, Image Reconstruction from Incomplete Data II*, ed: P. J. Bones, M. A. Fiddy, and R.P. Millane.

- Lites, B. W., Nordlund, Å., & Scharmer, G. B. 1989, in *Solar and Stellar Granulation*, R. J. Rutten & G. Severino, Dordrecht: Kluwer, 349
- Lites, B. W., Scharmer, G. B., Berger, T. E., Title, A. M. 2004, *Solar Physics*, 221, 65
- Mathew, S. K., Lagg, A., Solanki, S. K., Collados, M., Borrero, J. M., Berdyugina, S., Krupp, N., Woch, J., & Frutiger, C., 2003, *A&A*, 410, 695
- Muller, R. 1975, *Sol. Phys.*, 45, 105
- Muller, R. 1983, *Sol. Phys.*, 85, 113
- Muller, R., & Keil, S. L. 1983, *Sol. Phys.*, 87, 243
- Muller, R., & Roudier, T. 1984, *Sol. Phys.*, 94, 33
- Muller, R., Hulot, J. C., & Roudier, T. 1984, *Sol. Phys.*, 19, 229
- Muller, R. 1994, in *NATO ASI C*, ed. R. J. Rutten & C. J. Srijver, *Solar Surface Magnetism*, Vol. 433, 73
- Muller, R., Roudier, Th., Vigneau, J., Auffret, H. 1994, *A&A*, 283, 282
- Muller, R., Dollfus, A., Montagne, M., Moity, J., Vigneau, J. 2000, *A&A*, 359, 373
- Neckel, H., Labs, D. 1994, *Solar Physics*, 153, 91
- Neckel, H. 1996, *Solar Physics*, 167, 9
- Nesis, A., Bogdan, T. J., Cattaneo, F., Hanslmeier, A., Knoelker, M., Malagoli, A. 1992, *ApJ*, 399, 99
- Nesis, A., Hanslmeier, A., Hammer, R., Komm, R., Mattig, W., Staiger, J. 1993, *A&A*, 279, 599
- Nisenson, P., van Ballegooijen, A. A., de Wijn, A. G., Sütterlin, P. 2003, *ApJ*, 587, 458
- Noll, R.J. 1976, *Optical Society of America*, 66, 207
- Nordlund, Å 1984, in *Small-Scale Dynamical Processes in Quiet Stellar Atmospheres*, ed. S. K. Keil (Sunspot, NM: Sacramento Peak Observatory), 181
- Nordlund, Å 1986, in *Small Scale Magnetic Flux Concentrations in the Solar Photosphere*, ed. W. Deinzer, M. Knölker, and H.H. Voigt, 83
- November, L. J., Simon, G. W. 1988, *ApJ*, 333, 427
- Okunev, O. V., Kneer, F. 2004, *A&A*, 425, 321
- Orlov, V. G., Voitsekhovich, V. V., & Cuevas, S. 2003, *Revisita Mexicana de Astronomia y Astrofisica*, 33, 187

- Ortiz, A., Solanki, S. K., Domingo, V., Fligge, M., and Sanahuja, B. 2002, *A&A*, 388, 1036
- Paxman, R. G., Schulz, T. J., & Fienup, J. R. 1992, *Opt. Soc. America*, 9, 1072
- Paxman, R. G., Schulz, T. J., & Fienup, J. R. 1992, in *Technical Digest Series, Vol. 11, Signal Recovery and Synthesis IV*, Optical Society of America, 5-7
- Paxman, R. G., Seldin, J. H., Löfdahl, M. G., Scharmer, G. B., Keller, C. U. 1996, *ApJ*, 466, 1087
- Puschmann, K. G., Wiehr, E. 2006, *A&A*, 445, 337
- Pierce, A. K., Slaughter, C. D. 1977, *Sol. Phys.*, 51, 25
- Pierce, A. K., Slaughter, C. D., Weinberger, D. 1977, *Sol. Phys.*, 52, 179
- Press, W. H., Flannery, Brian P., Teukolsky, S. A. 1986, *Numerical recipes. The art of scientific computing*, (Cambridge: University Press)
- Ramsey, H. E., Schoolman, S. A., Title, A. M. 1977, *ApJ*, 215, 41
- Rees, D. E., Durrant, C. J., Murphy, G. A. 1989, *ApJ*, 339, 1093
- Restaino, S. R. 1992, *Appl. Opt.*, 31, 7442
- Roddier, F. 1990, *Optical Engineering*, 29(10), 1174
- Roddier, F, Roddier, C. 1991, *Appl. Opt.*, 30, 1325
- Rogerson, John B., Jr. 1961, *ApJ*, 134, 331
- Ruiz Cobo, B., del Toro Iniesta, J. C. 1992, *ApJ*, 398, 375
- Rutten, R. J. 1999, in *Magnetic Fields and Oscillations*, ed. B. Schmeider, A. Hofmann & J. Staude, 3rd *Advances in Solar Physics Euroconference*, ASP. Conf. Ser. 184, p. 181
- Rutten, R. J., Kiselman, D., Rouppe van der Voort, L., & Plez, B. 2001, *ASP Conf. Series 236, Advanced Solar Polarimetry – Theory, Observation, and Instrumentation*, ed. M. Sigwarth, p.445
- Rutten, R. J., de Wijn, A. G., & Sütterlin, P. 2004, *A&A*, 416, 333
- Rybák, J., Wöhl, H., Kučera, A., Hanslmeier, A., & Steiner, O. 2004, *A&A*, 420, 1141
- Sánchez Almeida, J. , Asensio Ramos, A., Trujillo Bueno, J., Cernicharo, J. 2001, *ApJ*, 555, 978
- Sánchez Almeida, J. 2003, in *AIP Conf. Proc., Solar Wind 10*, ed. M. Velli, R. Bruno, & F. Malara (Melville: AIP), Vol. 679, p. 293
- Sánchez Almeida, J., Domínguez Cerdeña, I., Kneer, F. 2003, *ApJ*, 597, 177

- Sánchez Almeida, J. 2004, in *The Solar-B Mission and the Forefront of Solar Physics*, ASP Conf. Ser., ed. T. Sakurai and T. Sekii, Vol. 325, p. 115
- Sánchez Almeida, J., Márquez, I., Bonet, J. A., Domínguez Cerdeña, I., Muller, R. 2004, *ApJ*, 609, 91
- Sánchez Cuebas, M., Vázquez, M., Bonet, J. A., & Sobotka, M. 2002, *ApJ*, 570, 886
- Sankarasubramanian, K., Rimmele, Thomas 2003, *ApJ*, 598, 689
- Scharmer, G. B., Kiselman, D., Löfdahl, M. G., Rouppe van der Voort, L. H. M. 2003, ASP Conference Series 307, in *Proc. Third International Workshop on Solar Polarization*, ed. J. Trujillo-Bueno and J.S. Almeida, Tenerife, Canary Islands, Spain
- Scharmer, G. B., Dettori, P. M., Peter, M., Löfdahl, M. G., & Shand, M. 2003, in *Proc. SPIE Vol. 4853, Innovative Telescopes and Instrumentation for Solar Astrophysics*, ed. S. L. Keil & S. V. Avakyan, p.370
- Schatten, K. H., Mayr, H. G., Omidvar, K., Maier, E. 1986, *ApJ*, 311, 460
- Scherrer, P. H., Bogart, R. S., Bush, R. I., Hoeksema, J. T., Kosovichev, A. G., Schou, J., Rosenberg, W., Springer, L., Tarbell, T. D., Title, A., Wolfson, C. J., Zayer, I., MDI Engineering Team 1995, *Solar Phys.*, 162, 129-188
- Schrijver, C. J. & Title, A. M. 2003, *ApJ* 597, 165
- Schulz, T.J. 1993, *Journal of the Optical Society of America*, A 10, 1064
- Schmidt, W., & Balthasar, H. 1994, *A&A*, 283, 241-246
- Schrijver, C. J., Zwaan, C. *Solar and Stellar Magnetic activity*, Cambridge Univ. Press, Cambridge, UK
- Schüssler, M., Shelyag, S., Berdyugina, S., Vögler, A., Solanki, S. K. 2003, *ApJ*, 597, 173
- Seldin, J. H., & Paxman, R. G. 1994, in *Proc. SPIE*, Vol. 2302, p. 268-280, *Image Reconstruction and Restoration*, ed: T. J. Schulz & D. L. Snyder
- Sheeley, N. R. 1967, *Sol. Phys.*, 1, 171
- Sheeley, N. R. 1971, *Sol. Phys.*, 20, 19
- Shelyag, S., Schüssler, M., Solanki, S. K., Berdyugina, S. V., & Vögler, A. 2004, *A&A*, 427, 335
- Shelyag, S. 2004, PhD thesis, University of Göttingen, Germany, <http://www.solar-system-school.de/alumni/shelyag.pdf>
- Simmons, G. J.; Blackwell, D. E. 1982, *A&A*, 112, 209
- Simon, G. W., Zirker, J. B. 1974, *Sol. Phys.*, 35, 331

- Solanki, S. K., Stenflo, J. O. 1985, A&A, 148, 123
- Solanki, S. K. 1986, A&A, 168, 311
- Solanki, S. K. 1987, Ph.D. Thesis, ETH, Zürich
- Solanki, S. K., 1987, The Photospheric Layers of Solar Magnetic Flux Tubes, Ph.D. Thesis, Zürich
- Solanki, S. K., Steiner, O., Uitenbroek H. 1991, A&A, 250, 220
- Solanki, S. K., Brigljevic, V. 1992, A&A, 262, 29
- Solanki, S. K., Rüedi, I. & Livingston, W. 1992, A&A, 263, 312
- Solanki, S. K. 1993, Space Science Review, 63, 1
- Solanki, S. K., Bruls, J. H. M. J. 1994, A&A, 286, 269
- Solanki, S. K., Rüedi, I., Bianda, M., Steffen, M. 1996, A&A, 308, 623
- Solanki, S. K., Steiner, O., Buente, M., Murphy, G., Ploner, S. R. O. 1998, A&A, 333, 721
- Spruit, H. C. 1976, Solar Physics, 50, 269
- Spruit, H. C. 1979, Solar Physics, 61, 363
- Spruit, H. C., Zwaan, C. 19781, Solar Physics, 70, 207
- Steffen, M., Ludwig, H.-G., Krüss, A. 1989, A&A, 213, 371
- Stein, R. F., Nordlund, Å 1989, ApJ, 342, 95
- Stein, R. F., Nordlund, Å 1998, ApJ, 499, 914
- Stein, R. F., Nordlund, Å 2002, in Magnetic Coupling of the Solar Atmosphere Euroconference and IAU Colloquium 188, ed. H. Sawaya-Lacoste, ESA SP-505 (Noordwijk, Netherlands), 83
- Steiner, O. 1990, in Solar Photosphere: Structure, Convection and Magnetic Fields, ed. J. O. Stenflo, IAU-Symp. No. 138, Kluwer, Dordrecht, p. 181
- Steiner, O., Grossmann-Doerth, U., Knölker, M., Schüssler, M. 1998, ApJ, 495, 468
- Steiner, O., Hauschildt, P., & Bruls, J. 2001, A&A, 372, 13
- Steiner, O., Hauschildt, P., & Bruls, J. 2003, Astron. Nachr., 324, 398
- Steiner, O. 2005, A&A, 430, 691
- Stenflo, J. O. 1973, Sol. Phys., 32, 41
- Stenflo, J. O. 1982, Sol. Phys., 80, 209

- Stenflo, J. O. 1993, in *Solar Magnetic Fields*, ed. M. Schüssler & W. Schmidt (Cambridge University Press), 301
- Sütterlin, P., Wiehr, E., Stellmacher, G. 1999, *Sol. Phys.*, 189, 57
- Tarbell, T. D., Title, A. M. 1977, *Sol. Phys.*, 52, 13
- Title, A. M., Berger, T. E. 1996, *ApJ*, 463, 797
- Topka, K. P., Tarbell, T. D., Title 1992, *ApJ*, 396, 351
- Topka, K. P., Tarbell, T. D., Title 1997, *ApJ*, 484, 479
- Trujillo Bueno, J. 1990, in *New Windows to the Universe*, ed. F. Sánchez & M. Vázquez, Cambridge University Press, 1, 119
- Trujillo Bueno, J., Shchukina, N., Asensio Ramos, A. 2004, *Natur.*, 430, 326
- Tritschler, A., Schmidt, W., Rimmele, T. 2002, In: *Solar variability: from core to outer frontiers. The 10th European Solar Physics Meeting, 9 - 14 September 2002, Prague, Czech Republic*. Ed. A. Wilson. ESA SP-506, Vol. 1. Noordwijk: ESA Publications Division, ISBN 92-9092-816-6, 2002, p. 477 - 478
- Tritschler, A. 2000, PhD thesis, Kiepenheuer-Institut für Sonnenphysik, Germany
- Trujillo Bueno, J., Shchukina, N., Asensio Ramos, A. 2004, *Natur.*, 430, 326
- Uitenbroek, H., Tritschler, A., *Apj* (submitted.)
- van Ballegooijen, A. A., Nisenson, P., Noyes, R. W., Löfdahl, M. G., Stein, R. F., Nordlund, Å., Krishnakumar, V. 1998, *ApJ*, 509, 435
- Vögler, A., Schüssler, M. 2003, *Astron. Nachr.*, 324,399
- Vögler, A., Shelyag, S., Schüssler, M., Cattaneo, F., Emonet, T., & Linde, T. 2003, *IAUS*, 210, 157
- Vögler, A. 2003, PhD thesis, University of Göttingen, Germany, <http://www.solar-system-school.de/alumni/voegler.pdf>
- Vögler, A., Shelyag, S., Schüssler, M., Cattaneo, F., Emonet, T., & Linde, T. 2005, *A&A*, 429, 335
- Walton, S. R., Preminger, D. G., & Chapman, G. A. 2003, *ApJ*, 590, 1088
- Wang, H., Spirock, T., Goode, P. R., Lee, C., Zirin, H., Kosonocky, W. 1998, *ApJ*, 495, 957
- Wang, H., Zirin, H. 1987, *Sol. Phys.*, 110, 281
- Weiss, N. O., Brownjohn, D. P., Matthews, P. C., & Proctor, M. R. E. 1996, *MNRAS*, 283, 1153

Wenzler, T., Solanki, S. K., Fluri, D. M., Frutiger, C., Fligge, M., & Ortiz, A. 2002, in Proceedings of the SOHO 11 Symposium on From Solar Min to Max: Half a Solar Cycle with SOHO, 11-15 March 2002, Davos, Switzerland, ed. A. Wilson, ESA SP-508, Noordwijk, p. 231

Wiehr, E. 1978, *A&A*, 69, 279

Wiehr, E., Bovelet, B., & Hirzberger, J. 2004, *A&A*, 422, 63

Woo, R., Habbal, S. R. 1997, *Geophys. Res. Lett.*, 24, 1159

Zayer, I., Stenflo, J. O., Keller, C. U., Solanki, S. K. 1990, *A&A*, 239, 356

Acknowledgements

The present PhD thesis has been written at the Max Planck Institute for Solar System Research, Katlenburg-Lindau. I thank the directors of the institute for offering me the possibility to study and work in the nice and creative environment of the institute. Financial support of the Max Planck Society is gratefully acknowledged.

Special thanks to my supervisors, Prof. S. K. Solanki and Dr. A. Gandorfer, for offering me the topic, which I have been working on, for their kind help and discussions during my PhD project and professional filtering out all crazy scientific ideas visiting my head sometimes. I thank my university supervisor, Prof. F. Kneer, for the possibility to defend my thesis at the University of Göttingen, for the seminars in the University Observatory and for helpful discussions. Many thanks to all of them for a very painstaking revision of the present thesis.

I would like to express my special gratitude to M. Löfdahl for teaching me many numerical tricks of contemporary phase diversity image reconstruction algorithms and for providing his code. Many thanks to A. Tritschler for her careful and very helpful introduction into the mathematical concepts of phase diversity and for discussions of the optical setup for my observations at the VTT. Many thanks for useful discussion concerning phase diversity to J. Bonet, C. Keller and O. von der Lühe.

I deeply appreciate the help of S. Berdyugina, S. Shelyag, M. Schüssler and S. Solanki in numerical modeling. Many thanks to R. Cameron and A. Vögler for providing me their MHD models.

An important part of my PhD study were several observational campaigns at the 1-m Swedish Solar Telescope on La Palma, without which the fulfilment of this thesis would be impossible. My greatest respect and thanks goes to G. Scharmer, the director of the observatory, who permitted my observations with this amazing telescope and to all technical staff of the observatory, P. Detori and R. Keizer. Many thanks to them for the tolerance and for the constant willingness to help in any technical problems.

In my PhD education I was participating in the seminars and other events of the International Max Planck Research School on Physical Processes in the Solar System and Beyond, for which I would like to thank the coordinator of the school, Dr. D. Schmidt.

Thank God, my parents and my real friends without who I would never exist.

Lebenslauf

Name: Vasily Zakharov

Geburtstag: 01. 01. 1978

Geburtsort: Moskau, Russland

Eltern: Nikolai Nikiforov
Sofia Nikiforova

Staatsbürgerschaft: russisch

Schulbildung: 9/1984–6/1995 Schule No 1249, Moskau

Studium: 9/1995–1/2001 Physikstudium an der Physikalischen
Fakultät der Staats-Universität Moskau,
Abteilung für Optik und Spektroskopie

9/1998–6/1999 Bachelorarbeit: “Propagation of the laser radiation
in the bottom atmosphere of the Earth”

9/1999–11/2000 Diplomarbeit: “Plasma-chemical reactor with
a controlled electronic component of plasma
on basis of non-self-sustained discharge”

1/2001–12/2002 Wissenschaftlicher Mitarbeiter des P. N. Lebedev
Instituts für Physik der russischen Akademie
der Wissenschaften, Moskau

1/2003–1/2006 Doktorarbeit am Max-Planck-Institut für
Sonnensystemforschung, Katlenburg-Lindau.